July 28, 2025

VIA EMAIL

Mr. John Clark, Chair
Menhaden Management Board
c/o Atlantic States Marine Fisheries Commission
1050 N. Highland Street, Suite 200 A-N
Arlington, VA 22201

RE: The Menhaden Work Group Report and Menhaden Technical Committee Tasking at the ASMFC Summer Meeting

Dear Chairman Clark:

In terms of the undoubted travails facing osprey in and around the Chesapeake Bay, there has been an inordinate amount of focus on menhaden generally, and the reduction fishery in particular. As the recent, record setting hypoxic zone in the upper and mainstem Chesapeake Bay,[1] coupled with the notable increase in the numbers of southern stocks like cobia, red drum, and Spanish mackerel, demonstrates,[2] the Bay is an ecosystem in the midst of change. While there is a tendency to look for easy answers, the likelihood is that there are a multitude of potential causes, as U.S. Geological Survey (USGS) osprey scientists recently pointed out.[3]

This tendency is apparent in the Menhaden Board's Atlantic Menhaden Work Group on Precautionary Management in Chesapeake Bay (Work Group) report. Rather than attempt to investigate the issue, the group charged forward with draconian management recommendations "without determining if there is or is not an adequate supply of menhaden to support predatory demand in the Bay." (Work Group Rpt., at 1.) Moving forward with such actions without investigating whether there are, in fact, fewer menhaden in the Bay or whether the fishery has

---

[1] Maryland Dept. of Nat. Res., "Chesapeake Bay Monitoring Shows Hypoxia Increased in June After Rainy May," (July 16, 2025), https://news.maryland.gov/dnr/2025/07/16/chesapeake-bay-monitoring-shows-hypoxia-increased-in-june-after-rainy-may/.

[2] Atl. Menhaden Work Group on Precautionary Mgmt. in Chesapeake Bay, "Precautionary Management in the Chesapeake Bay," ("Work Group Rpt."), at 17 (Apr. 23, 2025), https://asmfc.org/resources/management-technical-committee/atlantic-menhaden-work-group-report-on-chesapeake-bay-precautionary-management-april-2025//.

[3] Menhaden Fisheries Coal., "USGS Challenges Simple Narrative Linking Menhaden to Osprey Decline," (May 5, 2025), www.accessnewswire.com/newsroom/en/food-and-beverage-products/usgs-challenges-simple-narrative-linking-menhaden-to-osprey-decline-1023783.

any impact on osprey, risks gravely impacting a more than a 150-year-old industry and hundreds of jobs while doing nothing to improve the osprey situation.

From the agenda for the Atlantic States Marine Fisheries Commission's (ASMFC) Summer Meeting, it appears that the Menhaden Board may be preparing to task the Technical Committee (TC) to investigate issues raised by the Work Group Report. The Board should be mindful that the TC already has a significant amount of work ahead of the Annual Meeting, such as bringing the bait catch-at-age up to date and preparing projections. That said, there are several areas of science upon which the TC can usefully provide insights which would be useful in helping the Board determine an appropriate course of action.

1. **Is the phenomenon of reduced osprey production confined to the times and areas in which the menhaden reduction fishery operates?**

When the USGS gave its presentation to the Menhaden Board at its 2024 Summer Meeting, Dr. Ziolkowski, Jr. and Dr. Rattner indicated recent declines in osprey populations in California, Washington, Massachusetts, Florida, and North Carolina (following, as in the Bay, significant increases). Only New Jersey showed recent increases.[4] That presentation also contained a graphic that used data from Cornell University's eBird database that shows a net decline of osprey abundance in the Chesapeake Bay and the Maryland and Virginia coasts between 2012-2022 and increases in interior regions. USGS, at 5.

On a broader scale, more recent data from the eBird database shows a similar trend from Delaware to the mid-Florida coast[5]:

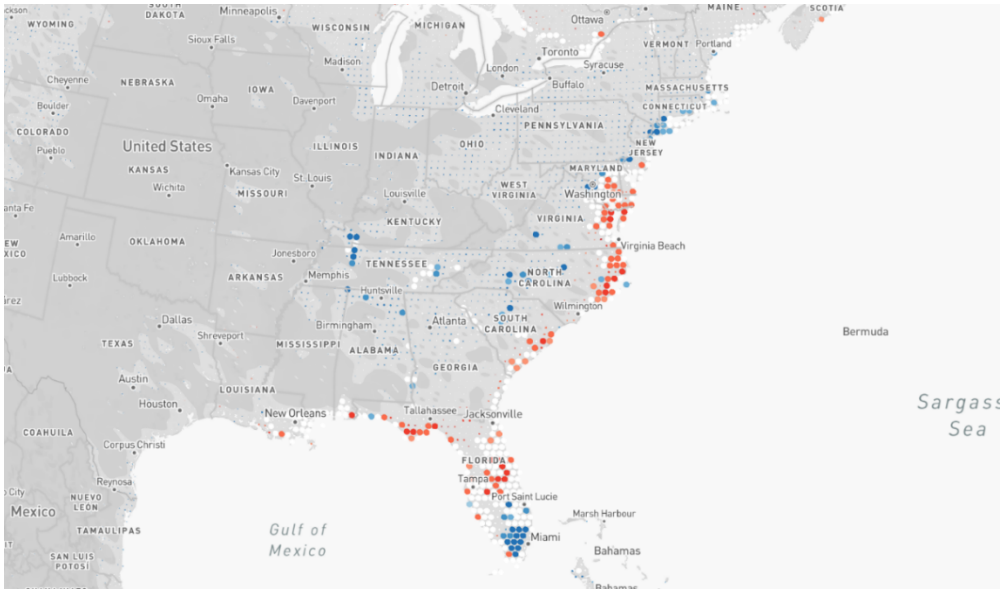

[4] USGS, Osprey in the Chesapeake, Life History, Reproduction, Population, Diet and Stressors, at 6 (2024), https://asmfc.org/wp-content/uploads/2025/01/AtlanticMenhadenBoardPresentations_Aug2024.pdf.

[5] Cornell Lab of Ornithology, Osprey *Pandion haliaetus,* Trends 2012-2022, https://science.ebird.org/en/status-and-trends/species/osprey/trends-map.

Finally, Dr. Bryan Watts of the Center for Conservation Biology at William & Mary University recently issued a news advisory indicating a 90% decline in ospreys nesting along the seaside of the Virginia portion of the Delmarva Peninsula between 1987 and 2025.[6] According to the USGS, migrant osprey arrive in the region from late February to early March, and begin building nests from mid-March to Mid-April (USGS 2024). The menhaden reduction fishery historically has not begun fishing until the first Monday in May or later (and cannot, by law, fish in Virginia waters before then), raising a question as to how the fishery could be influencing osprey's months-earlier decisions about where they nest.

This information suggests a useful question for the TC to investigate:

- Is the most likely cause of large-scale shifts in osprey populations from parts of the Atlantic coastal region to interior riverine habitats the menhaden reduction fishery, or may climate change-induced environmental factors such as increased severe storms, excessive heat, changes in prey distribution, etc., be playing a role?

2. What other species of bird and fish in the Bay have significant dependence on menhaden and are those species showing signs of food stress in a manner similar to osprey?

Were there a decline in the number of menhaden inhabiting the Chesapeake Bay generally, or if the reduction fishery, operating at its current historically low levels, was adversely impacting osprey, it seems likely that other predators which depend on menhaden would likewise be affected. In this regard, the Work Group Report provides useful information.

While striped bass are typically referred to as "menhaden dependent," a stomach contents study conducted from 2002 to 2020 indicate that bay anchovy make up 33% of their diet by weight, with menhaden comprising just under 16%. Nonetheless, according to both the Virginia Marine Resources Commission (VMRC) and Maryland's Department of Natural Resources (DNR), indices "would indicate the [striped bass] are not starving and would be considered healthy."[7]

The Report also discusses food habit data for other populations of fish that are (or appear to be, based on fishery-dependent data) increasing in the Chesapeake, including cobia, red drum,

---

[6] Dr. Bryan Watts, News Advisory (June 16, 2025), https://ccbbirds.org/2025/06/16/osprey-population-along-the-seaside-of-the-delmarva-peninsula-has-collapsed/.

[7] Work Group Rpt., at 23. VMRC uses "Fulton's Condition Factor," as explained in the report. Maryland DNR has its "traffic light index," which makes relative judgements about various facets of the Bay's menhaden and striped bass population, including striped bass condition. MD DNR, "Traffic light index (TLI) of forage balance of Atlantic Menhaden and resident Striped Bass in Maryland's portion of Chesapeake Bay - update through 2024," https://dnr.maryland.gov/fisheries/Documents/TLI%202025%20update.pdf. Each index supports the Work Group Report's finding that striped bass "[c]onditions appear to be trending upward." (Work Group Rpt., at 23.)

spotted seatrout, and Spanish mackerel. (Work Group Rpt., at 36 (Table 5).) Of these species, only cobia does not appear to heavily rely on menhaden. By contrast, menhaden have been found to make up from between 9% to as much as 40% of the diet of red drum, spotted seatrout, and Spanish mackerel, by weight, depending on the life stage and area studied.[8] The growing population of blue catfish is not dependent on menhaden, but studies of adult catfish in the upper portions of Virginia major tributaries (James, York and Rappahannock Rivers) found menhaden comprised 0.425 to 5.00% of blue catfish diet by weight." (Work Group Rpt., at 22.)

Populations of weakfish and bluefish – both predator species included in the Ecological Reference Point model – are in decline in the Chesapeake Bay. Both these species, however, are far less dependent on menhaden than those that appear to be taking their place in this estuary. Food habits studies show that menhaden comprise just 5% of bluefish diet by weight, while the same figure for weakfish is less than 1% (although that is "possibly due to truncation of the weakfish size range associated with high natural mortality of Age 1+ fishes.").[9] Nonetheless, across the full suite of fish predators in the Bay, the Report concludes: "In general, the health index measured by Fulton's Condition Factor, seems to be slightly increasing or stable for all species, suggesting the health of these species over time has not changed substantially." (Work Group Rpt., at 23.)

Likewise, there have been increases in avian predators of menhaden. "Double-crested cormorants and brown pelicans are two additional predators of menhaden whose numbers are increasing in Chesapeake Bay. Atlantic menhaden make up 50-55% of the diet of cormorants and 74% of the diet of brown pelicans by weight." (Work Group Rpt., at 16.) The scale of the increases in the populations of these significant predators is detailed in the Report (pages 16-17), but the increases have been exponential.

The increases in populations of menhaden predators since at least the turn of the century suggests this line of inquiry:

- Is it more likely that ospreys are being outcompeted or or that the reduction fishery uniquely impacts osprey, even though it generally does not operate in areas where brooding success has been poor during the critical time-period in the breeding season?[10]

[8] Work Group Rpt., at 20-22. Few of these studies were undertaken in in the Chesapeake Bay, so these results should be interpreted with caution.

[9] Work Group Rpt., at 19-20.

[10] See Work Group Rpt., at 42-45.

3. What role might the increase in the population of bald eagles throughout the Chesapeake Bay region in recent declines of osprey?

Maryland DNR just published a release announcing large increases in the state's bald eagle population.[11] A myriad of studies have noted the relationship between bald eagles and osprey, often referring to eagles as "kleptoparasitic" for their tendency to attack hunting osprey to steal their food and prey on osprey adults, young, and eggs.[12] A recent study goes so far as to suggest that increasing eagle populations can have a "top-down" adverse impact on competitors, including osprey.[13]

This study looked at recovering populations of bald eagles, ospreys, and great blue herons that repatriated Voyageurs National Park in northern Minnesota during the mid-20th century. The authors found that "[i]ncreased numbers of eagles were associated with a reduction in the numbers of osprey nests, their nesting success and heronry size." The authors were unable to determine the exact top-down mechanisms resulting in this relationship, noting that osprey would nest in proximity to eagles. They surmise that ospreys "were likely impacted by eagles outside their local surroundings, including non-breeding individuals," through kleptoparasitism and predation.

Voyageurs National Park is a different type of ecosystem (freshwater lakes) than the Bay and it is apparent that, for a long period of time, each of these species increased their repatriation of the area in tandem. This suggests a possibility that a localized abundance of bald eagles can reach a tipping point after which they may be able to exert top-down effects on osprey. Notably, the USGS also noted issues of intraspecific competition between bald eagles and osprey in its presentation. (USGS 2024). There is significant scientific and anecdotal evidence of the dominant and adverse impacts eagles have on osprey, suggesting a reasonable line of inquiry would be:

- Can issues of competition and depredation be ruled out as a cause of osprey's lack of breeding success, given that (i) bald eagles are kleptoparasitic and known to be particularly aggressive with osprey; and (ii) there are increasing populations of other piscivorous bird and fish species in the Chesapeake Bayad?

---

[11] MD DNR, "A Soaring Success: Maryland's Bald Eagle Population Recovery" (July 3, 2025), https://news.maryland.gov/dnr/2025/07/03/a-soaring-success-marylands-bald-eagle-population-recovery/

[12] See, for example, Bierregaard, R. O., Poole, A. F., Martell, M. S., Pyle, P., & Patten, M. A. (2016). Osprey (*Pandion haliaetus),* version 2.0. In P. G. Rodewald (Ed.), *The birds of North America.* Ithaca, NY: Cornell Lab of Ornithology; Prevost, Y. A. (1977). *Feeding ecology of ospreys in Antigonish County, Nova Scotia.* Masters M.Sc., McGill University, Montreal, QC, Canada; Vennesland, R. G., & Butler, R. W. (2011). Great blue heron (*Ardea herodias),* version 2.0. In A. F. Poole (Ed.), *The birds of North America.* Ithaca, NY: Cornell Lab of Ornithology.

[13] Cruz, Jennyffer, et al. "Top-down effects of repatriating Bald Eagles hinder jointly recovering competitors." *Journal of Animal Ecology* 88.7 (2019): 1054-1065.

4. What role could climate change, water temperature, dissolved oxygen levels, shoreline hardening, and other environmental factors play in the local abundance of menhaden and other forage species?

Fisheries managers have grappled with the issue of climate change and its effects on fisheries and the ecosystem. Stocks are shifting—for example the noted increase in red drum and Spanish mackerel in the Chesapeake Bay. Waters are warming. Storms are becoming more frequent and more destructive. The timing of migration for many species is changing.[14] All these impacts are well recognized and the subject of intense study.

As noted above, significant portions of the Chesapeake Bay were subject to extremely low dissolved oxygen in the critical rearing season for young osprey (June and July) this year and last. In 2023, the Forage Action Team (part of the NOAA Chesapeake Bay Program) found that "that the abundance of key forage species decreases when 10 to 30% of the shoreline is hardened."[15] As it is so shallow, the Bay is particularly vulnerable to warming, and the impacts of more frequent, and intense storms (as well as sea level rise).[16] Any or all of these factors can influence the local distribution of forage within the Bay, as well as foraging success.

Thus, the Technical Committee could be asked to consider the following question (while recognizing that this line of inquiry is wide-ranging, intensive, and may not lead to definitive answers):

- Noting that Watts (2024) found that deliveries of all forage species to osprey nests declined steadily from 1974 to 2021,[17] is it possible, or even likely, that ospreys' apparent lack of foraging success is tied to changes in local conditions that are impacting either local abundance of forage or osprey's hunting success?

---

[14] See, for example, Peer, A. C., and T. J. Miller. "Climate change, migration phenology, and fisheries management interact with unanticipated consequences." *North American Journal of Fisheries Management* 34.1 (2014): 94-110; Crear, Daniel P., et al. "Estimating shifts in phenology and habitat use of cobia in Chesapeake Bay under climate change." *Frontiers in Marine Science* 7 (2020): 579135; Wood, Robert J., Donald F. Boesch, and Victor S. Kennedy. "Future consequences of climate change for the Chesapeake Bay ecosystem and its fisheries." *American Fisheries Society Symposium*. Vol. 32. 2002.

[15] NOAA CBP, Forage Action Team, "Forage Status and Trends Report for the Chesapeake Bay," at 17 (Nov. 2023), https://www.chesapeakebay.net/what/publications/forage-status-and-trends-report.

[16] See, for example, Rezaie, Ali Mohammad, et al. "Quantifying the impacts of storm surge, sea level rise, and potential reduction and changes in wetlands in coastal areas of the Chesapeake Bay region." *Natural Hazards Review* 22.4 (2021): 04021044; St. Laurent, Kari A., Victoria J. Coles, and Raleigh R. Hood. "Climate extremes and variability surrounding Chesapeake Bay: Past, present, and future." *JAWRA Journal of the American Water Resources Association* 58.6 (2022): 826-854; Du, Jiabi, et al. "Worsened physical condition due to climate change contributes to the increasing hypoxia in Chesapeake Bay." *Science of the Total Environment* 630 (2018): 707-717.

[17] Watts, Bryan D., et al. "Demographic response of osprey within the lower Chesapeake Bay to fluctuations in menhaden stock." *Frontiers in Marine Science* 10 (2024): 1284462. Notably, menhaden comprised a higher percentage of delivers in 2021 compared to 2006-07, albeit at a lower absolute rate.

# # # #

The commission must be guided by science. Precipitous actions, taken in the name of precaution, are not always harmless. Neither Ocean Harvesters nor Omega Protein can survive without the current low level of access to the menhaden resource in the Bay. There simply are not enough "fishable days" – that is, days where the weather and sea conditions allow vessels to operate – in a year to safely conduct a profitable fishery solely in the ocean.

The menhaden fishery is managed in the most conservative manner in its 150 year or so history, and the reduction fishery is operating at its lowest sustained levels – in the Bay and overall – for as long as we have reliable records (*i.e.*, since the 1950s). Precaution is already the policy. Before taking actions that could cause irreversible economic harm to this historic fishery, the Board should ensure that all reasonable avenues of inquiry into the issues facing osprey are explored. Thank you for your time and attention.

Sincerely,

Peter Himchak
Senior Scientific Advisor, Omega Protein Corp.

July 29, 2025

Robert Beal, Executive Director
John Clark, Management Board Chair
Atlantic States Marine Fisheries Commission
1050 N. Highland Street, Suite 200 A-N
Arlington, VA 22201
rbeal@asmfc.org
john.clark@delaware.gov

Re: Atlantic Menhaden Revised Natural Mortality Rate Estimate

Dear Messrs. Beal and Clark,

We are writing to follow up on our letters of October 31, 2024, and February 28, 2025, to Mr. Beal regarding the science underlying the Atlantic menhaden stock assessment.[1] In these letters, we brought to the ASMFC's attention new analysis in a draft manuscript undergoing peer review for publication by Drs. Jerry Ault and Jiangang Luo. This analysis shows that the menhaden stock assessment science is fundamentally flawed due to significant mistakes affecting the natural mortality rate (M) estimate used in the stock assessment model since 2019 (SEDAR 69). We explained that these mistakes resulted in a substantial overestimation of M, which in turn likely drove a substantial underestimation of fishing mortality rates and an overestimation of the coastwide stock size and allowable catch for the fishery. As a result, overfishing of Atlantic menhaden has likely been occurring. Our previous letters also summarized the ASMFC's legal obligations under the Atlantic Coastal Fisheries Cooperative Management Act (ACFCMA) and the ASMFC's Rules and Charter that all Interstate Fishery Management Plans be based on the best available science (BAS) and prevent overfishing.

We thank you, Mr. Beal, for your responses, as well as to the SAS M Working Group for discussing Drs. Ault & Luo's analyses. While these discussions resulted in the admission of several significant mistakes and partial correction in the M estimate, the SAS declined to correct at least one critical mistake and further declined to reduce M to the level recommended by Drs. Ault & Luo. As a result, the overestimation of M persists, even with the Atlantic Menhaden Stock Assessment Subcommittee's (SAS) newly revised M estimate (from M=1.17 to M= 0.92). Further, it appears that staff leading the SAS analysis adjusted other critical model parameters, particularly the assumption for recruitment, which effectively offset the impact of the lower M estimate. Based on these adjustments, remarkably, the SAS concluded that even though M has been overestimated by at least 21 percent since 2019, the Atlantic menhaden stock is not overfished, overfishing is not occurring, and they project that continuing to fish at the current level presents little risk to the Atlantic menhaden resource. These conclusions are surprising, to say the least, and we are gravely concerned.

What is most concerning is that if Drs. Ault & Luo are correct that the M estimate should be even lower (M=0.52) because of a remaining uncorrected mistake in the analysis relied upon by the SAS (specifically, modeling time-area magnet efficiency as constants)—and the data and all

[1] Enclosed for reference.

other indicators suggest that Drs. Ault & Luo are correct—not only is it likely that overfishing has been occurring and that Atlantic menhaden are overfished, but the coastwide stock size could be only a fraction of the SAS estimate, perhaps as low as one quarter of the unfished biomass. The implications for Atlantic menhaden and the East Coast ecosystem are profound.[2] Because Atlantic menhaden is the key forage stock in the ASMFC's ecological reference point (ERP) model, menhaden stock assessment mistakes can ripple through other ASMFC assessments such as those for striped bass, the most valuable recreational gamefish in the country.

For these reasons, we request that you take steps to ensure a thorough and independent review of the SAS's work in view of the Ault & Luo analysis—in particular, the SAS's extraordinary findings regarding the appropriate M estimate and the status of the Atlantic menhaden resource. First, we understand that Drs. Ault & Luo's manuscript has been updated to reflect their significant engagement with the SAS and that publication is pending. To help ensure the August 12-15 Ecological Reference Point Peer Review fully examines these issues please include this letter and Drs. Ault & Luo's published paper or the most recent draft manuscript in the Peer Review materials. Second, please ensure that Drs. Ault & Luo's recommended M of 0.52 be included as a sensitivity run in the Beaufort Assessment Model (BAM)[3] and that the results – including impact on biomass and stock status - be available for consideration and adoption by the Menhaden Board. Note that the SAS stated it would introduce the Ault & Luo M analysis into the Peer Review through its inclusion as a sensitivity run, however this sensitivity run was not presented or discussed at the July SAS Technical Committee (SAS TC) meeting, nor were the full impacts of a lower M discussed. Third, please ensure that all of these materials are available to the Board and the ASMFC so that these management bodies can consider them and make their final decisions consistent with their legal duties to rely on the best available science and prevent overfishing.

Finally, as noted in our prior letters, Drs. Ault & Luo have raised concerns about the adoption of the extreme statistical outlier M recommended in the paper by Liljestrand, Wilberg & Schueller (2019)[4] since its inclusion in the 2019 SEDAR 69 benchmark stock assessment. Although the SAS M Working Group, SAS TC, and ERP Working Group discussed Drs. Ault & Luo's analyses and acknowledged some of the critical mistakes made by Liljestrand, Wilberg & Schueller, some of these authors also actively participated in the meetings, dominating much of the analysis and discussion and resisting Drs. Ault & Luo's findings. It is critical to prevent conflicts of interest and ensure impartiality in the Peer Review of the Atlantic menhaden M estimate and 2025 stock assessment. Thus, the authors of the Liljestrand, Wilberg & Schueller paper should be recused from participating in the Peer Review and additional related processes leading to the Board and ASMFC's final decisions. The ASMFC and NOAA Fisheries must

---

[2] Especially given there is an East Coast "forage fish crisis" as all critical forage species (i.e., Atlantic herring, Atlantic mackerel, blueback herring, alewife, and shad) are also severely overfished (depleted).

[3] BAM is the model used for the menhaden single species stock assessment, and the outputs from BAM, including the rate of natural mortality, serve as the baseline for the ERP assessment.

[4] Liljestrand EM, Wilberg MJ and Schueller AM (2019). Estimation of movement and mortality of Atlantic menhaden from 1966 to 1969 using a Bayesian multi-state mark-recovery model. *Fisheries Research* 210: 204-2013. Based on the mistakes acknowledged to date, let alone the remaining impactful mistake in magnet tag recovery efficiency, in our opinion the authors should retract the paper.

ensure that the best available science is used for management of Atlantic menhaden. Additional details are provided below.

The SAS Corrections and Revised M

Drs. Ault & Luo analyzed the data, model and results contained in the Liljestrand, Wilberg and Schueller paper related to the NMFS 1966-71 mark-recapture study, including the paper's recommended M that was adopted for use in the benchmark Atlantic menhaden single species stock assessment in 2019 (SEDAR 69). The Ault & Luo analysis identified at least five significant mistakes made in the Liljestrand, Wilberg & Schueller paper affecting its recommended M including: (1) overstated tag releases; (2) underreported tag recoveries; (3) overstated primary magnet tag recovery efficiency; (4) underreported annual fishing effort[5]; and (5) modeled time-area magnet efficiency as constants. The SAS agreed with much of the Ault & Luo analysis and addressed the first four significant mistakes, concluding that the current M adopted by ASMFC from the Liljestrand, Wilberg & Schueller paper was too high and should be revised downward from M = 1.17 to 0.92.

However, Drs. Ault & Luo's analysis concludes that the SAS' revised M is still almost double what it should be: M = 0.52. Initially, the SAS attributed the difference between the M estimate recommended by Drs. Ault & Luo to their inability to access confidential fishing effort data.[6] However, despite the lack of access to the allegedly confidential 55 year old industry data, Drs. Ault & Luo's method for generating nominal fishing effort by month and area effectively characterized effort during the period of the mark-recapture study. The SAS M Working Group determined Drs. Ault & Luo's effort characterization to be 99 percent accurate compared to the confidential fishing effort data. Comparative analyses with SAS showed that weighting the average area efficiencies by catches in the "constant" method produced minute differences (~2.2%) in estimated M in comparison to the SAS estimate. Thus, the lack of access to the confidential fishing effort data had a minimal effect on their results. Despite this, at the July 2025 SAS TC meeting the SAS presentation continued to highlight the data access issue as though it compromised Ault & Luo's analysis, instead of objectively presenting the competing approaches to magnet tag recovery efficiency as the basis for the difference.

The Remaining Uncorrected Mistake -- Magnet Tag Recovery Efficiency

After agreeing on the first four highlighted mistakes in the Liljestrand, Wilberg & Schueller paper, the only significant remaining factor accounting for the difference between the SAS's new

---

[5] Fishing effort was under-reported by Liljestrand, Willberg and Schueller by an annual average of -47.8 percent.

[6] This data was requested by Drs. Ault & Luo but was not provided by NMFS because the fishing industry (Ocean Harvesters) refused to authorize its release, despite the fact these data are over 55 years old and unlikely to include any information that reasonably can be considered confidential business information. The Atlantic ecosystem and menhaden fishery have changed significantly in the past 55 years. Further, Ocean Harvesters is (supposedly) not even the same fishing company that originally collected the data; that was Omega Protein. Failure to provide the fishery data in support of improving fisheries science for management is inconsistent with the intent of the Magnuson-Stevens Act's confidentiality provisions, which did not even exist at the time of the mark-recapture study. 16 U.S.C. § 1801 et seq. (1976), 16 U.S.C. § 1881a(b) (1996). Refusal to provide the data is also in conflict with the Magnuson-Stevens Act's and ASMFC's mandate to ensure conservation and managements measures be based on the best available scientific information available and that management be in the public interest. 16 U.S.C. § 1801(c)(3); 16 U.S.C. § 5104(a)(2). Drs. Ault & Luo are renewing their request for this data through a formal FOIA request.

recommended M=0.92 and Drs. Ault & Luo's recommended M=0.52 results from the SAS failure to apply the most scientifically sound method to correct the Liljestrand, Wilberg & Schueller approach to magnet tag recovery efficiency at the menhaden reduction plants. As explained by Drs. Ault & Luo, the Liljestrand, Wilberg & Schueller analysis incorrectly applied simple weighted arithmetic averages of magnet efficiency by area over time.[7]

A key decision in the analysis was how to best represent plant magnet efficiencies in the estimation process. Rather than relying on simple parametric averages of random non-parametric distributions of plant- and area-specific magnet efficiencies, Drs. Ault & Luo incorporated all the empirical data to ensure a comprehensive estimation framework for natural mortality. Integrating both recapture data and the variability of trial-based magnet efficiency distributions was critical for achieving reliable model fits and scientifically robust mortality estimates. Drs. Ault & Luo's analysis shows that using a "parameters" estimation approach, which allows the magnet efficiency parameters to be estimated directly from the observed recapture data, accounted for the random nonparametric distribution of magnet efficiencies and substantially improved model fits to data. The Liljestrand, Wilberg & Schueller approach of averaging data across all plants and areas over time was, and remains, an inappropriate, non-representative and inefficient use the data, resulting in unreliable estimates of natural mortality.

The failure to appropriately address the nonparametric distribution of magnet recapture efficiency data continues to significantly inflate the M adopted by the SAS. As stated in Dr. Ault's March 14 memorandum submitted to the SAS,

> "The ASMFC SAS has failed to apply standard objective statistical criteria in selecting the appropriate mark-recapture model estimates of natural mortality rate. Instead, they made a subjective, *ad hoc* choice for the value of M to be used in the upcoming stock assessment."

In contrast, Drs. Ault & Luo applied a more data-driven method for estimating magnet efficiencies, without prescribing any prior distribution or assumptions about full mixing.

Drs. Ault & Luo also applied a "Stepwise" approach to estimation of the natural mortality rate. In contrast to the characterization in the SAS TC presentation, Drs. Ault and Luo used the Stepwise method as a diagnostic tool, systematically estimating magnet efficiencies in stages to assess how sensitive model performance is to changes in M. As explained, the method was designed solely to explore the sensitivity of M estimates to increasing model complexity and spatio-temporal resolution of magnet efficiencies, not as a formal hypothesis-testing framework.

Both the "parameters" and "stepwise" methods better represent the empirical variability in magnet efficiencies observed in the plant trials, resulting in consistent and substantially lower natural mortality estimates. In the July 2025 SAS TC meeting, the SAS presentation selectively highlighted Drs. Ault & Luo's Stepwise approach, but failed to discuss the more statistically rigorous "parameters" estimation approach and its ability to improve model fits which effectively integrated both recapture data and the variability of trial-based magnet efficiency distributions, a

[7] Magnet efficiency is a measure of the efficiency by which the magnets in the menhaden processing plants captured known ferro-magnetic tags seeded into catches in the underlying tagging study. Each plant had up to nine magnets, with the first two (primary) magnets were used in the Coston study, and all nine used in the NMFS data analysis.

modeling process that was critical for achieving reliable model fits and scientifically robust mortality estimates.

The ASMFC Must Fully Address All of the Identified Mistakes in the Analysis Leading to the Adoption of the Severely Inflated M Used in the SEDAR 69 Stock Assessment

The remaining mistake that accounts for the difference between the SAS recommended M=0.92 and Drs. Ault & Luo's recommended M=0.52 is the SAS's failure to apply the most scientifically sound method to magnet tag recovery efficiency at the menhaden reduction plants. Drs Ault & Luo's conclusions are fully supported by every other indicator of the actual M for Atlantic menhaden, including the life history estimate of M = 0.54, indirect mortality estimation methods which indicate that M should fall within a reasonable range of 0.30 and 0.50 based on empirical life history principles, and the more than a dozen peer reviewed estimates of M ranging from 0.37 to 0.53. Drs. Ault & Luo also detail that the M=1.17 estimate adopted in the SEDAR 69 stock assessment was anomalously high compared to more than 60 recent U.S. and international fish stock assessments. The estimate represented a 2.3-fold increase over the M=0.50 used in SEDAR 40 (2015) assessment -- 14 standard deviations above the mean of 0.46 for the peer-reviewed publications.

Another red flag signaling problems with adopting the M=1.17 in SEDAR 69 stock assessment was the manipulation of other parameters that occurred, including the steeply increased recruitment assumptions needed in the model to account for the extremely high M.[8] The parameter manipulation apparent in the Liljestrand, Wilberg & Schueller paper, ultimately adopted and approved in SEDAR 69, is inconsistent with sound science. Unfortunately, it may be occurring again. The July SAS TC presentation stated that they were "scaling" the recruitment assumption to decrease the effect of fishing and increase stock biomass. This scaling appears to be a results-driven change in recruitment by 1.5 orders of magnitude (15 times) to account for the decline in the estimated M. As a result, the SAS were able to conclude that fishing at current levels would have no impact on the status of the menhaden resource.

The SAS recommendation of M=0.92 remains a significant statistical outlier, still several standard deviations above all other credible estimates. The SAS agreed to introduce the Ault & Luo M analysis into the Peer Review through its inclusion as a sensitivity run, however this sensitivity run was not presented or discussed at the July SAS TC meeting, nor were the full impacts of a lower M discussed. It appears that the SAS may be reluctant to admit the full magnitude of their prior mistakes. It is understandable that there may be some professional embarrassment to the original authors, some of whom are active members or have colleagues on the SAS. Representatives from Omega Protein also apply pressure as the dominant special interest in the fishery. And states will also be affected by decreases in the allowable catch. However, Atlantic menhaden is the only major East Coast forage species that is supposedly at relatively healthy levels. It is critical to the health of striped bass, osprey, and countless other predators, and is the key forage stock in the ERP model. The ASMFC must meet its legal obligations under ACFCMA and the ASMFC's Rules and Charter to base its Interstate Fishery

[8] SEDAR 69 continued a dramatic transition in how the health of the Atlantic menhaden population was viewed from less than 10 years prior when menhaden was considered likely overfished and overfishing occurring. SEDAR 69 not only concluded that menhaden was not overfished, but that the menhaden spawning stock was over 80 percent of the unfished population size.

Management Plans on the best available science and prevent overfishing and look to the long-term benefits of a healthy Atlantic menhaden population managed sustainably.

* * * * *

The work of the Atlantic Menhaden SAS and Drs. Ault & Luo is now consistent except for the SAS's mistaken application of the simple arithmetic average of plant- and area-specific magnet tag recovery efficiencies. The scientific evidence points to the method used by Drs. Ault & Luo as the best scientific approach for determining the M estimate. Given the magnitude of the difference between the M in use since 2019 (M=1.17) and Drs. Ault & Luo's estimate of M=0.52, there is a high risk that menhaden is overfished with overfishing occurring. Adopting their recommended M= 0.52 in the stock assessment will help prevent overfishing and rebuild the Atlantic menhaden resource.

For these reasons, we request that you do all that is possible to ensure that the August 12-15 Ecological Reference Point Peer Review fully examines the issues raised in this letter by first including Drs. Ault & Luo's paper[9] and our letter in the Peer Review materials. Second, please ensure that Drs. Ault & Luo's recommended (M=0.52) is included as a sensitivity run in the BAM and that the results – including impact on biomass and stock status - be available for consideration and adoption by the Menhaden Board. Third, please ensure that all of these materials are provided with the Peer Review results to the Board and ASMFC so that they can consider them and make their final decisions consistent with their legal duties to manage Atlantic menhaden based on the best available science and to prevent overfishing. And finally, to help ensure impartiality in the analysis and presentation of the issues raised here, please recuse the authors of the Liljestrand, Wilberg & Schueller paper from participating in the Peer Review and subsequent processes leading to the Board and ASMFC's final decisions.

Thank you for considering our concerns and recommendations.

Sincerely,

Roger Fleming, Esq., Blue Planet Strategies
47 Middle Street
Hallowell, ME 04347
(978) 846-0612
rflemingme7@gmail.com

[9] If Drs. Ault & Luo's paper is not published before the peer review begins, please provide the most recent manuscript and response to reviewer comments available.

David Reed, Esq., Chesapeake Legal Alliance
1212 West Street
Annapolis, MD 21401
(202) 253-5560
david@chesapeakelegal.org

Encl:

1. Dr. Jerald S. Ault Memorandum to the ASMFC Stock Assessment Subcommittee, (March 14, 2025).
2. Dr. Jerald S. Ault & Dr. and Jiangang Luo, Magnet Efficiency Parameters, (February 27, 2025).
3. Dr. Jerald S. Ault & Dr. and Jiangang Luo, Report on Estimation of Area Magnet Efficiencies and Natural Mortality, (February 25, 2025).
4. Dr. Jerald S. Ault Letter to ASMFC Menhaden Management Board, (January 31, 2020).
5. Roger Fleming, Esq. and David Reed, Esq., Letter to Mr. Robert Beal, Executive Director, (February 28, 2025).
6. Roger Fleming, Esq. and David Reed, Esq., Letter to Mr. Robert Beal, Executive Director, (October 31, 2024).

Cc:
Mr. Eugenio Piñeiro Soler, Director of NOAA Fisheries, eugenio.e.pineirosoler@noaa.gov
Dr. Clay Porch, Direcor of NOAA SEFSC, clay.porch@noaa.gov
Dr. Julie A. Neer, SEDAR Program Manager, julie.neer@safmc.net
Dr. Katie Drew, ASMFC Stock Assessment Team Lead, kdrew@asmfc.org
Mr. James Boyle IV, ASMFC Fishery Management Plan Coordinator, jboyle@asmfc.org
Dr. Jerry Ault, UMiami Rosenstiel School of Marine & Atmospheric Science, jault@miami.edu
Dr. Jiangang Luo, UMiami Rosenstiel Sch. of Marine & Atmospheric Science, jluo@miami.edu

Objective Criterion for Model Selection

The ASMFC SAS has failed to apply standard objective statistical criteria in selecting the appropriate mark-recapture model estimates of natural mortality rate. Instead, they have made a subjective, *ad hoc* choice for the value of M to be used in the upcoming stock assessment.

When using the Coston data, objective criteria for model selection should include three key metrics of model outputs for assessing the model efficacy:

(1) Aikake Information Criteria (AIC).
(2) Difference between observed and model-predicted recaptures.
(3) Visual inspection of the fit between observed and model-predicted recaptures.

Method	K	$\mathbf{neg(LL)}$	R	Δ	AIC	$\widehat{\mathbf{M}}$	$\widehat{\mathbf{M}}_{\mathbf{MCMC}}$
Constant:	106	10,579	102,992	92,611	21,370	0.8992	0.9039
Stepwise:	106	9,751	102,992	-6,570	19,714	0.5149	0.5102
Parameters:	206	9,484	102,992	10,123	19,380	0.5488	0.4965

Table 1.- Summary of findings from three analytical methods applied to the Coston mark-recapture data. Symbols are: K ≡ number of estimated model parameters; $\mathrm{neg(LL)}$ ≡ model's negative log-likelihood; R ≡ observed total recaptures; Δ ≡ difference estimated between predicted and observed recaptures; AIC ≡ Akaike Information Criterion; $\widehat{\mathrm{M}}$ ≡ estimated single-run annual natural mortality rate; $\widehat{\mathrm{M}}_{\mathrm{MCMC}}$ ≡ MCMC mean estimated annual natural mortality rate.

For the Coston data, **Table 1** clearly indicates that: $\mathrm{AIC}_{\mathrm{constant}} \gg \mathrm{AIC}_{\mathrm{stepwise}} > \mathrm{AIC}_{\mathrm{parameters}}$.

Focusing on the "Constant" and "Stepwise" approaches, and using the objective model selection criteria outlined above:

(1) There was a 7.7% reduction in AIC for the "Stepwise" versus "Constant" approach.
(2) The "Constant" approach overestimated recaptures by +89.9%, whereas the "Stepwise" approach underestimated recaptures by only 6.4%—a significantly more accurate estimation.
(3) Visualizations (**Fig. 1**) of single-run results for Coston data further support the superiority of the "Stepwise" approach.

These findings clearly indicate that the "Stepwise" approach is far superior to the "Constant" approach and should be selected as the best model choice.

Thus, the objective choice of the "base" case for Atlantic menhaden stock assessment should be the Stepwise approach with an $\widehat{M} = 0.52$ (sd $= 0.0234$); and on the other hand, the "sensitivity" case should be $\widehat{M} = 0.90$ (sd $= 0.0331$).

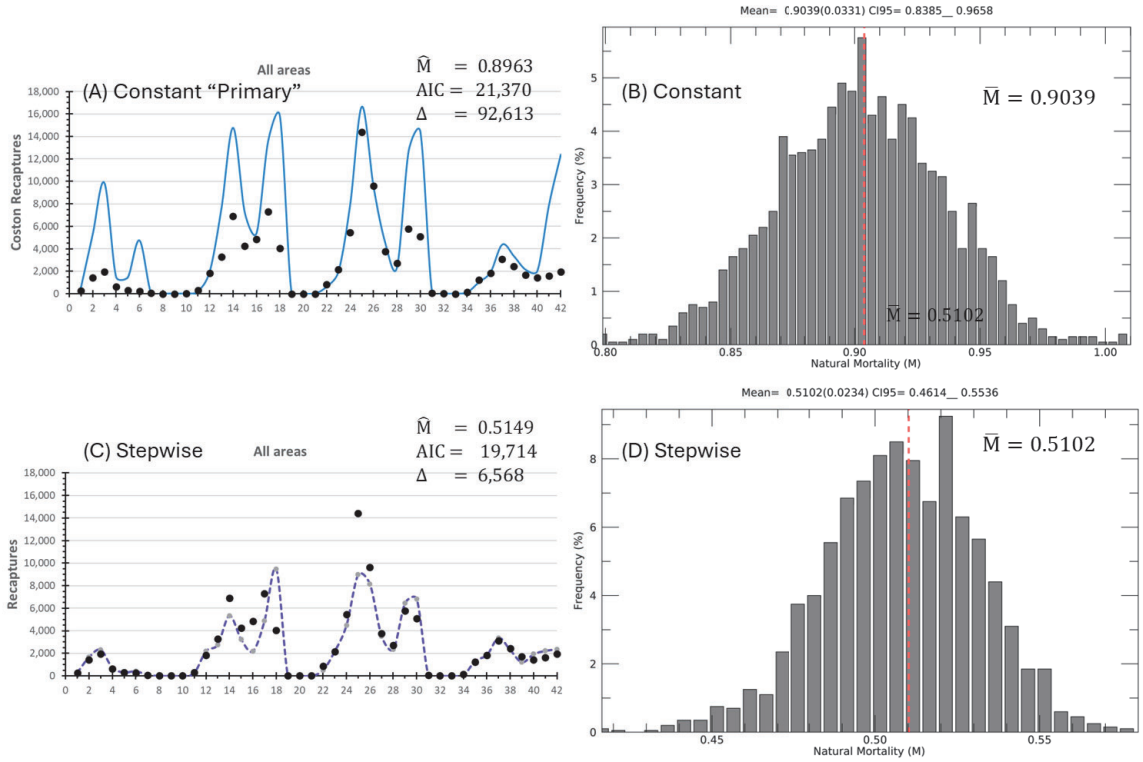

Figure 1.- Summary visualizations of single run results for Coston data: (A) "Constant" primary magnet efficiency coefficients; and (B) "Stepwise" (Step #4).

This analysis allows for a direct comparison of these estimates with other key mortality and survivorship parameters, including those generated by the single-species assessment model (BAM).

Magnet Efficiency Parameters

Some misunderstandings have been raised concerning the use and estimation of magnet efficiency parameters. Our objection to using the mean magnet efficiency from the Plant Test data is based on the fact that these frequency distribution(s) significantly deviate from a symmetrical normal distribution, instead appearing to resemble a uniform random distribution (**Figs. 1 & 2**). In fact, the true empirical distribution is neither normal nor uniform, but rather some type of a **random non-parametric distribution**.

In our model runs where magnet efficiencies were treated as parameters, we **did not** assume a uniform random distribution as a prior condition. Instead, the model estimated magnet efficiency parameters by fitting predicted recaptures to the observed recapture data using a **negative log-likelihood function** incorporated into an AIC to account for the additional estimated parameters. The resulting frequency distribution of magnet efficiency parameters emerged from the second half of a **4,000,000-step MCMC run**, saved every **1,000 steps** (**Fig. 1**).

The parameter frequency distributions by the four areas are shown in **Fig. 3**, demonstrating how the model-derived estimates reflect the underlying data structure(s) without imposing any predefined probability function. When magnet efficiency parameters are averaged by month and area, they exhibit slightly different patterns (**Fig. 4**). This pattern may not exactly match the Plant Test data *per se*, but there is no expectation that it would; however, It definitely covered the range of observed magnet efficiencies. This further highlights the limitations of using simple averages to represent these relatively complex data.

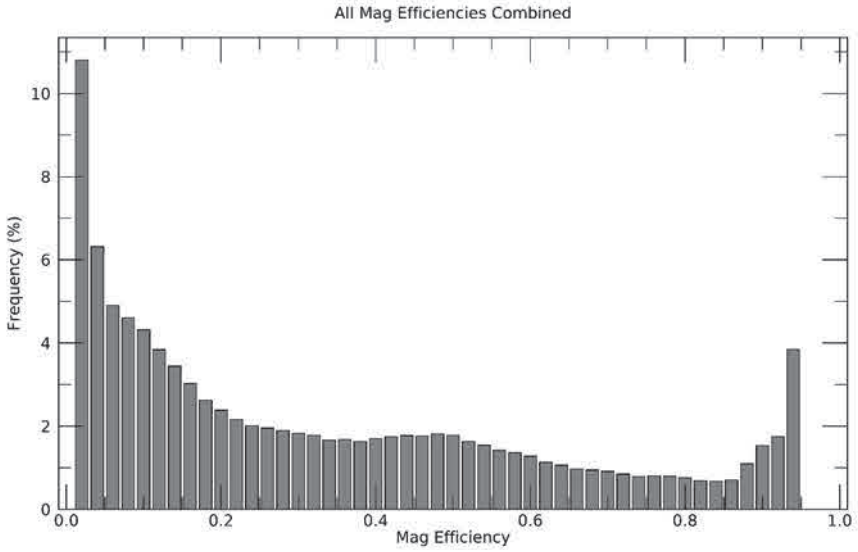

Figure 1.- Estimated primary magnet efficiency distribution corresponding to the Coston data for all months and areas combined. Data are from the second half of the 4 million step MCMC simulation, saved every 1000 steps and binned at 0.02 $(\mathrm{n} = 2{,}000)$.

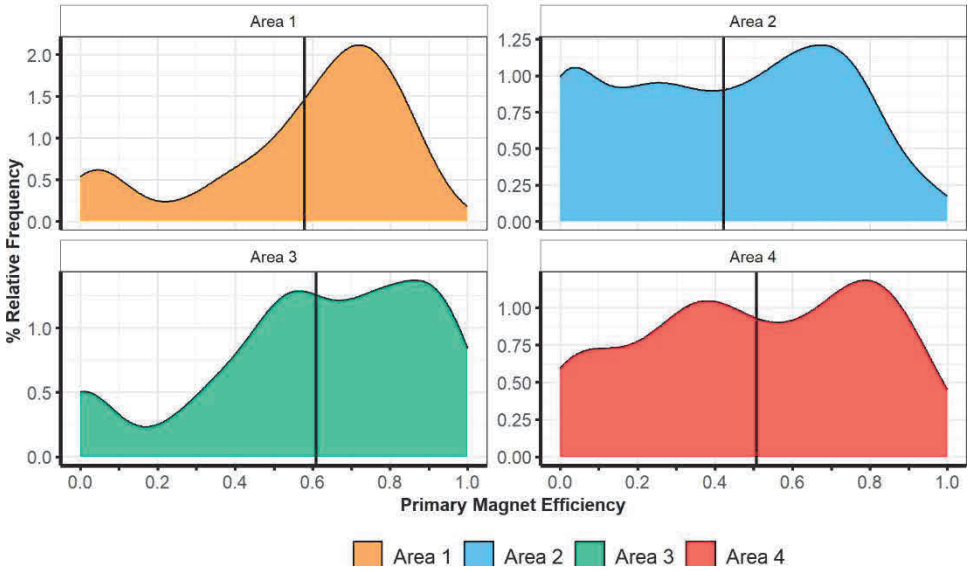

Figure 2.- Observed area-averaged primary magnet efficiency distributions from the 1966-1971 Plant Test data. Vertical black lines are the area-specific weighted means.

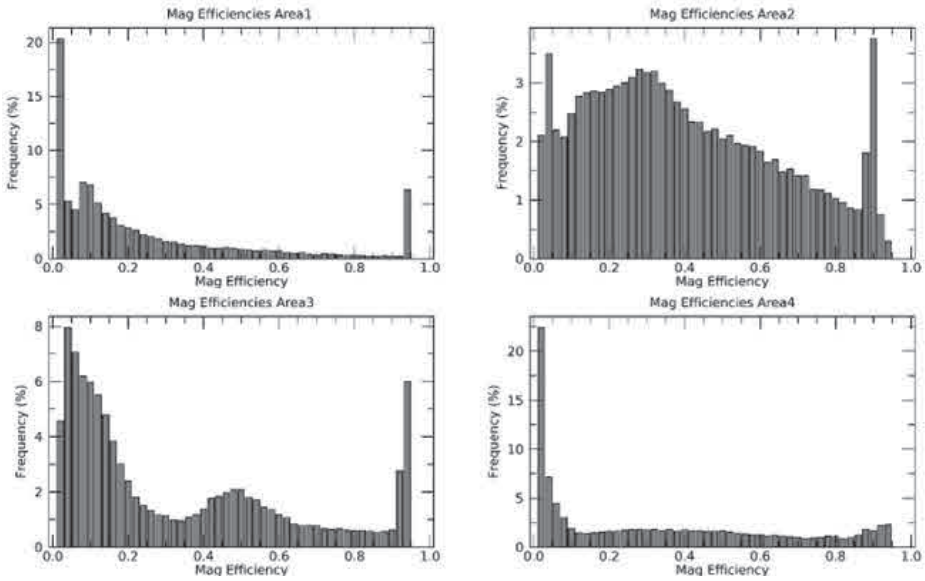

Figure 3.- Area-specific estimated primary magnet efficiency distribution for all 42 months from second half of the 4 million steps MCMC simulation saved every 1000 steps and binned at 0.02 $(\mathrm{n} = 2{,}000)$.

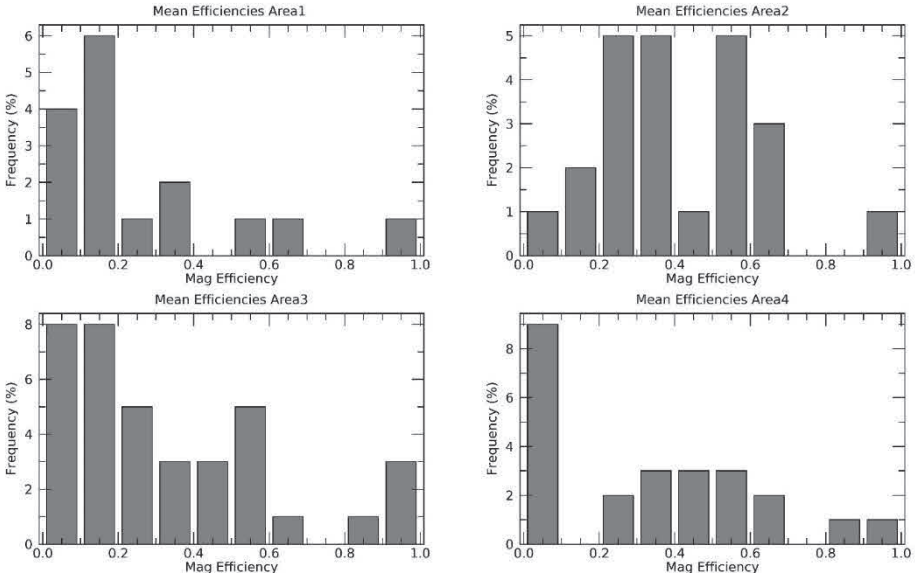

Figure 4.- Month and area averaged magnet efficiency distributions from second half of the 4 million step MCMC simulation saved every 1000 steps and binned at 0.05 ($\mathrm{n} = 2{,}000$).

This report addresses the ASMFC's SAS M workgroup's request, dated February 12, 2025, for a detailed description of our Stepwise method used to estimate magnet efficiencies (MEs). This report also compares this method to the "Constant" and "MEs as parameters" approaches. The results from these analyses were then incorporated into a comprehensive evaluation of the two Atlantic menhaden mark-recapture databases to derive the best estimate of the natural mortality rate (M) for the species. We concluded that $M = 0.52$ is the best estimate of the annual natural mortality rate for Atlantic menhaden.

I. Constant Average Plant and Area Magnet Efficiencies $(\varepsilon_{t,a})$

Appropriate use of the Coston (1971) data required establishment of a quantitative definition of what constituted "primary" magnets. Because NMFS data for 1966 completely overlapped with the releases given in Coston, we were able to determine that recovery stations 1 and 2 should be defined as "primary magnets (p12)" in the "Plant Test" database, aligning perfectly with the reported recaptures in the Coston (1971) technical report. Determination of plant and area magnet efficiencies during 1966-1971 was accomplished through analysis of 964 batch trials conducted at 19 processing plants in 4 geographical areas (**Table S1**; note: no batch trials were conducted at plant #8), as was done by the ASMFC SAS M workgroup. Each batch trial consisted of release of approximately 100 known tagged menhaden into vessel catches received at the respective plants. The fraction of the known tags recovered was assessed for each batch according to two different magnet configurations relative to the database being analyzed: (1) Coston data required only "primary magnets (p12 -- recovery stations 1 and 2)"; while, (2) NMFS data used "all magnets" (all recovery stations). Comparisons of magnet efficiencies by plants and areas for the two databases are shown in **Fig. I.1**.

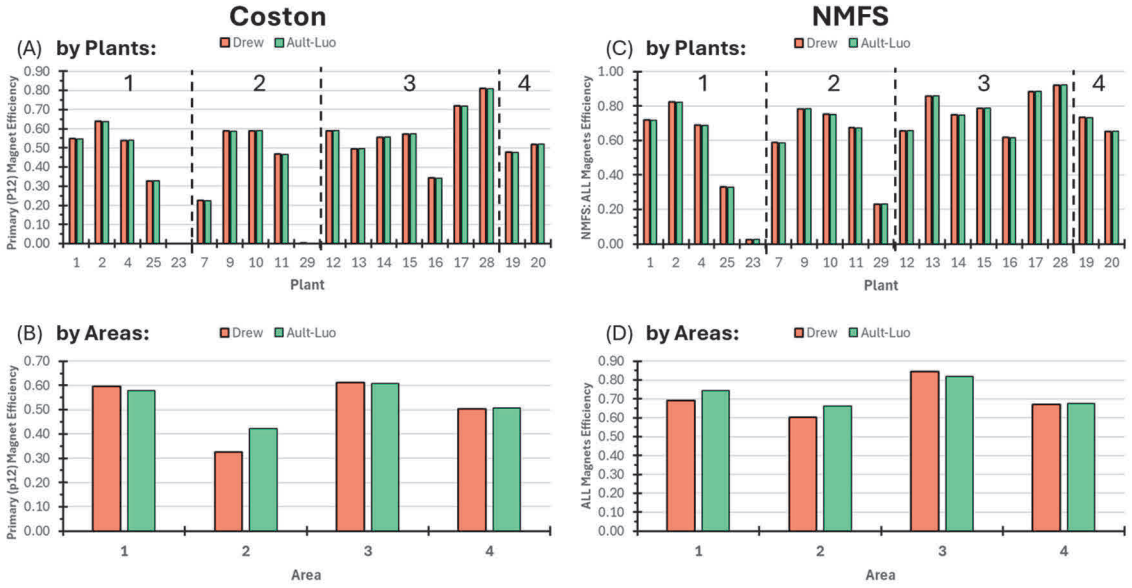

Figure I.1.- Average tag recovery magnet efficiencies over 1966-1971 at 19 reduction plants and four geographic areas for the two principal data sources: (A-B) "primary" magnets for Coston; and (C-D) "all" magnets for NMFS.

For the two data sources, average ME estimates were equivalent by plants (**Figs. I.1 A & C**); and, area averages were only marginally different due to the catch weighting of coefficients by ASMFC. However, inspection of the statistical distributions of magnet efficiencies for all plants and areas combined shows these data are not normally distributed and are not well represented by the arithmetic mean as the central value of these data; nor are they either by individual plants or areas (**Figs. I.2-I.4**).

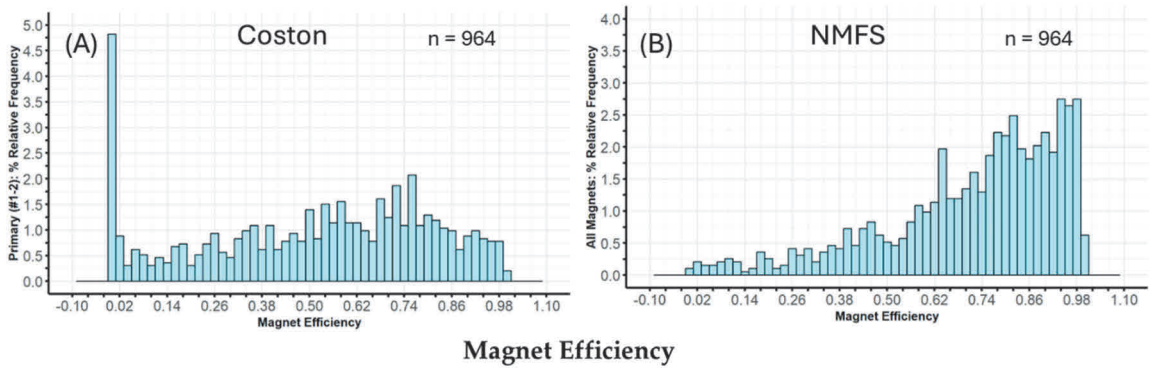

Figure I.2.- Distributions of combined magnet efficiencies for all plants and areas from 964 batch trials: (A) "primary" magnets (recovery stations 1 and 2) relevant to the Coston data; and (B) "all" magnets (all plant recovery stations) relevant to the NMFS data.

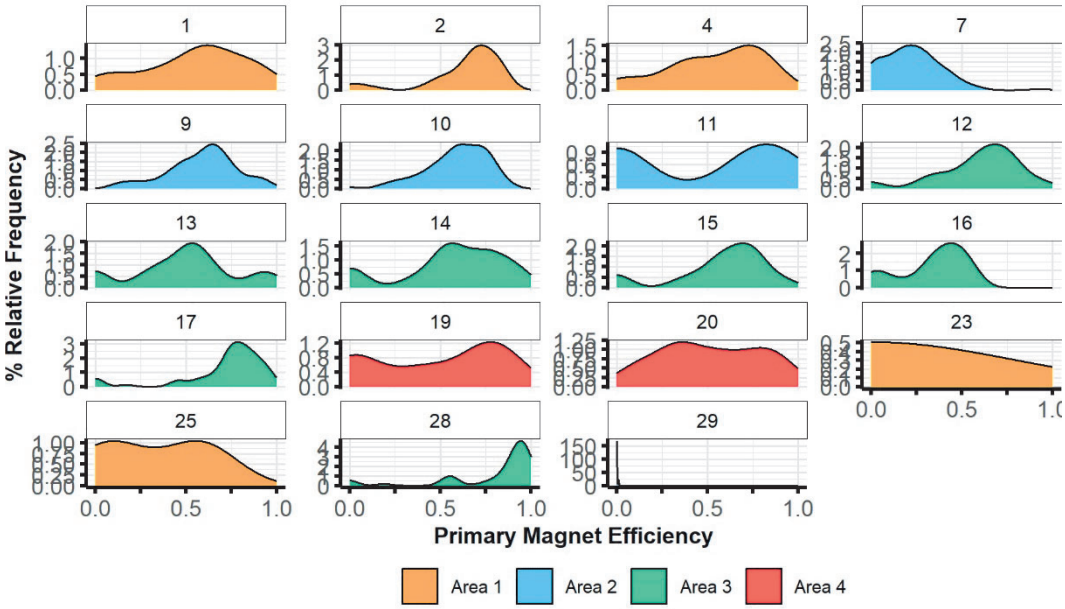

Figure I.3.- Plant-specific distributions of individual batch trial magnet efficiencies for "primary" (p12) magnets at 19 Atlantic menhaden reduction plants contained within four geographical areas (see **Table S1**) during 1966-1971.

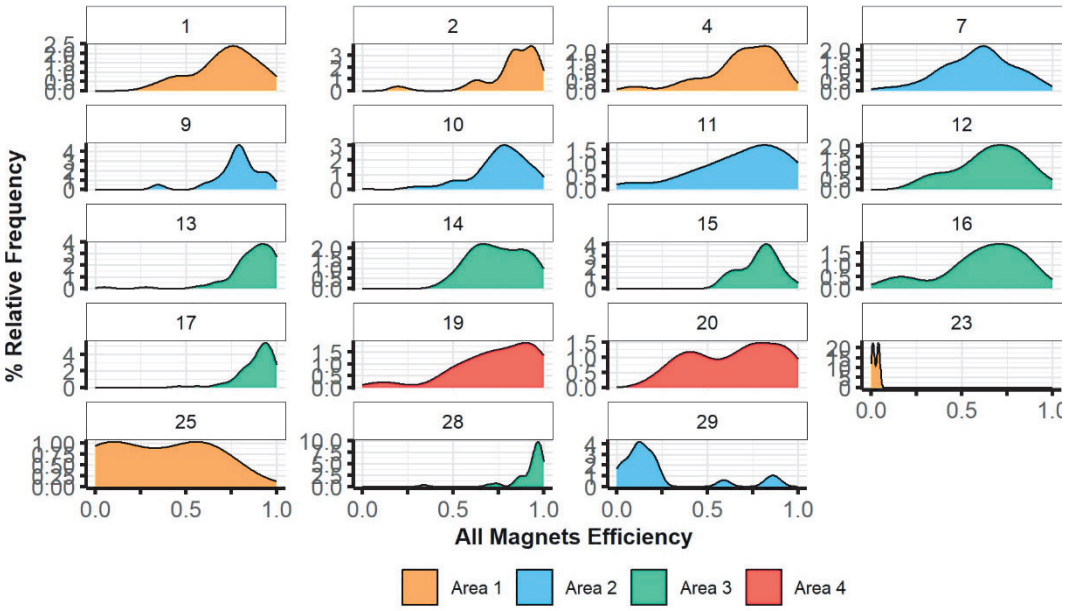

Figure I.4.- Plant-specific distributions of individual batch trials of magnet efficiencies for "ALL" magnets at 19 Atlantic menhaden reduction processing plants contained within four geographical areas (see **Table S1**) during 1966-1971.

Figs. I.2-I.4 each clearly show that the combined and individual magnet efficiency data were apparently distributed as uniform random variables ranging between 0 and 1, i.e., U(0,1). A "uniform distribution" means all possible outcomes in the range have an equal probability of occurring.

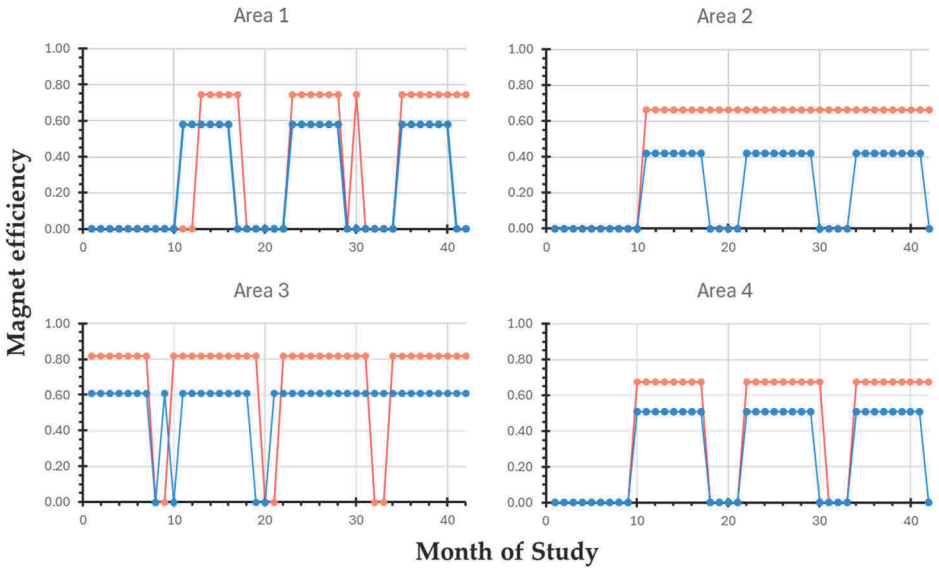

Figure I.5.- Temporal distribution of area averaged estimates of magnet efficiency within 4 geographical Areas over the 42 month (July 1966-December 1969) study. MEs are applied during months when recaptures were observed. Coston (p12) averages (blue closed dots) are from **Fig. I.1B**; while NMFS (all recovery stations) averages (red closed dots) are from **Fig. I.1D**.

In the null "Constant" modeling approach, Area averages were used by the SAS as monthly inputs by area for the estimated magnet efficiency matrix if recoveries were observed in that Area. However, given the uniform distributions of magnet efficiencies by plants, areas and all plants and areas combined, the Area mean is a poor descriptor of the underlying data.

As such, single run mean assessments were run. If the model converged, then and MCMC run of 4,000,000 trials was conducted to establish the mean and standard error of the estimated natural mortality parameter.

II. Stepwise Analysis of Magnet Efficiencies $(\boldsymbol{\varepsilon_{t,a}})$

Recoveries (theoretical catch of tagged cohorts of menhaden) for each month t and area a of tagged cohorts $(C_{T,A,t,a})$ is the product of the unknown time and area-specific tagged fish abundance, $N_{T,A,t,a}$, the proportion of mortality due to fishing $F_{t,a}$ and natural M causes, and the time and area specific plant magnet efficiency rate $\varepsilon_{t,a}$.

$$C_{T,A,t,a} = \left[N_{T,A,t,a}\frac{F_{t,a}}{(F_{t,a}+M)}\left(1-e^{(F_{t,a}+M)}\right)\right]\varepsilon_{t,a} \quad (1)$$

The Stepwise procedure is conducted as follows:

Step 0: Input the matrix of "Constant" average "primary" magnet efficiencies $\left[\hat{\varepsilon}_{0_{t,a}}\right]$ determined in the Section I analyses for each area a $(\mathrm{a}=1,\cdots,4)$ and month t $(\mathrm{t}=1,\cdots,42)$. Input these values and conduct a single run, letting the model estimate recaptures $C_0(t,a)$ according to Eq. (1).

Simple rearrangement of Eq. (1) produces a mean area-time estimate of magnet efficiency $\hat{\varepsilon}_{t,a}$.

$$\hat{\varepsilon}_{1_{t,a}} = \frac{\text{Observed } C_{t,a}}{N_{t,a}\frac{F_{t,a}}{(F_{t,a}+M)}\left(1-e^{(F_{t,a}+M)}\right)} = \frac{\text{Observed } C_{t,a}}{\hat{C}_0(t,a)} \quad (2)$$

where,

$$\hat{C}_0(t,a) = N_{t,a}\frac{F_{t,a}}{(F_{t,a}+M)}\left(1-e^{(F_{t,a}+M)}\right) \quad (3)$$

The denominator of Eq. (2) is calculated internally in the model through sequencing tagged cohorts released over time in the 4 areas, resulting in an updated estimate of magnet efficiency.

Step 1: Use the theoretical numbers of tagged fish (Eq. 1) from Step 0, or "actual unknown" recaptures $\left(\hat{C}_0(t,a)\right)$, without application of $\hat{\varepsilon}_{1_{t,a}}$, to re-estimate magnet efficiencies as: $\hat{\varepsilon}_{1_{t,a}} = \text{Observed } C_{t,a}/\hat{C}_0(t,a)$. Use these adjusted $\hat{\varepsilon}_{1_{t,a}}$ values as magnet efficiency parameters.

Additionally, minimum and maximum limits on the area-specific estimates of magnet efficiencies ($\hat{\varepsilon}_{t,a}$) were set to range between 0.10 – 0.98 for "primary" magnet when using the Coston data. This constraint was reduced to 0.20 – 0.98 for "all" (all recovery stations) when using NMFS data. Upon model convergence, the new matrix of magnet efficiencies $\left[\hat{\varepsilon}_{S_{t,a}}\right]$ was used in the Stepwise analysis process.

Step 2: Use Step 1's theoretical catch of tagged fish $\left(\hat{C}_1(t,a)\right)$ to re-estimate magnet efficiencies $\left[\hat{\varepsilon}_{1_{t,a}}\right]$ and use as Step 2 model inputs.

The Akaike Information Criterion (AIC) was the estimator of prediction error and thereby relative quality of the statistical models for the given sets of data. Given a collection of models for a given set of data, AIC estimates the quality of each model, relative to each of the other models. Thus, AIC provides an objective means for model selection.

$$\mathrm{AIC} = -2\ln(\mathrm{L}) + 2\mathrm{K} \qquad (4)$$

Where, K ≡ number of estimated parameters in the model; and, L ≡ maximum value of the likelihood function for the model. A lower AIC indicates a better fit and thus better model.

Step 3+: Continue stepwise procedure outlined above until an objective stopping criterion is met.

Step	$\widehat{\mathrm{M}}$	neg(LL)	$\widehat{\mathrm{R}}$	R	Δ	AIC
0	0.8963	10,579	195,603	102,992	92,611	21,370
1	0.7289	9,795	143,697	102,992	40,705	19,802
2	0.6891	9,777	100,340	102,992	-2,652	19,766
3	0.5956	9,744	97,346	102,992	-5,646	19,700
4	0.5149	9,751	96,422	102,992	-6,570	19,714
5	0.4406	9,763	96,044	102,992	-6,948	19,738
6	0.3790	9,773	95,753	102,992	-7,239	19,758
7	0.3243	9,784	95,569	102,992	-7,423	19,780

Table II.1.- Stepwise analysis of the Coston data. Symbols are: $\widehat{\mathrm{M}}$ ≡ estimated annual natural mortality rate: neg(LL) ≡ model's negative log-likelihood; $\widehat{\mathrm{R}}$ ≡ total estimated recaptures by the model; ; R ≡ observed total recaptures; Δ ≡ difference between predicted and observed recaptures; AIC ≡ Akaike Information Criterion.

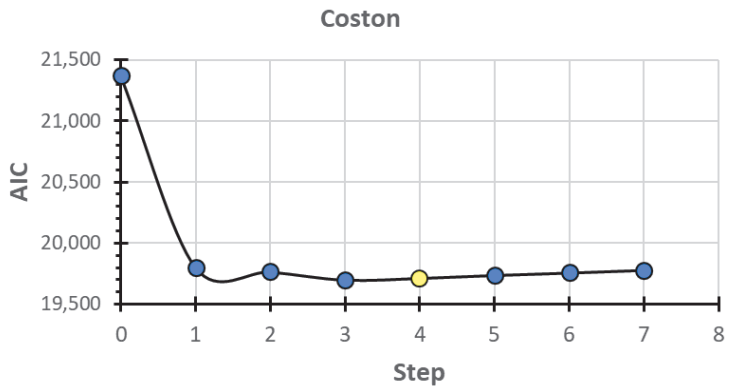

Figure II.1.- AIC reduction using the Stepwise iterative procedure for the Coston data. Minimum AIC was identified as Step 4.

Stepwise analysis for the NMFS data showed a minimum AIC in Step 7 (**Table II.2** & **Fig. II.2**).

Step	$\hat{M}$	neg(LL)	$\hat{R}$	R	Δ	AIC
0	0.8909	8,044	133,279	93,335	39,944	16,300
1	0.8174	7,532	94,784	93,335	1,449	15,276
2	0.7737	7,500	88,188	93,335	-5,147	15,212
3	0.6938	7,505	95,008	93,335	1,673	15,222
4	0.6564	7,515	95,649	93,335	2,314	15,242
5	0.6294	7,519	95,962	93,336	2,626	15,250
6	0.5609	7,405	113,129	93,337	19,792	15,022
7	0.5279	7,372	107,830	93,338	14,492	14,956
8	0.4863	7,373	108,519	93,339	15,180	14,958
9	0.4498	7,377	108,746	93,340	15,406	14,966

Table II.2.- Stepwise analysis of the NMFS data. Symbols are: $\hat{M} \equiv$ estimated annual natural mortality rate: neg(LL) ≡ model's negative log-likelihood; $\hat{R} \equiv$ total estimated recaptures by the model; ; R ≡ observed total recaptures; Δ ≡ difference between predicted and observed recaptures; AIC ≡ Akaike Information Criterion.

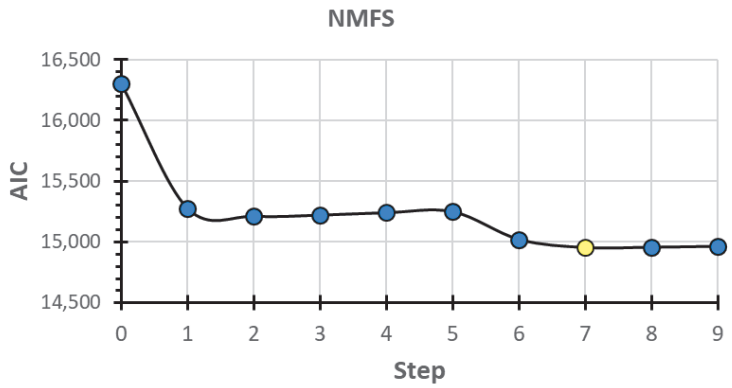

Figure II.2.- AIC reduction using the Stepwise iterative procedure for the NMFS data. Minimum AIC was identified as Step 7.

III. Magnet Efficiencies $(\varepsilon_{t,a})$ as Model Parameters

The probability distribution of estimated plant time-area magnet efficiencies closely resembled a uniform random distribution $\mathrm{U}(0,1)$ (**Fig. III.1**), and was not well represented by the average across all plants and areas over years. Thus, another reasonable method was to estimate magnet efficiencies $\hat{\varepsilon}_{t,a}$ by area and time $\hat{\varepsilon}_{t,a}$ by treating them as model parameters, done in the same way that the theta parameters (catchability $\Theta_{t,a}$) are already estimated in the model. To this end, we modified the model code to allow magnet efficiencies $\hat{\varepsilon}_{t,a}$ to be estimated as model parameters. The number (n) of non-zero recapture elements by area and time was used to determine the number of $\hat{\varepsilon}_{1-n}$ parameters, which map to the $\left[\hat{\varepsilon}_{0_{t,a}}\right]$ matrix. We employed a way similar to how the theta parameters were estimated as the natural log of theta, $\ln(\Theta)$, in the model, the log of magnet efficiencies, $\ln(\hat{\varepsilon}_{1-n})$, that were estimated in the model. We also constrained the log-parameter boundary to range from -3.5 to -0.05 for the Coston data, and from -2.0 to -0.05 for the NMFS data. The number of non-zero recaptures elements in Coston data is 100; thus, when estimating magnet efficiencies we have additional 106 parameters that needed to be estimated by the model, that is, a total of 206 parameters for the model. The model input data of releases and recaptures creates a matrix of:

$$\text{Months tagged} \times \text{Areas} \times \text{Months recaptured} \times \text{Areas} = 42 \times 4 \times 42 \times 4 = 28{,}224 \text{ d.f.}$$

For a total of 28,224 data points. Thus, the degrees of freedom are not significantly affected by the increase of 106 parameters to estimate time-area magnet efficiencies

$$28{,}224 - 106 = 28{,}118 \text{ d.f.}$$

IV. Summary

Results of these analyses are summarized graphically for the three model types and two data sources as comparative single model fits of observed data for the "Constant" (**Figs. IV.1A-C**), "Stepwise" (**Figs. IV.1B-E**) and "Parameters estimated" (**Figs. IV.1C-F**) methods for the Coston (left panels) and NMFS (right panels) data. The observed model fits to data are superior for both Stepwise and Parameter methods as compared to the Constant method.

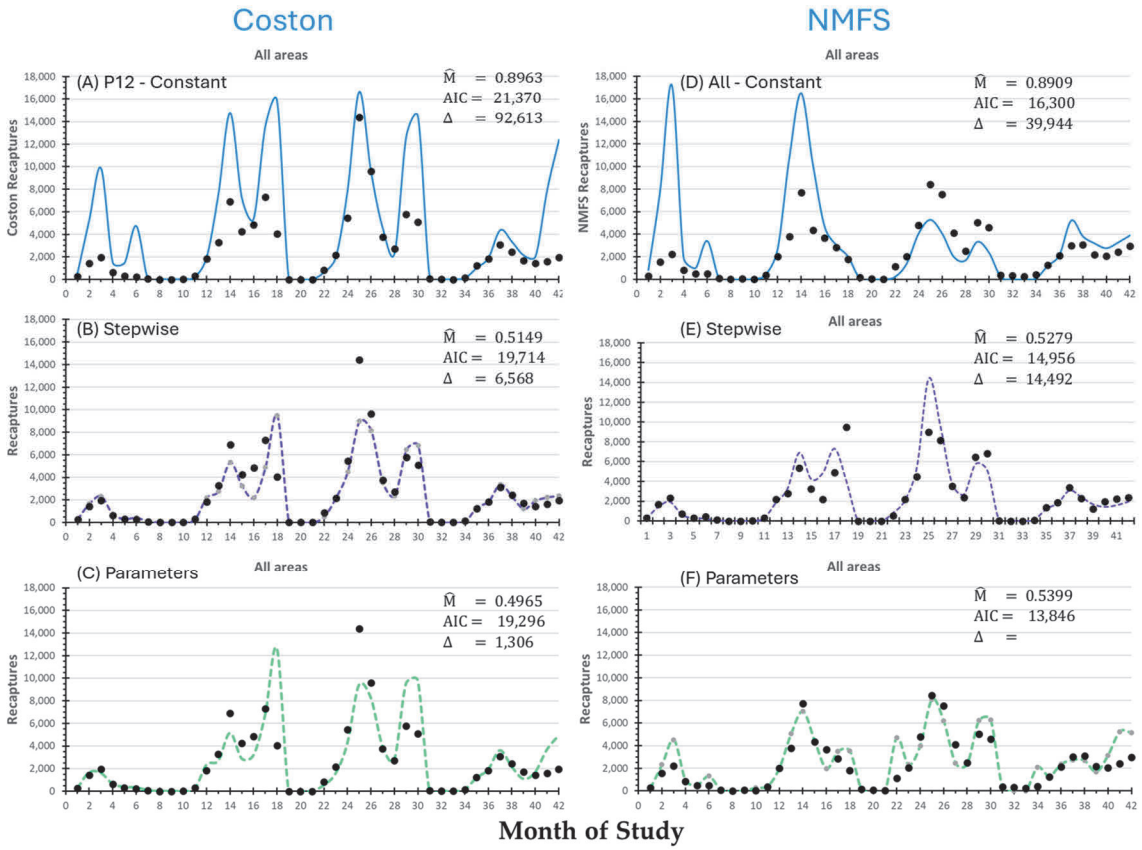

Figure IV.1.- Summary visualizations of single run results for the two data sources: **Coston**: (A) primary magnets with constant ME coefficients; (B) stepwise analysis (Step #4); (C) ME parameters estimated by model. **NMFS**: (D) all magnets with constant ME coefficients; (E) stepwise analysis (Step #7); (F) ME parameters estimated by model.

Given that all three models converged, MCMC analyses, each consisting of 4,000,000 trials, were completed (**Fig. IV.2**). While the unconstrained case for the ME parameter estimation was exploratory, it did produce an estimate of natural mortality lower than what we expected, and further, what we would probably consider to be unrealistic. In contrast, placing realistic constraints on the ME estimates marginally increased the AIC (Coston about +0.43%; NMFS about +1.8%), but significantly increased the value of M (Coston about +68.2%; NMFS about +83.6%) (**Tables IV.1** & **IV.2**).

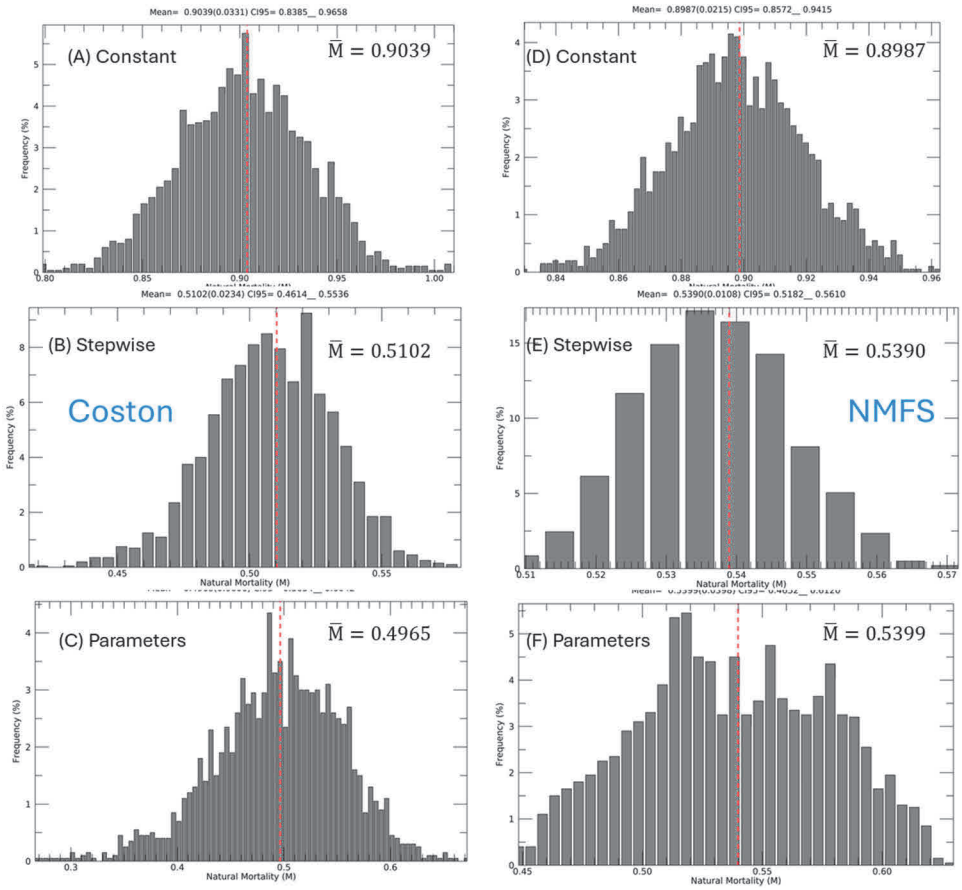

Figure IV.2.- Summary of MCMC trial results corresponding directly to the single-run results of **Fig IV.1**. **Coston**: (A) primary magnets with Constant MEs; (B) Stepwise analysis (Step #4); (C) ME Parameters estimated. **NMFS**: (D) ALL magnets with Constant MEs; (E) Stepwise analysis (Step #7); (F) ME Parameters estimated.

Method	K	neg(LL)	Δ	AIC	$\widehat{M}$	$\widehat{M}_{MCMC}$
Constant:	106	10,579	92,611	21,370	0.8992	0.9039
Step 4:	106	9,751	-6,570	19,714	0.5149	0.5102
As parameters:						
Unconstrained	206	9,442	8,296	19,296	0.3406	0.2939
Constrained	206	9,484	10,123	19,380	0.5488	0.4965

Table IV.1.- Summary of results from three analytical methods applied to the Coston data. Symbols are: K ≡ number of estimated model parameters; neg(LL) ≡ model's negative log-likelihood; Δ ≡ difference between predicted and observed recaptures; AIC ≡ Akaike Information Criterion; $\widehat{M}$ ≡ estimated annual natural mortality rate; $\widehat{\bar{M}}_{MCMC}$ ≡ MCMC mean estimated annual natural mortality rate.

Method	K	neg(LL)	Δ	AIC	$\widehat{M}$	$\widehat{M}_{MCMC}$
Constant:	106	8,044	39,944	16,300	0.8909	0.8987
Step 7:	106	7,372	14,492	14,956	0.5279	0.5390
As parameters:						
Unconstrained	206	6,717	1,306	13,846	0.2935	0.2940
Constrained	206	6,839	12,669	14,090	0.5689	0.5399

Table IV.2.- Summary of results from three analytical methods applied to the NMFS data. Symbols are: K ≡ number of estimated model parameters; : neg(LL) ≡ is the model's negative log-likelihood; Δ ≡ difference between predicted and observed recaptures; AIC ≡ Akaike Information Criterion. $\widehat{M}$ ≡ estimated annual natural mortality rate; $\widehat{\overline{M}}_{MCMC}$ ≡ MCMC mean estimated annual natural mortality rate.

Using the all the data, the three central and most important metrics for assessing the efficacy of the model analyses are: (1) the AIC; (2) differences (Δ) between observed and predicted recaptures; and (3) visual inspection of the plot of the observed versus model-predicted recaptures. In general, for both data sets: $AIC_{constant} \gg AIC_{stepwise} > AIC_{parameters}$, which suggests that MEs estimated as parameters should be the best model choice. For the Coston data, the reduction in AIC ranged between -7.7% to -9.3% for the stepwise versus parameters, respectively. For the NMFS data, the reduction in AIC ranged between -8.2% to -13.6% for the "stepwise" versus "$\varepsilon_{t,a}$ as estimated parameters" approaches, respectively. It is obvious that both stepwise and ME parameter estimation methods are better fits to the data than constant MEs (**Fig. IV.1**).

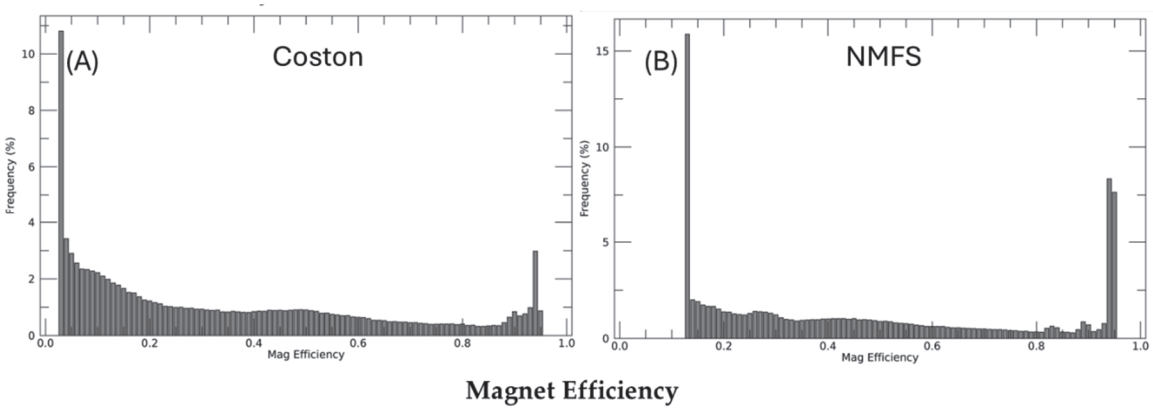

Figure IV.2.- Modeled magnet efficiency parameter estimates for: (A) Coston; and (B) NMFS data sources. Note the similarity to the observed empirical plant test magnet efficiency data shown in **Fig. I.2**.

V. Conclusions

As discussed by the SAS M workgroup, our analyses estimated a natural mortality rate (M) of approximately 0.54 or lower using multiple methods and two data sources. In contrast, Schueller et al. estimated an M of about 0.92 based solely on the averaged plant-area magnet efficiencies. As it turns out, the largest driver of this difference was not the confidential effort data withheld by industry, nor was it the underlying magnet efficiency data *per se*. It was simply methodological differences associated with how the tag recovery-magnet efficiency data were applied.

In our opinion, it is inappropriate to use arithmetic averages of plant- and area-specific magnet efficiencies. The Plant Test trial data show that magnet efficiencies are uniformly distributed, meaning any level of magnet recovery efficiency is equally possible (**Figs. I.2-I.4**). Consequently, averaging magnet efficiencies by area results in a poor and inefficient use of the Plant Tests data. Therefore, we employed two alternative methods: a "Stepwise" approach which was initiated with arithmetic mean efficiencies, and then in an iterative stepwise process used observed and theoretical recoveries to improve the $\left[\hat{\varepsilon}_{S_{t,a}}\right]$; and a "Parameter Estimation" approach which directly estimated the MEs as model parameters. Both of these alternative methods substantially improved model fits, and also substantially lowered the natural mortality rate (M) estimates.

The preferred method(s) should be one(s) that utilize the entire data set. For both datasets, model(s) that estimated magnet efficiency parameters as a distribution produced recapture estimates closest to those observed. Similar results were obtained between the Stepwise and Parameter Estimation methods, and between the two data sources (**Tables IV.1** & **IV.2**). Given the uniform random distribution of magnet efficiencies, the use of the simple weighted arithmetic averages of magnet efficiency by areas will naturally produce the highest estimates of natural mortality, and also the most unreliable.

In summary, our analyses that used appropriate statistical metrics strongly indicate that the most likely annual natural mortality rate estimate for Atlantic menhaden ranges between 0.50 to 0.54. These estimates represent a 43.3% and 40.0% reduction compared to the constant ME estimates derived from simple averaging of either the Coston and NMFS data, respectively. Therefore, we concluded that $\widehat{\mathrm{M}} = 0.52$ is the best estimate of annual natural mortality rate for Atlantic menhaden.

Supplemental

Area	Region	Code	Plant #	trials	Name	City	State
			1	29	Atlantic Processing Company	Amagansett	NY
	1	**NY**	23	4	Lipman Marine Products Co. (Gloucester Marine Protein)	Gloucester	ME
			25	2	Point Judith Byproducts Co.	Point Judith	RI
1							
	2	**NJ**	2	69	J. Howard Smith, Inc.	Port Monmouth	NJ
			4	25	New Jersey Menhaden Products Co.	Wildwood	NJ
			7	120	Standard Products Co.	Reedville	VA
			8	0	McNeal-Edwards (Standard Products Co.)	Reedville	VA
2	**3**	**CB**	9	21	Menhaden Co. (Standard Products Co.)	Reedville	VA
			10	151	Virginia Menhaden Products (Reedville Oil & Guano Co.)	Reedville	VA
			11	52	Standard Products Co.	White Stone	VA
			29	18	Cape Charles Processing Co.	Cape Charles	VA
			12	31	Fish Meal Co.	Beaufort	NC
			13	75	Beaufort Fisheries Inc.	Beaufort	NC
			14	31	Standard Products Co.	Beaufort	NC
3	**4**	**NC**	15	16	Standard Products Co.	Morehead City	NC
			16	22	North Carolina Menhaden Produxts	Morehead City	NC
			17	64	Standard Products Co.	Southport	NC
			28	49	Seashore Packing Co.	Beaufort	NC
4	**5**	**FL**	19	52	Quinn Menhaden Fisheries Inc.	Fernandina Beach	FL
			20	133	Nassau Oil & Fertilizer Inc.	Fernandina Beach	FL
			20	**964**			

Table S1.- Regional reduction processing plants distributed across four areas along the Atlantic coast that were involved in the 1966-1971 plant-area magnet efficiency trials as part of the Atlantic menhaden mark-recapture study conducted by the National Marine Fisheries Service.

UNIVERSITY OF MIAMI
ROSENSTIEL
SCHOOL of MARINE &
ATMOSPHERIC SCIENCE

January 31, 2020

Nichola Meserve, Chair
ASMFC Menhaden Management Board

Dear Ms. Meserve & Board Members,

I greatly appreciate the immense amount of effort dedicated to the production of the SEDAR 69 Atlantic menhaden Stock Assessment (SA) and Ecological Reference Point (ERP) Working Group (WG) reports. I would further like to acknowledge both the scientists and the Menhaden Management Board (MMB) for their continued efforts to pursue ecological management of Atlantic menhaden. This is ground-breaking work made successful by the outstanding leadership, professional dedication and exceptional insights of the MMB and Drs. Matt Cieri, Dave Chagaris, Jason McNamee, Amy Schuller and, Katie Drew.

I also certainly appreciate the enormous challenges associated with this unprecedented paradigm shift by the ASMFC MMB to ecological management, and I commend the ERP WG for their diligent pursuit and evaluation of multiple relatively complex ERP models. It is clear that the SA and ERP reports provide the initial roadmap for the necessary move to ecological management, thereby allowing ASMFC to begin to manage from multispecies and ecological perspectives. I encourage the Board to move forward to adopt ERPs as soon as possible and achieve this objective.

However, I have substantial concerns about the underlying data and model parameter assumptions, which if validated, mean that the SEDAR 69 benchmark stock assessment paints an overly rosy picture of Atlantic menhaden stock status.

In particular, my greatest concern relates to extremely high rates of natural mortality (M) used in the SEDAR 69 benchmark stock assessment. The new M estimate used was based on Liljestrand et al.'s (2019) re-evaluation of a 1960s tagging data set. They acknowledged that their estimated M was substantially greater than previously reported, particularly since several other published studies using the same data produced estimates that were ¼ of those of Liljestrand et al.'s (2019). Setting aside questions of whether it was appropriate to use data more than 55 years old, or whether in fact the Bayesian analysis was appropriate given the assumptions about parameter priors required, in the SEDAR 69 SA the HIGHEST rates of M-at-age were seemingly cherry-picked from the Liljestrand et al. (2019) paper, NOT the average rates. With the new rates and no fishing, only 0.6 of 1% of menhaden survive to reach their 4th birthday. In **Figure 1** below you can clearly see that those rates chosen were far greater (i.e., >2.9 times greater) than those found in any other national or international fishery stock assessments, including stocks which had similar short-lived forage fish life histories. It should also be noted that the Ms used in ASMFC menhaden assessments over the past decade have been steadily increasing, and this trend has had substantial impacts on reported estimates of stock size (both abundance & biomass), recruitment, exploitation rates, and sustainability metrics.

Jerald S. Ault, Ph.D., Professor & Chair
Department of Marine Ecosystems and Society
4600 Rickenbacker Causeway, Miami, FL 33149
305-421-4884 w 305-546-3223 c jault@rsmas.miami.edi

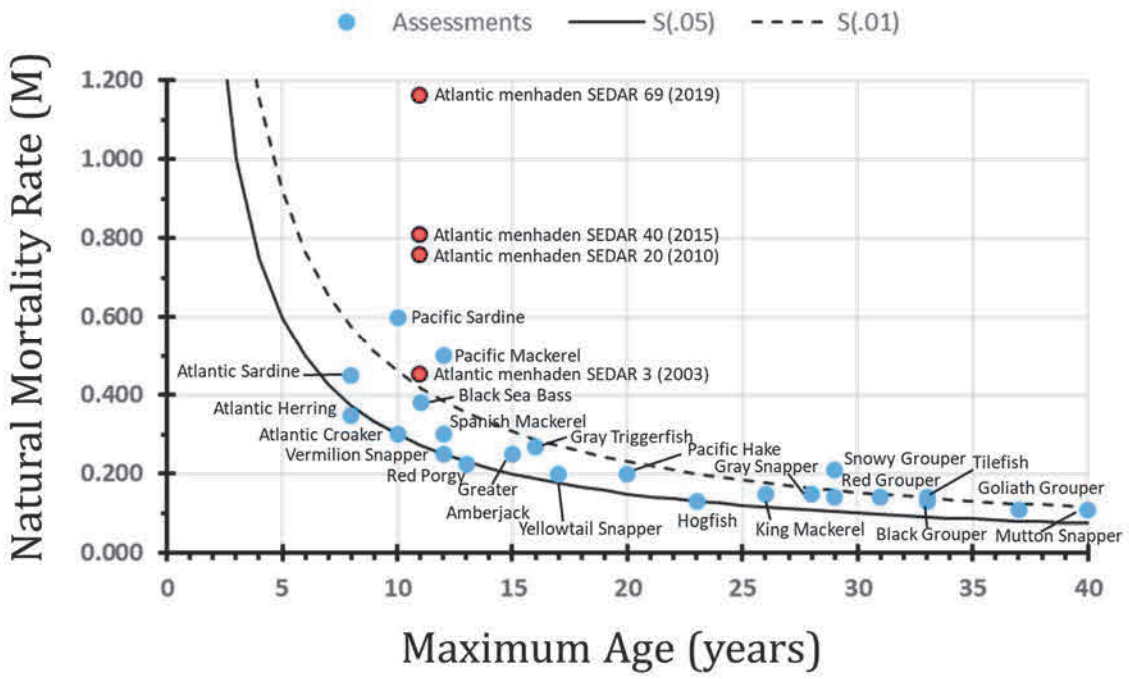

Figure 1.- Natural mortality rates $\widehat{M}$ as a function of maximum age used in various national and international Commission/Council's (i.e., NOAA Southeast Data & Assessment Review, SEDAR); Pacific Fishery Management Council, PFMC; and the International Council for Exploration of the Seas (ICES) species stock assessments during 2003-2019. Labeled red dots show the temporal progression of estimated $\widehat{M}$ used in four sequential SEDAR Atlantic menhaden stock assessment reviews conducted by the Atlantic States Marine Fisheries Commission (ASMFC). Lifespan $\widehat{M}$ model for 5% (solid line) and 1% (dotted line) survivorship to maximum age are also shown.

The upshot of employing such high M rates is the suggestion that mortality from fishing has had little to no impact on the Atlantic menhaden stock, leading to the most recent assertion that the Atlantic menhaden stock biomass is currently at 85% of the virgin (unfished) stock size (B_0). This is a highly unlikely conclusion. With the uncertain estimates being used for M, in a single species context, fishing effort could be cranked up to levels never seen before in the fishery. At a minimum, the stock assessment should have at least adjusted M downward to no higher than the average rates in the Liljestrand et al. (2019) paper.

In fact, the ERP WG report highlighted the issue of "unaccounted mortality" shown in **Figure 2** below. The ERP result suggests that the M is too high and cannot be reconciled, even when predators are considered in the Ecopath model.

For the single species modeling, in order to make the Beaufort Assessment Model (BAM) model work with these new extremely high rates of M, model estimates of recruitment had to be raised to levels more than ten times reported in the SEDAR 40 (2015) assessment, levels never before recorded. However, contra to this conclusion, observations from the young-of-the-year (YOY) surveys suggest that menhaden recruitment in 2017 was dangerously low. To this point, during their deliberations the SAS acknowledged there is a substantial risk that three bad years of recruitment in a row--which would not be picked up in the modeling until it is too late -- set the stock up for disaster. That is because the

reduction fishery only fully selects menhaden after all fish reach three years of age. This kind of deleterious outcome is exactly what happened in the Atlantic herring fishery and we cannot afford to do the same with Atlantic menhaden.

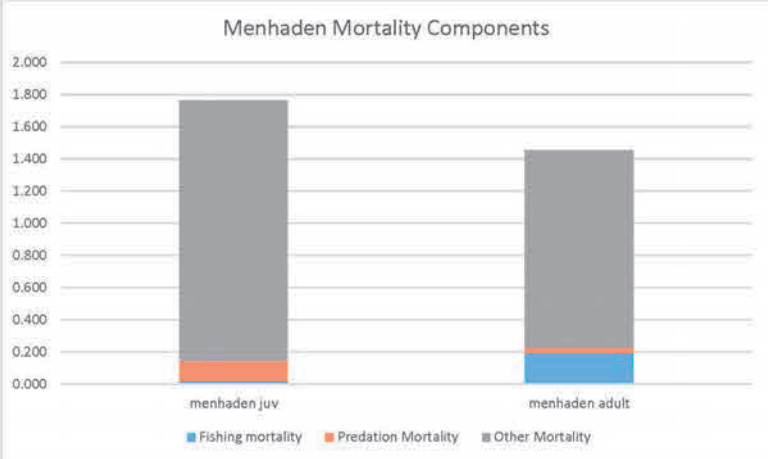

Figure 2.- Ecopath Atlantic menhaden mortality components from the NWACS-MICE model (Figure 129 from the ERP Stock Assessment Report, 2019).

Over the past year, I have shared these concerns with the SEDAR Peer Review Panel, Stock Assessment Subcommittee (SAS) and ERP Technical Committee. In addition, I have been in touch with key members of both the SAS and ERP WG to share my concerns. Now it is up the MMB to adopt a precautionary approach moving forward. The Board has a momentous opportunity and should immediately move forward with approval and implementation of ERPs; however, given the significant uncertainty and resource risks, menhaden catch should not be increased, and in fact, in my view it should be substantially reduced.

I look forward to working with the MMB and the SAS in the near future to closely evaluate the data and model parameter assumptions. I am particularly interested in assisting the ongoing analysis around M and strategies for improvement.

Sincerely,

Jerald S. Ault, Ph.D.
Professor and Chair, Department of Marine Ecosystems and Society
University of Miami

References

Liljestrand, E.M., Wilberg, M.J., Schueller, A.M. 2019. Estimation of movement and mortality of Atlantic menhaden during 1966–1969 using a Bayesian multi-state mark-recovery model. Fisheries Research 210: 204-213.

February 28, 2025

Robert Beal, Executive Director
Atlantic States Marine Fisheries Commission
1050 N. Highland Street, Suite 200 A-N
Arlington, VA 22201
rbeal@asmfc.org

Re: Atlantic Menhaden Revised Natural Mortality Rate Estimate

Dear Mr. Beal,

We are writing to follow up on our letter of October 31, 2024 regarding the science underlying the Atlantic menhaden stock assessment. In that letter, we explained that based on a recent paper currently in peer review by Drs. Jerry Ault and Jiangang Luo we are concerned that the menhaden stock assessment science may be flawed due to significant data errors affecting the natural mortality rate estimate (M) used in the stock assessment model. We explained that the scientific flaws have likely resulted in a substantial overestimation of the natural mortality rate, and in turn substantial overestimation of the coastwide stock size and allowable catch for the fishery, which could result in overfishing of the Atlantic menhaden resource. We also highlighted the ASMFC's obligation to base its conservation programs and management measures on the best scientific information available and to prevent overfishing. Our October 31 letter is enclosed for reference.

We extend our thanks to you for responding to our letter and related emails, as well as to the ASMFC Atlantic Menhaden Stock Assessment Subcommittee (SAS) and its Natural Mortality Work Group for considering the issues raised related to the M estimate used in the menhaden single species stock assessment since 2020. The SAS review confirmed that important mistakes were made in the paper that was relied on to establish the current estimated M (Liljestrand *et al.,* 2019). As a result, the SAS concluded that the current M is at least 20 percent too high -- 1.17 compared to 0.92. However, the enclosed additional analysis by Drs. Ault and Luo shows that the best available science requires an even more substantial revision.

This is largely because after uncovering critical errors made in the Liljestrand *et al.* paper, the SAS did not carefully apply the most scientifically sound methodological approach to correcting those errors. As explained in detail in the enclosed analyses, the use of simple weighted arithmetic averages of magnet efficiency by area[1] is inappropriate in this case. Instead, "Stepwise" or "Parameter Estimation" approaches account for the random distribution of magnet efficiencies and substantially improve model fits. Both methods also substantially lower the M estimates. This can be easily corrected based on the attached analysis. After applying the appropriate statistical metrics, the analysis strongly indicates that the most likely annual natural mortality rate estimate for Atlantic menhaden ranges between 0.50 to 0.54. This M estimate range is not only supported in the analysis because it results from the best model fit, an estimated

[1] Magnet efficiency is a measure of the efficiency by which the magnets in the menhaden processing plants captured tags in the underlying tagging study. Each plant had up to nine magnets, with the first two used in the Costen study, and all nine used in the NMFS data analysis.

M in this range would also be consistent with the prior 12 peer reviewed M estimates, adding credibility to its scientific soundness. In contrast, the SAS recommendation of 0.92 remains a significant statistical outlier, still several standard deviations above all prior estimates.

As you review the enclosed scientific analysis you will see that it is consistent with the work of the SAS and M Work Group leading up to the final step where the SAS inappropriately applied the simple arithmetic average of plant- and area-specific magnet efficiencies. We request that the ASMFC through its Ecological Reference Point Workgroup, which is meeting from March 3 to March 6, 2025, consider the enclosed analysis, apply one of the more statistically sound methods described, and adopt the resulting M estimate (expected to be in the range of 0.50 to 0.54) in the base run Beaufort Assessment Model (BAM)[2].

The importance of the ASMFC meeting its requirement to rely on the best scientific information available is amplified in this case because the magnitude of the substantial differences between the natural mortality rate currently being used (1.17), or alternatively currently recommended by the SAS (0.92), and that indicated by the Ault and Luo analysis (0.50 to 0.54). This suggests that there is high risk that overfishing may occur if not changed immediately, and that Atlantic menhaden could already be overfished with overfishing occurring because the incorrect natural mortality rate assumption has been used since the 2020 assessment. It is critical that the ASMFC make the scientifically and legally sound decisions at this juncture necessary to ensure the Atlantic menhaden resource and the East coast ecosystem it supports are protected.

Thank you for considering our concerns and recommendations.

Sincerely,

Roger Fleming, Esq., Blue Planet Strategies
47 Middle Street
Hallowell, ME 04347
(978) 846-0612
rflemingme7@gmail.com

David Reed, Esq., Chesapeake Legal Alliance
106 Ridgely Avenue
Annapolis, MD 21401
(202) 253-5560
david@chesapeakelegal.org

Encl:

[2] BAM is the model used for the menhaden single species stock assessment, and the outputs from BAM, including the rate of natural mortality, serve as the baseline for the ERP assessment.

1. Dr. Jerald S. Ault Dr. and Jiangang Luo, Report on Estimation of Area Magnet Efficiencies and Natural Mortality, (February 25, 2025).
2. Dr. Jerald S. Ault Dr. and Jiangang Luo, Magnet Efficiency Parameters, (February 27, 2025).
3. Roger Fleming, Esq. and David Reed, Esq., Letter to Mr. Robert Beal, Executive Director, (October 31, 2024).

Cc:
Emily Menashes, emily.menashes@noaa.gov
Dr. Clay Porch, clay.porch@noaa.gov
Dr. Amy Schueller, amy.schueller@noaa.gov
Dr. Katie Drew, kdrew@asmfc.org
Dr. Mike Wilberg, wilberg@umces.edu
Dr. Emily Liljestrand, emily.liljestrand@noaa.gov
Dr. Jiangang Luo, jluo@miami.edu
Dr. Jerry Ault, jault@miami.edu

October 31, 2024

Robert Beal, Executive Director
Atlantic States Marine Fisheries Commission
1050 N. Highland Street, Suite 200 A-N
Arlington, VA 22201
rbeal@asmfc.org

Re: Atlantic Menhaden Natural Mortality Rate Estimates

Dear Mr. Beal,

We are writing because it has come to our attention that the science that undergirds the Atlantic menhaden stock assessment may be flawed due to significant data errors affecting the natural mortality rate assumption used in the Atlantic menhaden stock assessment model. This has likely resulted in a substantial overestimation of the natural mortality rate (M), and in turn of the estimated coastwide stock size and catch limits for the fishery. Among other problems, this could result in overfishing of the Atlantic menhaden resource. We are encouraged to hear that the Atlantic Menhaden Single Species and ERP Methods Workshop from November 4th to 8th will begin a process for evaluating and potentially updating M as part of the ERP Benchmark Assessment. As this discussion and work aimed at resolving this matter are completed, we ask that the ASMFC, Atlantic Menhaden Management Board, and related committees remain cognizant of the ASMFC's legal obligations to base its decisions on the best scientific information available and to prevent overfishing. We also request that you address this matter immediately to protect the Atlantic menhaden resource and all the species that depend on it.

On September 25, 2024, Dr. Jerry Ault presented a paper he coauthored with Dr. Jiangang Luo, both from the University of Miami Rosenstiel School of Marine, Atmospheric and Earth Sciences, to the Atlantic Menhaden Stock Assessment Subcommittee (SAS) titled "Investigation of Atlantic menhaden mortality rates." This paper concludes that the extremely high M used in the menhaden assessment is based on flawed data inputs contained in the paper by Emily Liljestrand *et al.*, titled "Estimation of movement and mortality of Atlantic menhaden from 1966 to 1969 using a Bayesian multi-state mark-recovery model." In 2020, Dr. Ault submitted a letter to the Atlantic Menhaden Management Board highlighting what an extreme outlier the current M is, and his paper is a follow up investigation. See attached. Dr. Ault contacted Dr. Liljestrand and her coauthors several times when writing his paper, and again before the September 25th meeting, inviting them to review his draft and provide him with any mistakes, other concerns, or areas for improving his analysis. The SAS reviewed and discussed the paper at length. Neither Dr. Liljestrand nor members of the SAS articulated any significant flaws with the new analysis.

The authors have since submitted the paper for peer review and publication at the same respected journal, *Fisheries Research*, as the original paper.

Natural mortality is a key factor in determining stock status, so it is vital to use the most accurate M estimate during assessments. The authors noted that Dr. Liljestrand's M estimate is 2.3 times higher than the previous M estimate and more than 14 standard deviations above the average of 12 previously peer-reviewed estimates—an extraordinary outlier. This single parameter could be the deciding factor between a stock being considered as overfished or healthy. It is important to recognize that Ault and Luo attribute this result to underlying data errors, not to problems with the modeling methodologies used by Liljestrand *et al.* or the stock assessment team. Addressing these errors is critical and can be accomplished relatively quickly within the current assessment processes.

The Atlantic Coastal Fisheries Cooperative Management Act (ACFCMA) and the ASMFC's Rules and Charter all require that all Interstate Fishery Management Plans be based on the best available science (BAS) and prevent overfishing. ACFCMA requires that the Commission establish standards and procedures ensuring that IFMPs "promote the conservation of fish stocks throughout their ranges and are based on the best scientific information available[.]" 16 U.S.C. §5104(a)(2). Consistent with ACFCMA, Article VI Section 3 of the ASMFC's Rules and Regulations require that "fishery management plans, and any actions taken according thereto, promote conservation [and] use the best scientific information available." The ASMFC Charter, Section 1(c) establishes that it "is the policy of the Commission that its ISFMPs promote the conservation of Atlantic coastal fishery resources, be based on the best scientific information available, and provide adequate opportunity for public participation."

This policy is directly reflected in Charter Section 6, which provides 6 Standards and Procedures for IFMPs (similar to the Magnuson-Stevens Act's 10 National Standards for Fishery Conservation and Management), including that "(2) Conservation programs and management measures shall be based on the best scientific information available." These Standards also require that overfishing be prevented and that where necessary rebuilding plans be established providing for their long-term sustainability: "(1) Conservation programs and management measures shall be designed to prevent overfishing and maintain over time, abundant, self-sustaining stocks of coastal fishery resources. In cases where stocks have become depleted as a result of overfishing and/or other causes, such programs shall be designed to rebuild, restore, and subsequently maintain such stocks so as to assure their sustained availability in fishable abundance on a long-term basis."

These provisions make clear that the ASMFC's conservation programs and the management measures implemented through its IFMPs be based on the best available science and prevent overfishing. The Atlantic menhaden stock assessment is integral to the ASMFC's conservation

programs and management, so it must be based on the BAS. The importance of meeting this requirement is amplified in this case because the magnitude of the difference between the natural mortality rate currently being used and that indicated by the Ault and Luo analysis suggests that there is significant risk that overfishing may occur if not changed immediately, and that Atlantic menhaden could already be overfished with overfishing occurring since the mortality rate has been used since the 2020 assessment.

As representatives of the conservation community, we want to emphasize that this is a pivotal time for the marine ecosystem on the East Coast. Most of the keystone forage species including Atlantic herring, Atlantic mackerel, river herring, shad, and American eel are at or near historic low levels of abundance. Over one-half of the coastal species managed by the ASMFC are classified as overfished, overfishing, depleted, or status unknown. It is important that the status of the most important ASMFC managed species remains healthy. The difference between an overfished menhaden stock and an abundant one may well determine how resilient marine life on the East coast are to a rapidly changing climate. The identified error in the stock assessment is coincident with dire new findings regarding the striped bass and osprey regional population health, making any corrections to the catch limit(s) all the more urgent for these menhaden-dependent species. From a management perspective, the application of the BAS and measures to prevent overfishing are cornerstones of effective fisheries management and healthy fisheries. Failure to address any data errors found in the science used to develop the Atlantic menhaden assessment's natural mortality rate risks a cascading ecosystem crisis.

Thus, in our view, it is critical that the ASMFC resolve this matter now. A corrected M estimate using a "realistic" M such as the one suggested by Ault and Luo will likely show a need to substantially reduce catches. As such, it is too risky to wait until the Assessment Update in 2028 or the next Benchmark Assessment in 2031 to address this issue. Options we have identified that are in line with the ASMFC's BAS and overfishing requirements that can be taken now, include the following: (1) adopt the recommended M from the Ault and Luo manuscript (pending confirmation of peer review) via the current "update" assessment process, as the M parameter methodologies would not change and only data errors would be corrected; (2) upgrade this cycle's assessment to a "benchmark" as was originally planned. These data concerns have been known to scientists since at least 2023, before the decision to downgrade the assessment to an "update" in February of 2024; (3) delay the single species assessment for approximately 3 months to accommodate the peer review and publication process; or (4) take emergency action to substantially increase the uncertainty buffer when setting specifications until this matter is resolved.

Thank you for considering our concerns and recommendations. We share the concern that addressing this matter now could result in a delay in the schedule for the 2025 ERP Benchmark Assessment, however we think this discussion demonstrates that it is critical that the ASMFC

make the scientifically and legally sound decisions at this juncture necessary to ensure the Atlantic menhaden resource and the East coast ecosystem it supports are protected. For these reasons, we suggest that, if necessary, you consider moving forward with both assessments using more than one M as alternates until the peer review of the Ault and Luo paper, or other work necessary to make a final decision on the appropriate M, is complete.

Sincerely,

Roger Fleming, Esq., Blue Planet Strategies
47 Middle Street
Hallowell, ME 04347
(978) 846-0612
rflemingme7@gmail.com

David Reed, Esq., Chesapeake Legal Alliance
106 Ridgely Avenue
Annapolis, MD 21401
(202) 253-5560
david@chesapeakelegal.org

Cc:
Janet Coit, Esq., janet.coit@noaa.gov
Dr. Clay Porch, clay.porch@noaa.gov
Dr. Amy Schueller, amy.schueller@noaa.gov
Dr. Katie Drew, kdrew@asmfc.org
Dr. Mike Wilberg, wilberg@umces.edu
Dr. Emily Liljestrand, emily.liljestrand@noaa.gov
Dr. Jiangang Luo, jluo@miami.edu
Dr. Jerry Ault, jault@miami.edu

BALD EAGLE RECOVERY IN CHESAPEAKE BAY RAISES RED FLAGS FOR OSPREY

Saving Seafood

July 28, 2025 — The Chesapeake Bay is once again teeming with bald eagles, a testament to decades of successful conservation efforts. A recent feature by the Maryland Department of Natural Resources (DNR), "A Soaring Success: Maryland's Bald Eagle Population Recovery" by science writer Joe Zimmermann, highlights this remarkable comeback.

In 1977, a mere **44 breeding pairs** of bald eagles were recorded in Maryland. Today, that figure has soared to **over 1,400**, according to estimates from the Maryland Bird Conservation Partnership. This dramatic rebound has established the Chesapeake Bay as a national stronghold for bald eagles, boasting the highest concentration of breeding pairs outside Alaska.

This recovery is largely attributed to sustained, science-driven policy. The **1972 federal ban on the pesticide DDT**, which caused reproductive failure and eggshell thinning, was a pivotal moment. In Maryland, the **1984 Chesapeake Bay Protection Act** further safeguarded critical habitat within 1,000 feet of tidal waters. These combined measures helped restore nesting conditions and bolster survival rates.

The scale and speed of this recovery have made bald eagles a symbol not just of national pride, but also of effective conservation action. "Bald eagles are a very good example of what happens when you find the solutions and take action, and now you can look at how they've come back," said DNR conservation ecologist Dave Brinker.

Today, bald eagles nest in every Maryland county and in Baltimore City. The Bay supports not only year-round resident eagles but also seasonal visitors from both the North and South. "Through the year, we have three pretty unique populations of bald eagles," Brinker explained. "There are local birds that are here all year long. Then southern breeding eagles disperse to the Chesapeake Bay to spend summer here because food resources are so good. And in the winter, northern populations that need a warmer place,

they come down to the Chesapeake Bay."

Bald Eagle Recovery and Its Interspecies Consequences

While the recovery of the bald eagle in North America, particularly along the Chesapeake Bay, is a significant conservation milestone, its resurgence raises questions about its impact on other piscivorous bird species that have also been rebounding from decades of decline. Chief among these is the **osprey**, a fish-eating raptor that shares habitat and prey with bald eagles throughout coastal and inland waters. The Chesapeake Bay, now home to one of the largest bald eagle populations in the continental United States, is also crucial osprey habitat, making it an ideal region for observing interactions between the two species.

In recent years, environmental organizations like the Chesapeake Bay Foundation and sportfishing advocates such as the Theodore Roosevelt Conservation Partnership have repeatedly claimed that industrial menhaden fishing is the primary driver of osprey reproductive failures in the Bay. Their public campaigns, regulatory letters, and media statements link declining nest success to a perceived, yet scientifically undocumented, drop in Atlantic menhaden availability—a key prey species for ospreys during chick-rearing season. Much of this advocacy draws on research by Dr. Bryan Watts of the Center for Conservation Biology at William & Mary, whose studies have indicated increased nest failure in parts of the lower Chesapeake. However, even Watts has cautioned against definitive conclusions. In a 2024 Associated Press article, he stated, "We do not know why menhaden have become less available to osprey," and suggested climate change as a possible factor.

Beyond climate shifts, other ecological dynamics may be at play, but the menhaden-focused narrative has recently overshadowed attention to other potential pressures. Given the Maryland Department of Natural Resources' announcement that the Bay now hosts one of the nation's largest bald eagle populations, **interspecies competition deserves closer scrutiny**—particularly food competition stemming from **kleptoparasitism**, the well-documented behavior in which eagles steal fish from ospreys. These interactions, studied for decades by field biologists and ornithologists, warrant renewed attention in light of the bald eagle's increasing population.

While the ecological relationships between bald eagles and ospreys are not yet fully understood, evidence from multiple regions suggests that competitive pressures—especially kleptoparasitism and nest harassment by eagles—may hinder osprey nesting success in areas with high eagle densities. It is possible that the recovery of one iconic raptor is, in part, coming at the expense of another. These dynamics deserve greater consideration from scientists, wildlife managers, and policymakers.

Top-Down Pressure: A 35-Year Body of Research Shows Bald Eagle

Competition May Threaten Osprey Nesting Success

As bald eagle populations have steadily rebounded across North America, particularly in strongholds like the Chesapeake Bay, a longstanding body of scientific research suggests that their recovery may come at the expense of other raptors, especially ospreys. For more than three decades, field biologists and ornithologists have documented the effects of interspecific competition and kleptoparasitism, the act of stealing food, as a factor contributing to osprey nesting failures.

One of the most comprehensive analyses of these dynamics comes from a **2019 study published in the *Journal of Animal Ecology*** titled "Top-down effects of repatriating bald eagles hinder jointly recovering competitors." Led by Jennyffer Cruz and co-authored by Steve K. Windels, Wayne E. Thogmartin, Shawn M. Crimmins, Leland H. Grim, James H. Larson, and Benjamin Zuckerberg, the study evaluated 26 years of nesting data in Voyageurs National Park, Minnesota. The researchers found that as bald eagle numbers increased due to intensive protections, the populations of ospreys and great blue herons declined.

"Bald eagles are top predators and a flagship species of conservation that have benefited from intensive protection," they wrote, "but this likely hindered the recovery of ospreys and herons." The study documented that "eagle abundance was negatively associated with nest reuse (i.e., persistence) and success of ospreys," and concluded: "The top-down effects of returning bald eagles were the main predictors of declining nesting demographics for ospreys and herons resulting in their failed recoveries." Importantly, the authors found "little evidence of bottom-up limitations," such as poor weather, habitat loss, or declining fish stocks, implicating competition and interference from eagles as a primary driver.

The literature documenting these dynamics stretches back decades.

In a **1994 field note published in *The Journal of Raptor Research***, Professors J. MacDonald and N.R. Seymour of St. Francis Xavier University in Nova Scotia documented a lethal encounter in which a bald eagle pursued and killed an adult male osprey that was carrying a white perch. A second eagle joined the chase, and after a brief pursuit, one eagle seized the osprey midair, dragged it to shore, and ate it. The authors believed the attack originated as an act of kleptoparasitism—food theft—a behavior they note is well documented between eagles and ospreys and which they described as "a common occurrence." They also referenced a second lethal attack, described by Flemming and Bancroft in 1990, in which a bald eagle attacked an osprey nestling shortly after it had received a fish.

In **2013**, four U.S. Army Corps of Engineers (USACE) staff members working at Lake Sonoma in Geyserville, California, documented what was believed to be the first officially recorded case of **"cooperative kleptoparasitism"** in which a pair of bald eagles worked together to steal a fish from an osprey. Their observations were formally published in **2014 in *The Journal of Raptor Research*** and summarized in a March 20, 2014, article on Army.mil, which likened the coordinated and calculated nature of the predation to something out of *Jurassic Park*. "Rarely have humans seen them cooperating to hunt as a pair," USACE ecologist Wade Eakle explained. "This was the first time we witnessed them actually cooperating to steal, from another species." The two eagles forced the osprey to drop its trout, after which

the larger female swiftly seized the fish and flew off. Rangers had been monitoring the nesting pair since 2001, but this behavior marked a milestone in understanding the extent of eagle dominance over other raptors.

Evidence for this behavior also includes a **1988 study by Dennis G. Jorde and G.R. Lingle**, published in the *Journal of Field Ornithology*, which observed repeat patterns of interspecific kleptoparasitism along the Platte River in Nebraska. Their findings indicated that bald eagles not only routinely stole food from other raptors but developed learned strategies for doing so efficiently, particularly during important foraging periods.

Even outside peer-reviewed journals, naturalists and field reporters have provided consistent anecdotal corroboration. *BirdWatching Magazine* similarly observes: "Bald Eagles are known to steal fish from other birds, particularly Ospreys. They will aggressively chase Ospreys in flight until the Osprey drops its catch, which the eagle will then snatch midair or retrieve from the water." Another article in the same publication added, "It is common for ospreys and eagles to be in the same hunting grounds. As the more aggressive raptors, eagles will often fight the Osprey and force it to let go of the captured prey. The eagle will typically swoop in to catch the stolen prey." The Cornell Lab of Ornithology's *All About Birds* guide echoes these observations: "A Bald Eagle will harass a hunting Osprey until the smaller raptor drops its prey in midair, where the eagle swoops it up", a classic example of kleptoparasitism.

Collectively, these studies and field reports spanning decades point to a clear and well-established pattern: as eagle populations recover and concentrate in resource-rich areas like the Chesapeake Bay, their aggressive behavior and dominance in the food web may have measurable negative consequences for ospreys. The repeated harassment and food theft increase energetic costs for osprey parents, reduce feeding efficiency, and may contribute to nest failures.

While the recovery of the bald eagle in the Chesapeake Bay region is unquestionably a landmark conservation success story, it does not exist in ecological isolation. As concerns continue to emerge about osprey reproductive success in key habitats like the Bay, it is increasingly important to view this predator's return within the broader dynamics of interspecies competition. Over the past 35 years, a robust and diverse body of scientific literature—supported by peer-reviewed studies, field notes, and firsthand accounts—has documented the kleptoparasitic behavior of bald eagles, particularly their tendency to steal fish from ospreys and, at times, directly harass or even kill them. This behavior, while natural, may contribute to the energetic costs and nest failures observed in osprey populations where eagle densities are high.

Even Benjamin Franklin, in an often-cited letter, criticized the selection of the bald eagle as the national bird due in part to its scavenging habits and its theft of fish from "the fishing hawk," known today as osprey.

> For my own part I wish the bald eagle had not been chosen as the representative of our country. … he watches the labour of the fishing hawk; and when that diligent bird has at length taken a fish, and is bearing it to his nest for the support of his mate and young ones, the bald eagle pursues him, and takes it from him.

While his concerns were framed with a satirical flourish, he anticipated a tension now supported by decades of ecological research. As wildlife managers and policymakers evaluate recent reports of declining osprey productivity, it is essential that they consider not only fishery-related factors but also the well-documented competitive interactions between these two raptor species.

References

- BirdWatching Magazine. (2025, March 7). *What time of day do Osprey hunt?* BirdWatching Daily. https://www.birdwatchingdaily.com/beginners/birding-faq/what-time-of-day-do-osprey-hunt/
- BirdWatching Magazine. (2025, May 19). *What do Bald Eagles eat?* BirdWatching Daily. https://www.birdwatchingdaily.com/beginners/birding-faq/what-do-bald-eagles-eat/
- Cornell Lab of Ornithology. (n.d.). *Bald Eagle – Life history*. All About Birds. Retrieved July 23, 2025, from https://www.allaboutbirds.org/guide/Bald_Eagle/lifehistory
- Cruz, J., Windels, S. K., Thogmartin, W. E., Crimmins, S. M., Grim, L. H., Larson, J. H., & Zuckerberg, B. (2019). Top-down effects of repatriating bald eagles hinder jointly recovering competitors. *Journal of Animal Ecology*, *88*(12), 1792–1804. https://doi.org/10.1111/1365-2656.12990
- Eakle, W. L., Lishka, J. J., Kirven, M. N., & Hawley, J. (2014). Cooperative Kleptoparasitism by a Pair of Bald Eagles at Lake Sonoma, California. *Journal of Raptor Research*, *48*(1), 89–91. https://doi.org/10.3356/JRR-13-45.1
- Flemming, S. P., & Bancroft, R. P. (1990). Bald eagle attacks osprey. *Journal of Raptor Research*, *24*(2), 122. https://sora.unm.edu/sites/default/files/journals/jrr/v028n02/p00122-p00122.pdf
- Franklin, Benjamin. "To Sarah Bache, 26 January 1784." Founders Online, National Archives of the United States. https://founders.archives.gov/documents/Franklin/01-41-02-0327 .
- Gerrard, J. M., & Bortolotti, G. R. (1988). *The Bald Eagle: Haunts and habits of a wilderness monarch*. Smithsonian Institution Press.
- Jorde, D. G., & Lingle, G. R. (1988). Kleptoparasitism by Bald Eagles wintering along the Platte River, Nebraska. *Journal of Field Ornithology*, *59*(1), 104–105. https://pubs.usgs.gov/publication/1001515
- Macdonald, J.; Seymour, N.R. (1994). "Bald Eagle attacks adult Osprey" (PDF). *Journal of Raptor Research*. *28*(2): 122.
- Northern Woodlands. (2021, June 7). *Kleptoparasitism*. The Outside Story. https://northernwoodlands.org/outside_story/article/kleptoparasitism
- Poole, A. F. (2002). *Ospreys: A natural and unnatural history* (2nd ed.). University Press of New England.
- Stalmaster, M. V. (1987). *The Bald Eagle*. Universe Books.
- U.S. Army. (2014, March 20). *Raptors Witnessed Cooperatively Hunting at Lake Sonoma*. https://www.army.mil/article/122302/Raptors_Witnessed_Cooperatively_Hunting_at_Lake_Sonoma/
- Wade L. Eakle, Joseph J. Lishka, Monte N. Kirven, and John Hawley "Cooperative Kleptoparasitism by a Pair of Bald Eagles at Lake Sonoma, California," *Journal of Raptor Research* *48*(1), 89-91, (1 March 2014). https://doi.org/10.3356/JRR-13-45.1
- Zimmermann, J. (2025, July 3). *A soaring success: Maryland's bald eagle population recovery*. Maryland

Department of Natural Resources News. https://news.maryland.gov/dnr/2025/07/03/a-

Categories: Science Tags: Bald Eagle, Chesapeake Bay, Maryland, Mid-Atlantic, osprey

Recent Headlines

- NORTH CAROLINA: Blue crabs from North Carolina could be harder to find, too
- Bald Eagle Recovery in Chesapeake Bay Raises Red Flags for Osprey
- Warming oceans drive tuna from Pacific islands
- NOAA Fisheries confirms 64 large whale 'entanglements' in 2023
- EU agrees to trade deal with US, setting tariff rate for goods at 15 percent
- Fishing groups push to postpone protections for endangered right whale to 2035
- FLORIDA: Nets torn 'all to hell': Port Canaveral fishermen worry about increasing rocket launches, debris
- Trump revokes agreement to protect salmon

Most Popular Topics

Alaska Aquaculture ASMFC Atlantic States Marine Fisheries Commission BOEM California China Climate change Coronavirus COVID-19 Donald Trump groundfish Gulf of Maine Gulf of Mexico Hawaii Illegal fishing IUU fishing Lobster Maine Massachusetts Mid-

FOR IMMEDIATE RELEASE
Stove Boat Communications
(202) 595-1212
contact@stoveboat.com

July 29, 2025

Omega Protein and Ocean Harvesters Urge Science-Based Review Before Imposing New Menhaden Restrictions

Letter from Veteran Biologist Addresses Scientific Questions Over Osprey Declines

Washington, DC – In a letter submitted to the Atlantic States Marine Fisheries Commission (ASMFC), Peter Himchak, Senior Scientific Advisor to Omega Protein, warned that "there has been an inordinate amount of focus on menhaden generally, and the reduction fishery in particular" in discussions about recent osprey declines in the Chesapeake Bay.

Omega Protein, which processes menhaden into fishmeal, fish oil, and related nutritional products, is supplied by Ocean Harvesters under a long-term harvesting agreement. Himchak submitted the letter on behalf of the company ahead of the ASMFC's Summer Meeting.

Himchak, who served for 39 years as a fisheries biologist with the New Jersey Division of Fish and Wildlife and as a long-time advisor to both the ASMFC and the Mid-Atlantic Fishery Management Council, sat on the ASMFC's Atlantic Menhaden Technical Committee and Stock Assessment Sub-Committee from 1988 until 2006.

In the letter, Himchak criticized the ASMFC's Work Group on Precautionary Management in Chesapeake Bay for proposing "draconian management recommendations 'without determining if there is or is not an adequate supply of menhaden to support predatory demand in the Bay.'" He warned that moving forward with such actions without first determining whether there are, in fact, fewer menhaden in the Bay or whether the fishery has any impact on osprey "risks gravely impacting a more than 150-year-old industry and hundreds of jobs while doing nothing to improve the osprey situation."

Himchak wrote that the ASMFC's Technical Committee (TC) already has a significant workload in advance of the Commission's Annual Meeting, but raised four areas of scientific inquiry the TC could investigate that would provide the Board with more complete information. 1) He asked whether "the phenomenon of reduced osprey production [is] confined to the times and areas in

which the menhaden reduction fishery operates," referencing USGS data showing declines in osprey abundance in coastal areas of multiple states—not just the Chesapeake—and increases in interior regions. He also noted that the fishery does not begin fishing until May or later—after migrant ospreys arrive in the region from late February to early March and begin building nests from mid-March to mid-April—raising questions about how the fishery could influence osprey's months-earlier decisions about where to nest.

2) He wrote that there have been sizable increases in populations of multiple menhaden-dependent predators since at least the turn of the century, and that a stomach contents analysis of striped bass, which are only somewhat dependent on menhaden, indicated they "are not starving and would be considered healthy." Therefore, he asked, "is it more likely that ospreys are being outcompeted or that the reduction fishery uniquely impacts osprey?"

3) Regarding eagle-osprey interactions, he noted a recent Maryland DNR release announcing "large increases in the state's bald eagle population." He referenced myriad studies finding that bald eagles are "kleptoparasitic"—a term used to describe their well-documented habit of attacking hunting osprey to steal their food or prey on adults, young, and eggs. Citing a study from Voyageurs National Park, he wrote that "increased numbers of eagles were associated with a reduction in the numbers of osprey nests, their nesting success and heronry size," and asked whether "issues of competition and depredation [can] be ruled out as a cause of osprey's lack of breeding success." He further pointed to "significant scientific and anecdotal evidence of the dominant and adverse impacts eagles have on osprey."

That concern was echoed in a newly released *Saving Seafood* special report titled **"Bald Eagle Recovery in Chesapeake Bay Raises Red Flags for Osprey."** The report compiled over three decades of peer-reviewed research, field observations, and published accounts documenting instances in which eagles had a negative impact on osprey populations. In one study, researchers found "eagle abundance was negatively associated with nest reuse (i.e., persistence) and success of ospreys." Significantly, the researchers found "little evidence of bottom-up limitations," such as poor weather or declining fish stocks, and emphasized the role of eagle aggression, including harassment and food theft. While this body of research does not prove the resurgence of bald eagles in the Chesapeake to be the cause of osprey reproduction issues, it does indicate it is a possibility deserving of further investigation.

The full report is available at: https://www.savingseafood.org/science/bald-eagle-recovery-in-chesapeake-bay-raises-red-flags-for-osprey

4) Himchak also asked the Technical Committee to consider whether osprey foraging success is being affected by climate-driven environmental changes, including storm frequency, shoreline hardening, warming waters, or hypoxia. Citing a 2024 study by Bryan Watts, he noted that "deliveries of all forage species to osprey nests declined steadily from 1974 to 2021," and asked whether "ospreys' apparent lack of foraging success is tied to changes in local conditions that are impacting either local abundance of forage or osprey's hunting success."

He concluded the letter by writing, "The commission must be guided by science. Precipitous actions, taken in the name of precaution, are not always harmless. Neither Ocean Harvesters nor

Omega Protein can survive without the current low level of access to the menhaden resource in the Bay. There simply are not enough 'fishable days' – that is, days where the weather and sea conditions allow vessels to operate – in a year to safely conduct a profitable fishery solely in the ocean. The menhaden fishery is managed in the most conservative manner in its 150 year or so history, and the reduction fishery is operating at its lowest sustained levels – in the Bay and overall – for as long as we have reliable records (i.e., since the 1950s). Precaution is already the policy. Before taking actions that could cause irreversible economic harm to this historic fishery, the Board should ensure that all reasonable avenues of inquiry into the issues facing osprey are explored."

James Boyle

From: Jeff Kaelin <jKaelin@lundsfish.com>
Sent: Friday, July 25, 2025 8:14 AM
To: Katie Drew
Cc: Bob Beal; john.clark@state.de.us; James Boyle; Glen Gawarkiewicz; Kim Hyde - NOAA Federal
Subject: [External] FW: Ocean Conditions Meeting slides + papers
Attachments: TaenzerEtAl2025_SeasonalSalinificationUSNortheastColdPool.pdf; JGR Oceans - 2023 - Taenzer - Categorization of High-Wind Events and Their Contribution to the Seasonal Breakdown of.pdf; Ocean Conditions Meeting July 15 2025.pdf; 4a. Final_Menhaden WG Full Report_4.18.25.pdf; Fwd: Spring 2025 Seasonal Summary

Good morning, Katie – I hope this note finds you well.

I am writing to you, as Chair of the TC, to forward a presentation by Dr. Glen Gawarkiewicz, from the Woods Hole Oceanographic Institution https://ieeexplore.ieee.org/author/37726309400 , to a Commercial Fisheries Research Foundation / WHOI Oceans Conditions Meeting last week, which documents cold water on the Continental Shelf in recent years; likely the reason menhaden fishing in the Chesapeake Bay was delayed during the 2022-2024 fishing seasons, as documented in the CB menhaden WG full report.

From information we received from NJ DEP, as part of the Atlantic menhaden purse seine fishery's sustainability certification by the Marine Stewardship Council, the New Jersey menhaden fishery was similarly affected by this cold-water phenomenon during this same period:

Landings / catch history / % of quota caught:
2021 45,694,424 May 21 through December 14 81%
2022 46,888,789 June 29 through December 5 83%
2023 40,857,329 June 28 through December 15 72%
(NJ's quota is 11% of the coastwide TAC of 233,550; 56.6 million lbs., by my math)

I'm raising this issue in the context of our upcoming discussion at the menhaden board, on TC direction in response to the work group report, and asking that the TC evaluate the possible effects of cold water in inshore habitat during this period, relative to the lack of menhaden being available for osprey in the CB and, specifically, in the context of the report's research recommendation, 'Investigate menhaden environmental condition preferences to analyze potential shift in seasonal availability'.

The Sea Surface temperature maps in the report illustrate the occurrence of cold water in 2024. These maps are available, on a daily basis, throughout the 2022-2024 period captured in Table 3 (WG report page 34) and can be made available to the TC from Kim Hyde, who has been hosting the Squid Squad, which was created during the time of the 2022 research track assessment (RTA) for the Illex (shortfin) squid fishery, and taking place weekly since that time. The Squid Squad continues to meet, with the RTA for Loligo (longfin) squid now taking place.

Dr. Hyde is a biological oceanographer in NOAA's Ecosystem Dynamics and Assessment Branch and weekly host of the Squid Squad for most of the last 100+ Friday morning meetings. Her expertise includes

ocean color remote sensing and phytoplankton ecology https://www.fisheries.noaa.gov/contact/kimberly-hyde-phd. In addition to the availability of the Clark Chart maps, Kim suggested to me that the TC might also review the seasonal summaries of water quality parameters in the Chesapeake Bay, from the NOAA Chesapeake Bay office, to track oceanographic effects on menhaden distribution there. The Spring 2025 summary is attached.

Thank you for your consideration of this information, specifically in the context of the WG's research recommendation related to seasonal distributions of Atlantic menhaden in the CB.

I look forward to seeing you in Arlington next month.
With best regards,
Jeff

Jeff Kaelin
Director of Sustainability
and Government Relations
Lund's Fisheries, Inc.
997 Ocean Drive
Cape May, NJ 08204
C-207-266-0440

SQUID-SCALLOPS-FINFISH
www.lundsfish.com

From: Jeff Kaelin <jKaelin@lundsfish.com>
Sent: Friday, July 18, 2025 9:05 AM
To: nolsen@cfrfoundation.org
Cc: Glen Gawarkiewicz <ggawarkiewicz@whoi.edu>
Subject: FW: Ocean Conditions Meeting slides + papers

Thanks Noelle and Glen…great presentation Tuesday evening, Glen.

As I mentioned, I want to make this cold water on the shelf information available to Dr. Katie Drew, the ASMFC stock assessment team lead, and TC Chair for Atlantic menhaden. As a member of the Commission's menhaden management board, I'm motivated by our upcoming August 7 agenda item, "Discuss Technical Committee direction in response to Work Group Report on precautionary management in Chesapeake Bay."

Attached is that April report to the Commission, from the menhaden workgroup tasked to consider osprey health concerns in the Chesapeake Bay.
At page12 the report states that "The presence of menhaden schools is dependent on water temperature, as such, catch and effort varies across the season."; and … "this is highly variable with the

past two years' catch and effort significantly below average until the end of June." See Table 3 (page 34), which records late starts for the menhaden fishery there in the years 2022-2024.

We experienced the same, here in NJ and, as we all know tracking the oceanographic and climate information coming from the Squid Squad over the last few years, while the common wisdom is that the coastal waters of the Atlantic are continuing to warm, they have actually been colder in the last 3-4 years, which has resulted in seasonal delays in menhaden fishing during that time.

These papers and your presentation, Glen, will help the TC to understand that this cold water has extended south to the Chesapeake Bay in recent years and is likely a factor in the recent, seasonal delays in catch there.

When I reach out to Katie, I will copy you, Glen, in case she would like to follow up with you, or vice versa.

If possible, I would like to make the Clark Charts depicting spring water temperatures during 2022-2024 available to Katie and the TC before our August meeting.

With best regards,
Jeff

From: Noelle Olsen <nolsen@cfrfoundation.org>
Sent: Thursday, July 17, 2025 1:51 PM
To: Jeff Kaelin <jKaelin@lundsfish.com>
Cc: Glen Gawarkiewicz <ggawarkiewicz@whoi.edu>
Subject: Ocean Conditions Meeting slides + papers

Hey Jeff,

Thank you for tuning into our meeting on Tuesday. Here is a copy of the presentation as well as those two papers Glen mentioned.

Best,
Noelle

--

Noelle A. Olsen (she/her)
Senior Research Biologist
Commercial Fisheries Research Foundation
www.cfrfoundation.org
CFRF's Data Access Portal

The CFRF-WHOI Ocean Conditions Meeting

July 15, 2025

Research Team

Commercial Fisheries Research Foundation (CFRF)

Noelle Olsen and Linus Stoltz

Woods Hole Oceanographic Institution (WHOI)

Glen Gawarkiewicz, Frank Bahr, Svenja Ryan,

Caroline Ummenhofer, and Finn Wimberly

Cape Cod Commercial Fishermen's Alliance (CCCFA)

Aubrey Ellertson Church and Mel Sanderson

Shelf Research Fleet

- Started in 2014 to better monitor the ocean conditions off the shelf break in tandem with the OOI Pioneer Array
- The project has grown with >20 vessels collecting data
- We partnered with the Cape Cod Commercial Fishermen's Alliance to expand sampling

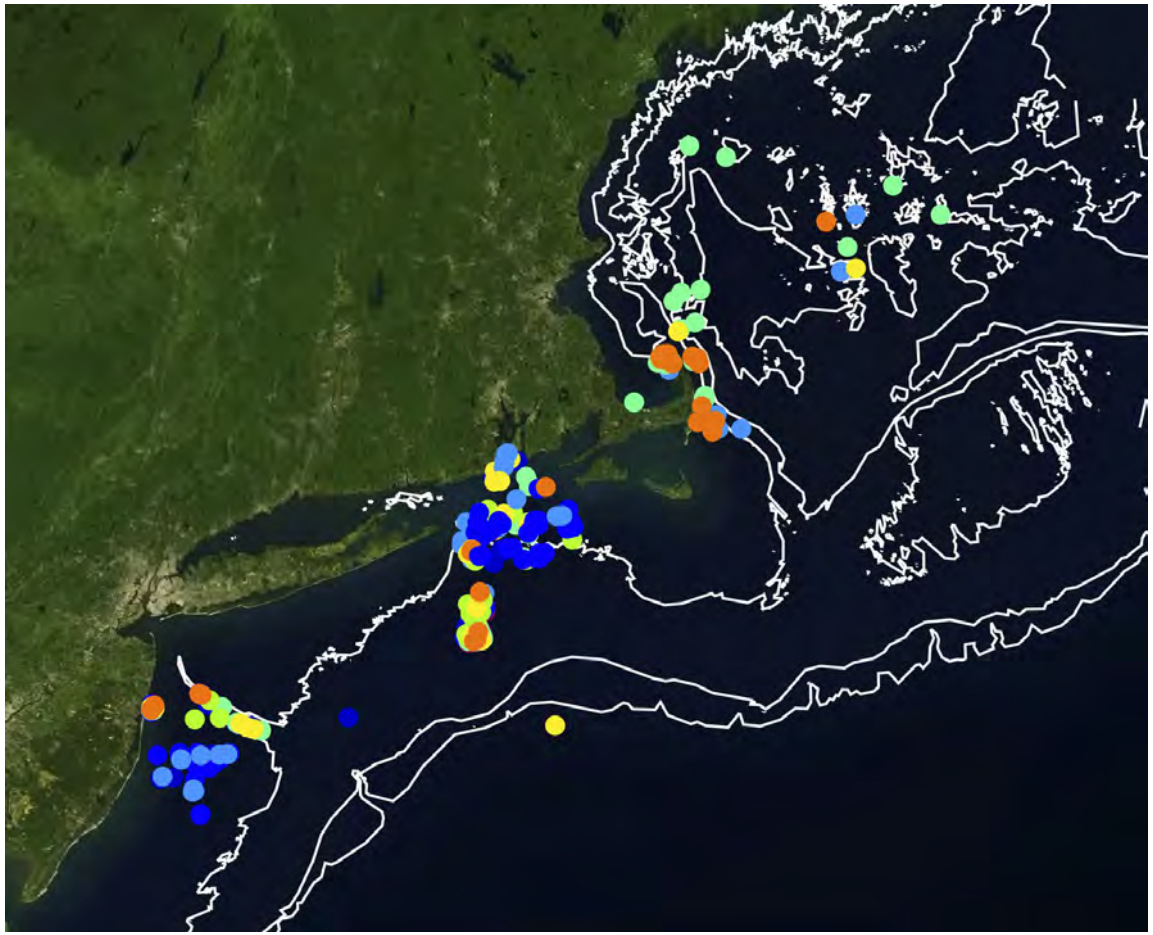

CTD profile locations since January 1, 2024.

Research Fleet Vessels

CFRF

- FV Brooke C - Point Judith, RI
- FV Finast Kind II - Tiverton, RI
- FV J-Mar - Point Pleasant, NJ
- FV Mister G - Point Judith, RI*
- FV TNT - Barnegat, NJ*

*CTD has a chlorophyll sensor

CCCFA

- FV Lisa Marie – Saquatucket, MA
- FV Miss Lilly – Provincetown, MA

Data Access Tools

CFRF's Data Access Portal – https://ondeckdata.com/

- Shelf Dash, Wind Dash, and ERDDAP
- Linus Stoltz (lstoltz@cfrfoundation.org)

CCCFA's Cape Cod Ocean Watch – https://ccocean.whoi.edu/

- Profiles with satellite and FIShBOT layers
- Finn Wimberly (finn.wimberly@whoi.edu)

Climate, Fisheries, & Cooperative Research Documentary

Zack O'Connor
Wesleyan University Student
zoconnor@wesleyan.edu

CFRF Research Opportunities

- **Lobster and Jonah crab Research Fleet** – looking for 2-3 offshore lobster and/or Jonah crab vessels
  - Contact Noelle Olsen (nolsen@cfrfoundation.org)

- **Sea Scallop Image-Based Research Fleet** – looking for 6 LAGC scallop vessels, due 7/31
  - Contact Becky Smoak (rsmoak@cfrfoundation.org)

- **eMOLT expansion** – looking for vessels to deploy temperature and dissolved oxygen sensors
  - Contact Linus Stoltz (lstoltz@cfrfoundation.org)

Fundraiser: CFRF License Plate

- Collecting pre-orders for RI passenger, commercial, and combination plates
- CFRF will get $20 for every plate purchased
- For out-of-state folks, we are collecting donations & selling merchandise

www.cfrfoundation.org/license-plate

Questions? Contact Hannah Verkamp (hverkamp@cfrfoundation.org)

Outline

- Overview of Shelf Fleet and 2025 Statistics
- 2024 Review- The Cold Fresh Pulse and its impacts
- 2025 Shelf, Gulf Stream, and Continental Slope
- Some Squid Squad notes on shifting patterns
- Pending NSF Proposal and Potential Jaiabot Fleet

Shelf Fleet in Review

- Six Zones across the continental shelf south of Rhode Island
- Fleet expanded to New Jersey
- Sea Grant project funded a new fleet in Chatham MA with Cape Cod Commercial Fishermen's Alliance (S. Ryan, C. Ummenhofer, F. Wimberley WHOI)
- Critical Improvement- Linus automating the processing (consistent with Frank Bahr methods) to improve timeliness of data serving and appearance on website

Original Zones

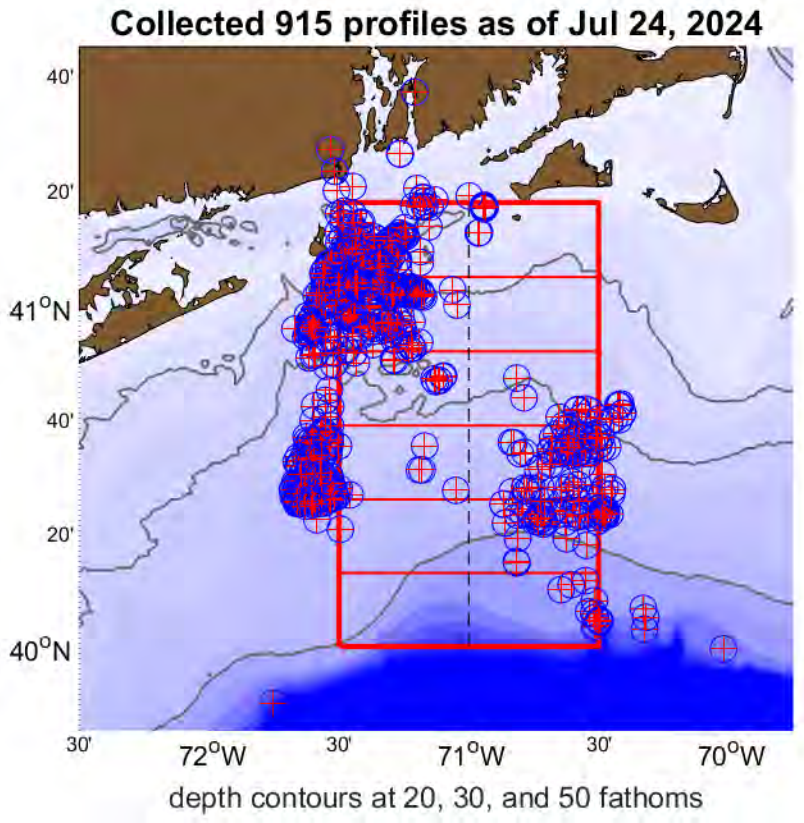

2025 to Date

- 89 Profiles, 938 casts total in the archive

Spatial pattern of Casts from 2025

NJ casts primarily near Hudson canyon

Chatham Fleet casts along Outer Cape and near Provincetown

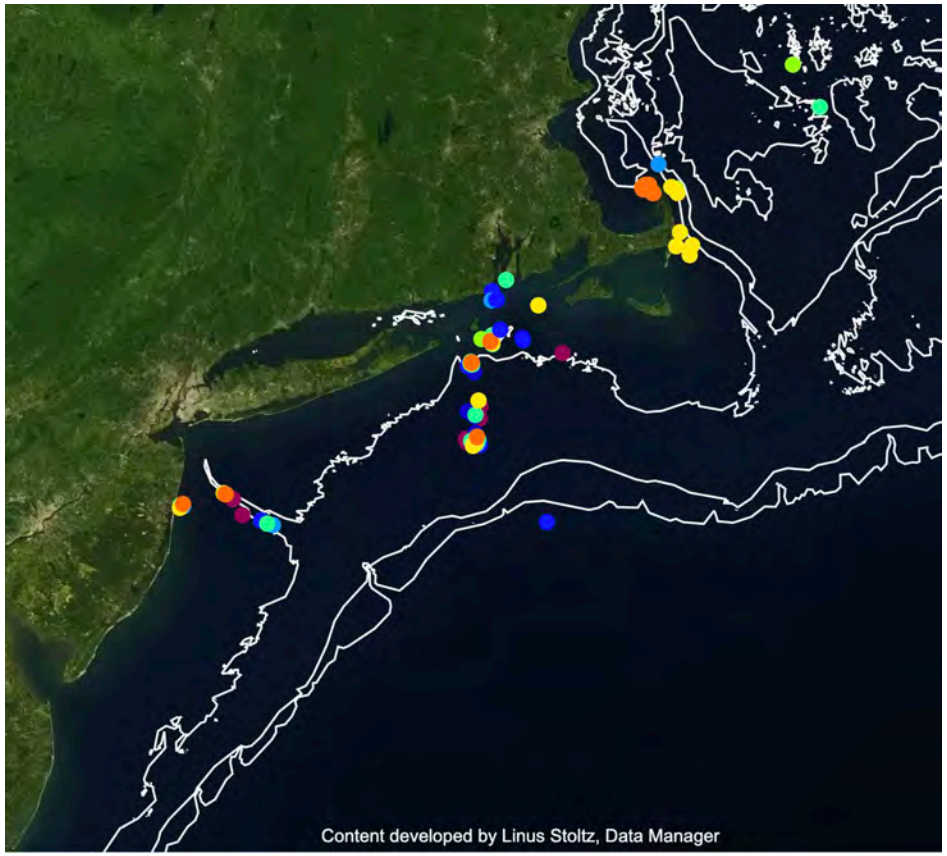

Temperature and Salinity Profiles

Profiles color coded with time, Maroon-blue-green-yellow-orange

Start of the year T~47-49 Deg F
Salinity~33.5-33.7

Minimum Temperatures in March 40 Deg. F, Salinity 33

Steady warming through spring, Temperatures now up to mid 70s

Freshening, as low as 30.5

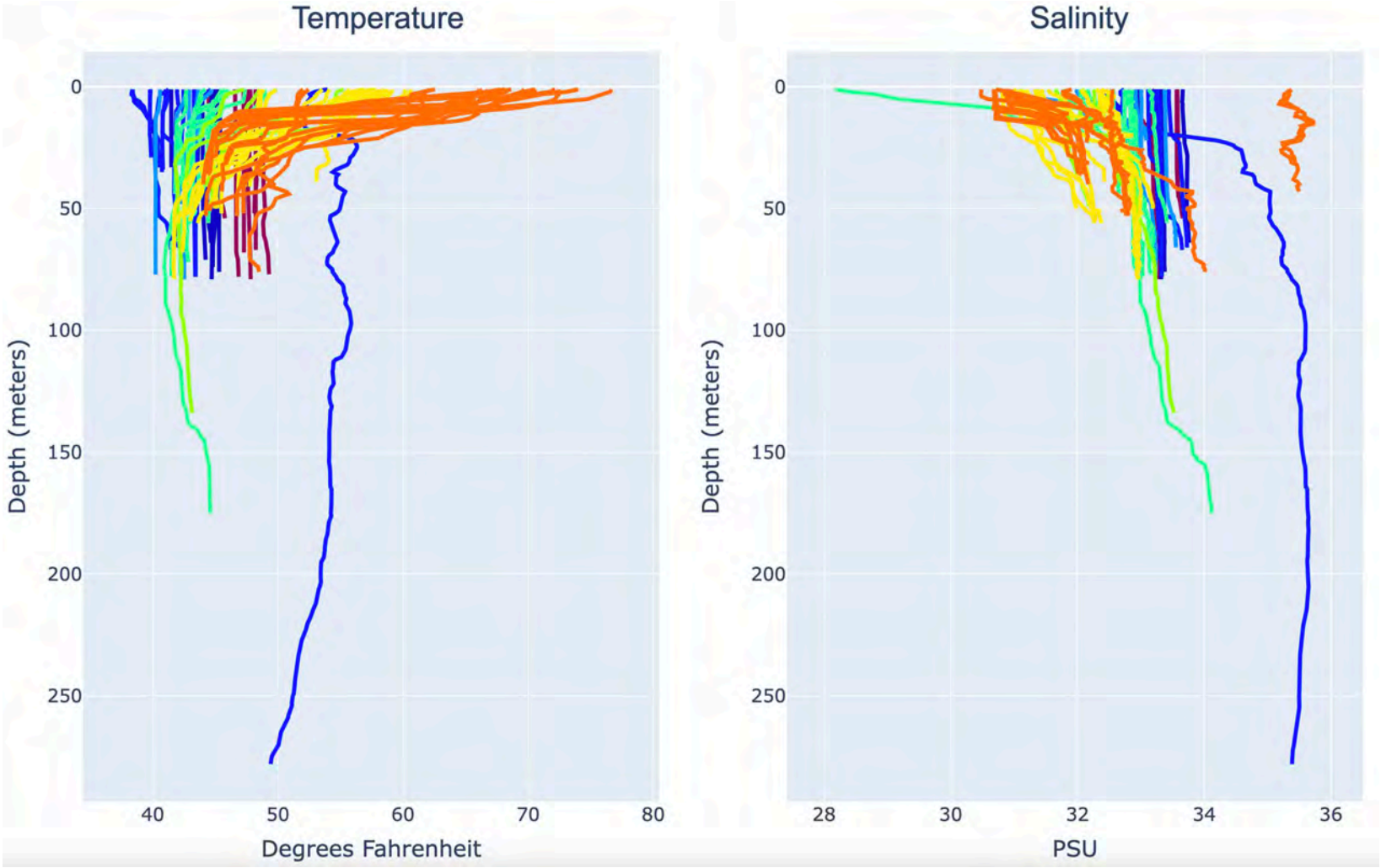

Density and Chlorophyll a Profiles

Density increases from January to March as cooling progresses

Formation of thermocline and Pycnocline in April-May

VERY buoyant surface water in July. VERY high stratification

Chlorophyll maxima at 10-15 Fathoms depth (20-30 m)

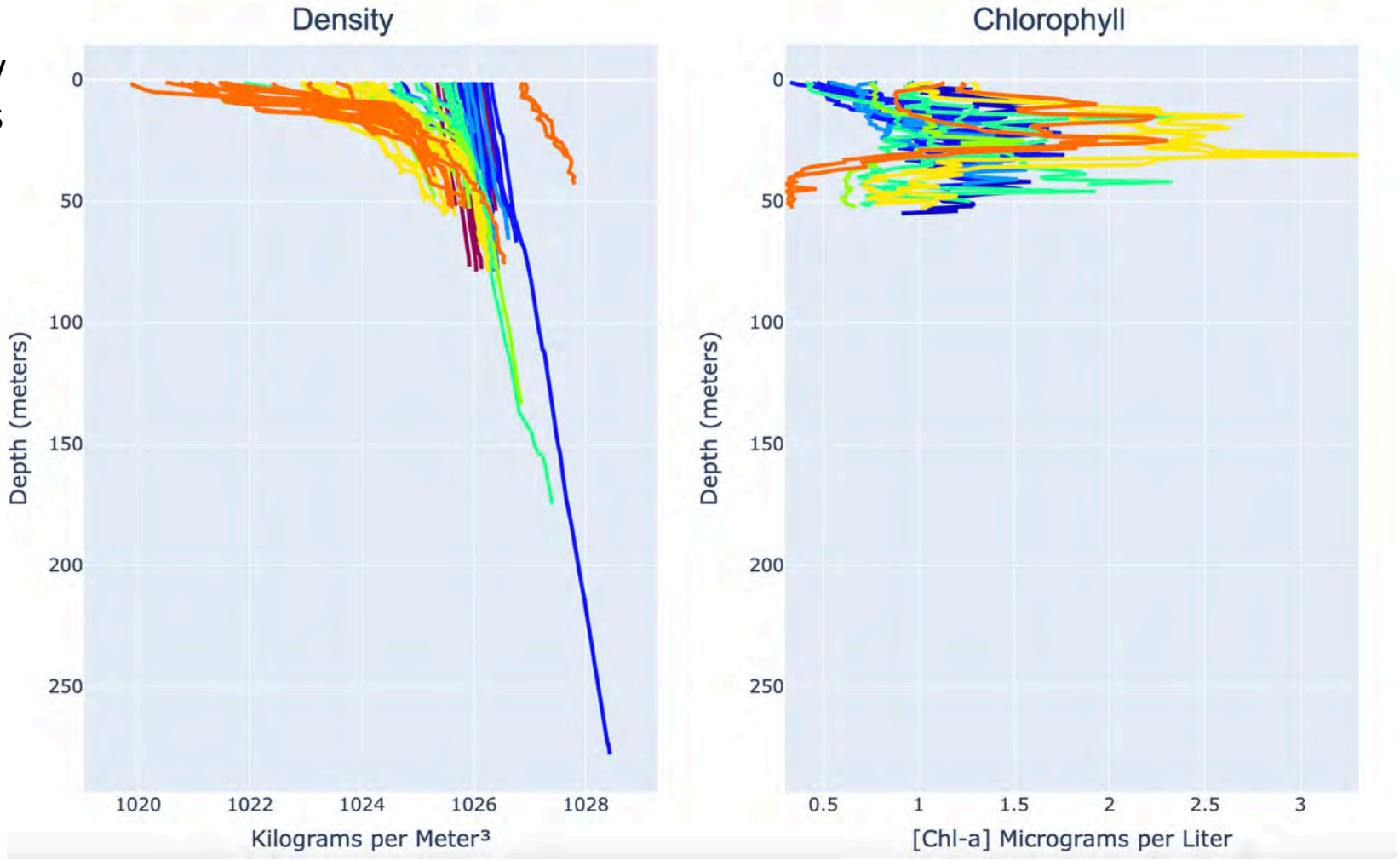

2024 Profile Locations

110 Profiles collected by July 14

No Chatham Fleet profiles

Good New Jersey coverage

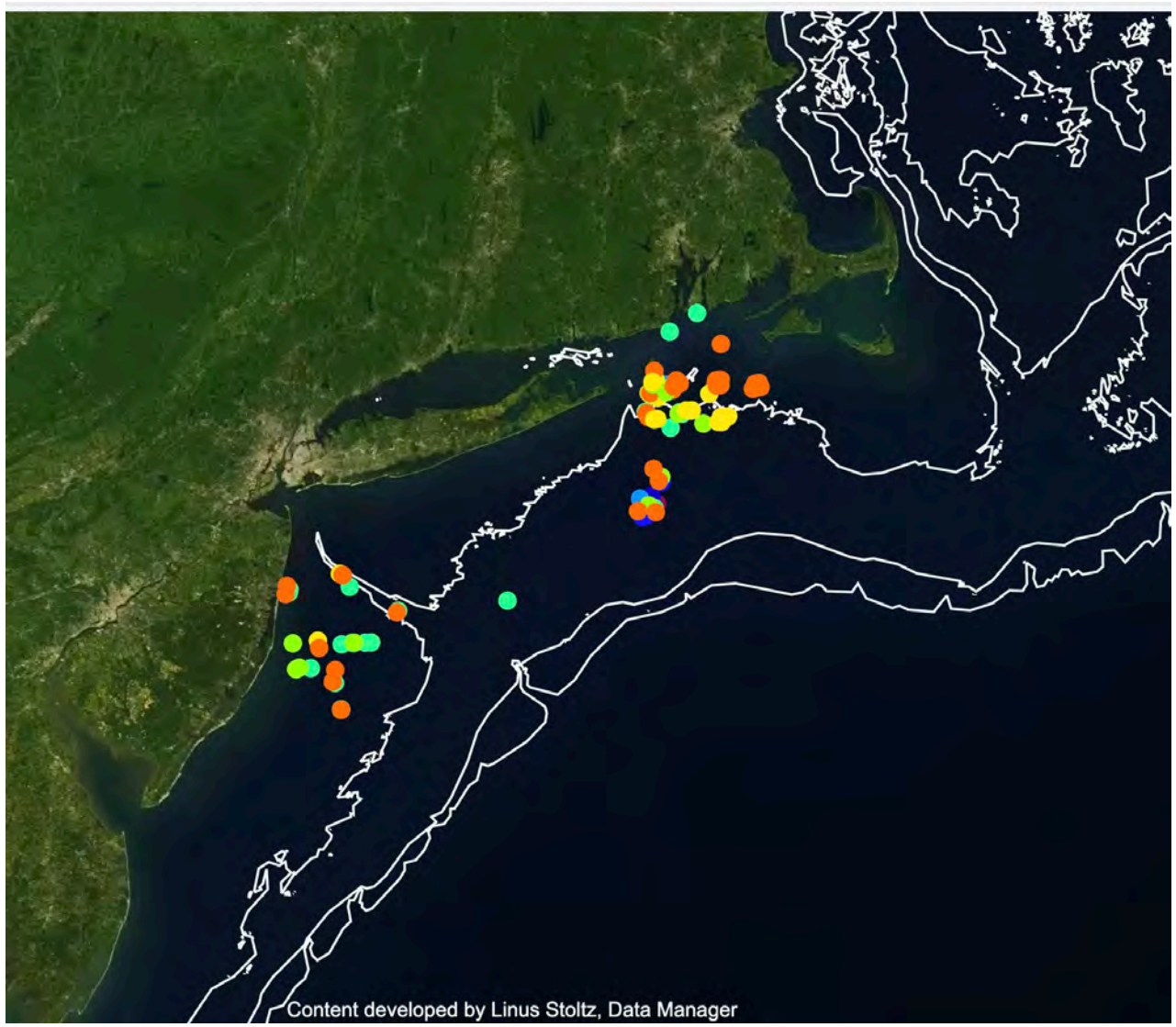

2024 Temperature and Salinity Profiles

Very cold temperatures in March, 42-43 Deg. F

Bulk of June-July temperatures Less than 70 Deg. F

Very fresh conditions in May-June < 30

Even at the start of the year Salinities were relatively fresh, 32.5

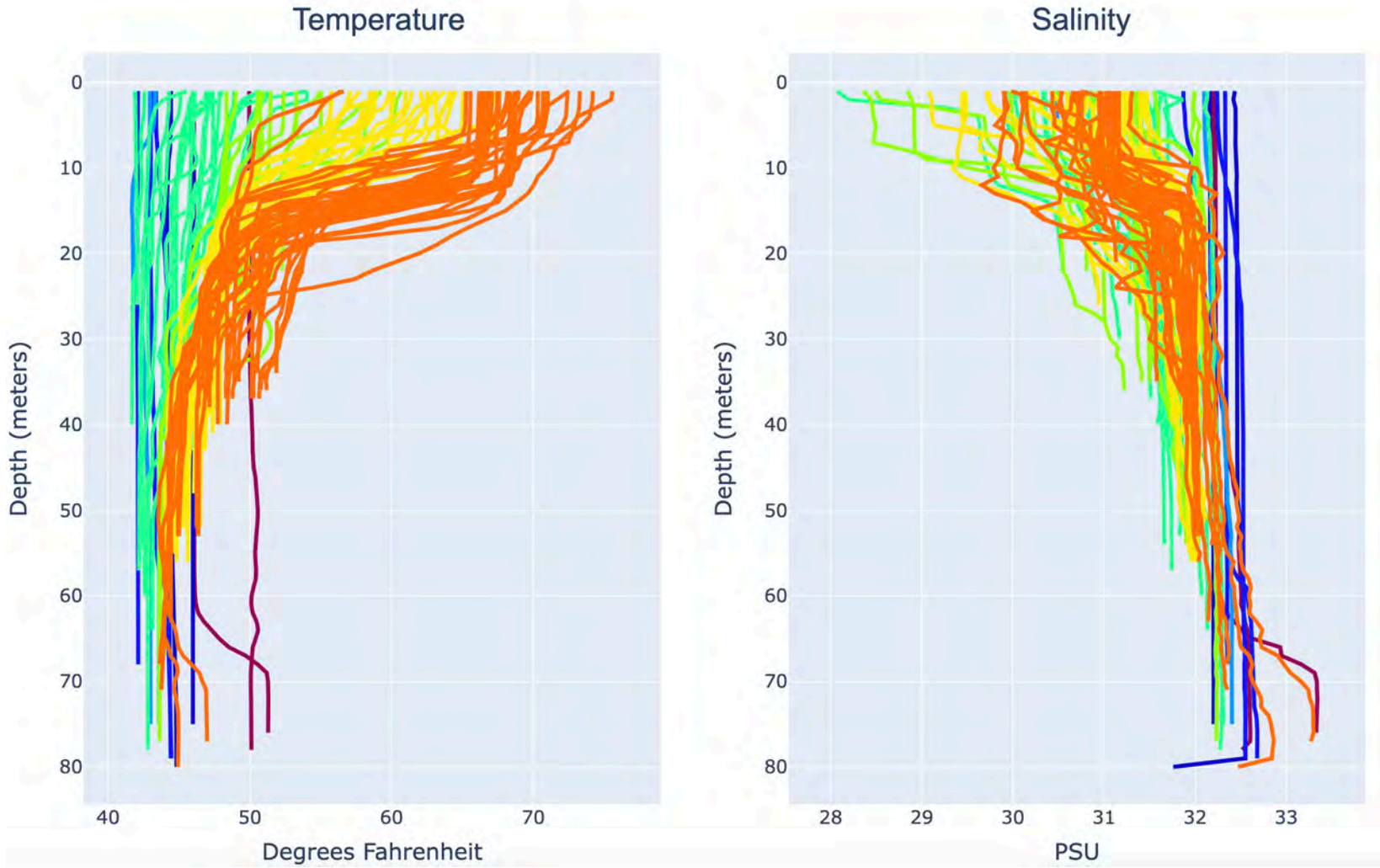

2024 Density and Chlorophyll a

More dense near the
Surface (cooler conditions)

Chlorophyll a maximum is
Fairly shallow (7-10 fathoms)

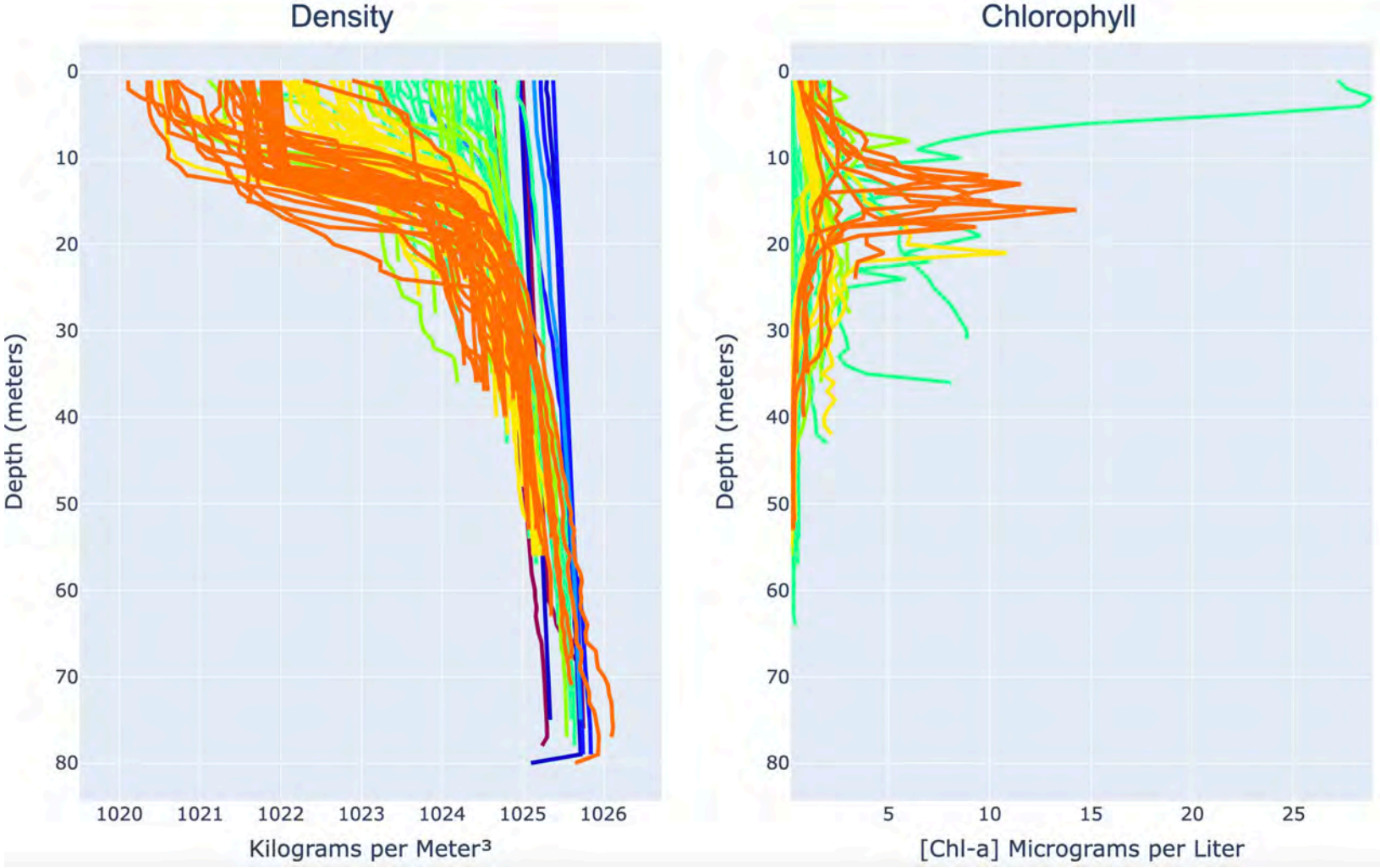

Salinity 2015-2024 Shelf Research Fleet

Monthly averaged vertical profiles from 6 Zones fcross the Shelf

Red indicates Warm Core Ring or Slope Water

Note the big shift towards solid blue in the second half of 2023

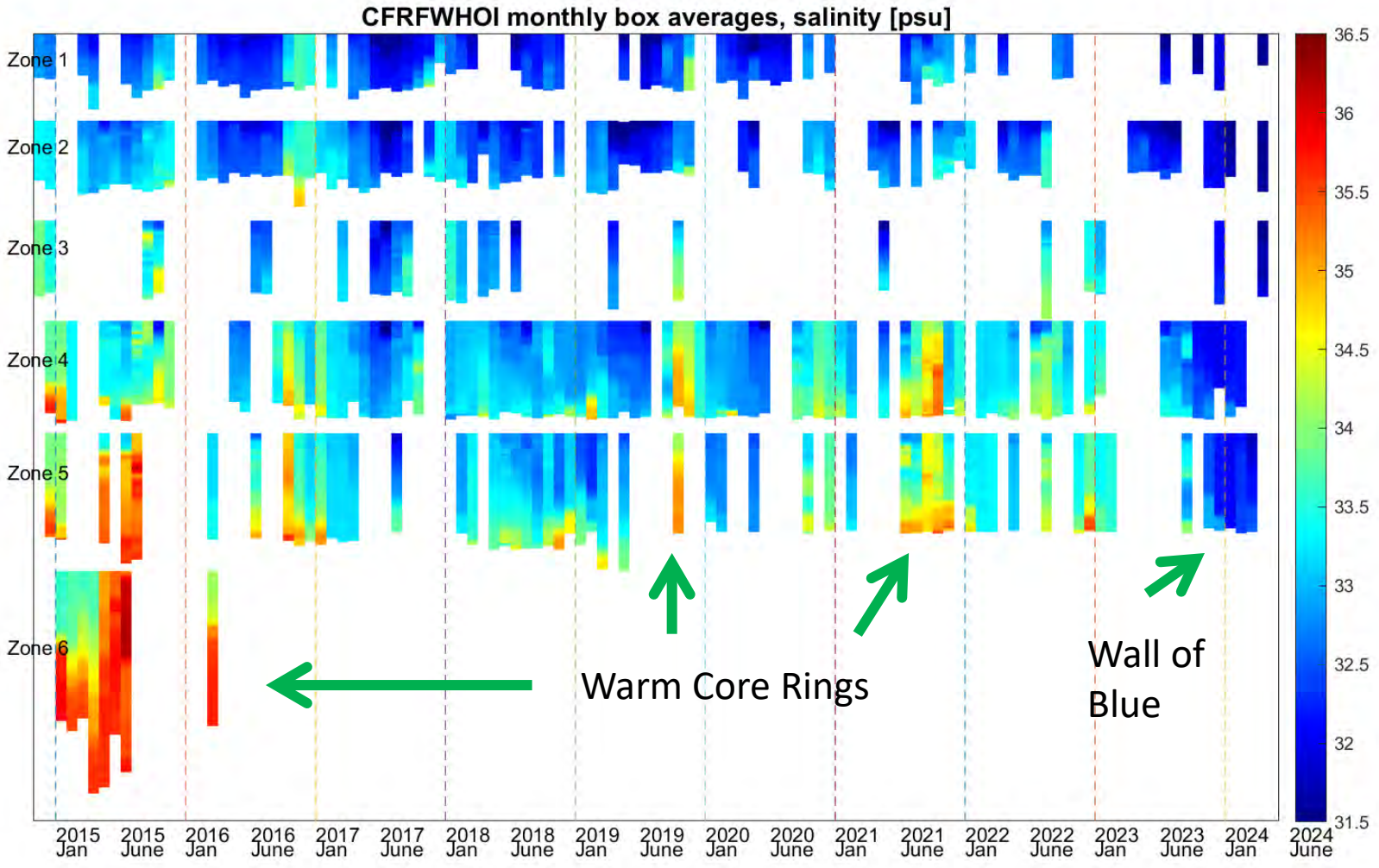

Figure from Frank Bahr

What happened in 2024?

Sea Surface Temperature map from Mid-May 2024

Temperature anomaly over continental shelf and slope of 5.4 to 9 Deg. F. !!!

Gulf of Maine slightly warmer than usual

Cold anomaly over the entire continental shelf and slope

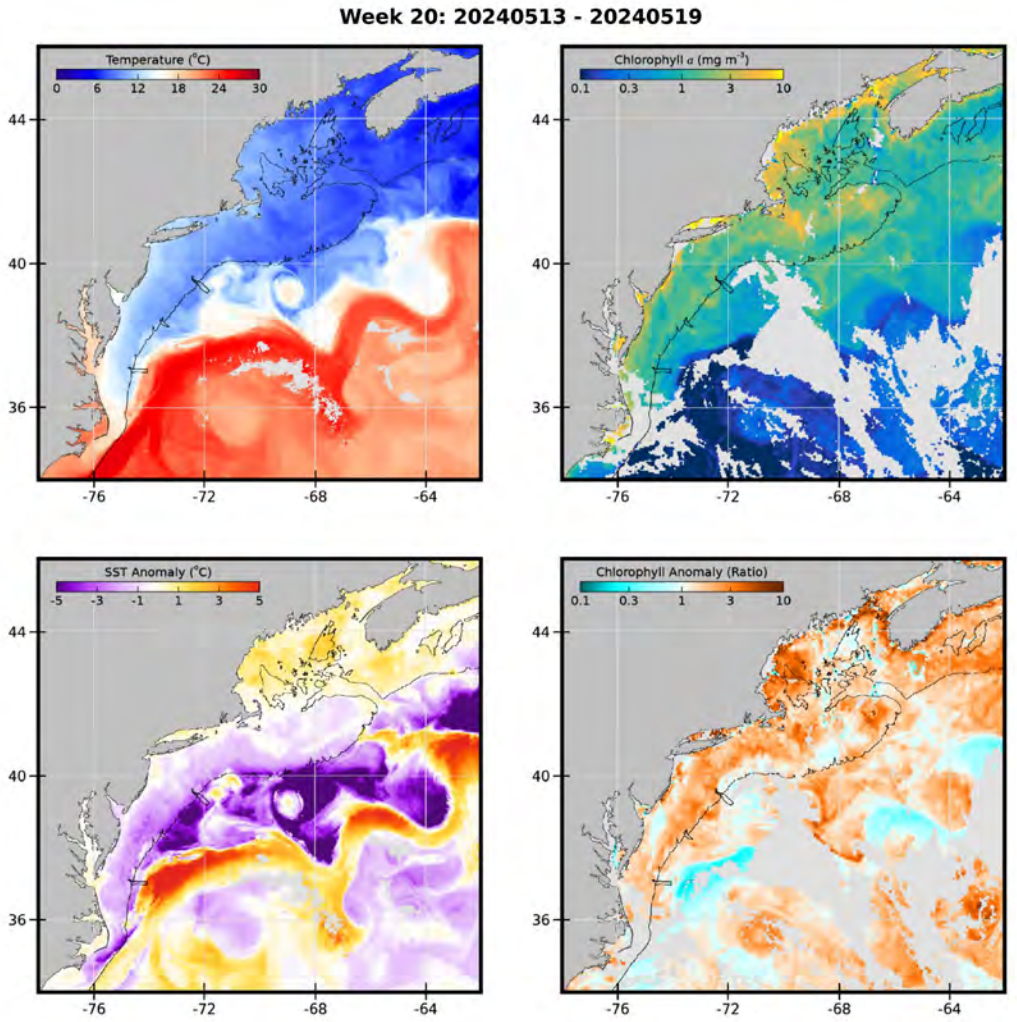

WHOI Glider Transect- March 14-29 2024

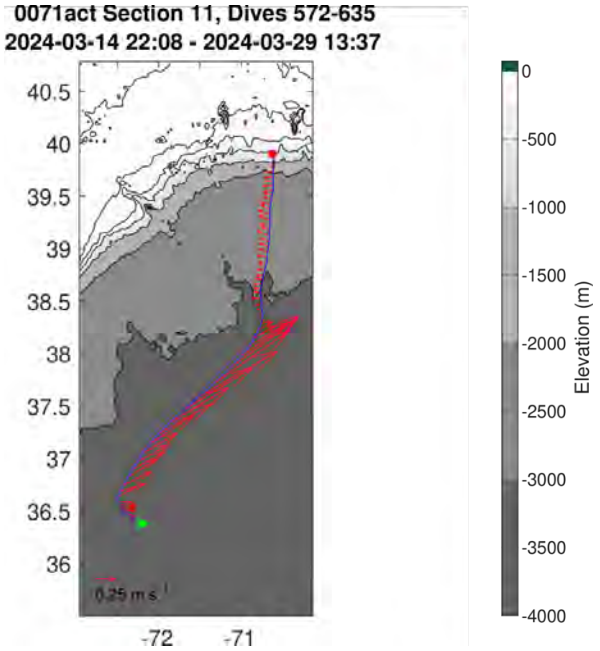

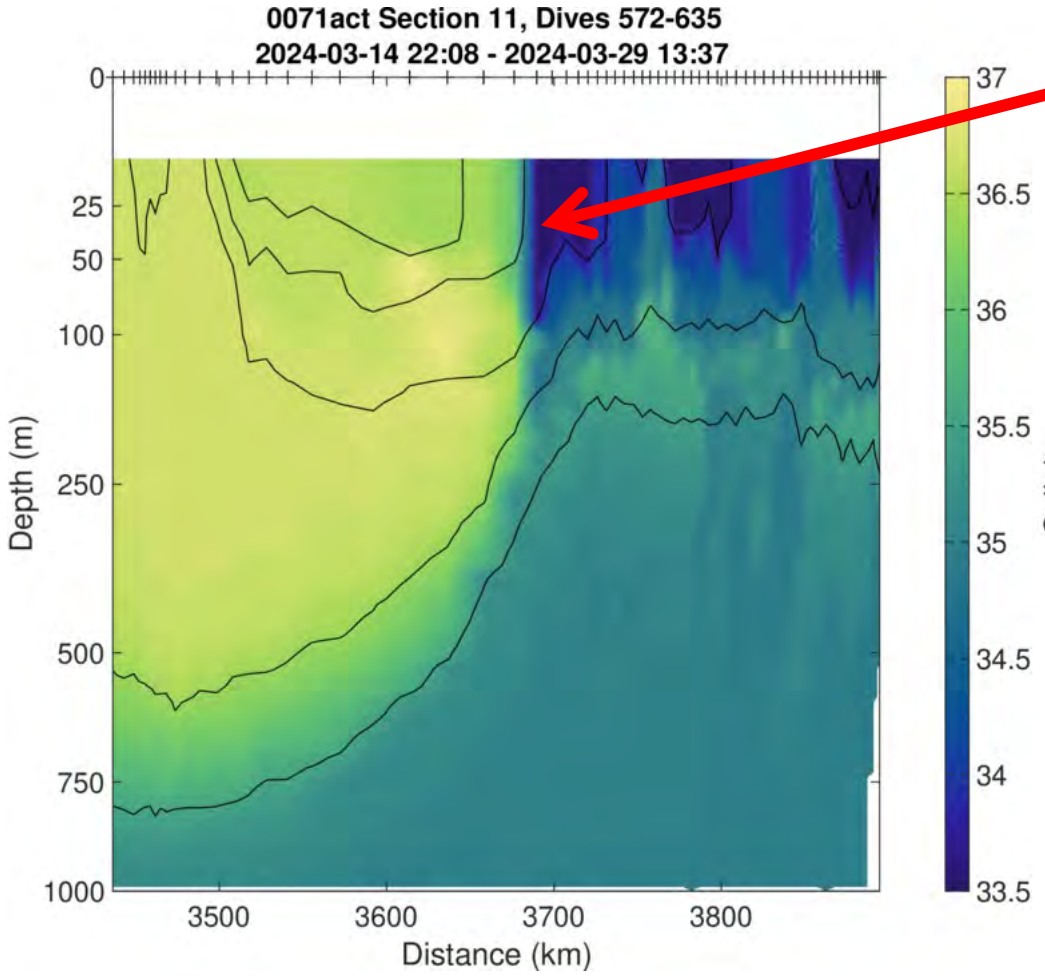

Shelf water reaching North Wall of the Gulf Stream!!!!!

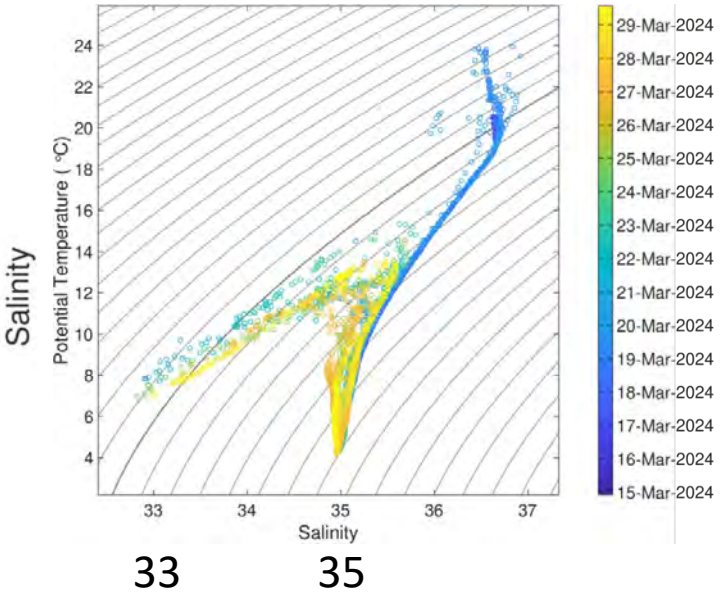

33 35

Courtesy Robert Todd WHOI

Shelf water surface layer extends to North Wall of Gulf Stream

Inter-annual Variability of Salinity from Shelf Research Fleet Zone 2

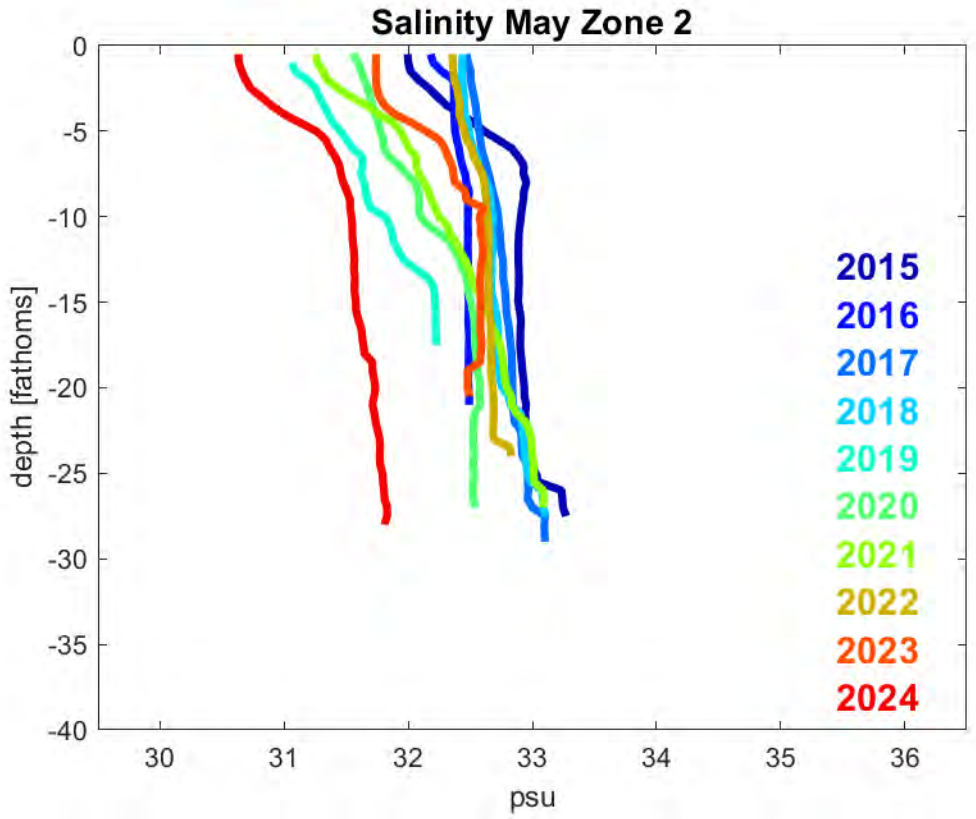

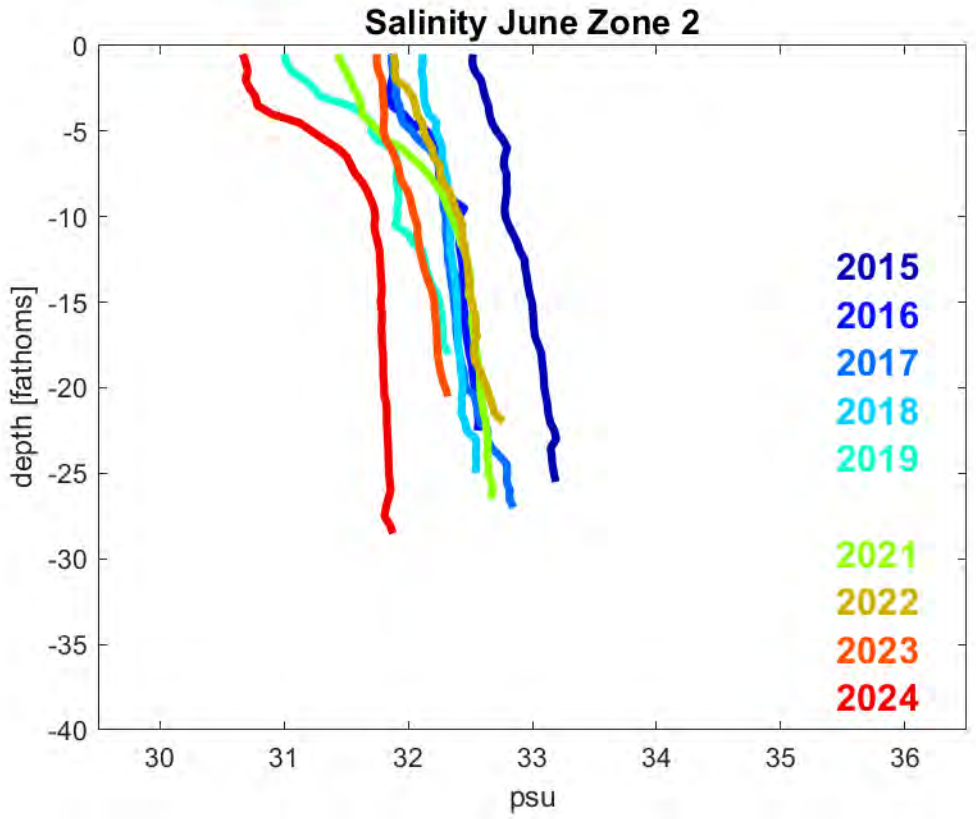

Inter-Annual Variability of Density from Shelf Research Fleet Zone 2

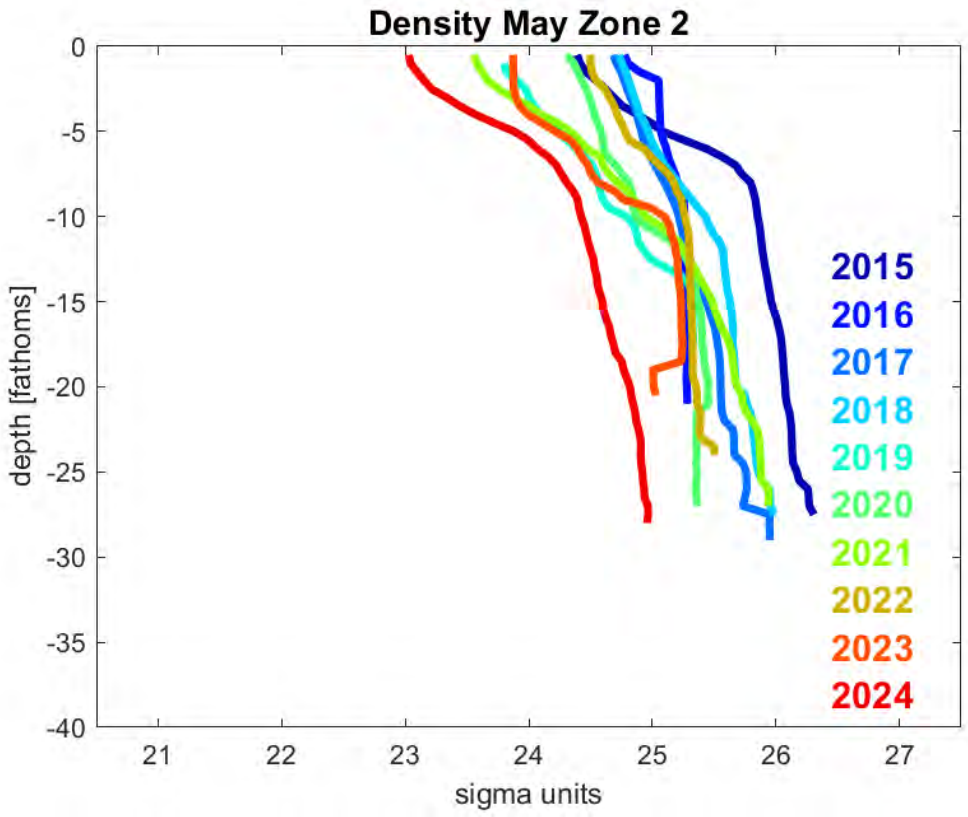

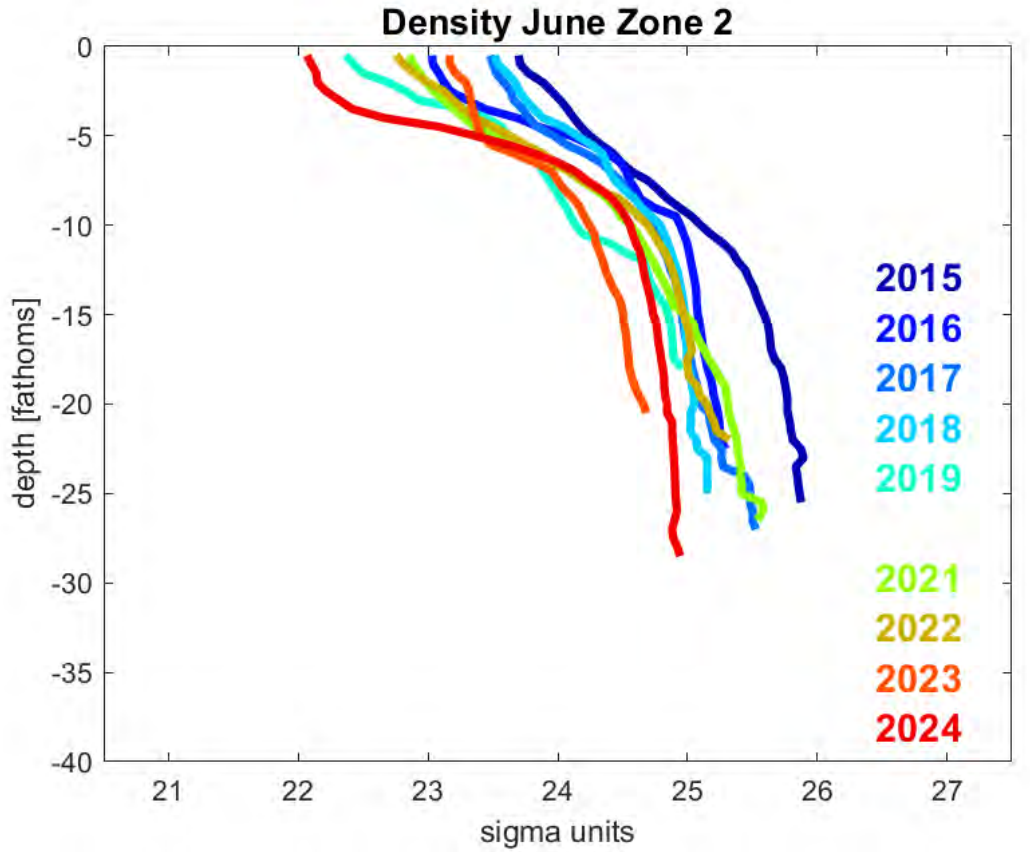

Nantucket Shoals Temperature NDBC 44008

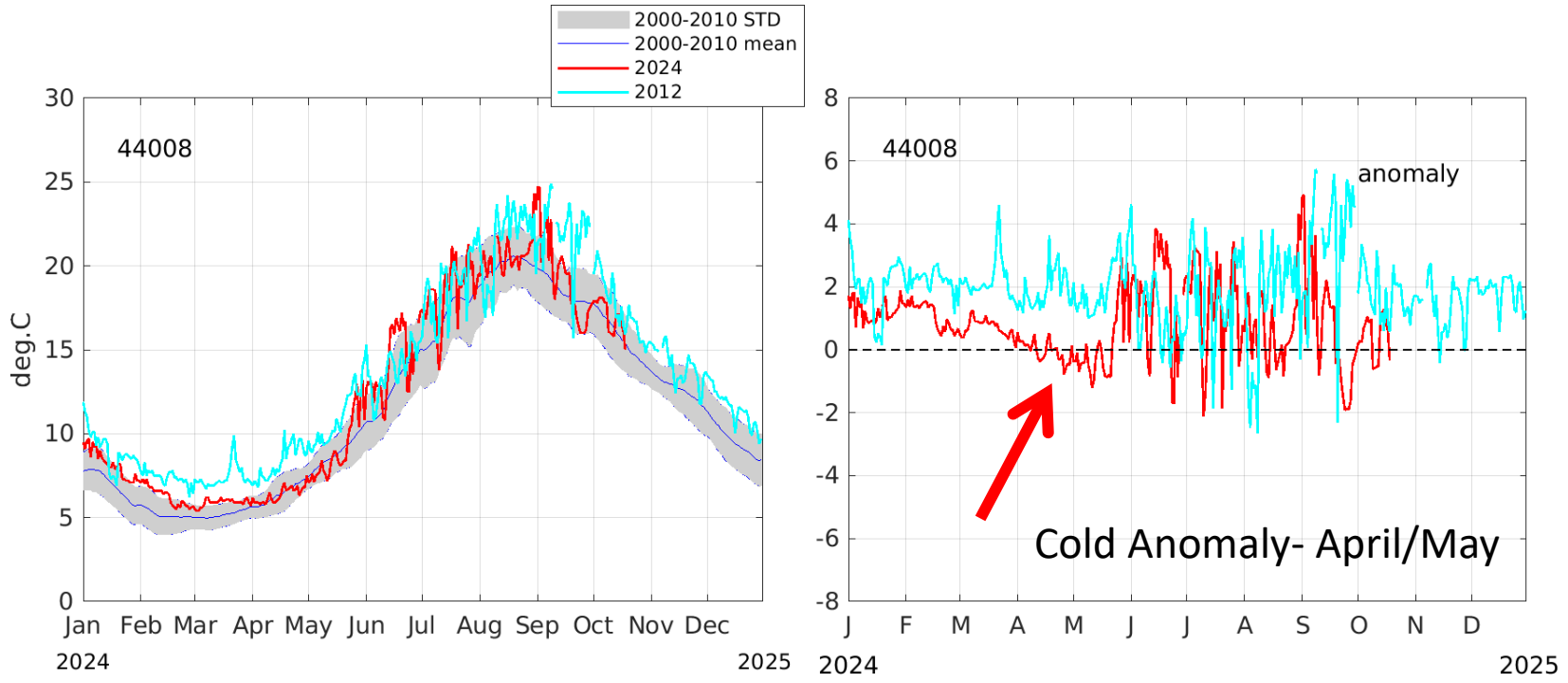

Red Line- 2024. Light blue line- 2012. Blue line- 2000-2010 average

Some Fishing Impacts in 2024

- Various species showed up 4-5 weeks late off New Jersey SEASONAL MOVEMENTS DELAYED
- Illex not present for much of the season
- Loligo appeared mid-August, south of Hudson Canyon
- Unusual patterns of Marine Mammals, Sei Whales off New Jersey for the first time in over 10 years
- Abundant mackerel and herring

Sea Surface Temperature Jan-Feb 2025

January 2, 2025

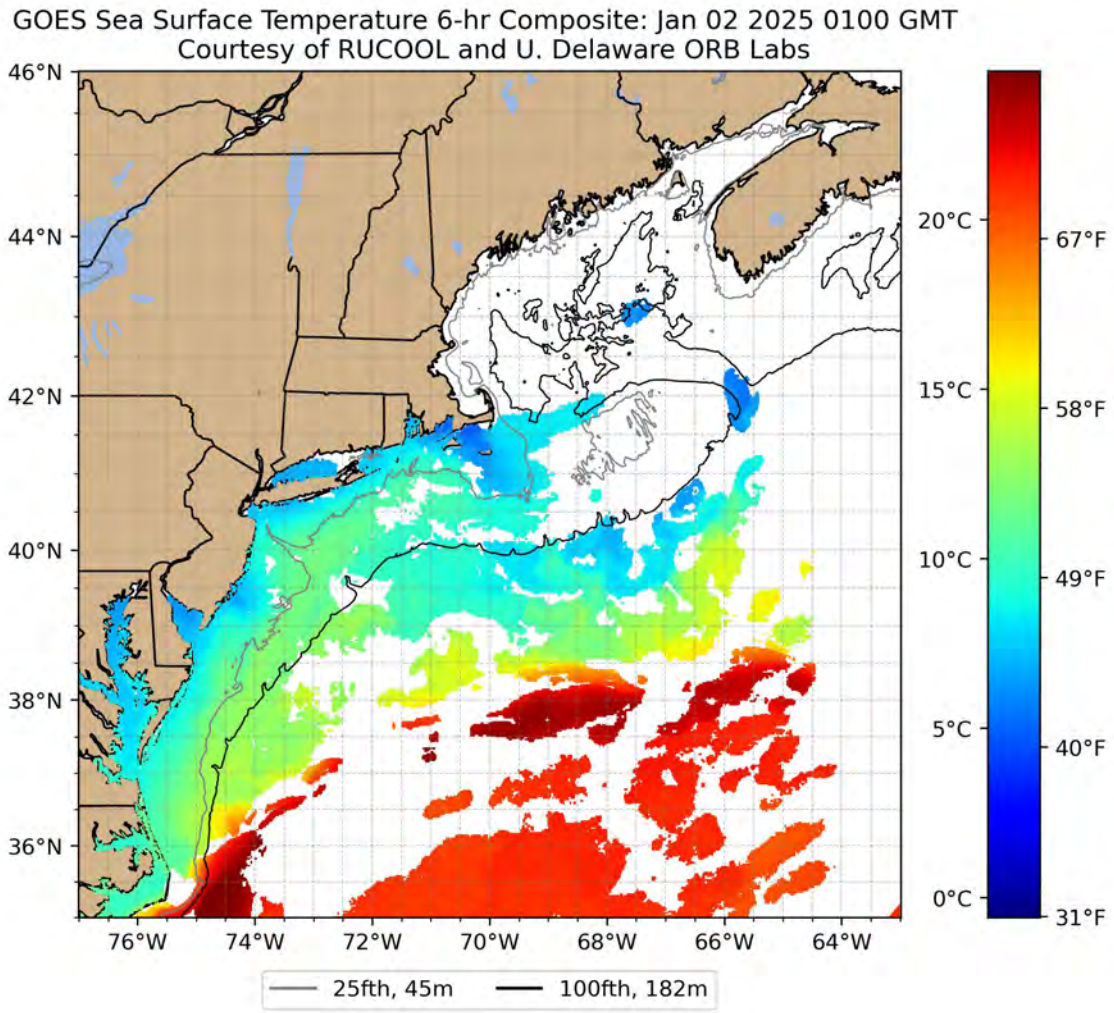

February 26, 2025

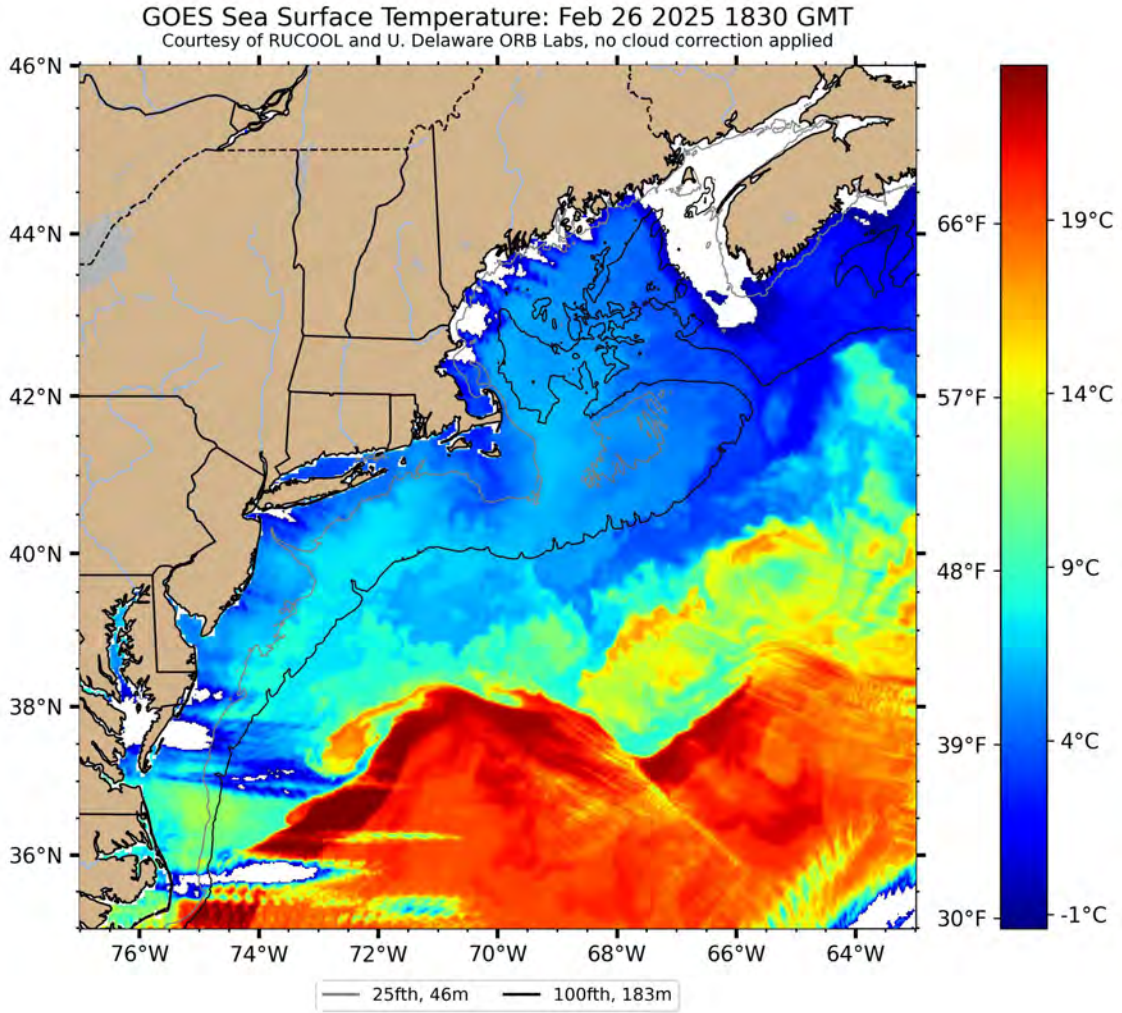

Sea Surface Temperature March-April 2025

March 23, 2025

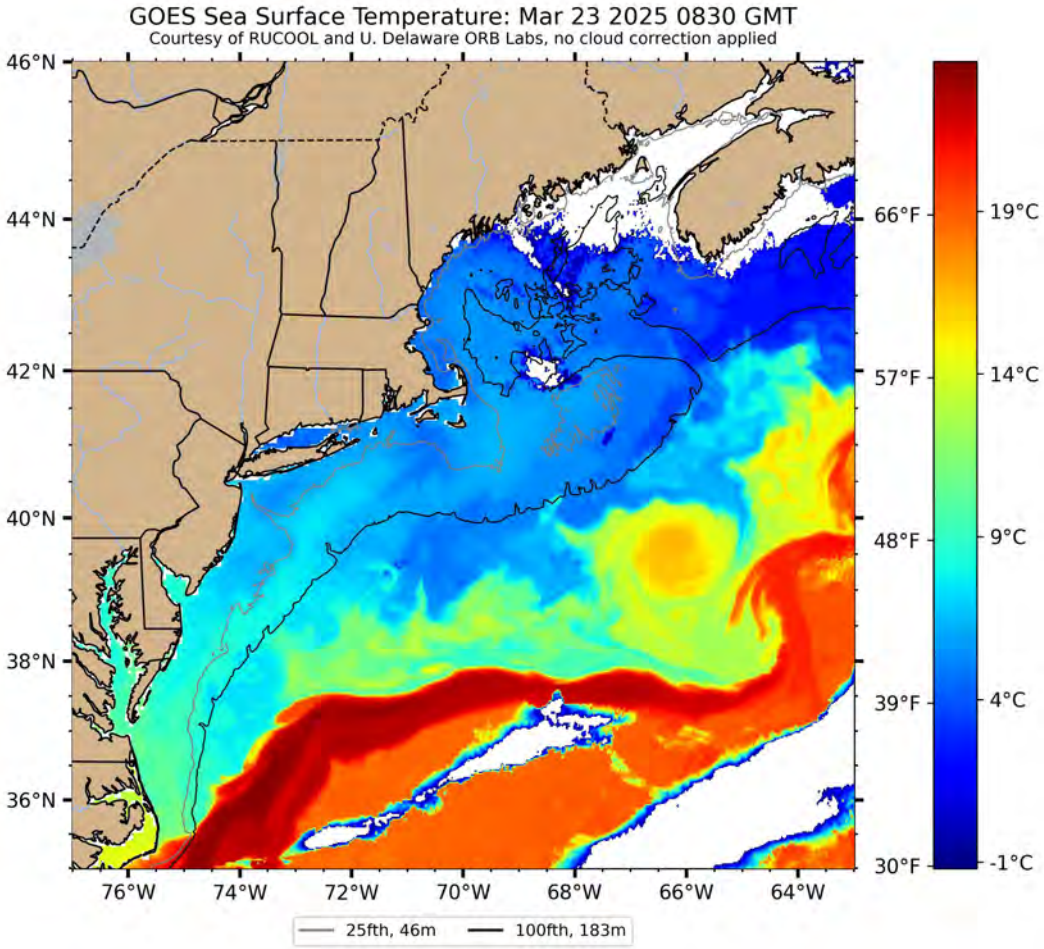

April 29, 2025

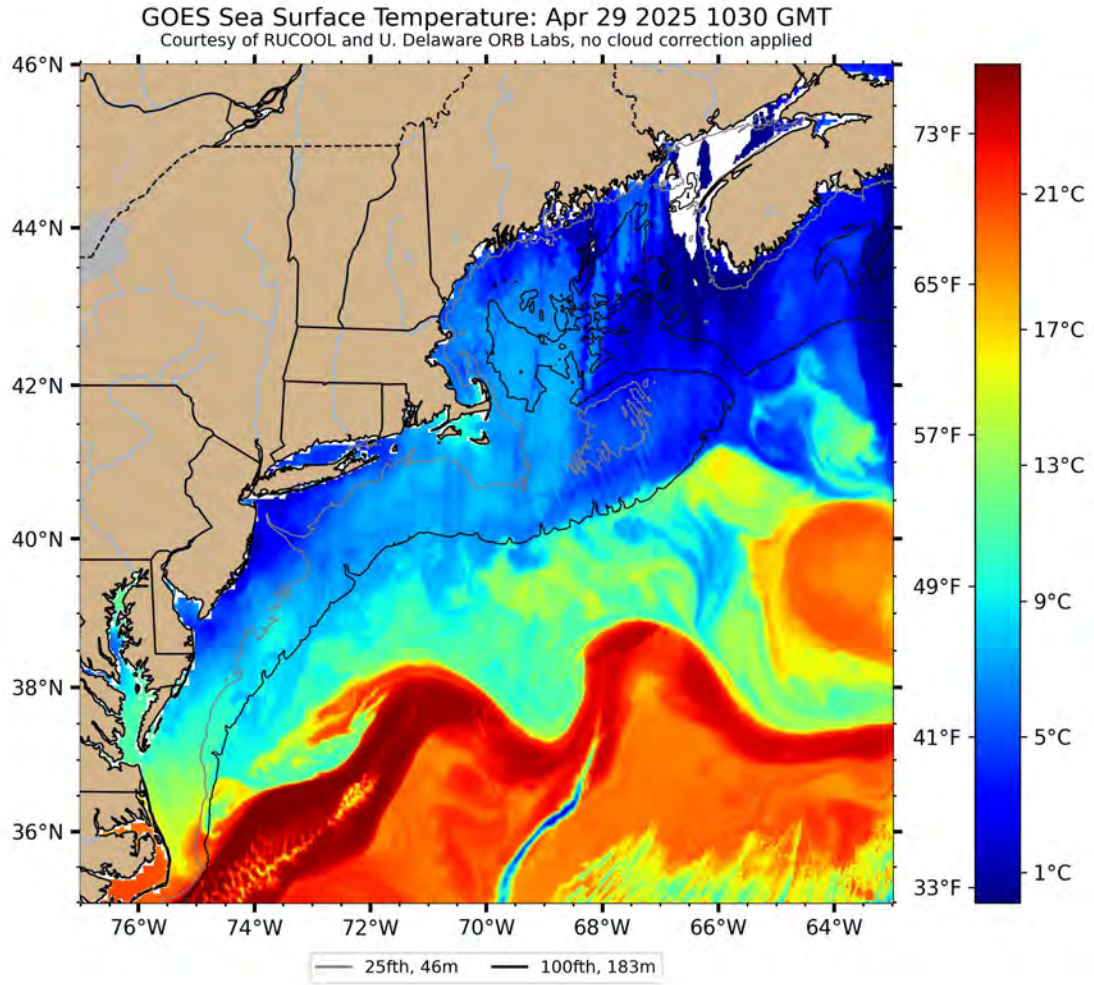

Sea Surface Temperature June-July 2025

June 19, 2025

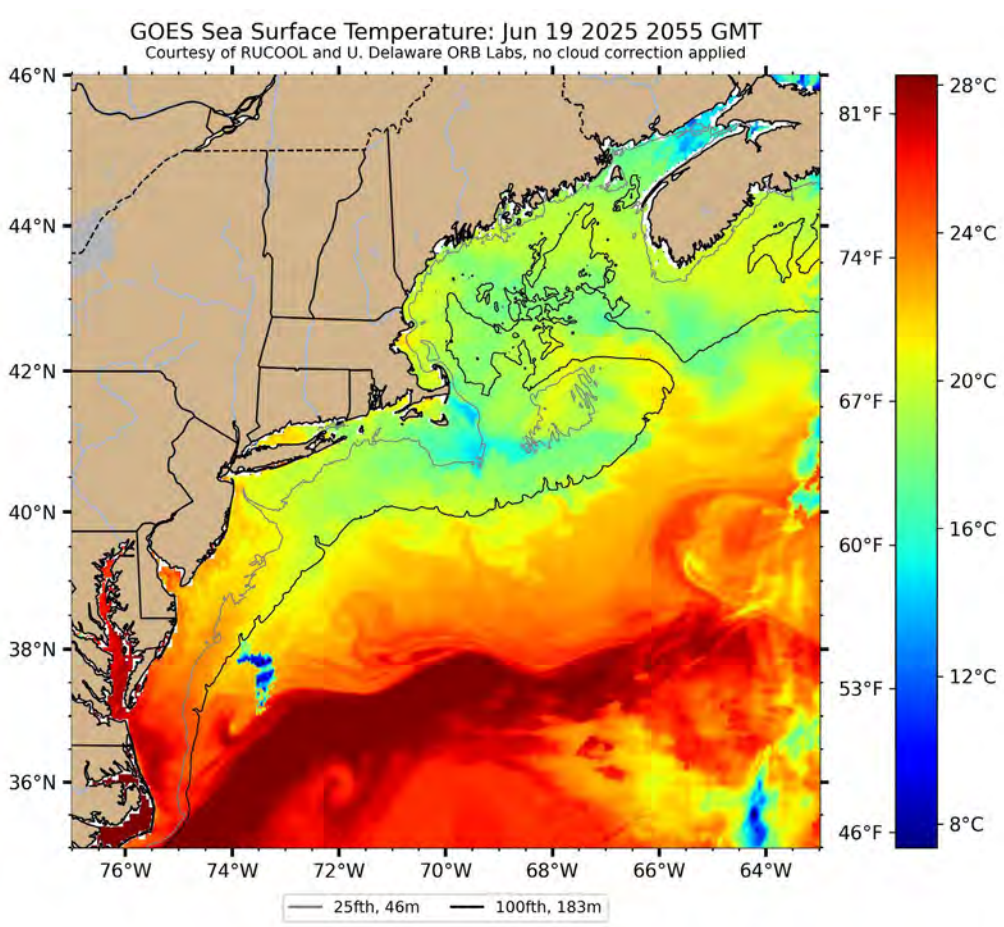

July 5, 2025

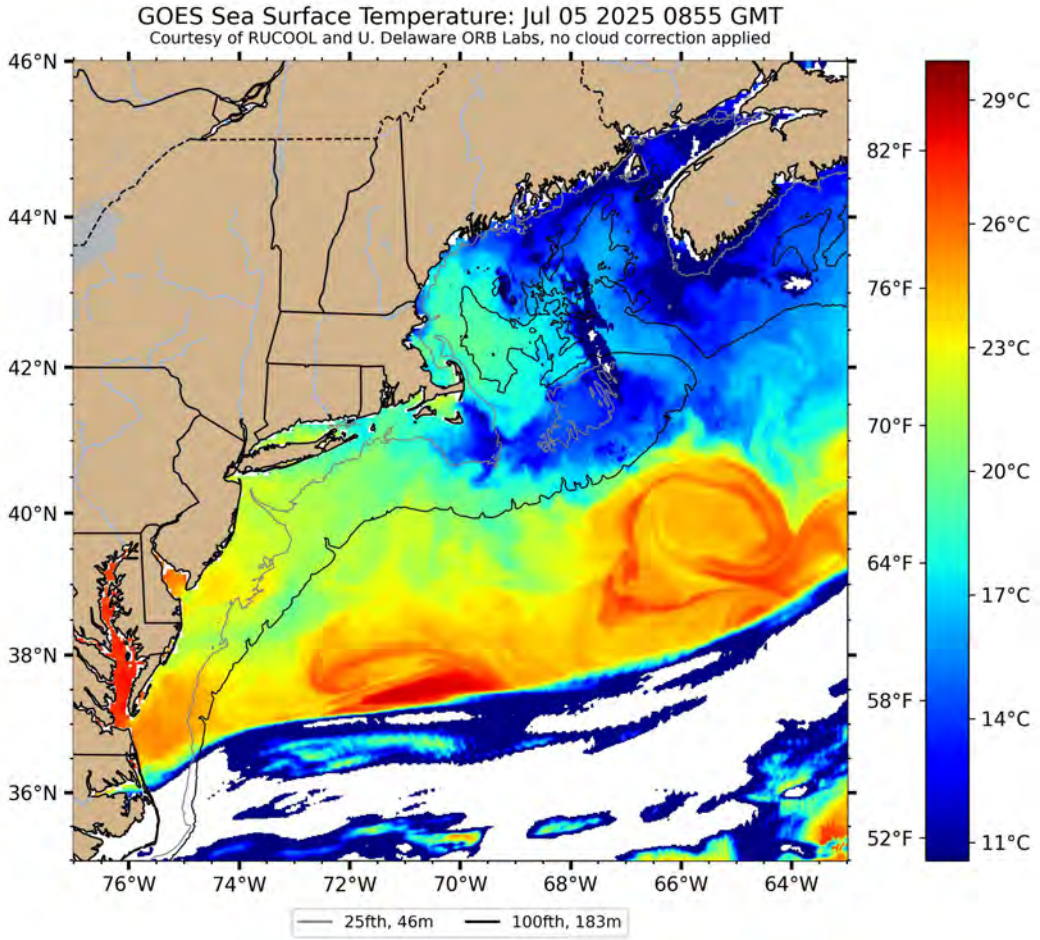

Squid Catch and Quotas

Illex

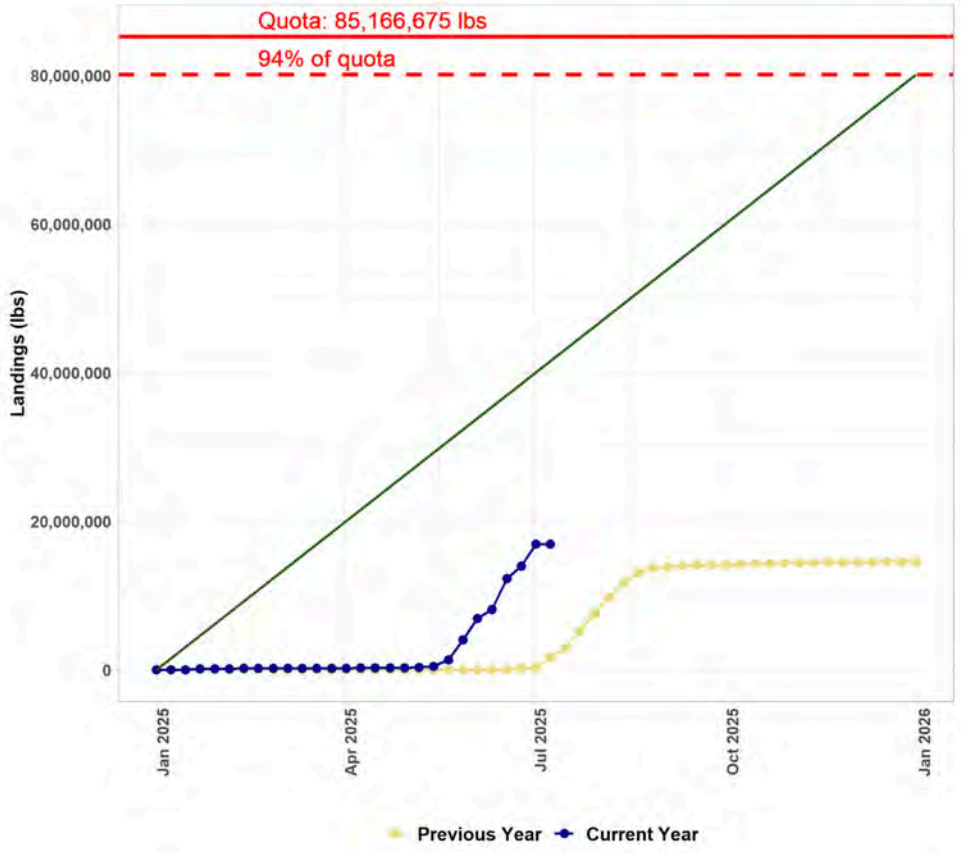

Loligo

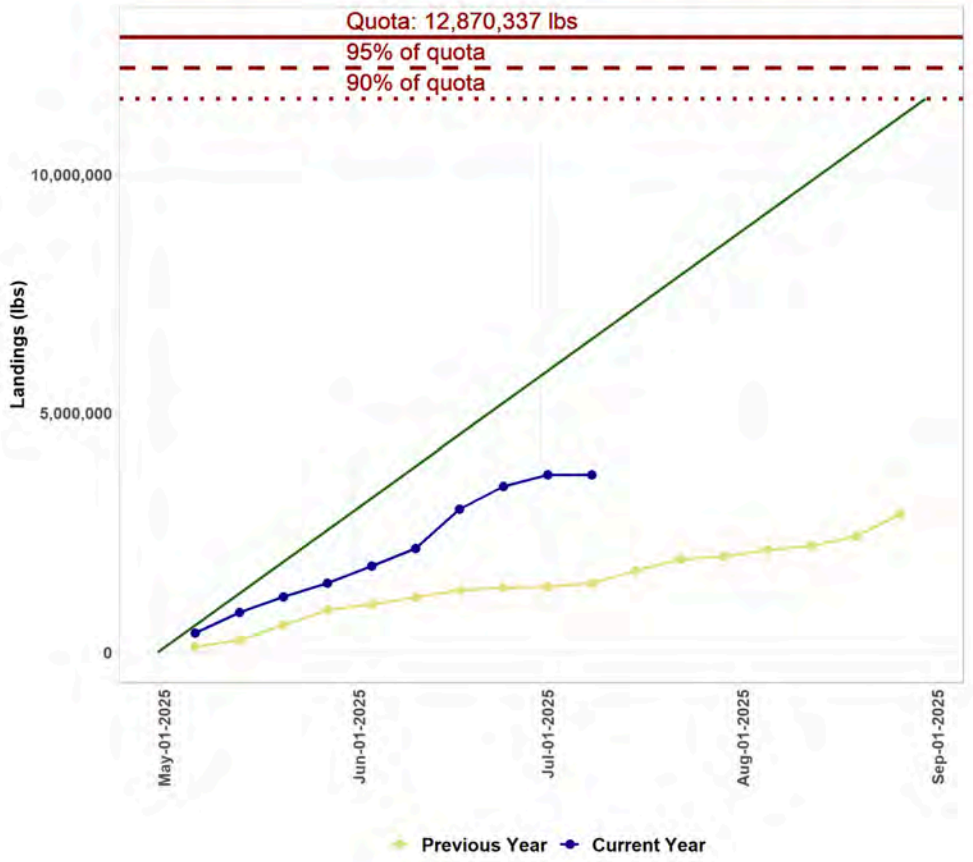

Atlantic Mackerel

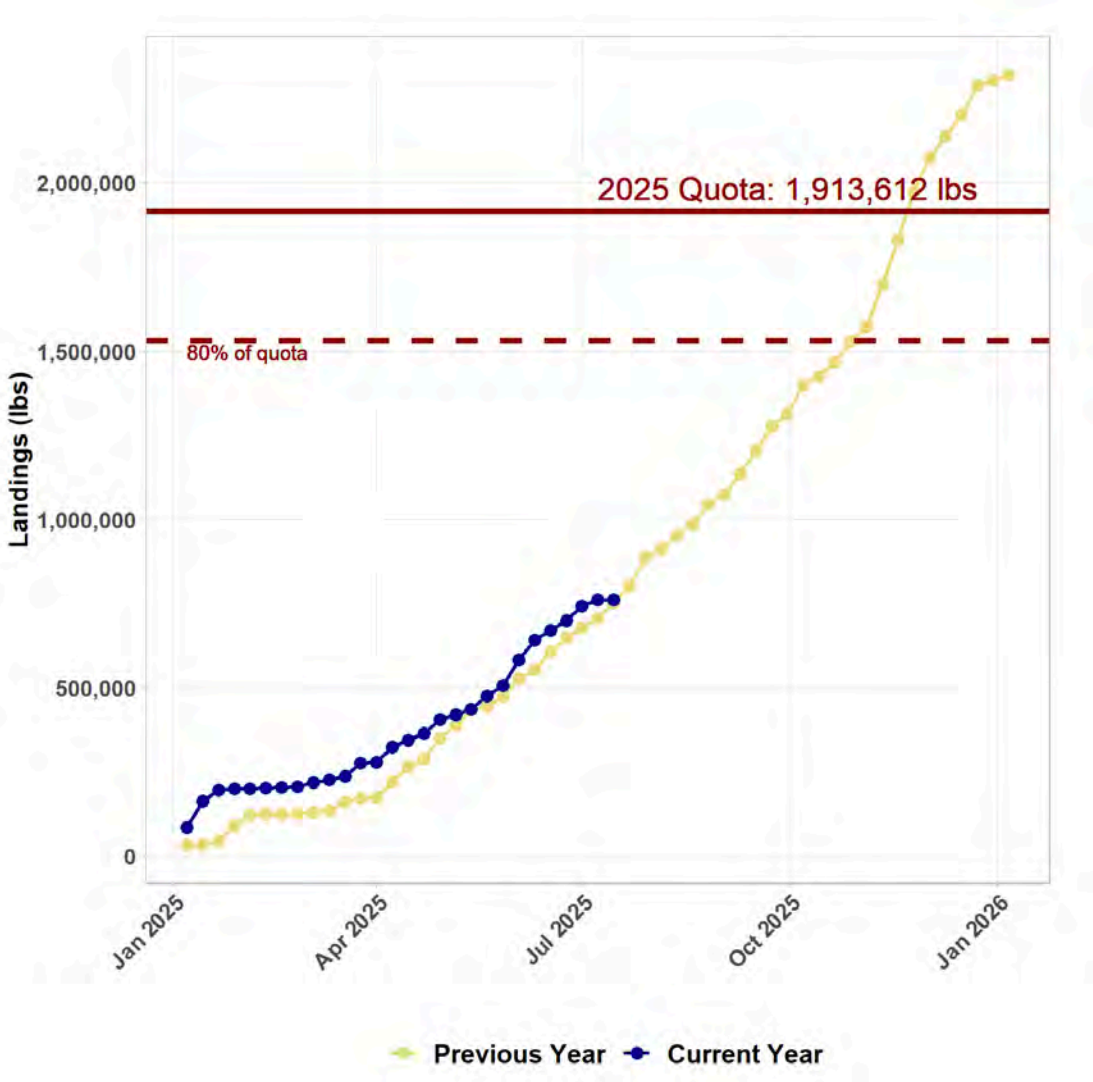

Sea Surface Temperature Anomaly May 15 2024

earth.nullschool.net

Maximum on colorbars are
-10.8 Deg C to 10.8 Deg C

-19.44 Deg F to 19.44 Deg F

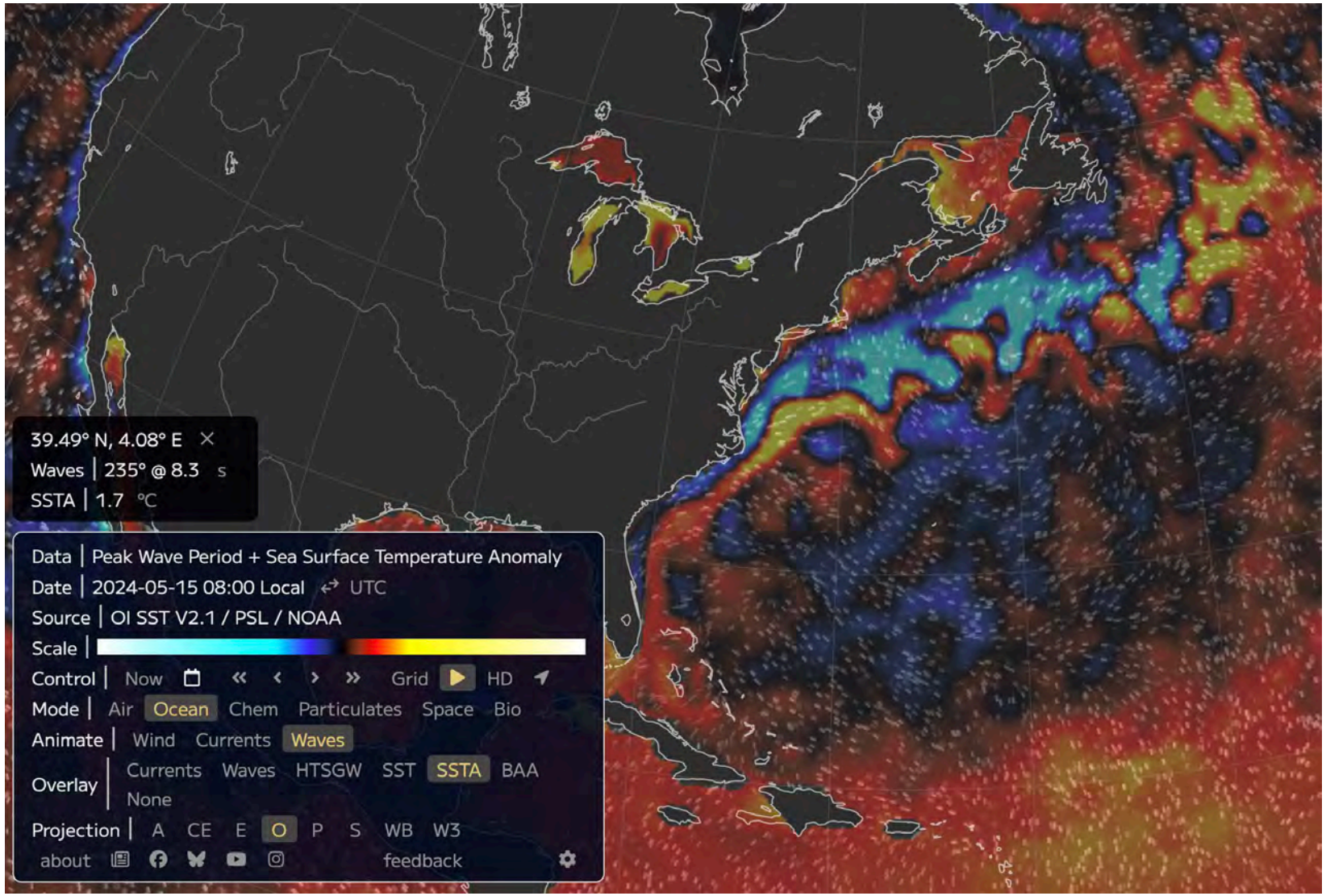

Sea Surface Temperature Anomaly January 15 2025

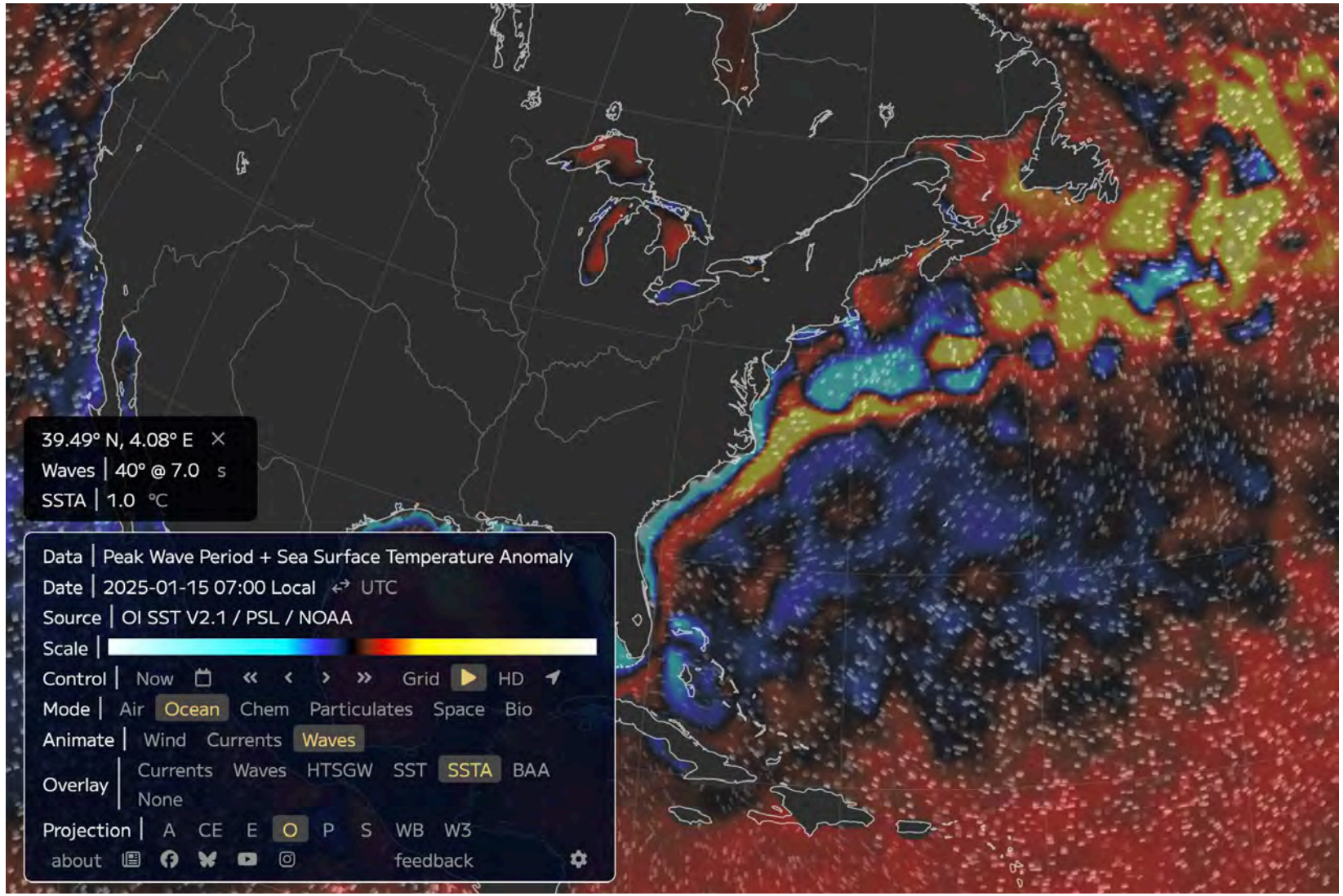

Sea Surface Temperature Anomaly July 13 2025

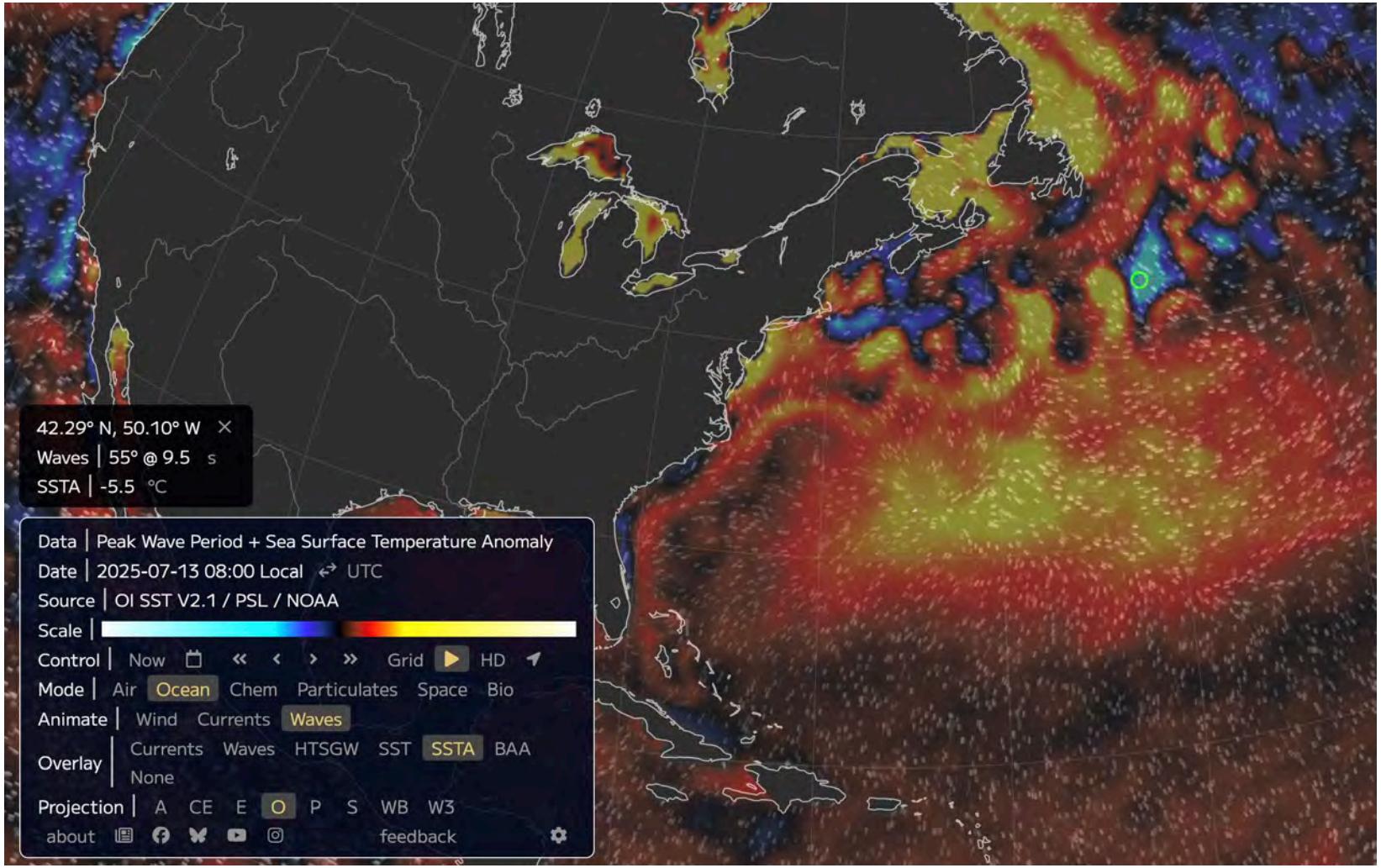

Summary

- Cold start to 2025 but anomalies mostly over the continental slope
- Very warm salty water over the continental shelf north of Cape Hatteras in April
- Gulf Stream initially straight but developed large meanders in May
- Two large Warm Core Rings currently south of Nova Scotia
- Very strong stratification, may lead to problems with low oxygen levels again off New Jersey in late August/early September

Links to Recommended Papers & Reports

- Papers from Glen's former student, Lukas Taenzer
  - Seasonal Salinification of the US Northeast Continental Shelf Cold Pool Driven by Imbalance Between Cross-Shelf Fluxes and Vertical Mixing
    - https://doi.org/10.1029/2024JC021270
  - Categorization of High-Wind Events and Their Contribution to the Seasonal Breakdown of Stratification on the Southern New England Shelf
    - https://doi.org/10.1029/2022JC019625
- Meghan Lapp – History of Soviet fishing along Atlantic coast
  - "From Cape Hatteras to Cabot Strait: the history of the Soviet fishery on the Atlantic continental shelf of the United States and Canada"
    - https://repository.library.noaa.gov/view/noaa/23332

Synthesis of Environmental Conditions and Potential Effects on Key Fishery Resources in the Chesapeake Bay

Spring 2025 Seasonal Summary

Spring 2025 Headlines

- **Salinity remained above average through most of spring as a result of drier conditions in winter and early spring. Higher salinity supports oyster growth and reproduction.**
- **Hypoxia remained low compared with the early onset of hypoxia in spring 2024. This is good for crabs, oysters, and striped bass.**

Summary of Potential Impacts of Environmental Conditions on Species from Most Recent Four Seasons

	Summer 2024	Fall 2024	Winter 2024–25	Spring 2025
Striped Bass	WT, DO, Sal, Flow	WT, DO, Sal, Flow	WT, DO, Sal, Flow	**WT, DO, Sal, Flow**
Blue Crabs	WT, DO, Sal, Flow	WT, DO, Sal, Flow	WT, DO, Sal, Flow	**WT, DO, Sal, Flow**
Oysters	WT, DO, Sal, Flow	WT, DO, Sal, Flow	WT, DO, Sal, Flow	**WT, DO, Sal, Flow**
Bay Anchovy	WT, DO, Sal, Flow	WT, DO, Sal, Flow	WT, DO, Sal, Flow	**WT, DO, Sal, Flow**
Summer Flounder	WT, DO, Sal, Flow	WT, DO, Sal, Flow	WT, DO, Sal, Flow	**WT, DO, Sal, Flow**

WT = Water Temperature
Sal = Salinity
Flow = Streamflow
DO = Dissolved Oxygen

Green = Potentially positive impact
Red = Potentially negative impact
Black = Neutral or unknown impact

Purpose

The National Oceanic and Atmospheric Administration's (NOAA) Chesapeake Bay Office (NCBO) develops seasonal summaries of water-quality parameters in the Chesapeake Bay to provide fisheries managers and the public information about recent environmental conditions, how they compare with long-term averages, and how these conditions might affect key fishery resources such as striped bass (*Morone saxatilis*), blue crab (*Callinectes sapidus*), eastern oysters (*Crassostrea virginica*), and summer flounder (*Paralichthys dentatus*). The intent is to provide information linking changes in environmental conditions to potential effects on living resources that can inform ecosystem-based management at state and regional levels. The seasons are defined as winter (December–February), spring (March–May), summer (June–August), and fall (September–November).

The primary data sources for these seasonal summaries are the NOAA Chesapeake Bay Interpretive Buoy System (CBIBS) for real-time, surface water temperature and salinity information at four locations throughout the Chesapeake Bay (Figure 1); the NOAA CoastWatch Program for Bay-wide, satellite-based sea surface temperature (SST) anomalies; the NOAA National Weather Service PREcipitation Summary and Temperature Observations (PRESTO) reports for regional precipitation and air temperature information; the National Centers for Environmental Information for precipitation data; and the U.S. Geological Survey (USGS) National Water Information System for local streamflow information at various locations throughout the Bay. In summer, the Chesapeake Bay Environmental Forecast System (CBEFS)

provides estimates of the volume and duration of seasonal hypoxia. NCBO uses these seasonal summaries to develop an annual synthesis for inclusion in the Mid-Atlantic State of the Ecosystem Report, which is developed by the Northeast Fisheries Science Center and presented to the Mid-Atlantic Fishery Management Council each year.

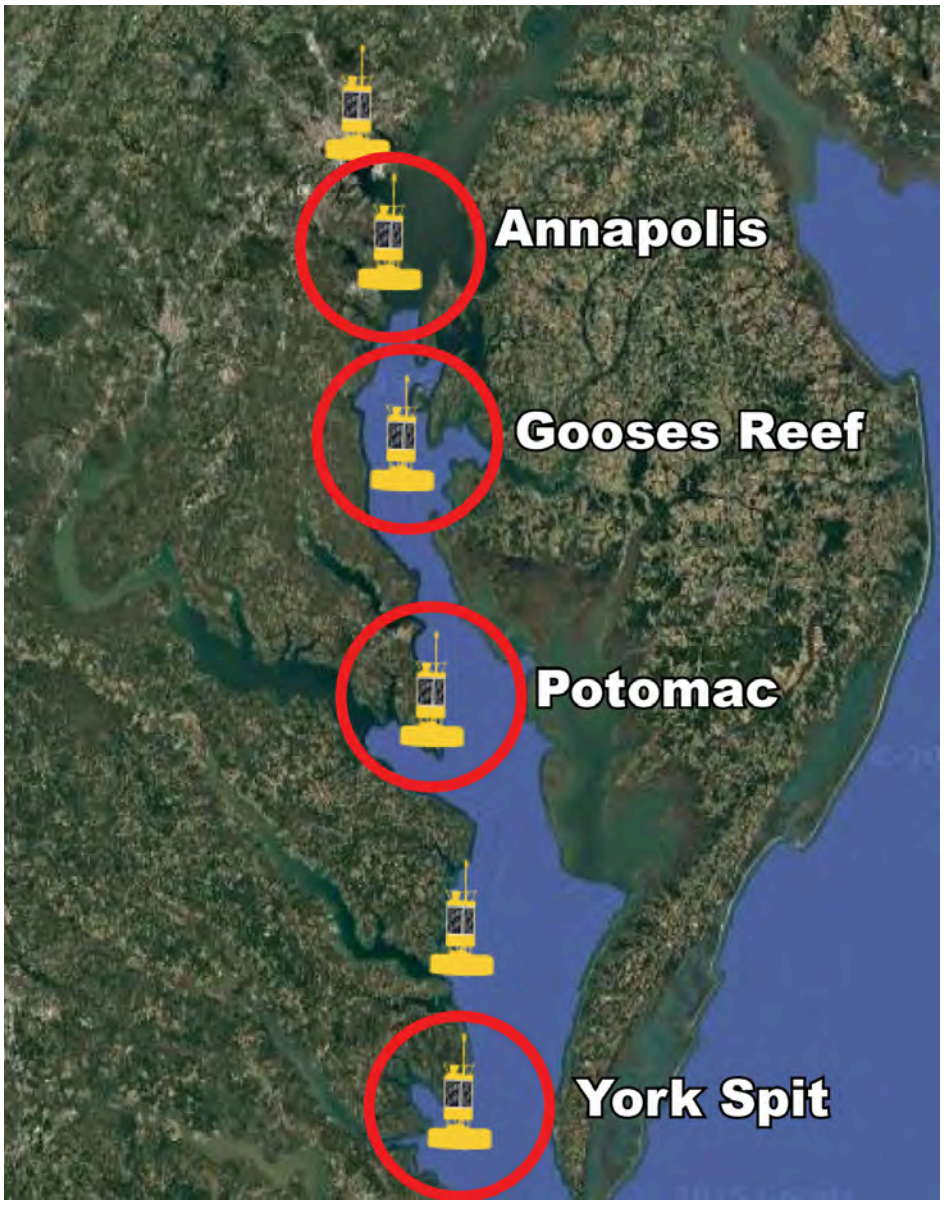

Figure 1. Map of Chesapeake Bay Interpretive Buoy System (CBIBS) observation platforms. The buoys used in these summaries are Annapolis, Gooses Reef, Potomac, and York Spit.

Water Temperature

Coastal sea-surface temperatures (SST), as observed by NOAA satellites, deviated both above and below average. Anomalies in the Bay were greatest in the southern and southeastern regions (where water temperatures were slightly warmer) and in the northern Bay (where temperatures were slightly cooler) (Figure 2). However, the SST anomalies were within about 1°C of average in most places. This contrasts with spring 2024, where temperatures Bay-wide were higher than average.

Observations from NOAA Chesapeake Bay Interpretive Buoy System (CBIBS) buoys show a similar and expected pattern of increasing water temperatures from March through May. At the Annapolis, Gooses Reef, Potomac, and York Spit CBIBS stations, overall, water temperatures warmed through spring (Figures 3, 4, 5, and 6). Water temperatures at all stations were below average in March, several degrees above average from the beginning of May to mid May, and then again below average at the end of May.

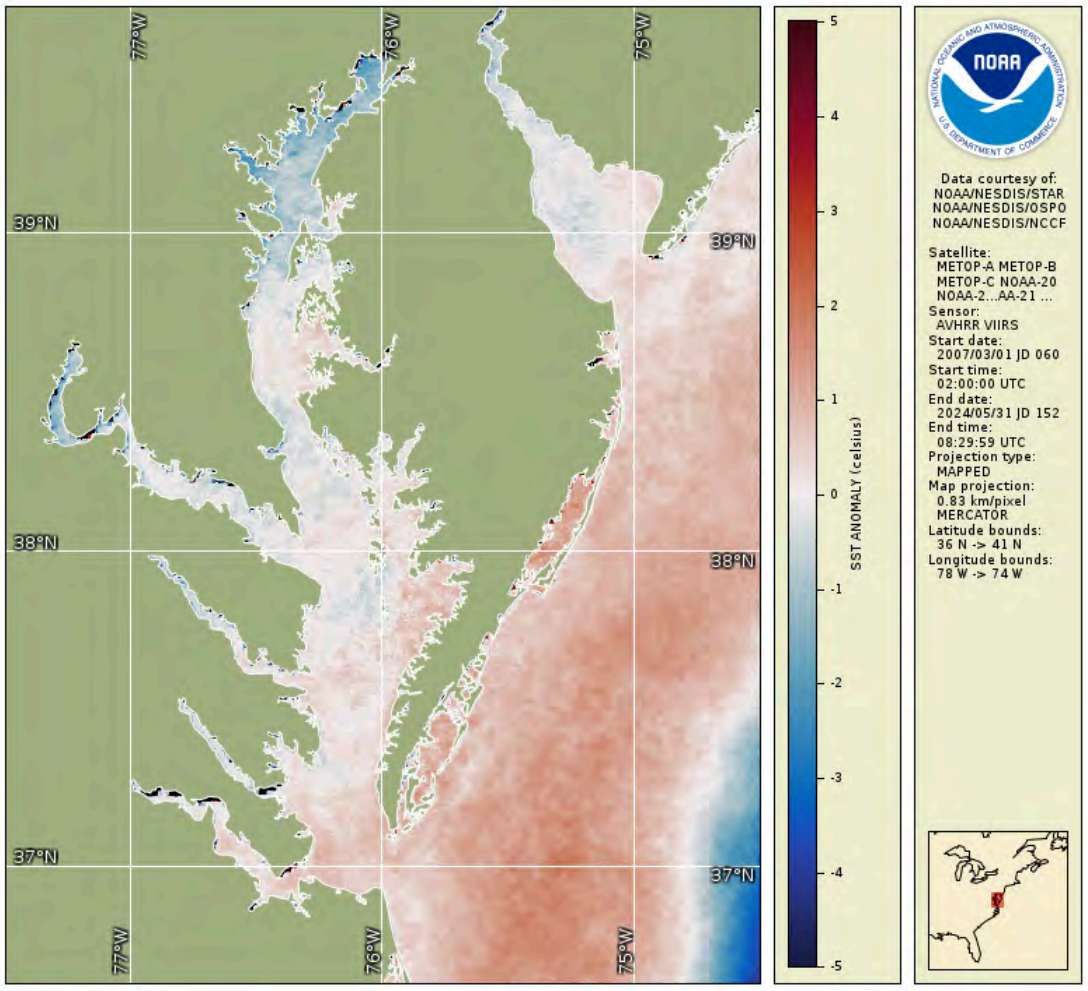

Figure 2. Sea surface temperature (SST) anomalies observed by NOAA satellites March–May 2025 relative to the average of this seasonal period 2007–2024.

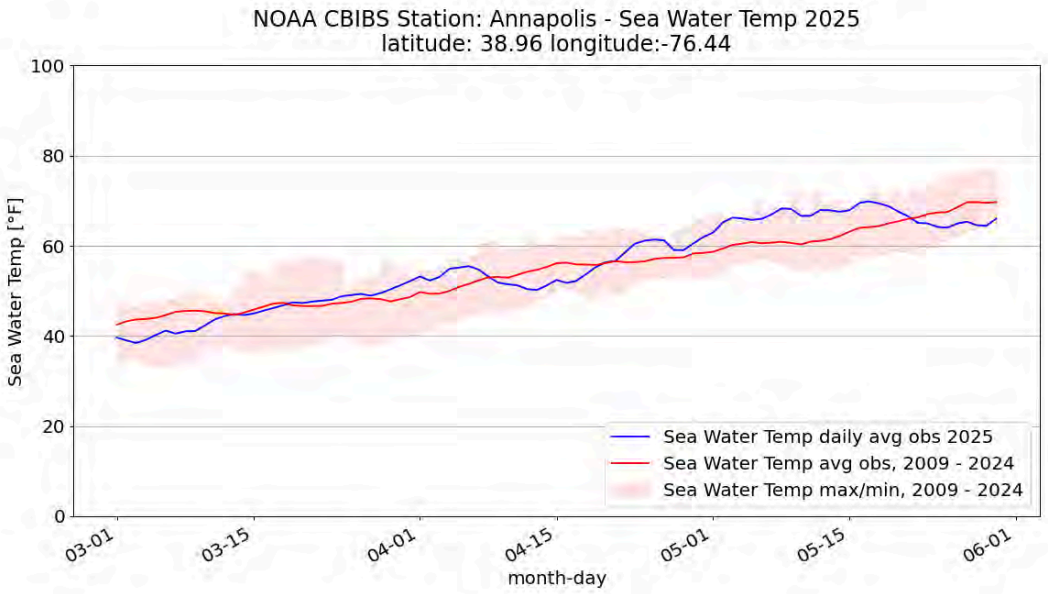

Figure 3. Surface water temperatures at the Annapolis CBIBS buoy March–May 2025 relative to the long-term average (2009–2024). The shaded area represents the full range of observations (minimum to maximum) over the time period.

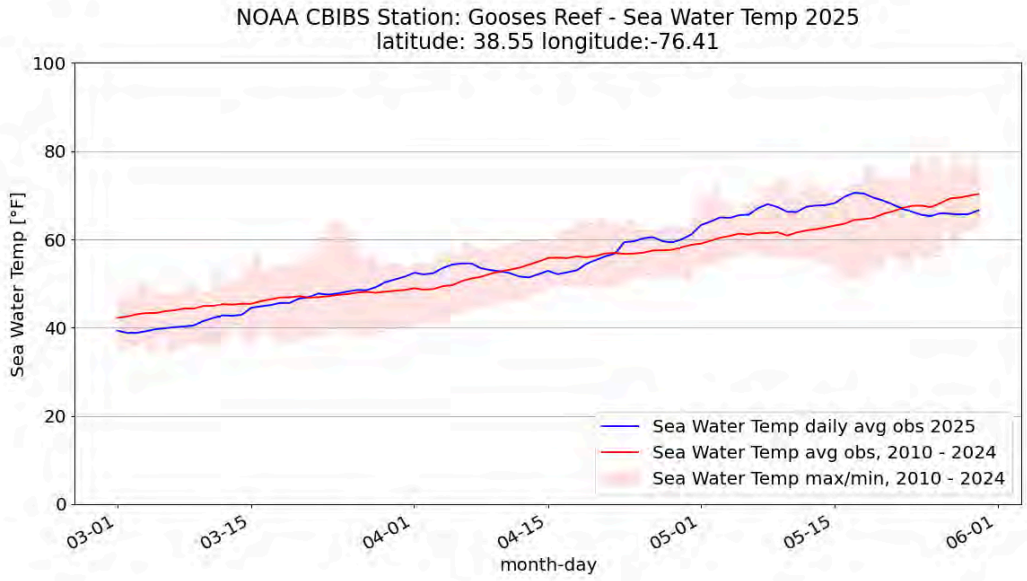

Figure 4. Surface water temperatures at the Gooses Reef CBIBS buoy March–May 2025 relative to the long-term average (2010–2024). The shaded area represents the full range of observations (minimum to maximum) over the time period.

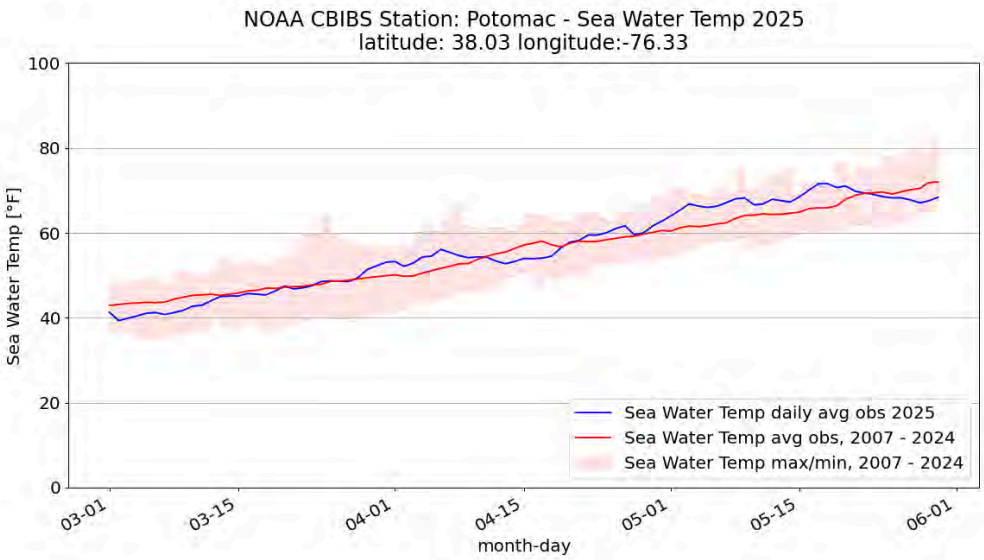

Figure 5. Surface water temperatures at the Potomac CBIBS buoy March–May 2025 relative to the long-term average (2007–2024). The shaded area represents the full range of observations (minimum to maximum) over the time period.

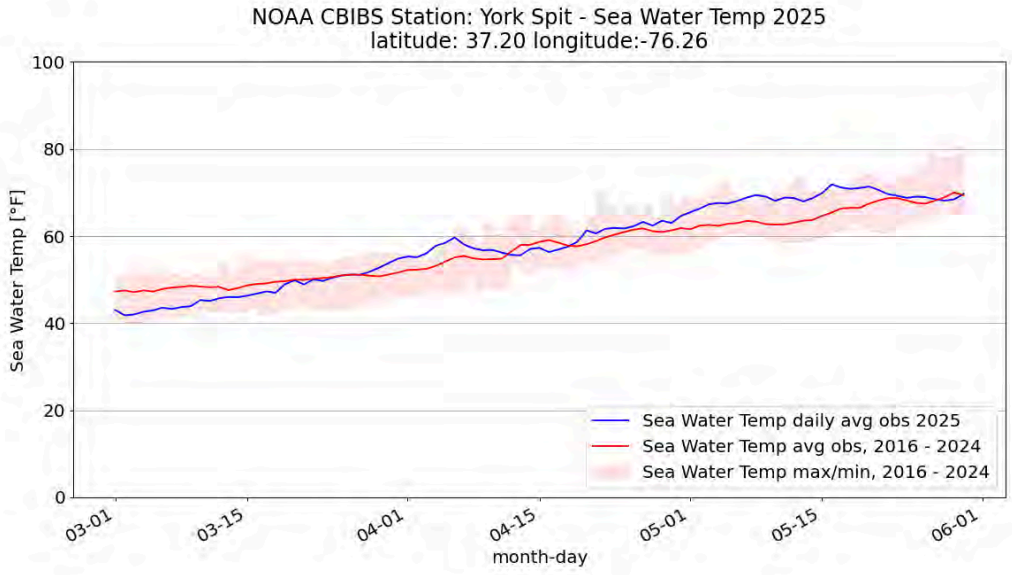

Figure 6. Surface water temperatures at the York Spit CBIBS buoy March–May 2025 relative to the long-term average (2007–2024). The shaded area represents the full range of observations (minimum to maximum) over the time period.

Salinity

Salinity was above average at the Annapolis, Gooses Reef, Potomac, and York Spit CBIBS buoys from most of March into May (Figures 7, 8, 9, and 10). This continues the trend from winter 2025, when salinity was above average at all buoy stations. It is in contrast to spring 2024, when salinity was below average. The Annapolis CBIBS buoy showed a large drop in salinity in early March; salinity then rose and fell at that location through May (Figure 7) while staying above the long-term average. Salinity at Annapolis and Gooses Reef was about average from mid to late May (Figures 7 and 8).

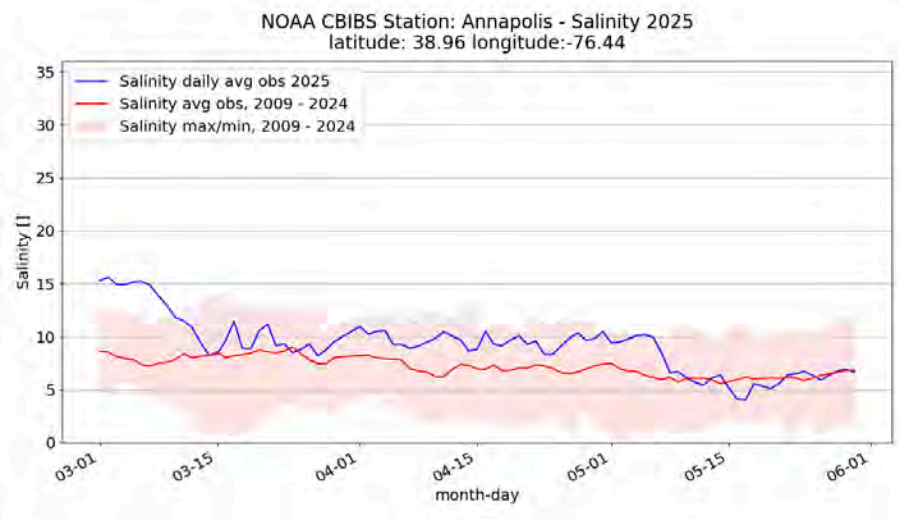

Figure 7. Salinity observations at the Annapolis CBIBS buoy March–May 2025 (blue line) relative to the average at each buoy over this seasonal period 2009–2024 (red line). The shaded area represents the full range of observations (minimum to maximum) over the time period.

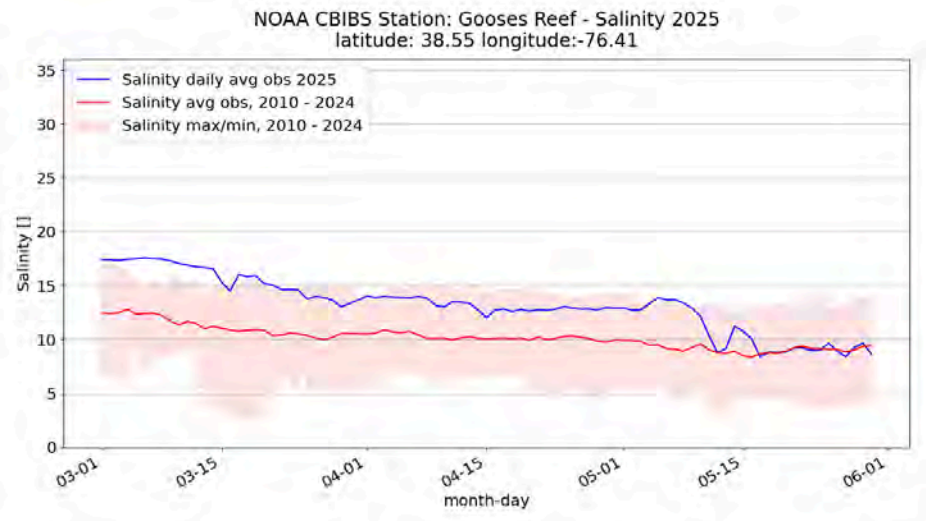

Figure 8. Salinity observations at the Gooses Reef CBIBS buoy March–May 2025 (blue line) relative to the average at each buoy over this seasonal period 2010–2024 (red line). The shaded area represents the full range of observations (minimum to maximum) over the time period.

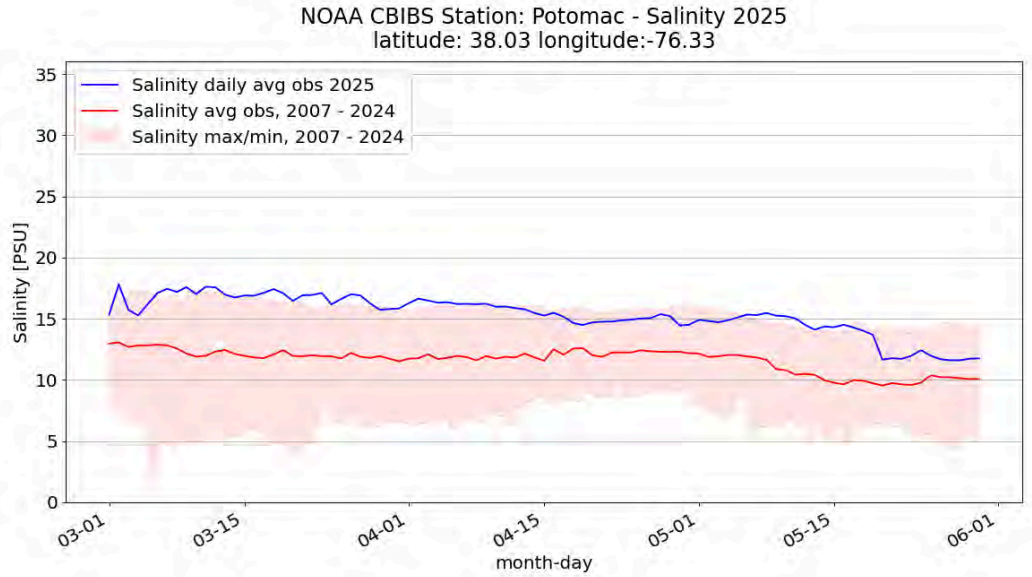

Figure 9. Salinity observations at the Potomac CBIBS buoy March–May 2025 (blue line) relative to the average at each buoy over this seasonal period 2007–2024 (red line). The shaded area represents the full range of observations (minimum to maximum) over the time period.

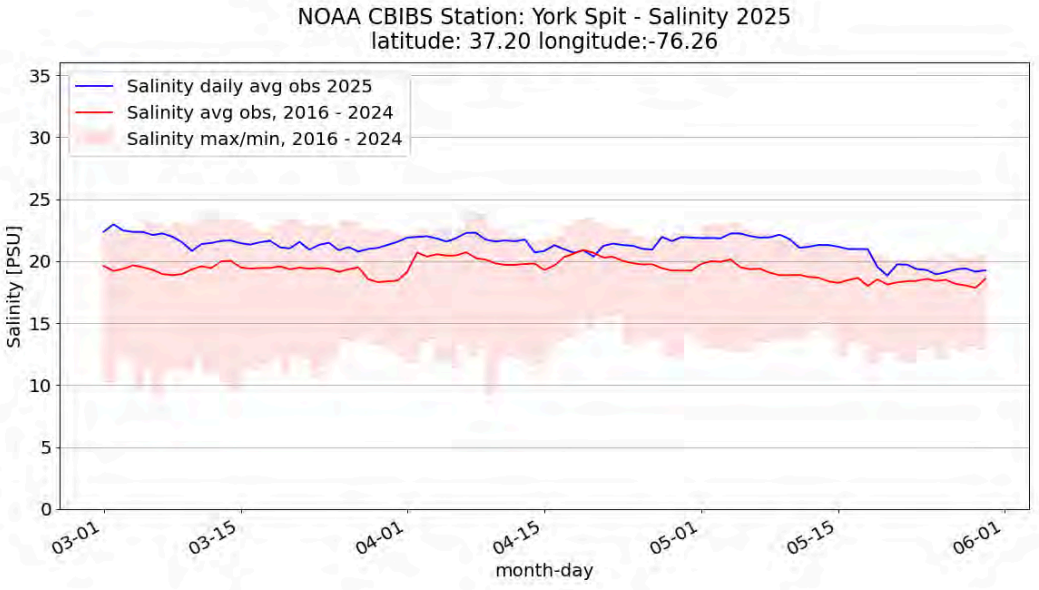

Figure 10. Salinity observations at the York Spit CBIBS buoy March–May 2025 (blue line) relative to the average at each buoy over this seasonal period 2007–2024 (red line). The shaded area represents the full range of observations (minimum to maximum) over the time period.

Precipitation and Freshwater Flow

According to precipitation data from NOAA's National Centers for Environmental Information, rainfall amounts for tidewater Virginia and southern Maryland were the third and fourth highest, respectively, since 2007 (Figures 11 and 12). Higher precipitation results in higher freshwater flow to the Bay. Pulses of flow above historic flow were observed at Choptank, Pamunkey, and Zekiah Swamp (Figure 13). Higher precipitation resulted in declines in salinity toward the end of spring, as observed by the Annapolis and Gooses Reef CBIBS buoys (Figures 7 and 8). While precipitation was relatively high for spring compared to the 2007–2025 mean, it is important to note the region has experienced drier conditions since fall 2024. Some areas continued to be in moderate drought conditions at the end of spring.

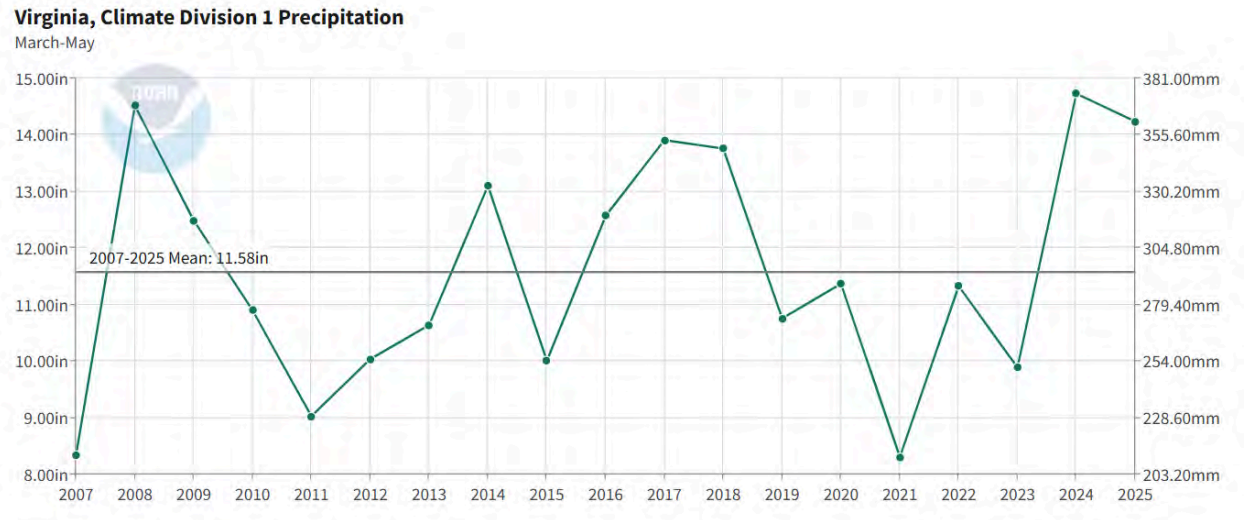

Figure 11. Precipitation data from 2007–2025 for March–May for Tidewater Virginia. Data from NOAA Centers for Environmental Information.

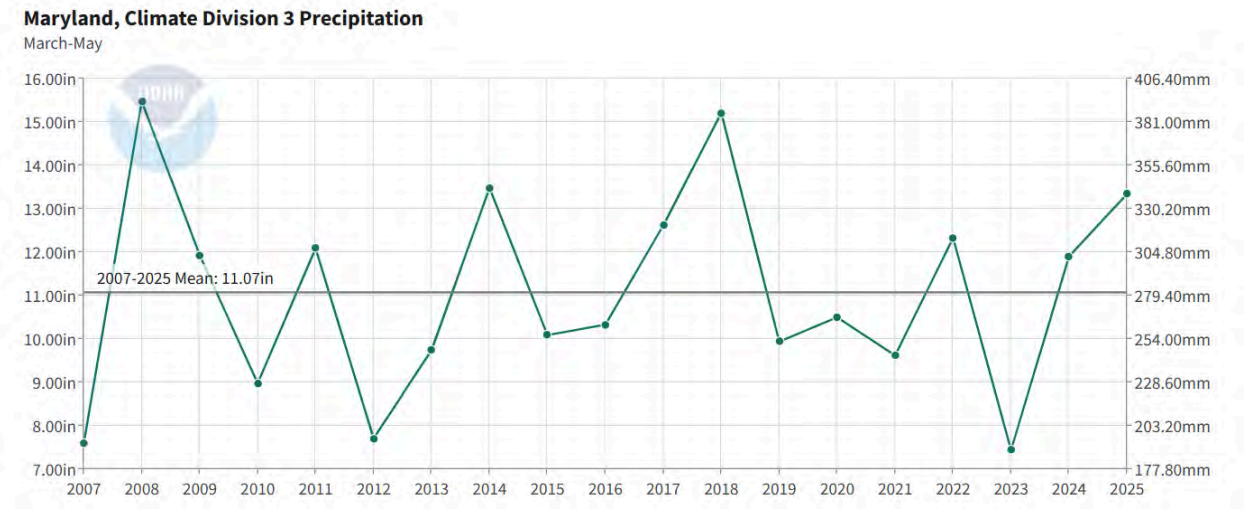

Figure 12. Precipitation data from 2007–2025 for March–May for southern Maryland. Data from NOAA Centers for Environmental Information.

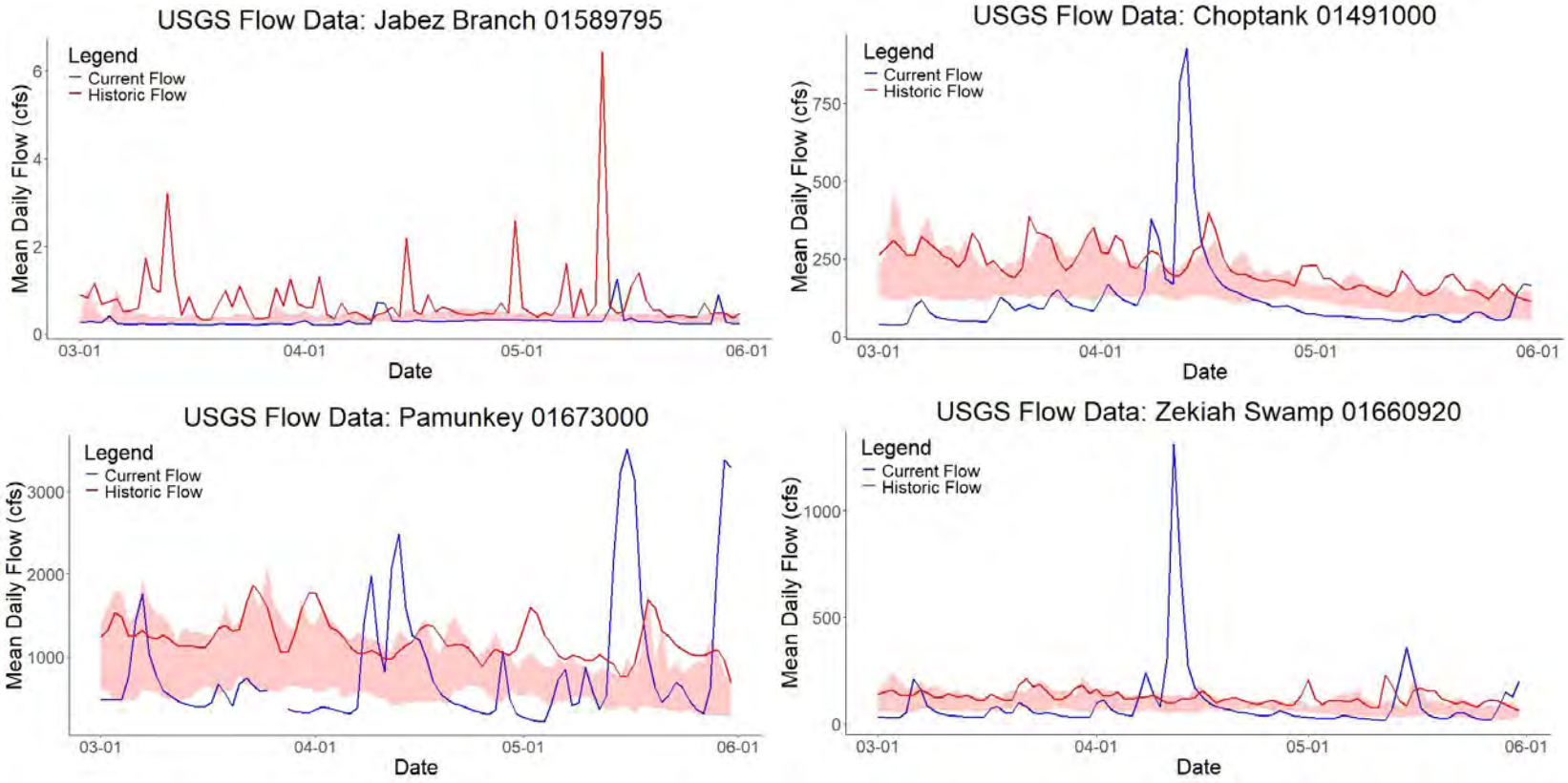

Figure 13. Daily mean streamflow observations (discharge, cubic feet/second) from the upper to lower Chesapeake Bay at U.S. Geological Survey monitoring sites at the (A) Jabez Branch, Severn River (B) Choptank River, (C) Pamunkey River, and (D) Zekiah Swamp, Potomac River throughout spring 2025 relative to the daily averages over this seasonal period from 2000–2024. The red shading indicates the interquartile range (25%-75%), where 50% of the historical values fall. These locations were chosen because they are fairly near the CBIBS Annapolis, Gooses Reef, York Spit, and Potomac locations respectively.

Dissolved Oxygen

Dissolved oxygen (DO) levels as tracked at NCBO's Lower Choptank and Sharps Island hypoxia monitoring buoys remained mostly within the historical range of values, with Lower Choptank remaining well above the biological threshold of 4 mg/L. Sharps Island daily averages hovered above or around the historical mean.

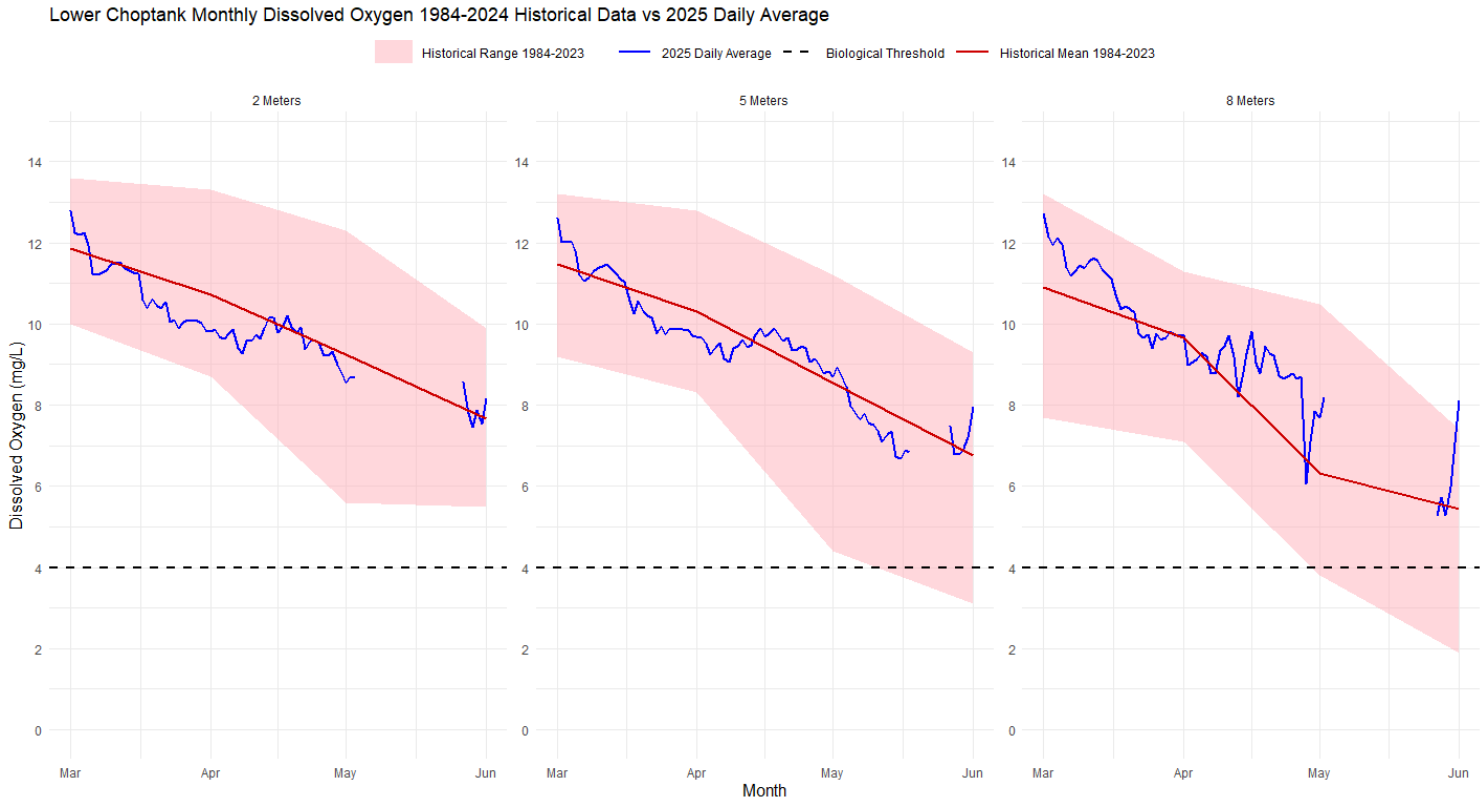

Figure 14. Dissolved oxygen (DO) daily averages at the Lower Choptank buoy for March–May 2025 compared with long-term averages (1984-2024) from the DNR EE2.1 fixed monthly monitoring station. The plots are separated by sensor depth, with the 8-meter plot using historical data from a 7-meter depth due to the absence of 8-meter historical data. The shaded area represents the historical range (minimum to maximum) of DO observations from the EE2.1 station, while the red line represents the historical mean. The 2025 daily average DO is shown by the blue line, and the black dashed line represents the biological threshold, marking the point at which aquatic life may alter its behavior to avoid low DO areas. Gaps in dissolved oxygen data are the result of station outages, sensor outages, or sensor data that does not meet QA/QC standards.

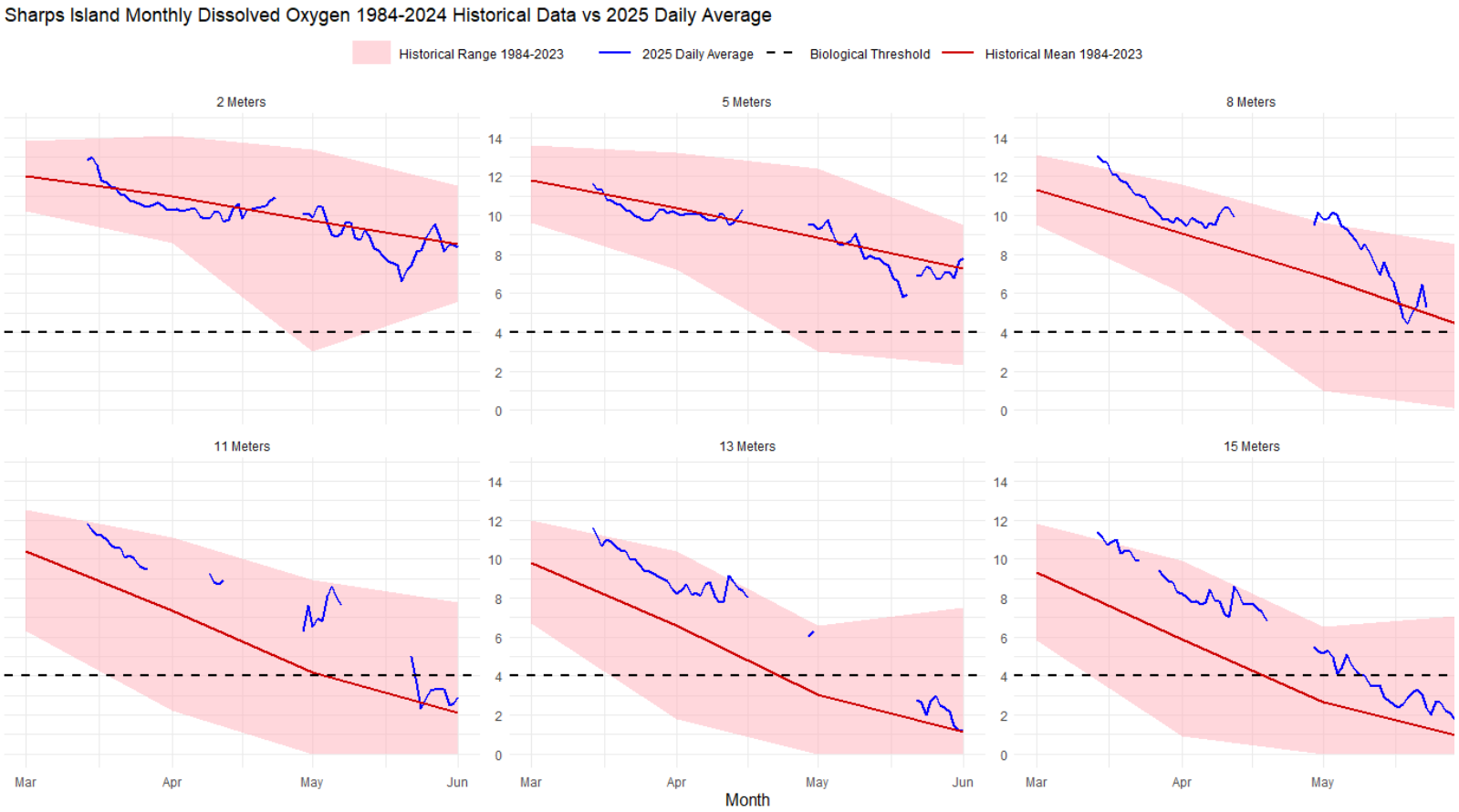

Figure 15. Dissolved oxygen (DO) daily averages at the Sharps Island buoy for March–May 2025 compared with long-term averages (1984-2024) from the DNR CB4.2C fixed monthly monitoring station. The shaded area represents the historical range (minimum to maximum) of DO observations from the CB4.2C station, while the red line represents the historical mean. The 2025 daily average DO is shown by the blue line, and the black dashed line represents the biological threshold, marking the point at which aquatic life may alter its behavior to avoid low DO areas. Gaps in dissolved oxygen data are the result of station outages, sensor outages, or sensor data that does not meet QA/QC standards.

Potential Effects of Anomalous Spring Conditions on Living Resources

Striped Bass
Temperature affects the timing of striped bass spawning activity, and recruitment success appears to be related to freshwater inflow (Martino & Houde 2010). Striped bass typically begin spawning in the spring when water temperatures reach 60°F, with most spawning occurring between 61°F and 69°F. This threshold was met at all buoy locations by about mid April (a month later than in spring 2024). The spawning season usually lasts from April to mid June.

Cold winter temperatures and high freshwater flow enhance striped bass recruitment by optimizing feeding opportunities. High freshwater flows promote the retention of larvae and zooplankton near the estuarine turbidity maximum, increasing coincidence of larvae and zooplankton (Martino & Houde, 2010). Cold winter temperatures help slow copepod development, which in turn creates peaks in spring copepod abundance (Millette et al., 2020).

Although winter 2025 experienced colder-than-average sea surface temperatures (which would benefit striped bass recruitment), the sporadic and lower flow observed in winter 2025 and at the beginning of spring 2025 may diminish striped bass spawning and recruitment success by altering the spatial coincidence of striped bass larvae and their preferred zooplankton prey (Martino & Houde, 2010; Millette et al., 2020).

Blue Crab
Blue crabs emerge from overwintering burrows at 50°F. This threshold was met at all buoy locations in the later half of March. Spring's warmer water temperatures cue blue crabs to begin reproducing. The minimum temperature for reproductive activity (mating, ovarian development) is 53.6°F; 66.2°F is the minimum temperature for spawning (Schneider et al., 2024). Across all buoy locations, the minimum temperature for spawning was reached in the beginning of May. The pattern observed from the CBIBS buoys of increasing water temperatures from March through May may lead to spawning beginning earlier in the spring and thus a longer blue crab growing season (Schneider et al., 2024).

Oysters
Oyster spawning can be triggered at about 60°F; this threshold was met at all buoy locations by about mid April (a month later than in spring 2024). Higher salinity is generally better for oyster reproduction and hatchery operations. As sessile organisms, oysters are particularly susceptible to hypoxia. Spring 2025's relatively low levels of hypoxia bode well for oyster survival.

Blue Catfish
Blue catfish are limited to water with salinity below 14 PSU. Because of this, their movement may have been constrained to upstream in fresher-water areas of southern rivers like the York and Potomac, as CBIBS salinity observations at the mouths of those rivers there remained above 14 all spring. For more northern tributaries like the Severn River, salinity dropped from more than 15 PSU in early spring, enabling blue catfish to move more freely.

References

Martino, E.J., and Houde, E.D. 2010. Recruitment of striped bass in Chesapeake Bay: spatial and temporal environmental variability and availability of zooplankton prey. Marine Ecology Progress Series, 409: 213–228.

Millette, N.C., Pierson, J.J., and North, E.W. 2020. Water temperature during winter may control striped bass recruitment during spring by affecting the development time of copepod nauplii. ICES Journal of Marine Science, 77: 300–314.

M.S. Rome, A.C. Young-Williams, G.R. Davis, A.H. Hines. Linking temperature and salinity tolerance to winter mortality of Chesapeake Bay blue crabs (*Callinectes sapidus*), Journal of Experimental Marine Biology and Ecology, Volume 319, Issues 1–2, 2005, Pages 129-145, ISSN 0022-0981, https://doi.org/10.1016/j.jembe.2004.06.014.

Pierson, J.J., Kimmel, D.G., and Roman, M.R. 2016. Temperature impacts on Eurytemora carolleeae size and vital rates in the Upper Chesapeake Bay in winter. Estuaries and Coasts, 39: 1122–1132. doi: 10.1007/s12237-015-0063-z.

Schneider A.K., Fabrizio M.C., and Lipcius R.N. 2024. Reproductive phenology of the Chesapeake Bay blue crab population in a changing climate. Front. Ecol. Evol., 11:1304021. doi: 10.3389/fevo.2023.1304021.

JGR Oceans

RESEARCH ARTICLE
10.1029/2022JC019625

Key Points:

- The summer stratification on the outer shelf breaks down by the end of October ±15 days, induced mainly by high-wind events during early fall
- Cyclones passing south of the shelf and large-scale high-pressure systems over East Canada are most impactful in removing stratification
- Differences in the dominant mixing processes likely lead to opposite *T*/*S*-contributions to destratification for the impactful wind patterns

Correspondence to:
L. L. Taenzer,
lukas.taenzer@whoi.edu

Citation:
Taenzer, L. L., Gawarkiewicz, G., & Plueddemann, A. (2023). Categorization of high-wind events and their contribution to the seasonal breakdown of stratification on the Southern New England shelf. *Journal of Geophysical Research: Oceans*, *128*, e2022JC019625. https://doi.org/10.1029/2022JC019625

Received 8 JAN 2023
Accepted 9 JUN 2023

Author Contributions:
Conceptualization: Lukas L. Taenzer, Glen Gawarkiewicz, Albert Plueddemann
Data curation: Lukas L. Taenzer
Formal analysis: Lukas L. Taenzer
Funding acquisition: Lukas L. Taenzer, Glen Gawarkiewicz, Albert Plueddemann
Investigation: Lukas L. Taenzer, Glen Gawarkiewicz, Albert Plueddemann
Methodology: Lukas L. Taenzer, Glen Gawarkiewicz, Albert Plueddemann
Project Administration: Glen Gawarkiewicz, Albert Plueddemann
Resources: Glen Gawarkiewicz, Albert Plueddemann
Software: Lukas L. Taenzer
Supervision: Glen Gawarkiewicz, Albert Plueddemann
Validation: Lukas L. Taenzer
Visualization: Lukas L. Taenzer

Categorization of High-Wind Events and Their Contribution to the Seasonal Breakdown of Stratification on the Southern New England Shelf

Lukas L. Taenzer[1,2], Glen Gawarkiewicz[1], and Albert Plueddemann[1]

[1]Woods Hole Oceanographic Institution, Woods Hole, MA, USA, [2]Massachusetts Institute of Technology, Cambridge, MA, USA

Abstract High-wind events predominantly cause the rapid breakdown of seasonal stratification on the continental shelf by the end of October. In particular the timing of events leads to considerable interannual variability in the stratification breakdown with a standard deviation of 15 days. Although previous studies have shown how coastal stratification depends on local wind-forcing characteristics, the locally observed ocean forcing has not yet been linked to regional atmospheric weather patterns that determine the local wind characteristics. Establishing such a connection is a necessary first step toward examining how an altered atmospheric forcing due to climate change affects coastal ocean conditions. Here, we propose a categorization scheme for high-wind events that links atmospheric forcing patterns with changes in stratification. We apply the scheme to the Southern New England shelf utilizing observations from the Ocean Observatories Initiative Coastal Pioneer Array (2015–2022). Impactful wind forcing patterns occur predominantly during early fall, have strong downwelling-favorable winds, and are primarily of two types: (a) Cyclonic storms that propagate south of the continental shelf causing anticyclonically rotating winds, and (b) persistent large-scale high-pressure systems over East Canada causing steady north-easterly winds. These patterns are associated with opposite temperature and salinity contributions to destratification, implying differences in the dominant processes driving ocean mixing based on a high-wind pattern's overall strength and wind direction steadiness. The high-wind event categorization scheme allows a transition from solely focusing on local wind forcing to considering realistic atmospheric weather patterns when investigating their impact on stratification in the coastal ocean.

Plain Language Summary While coastal waters are strongly density-layered during the summer (called "seasonal stratification"), high-wind events during the fall mix the water column and homogenize it. While it is known which local wind conditions tend to mix coastal waters the most, these conditions have not yet been linked to regional atmospheric weather patterns. Drawing such a connection is a necessary step toward understanding how atmospheric climate change may affect the coastal ocean. Here, we propose a categorization scheme to identify which atmospheric patterns have the strongest impact on coastal ocean stratification in the fall. The scheme is applied to the coastal ocean south of New England using 7 years of mooring observations. Two weather categories are particularly impactful: Storms passing south of the coastal ocean and large-scale high-pressure systems over East Canada. Both categories occur mainly during early fall and bring northeasterly winds associated with the onshore movement of more dense open-ocean water which results in enhanced mixing. Differences in their ocean impact are likely caused by the difference in wind direction steadiness of the two categories. The categorization scheme allows a transition from solely investigating the ocean impacts from local wind forcing to incorporating more realistic atmospheric weather patterns.

1. Introduction

The annual cycle of stratification is the dominant mode of variability on the Southern New England continental shelf (Beardsley et al., 1976), abbreviated as Southern New England shelf (SNES) and shown in the inset of Figure 1. The seasonal stratification controls the phytoplankton productivity (Schofield et al., 2008) in one of the biologically most productive regions worldwide (O'Reilly & Zetlin, 1998) and regulates the timing and strength of the fall and spring phytoplankton bloom when light availability and stratification strengths change rapidly. Wind-induced mixing is particularly influential for setting the bloom variability at the shelfbreak (Xu

Writing – original draft: Lukas L. Taenzer
Writing – review & editing: Lukas L. Taenzer, Glen Gawarkiewicz, Albert Plueddemann

et al., 2013). Lentz et al. (2003) observed that the rapid shelf stratification breakdown in the fall is clustered around storm events, suggesting that seasonal surface cooling plays a less crucial role than high-wind events.

The leading-order interactions between wind-forcing and coastal bathymetry and their effects on shelf stratification are well understood. In the region, northeasterly high-wind forcing during fall with the coast to its right is associated with rapid destratification (Lentz et al., 2003), following a simple Ekman-forcing argument for the coastal ocean (Gill, 1982): Steady downwelling-favorable (easterly) winds are associated with destratification since they advect denser surface water from the Slope Sea onshore over more buoyant shelf water and can cause enhanced mixing at the shelfbreak due to frontal steepening (shelfbreak frontal zone is shown in Figure 1). In contrast, upwelling-favorable winds are typically associated with restratification. Including such advection processes across the shelfbreak front is necessary to explain the rapidity of the stratification breakdown on the New Jersey shelf (Forsyth et al., 2018). As their model study was based significantly further inshore than observations used in this study, an even larger influence of frontal processes contributing to the observed variability can be expected on the outer shelf.

Even though the leading-order characteristics of wind-driven stratification changes along continental shelfbreaks are well understood, it remains unclear which spatio-temporal atmospheric weather patterns cause the locally detected wind signals that contribute most dominantly to the fall stratification breakdown. In addition, wind pattern characteristics beyond their along-shelf wind component have not been investigated, yet. By identifying the synoptic weather patterns that cause destratification, a more holistic view on wind-driven ocean forcing improves predictability efforts, rather than just diagnosis based on local analysis. However, demonstrating that distinct atmospheric patterns are consistently associated with different ocean impact strengths requires the investigation of a large number of events. The Ocean Observatories Initiative (OOI) Coastal Pioneer Array facilitates such an assessment by providing the first comprehensive multi-year observational (sub-)surface data set of a shelfbreak system. Matching the ocean impact on stratification with real atmospheric patterns is a necessary first step toward elucidating how the seasonal cycle of stratification on the SNES responds to changes in the atmospheric forcing.

Here, we introduce a categorization scheme based on the spatio-temporal characteristics of high-wind events to identify which atmospheric patterns contribute most to the annual breakdown of stratification. The approach of categorizing high-wind forcing patterns to identify differences in the coastal ocean response has been proven successful for the Beaufort Sea continental shelfbreak (Foukal et al., 2019). Scalar metrics, encapsulating simplified wind forcing and ocean response variables, allow for easy comparison between events across multiple years of observations. While these simplifying metrics cannot capture the full dynamics of a high-wind forcing event, they allow focusing on the first-order forcing and impact characteristics to determine which events are most important for the seasonal destratification. By focusing not only on cyclones but on all types of weather systems associated with high-wind forcing, a more comprehensive understanding of the factors contributing the most to the seasonal breakdown of ocean stratification in the fall can be gained.

Section 2 introduces the data and methods used to identify high-wind events and their ocean impact on the SNES, followed by Section 3 covering the observed interannual variability in destratifying the continental shelf during fall. The spatio-temporal high-wind event categorization scheme is described in Section 4 before Section 5 applies the scheme to distinguish between forcing and ocean impact characteristics. The manner in which the categorization scheme helps explain the variability of the seasonal impact, event timing, and mixing contributions are discussed in Section 6.

2. Data and Methods

2.1. OOI Coastal Pioneer Array

Local atmospheric and subsurface information from the SNES has been recorded by the inshore moorings of the OOI Coastal Pioneer Array (abbreviated CP Array and mooring locations marked Figure 1), a process-oriented shelfbreak observatory in operation between 2015 and 2022. The CP Array spans across the shelfbreak and is located close to the so-called "40/70 benchmark" at 40°N and 70°W, used by weather forecasters to estimate winter storm impacts for the US Northeast based on storm track positions relative to this point (Roller et al., 2016). The CP Array moorings feature surface buoys with meteorological sensors to determine bulk surface fluxes. Subsurface information is provided through wired profilers with Conductivity-Temperature-Depth (CTD)

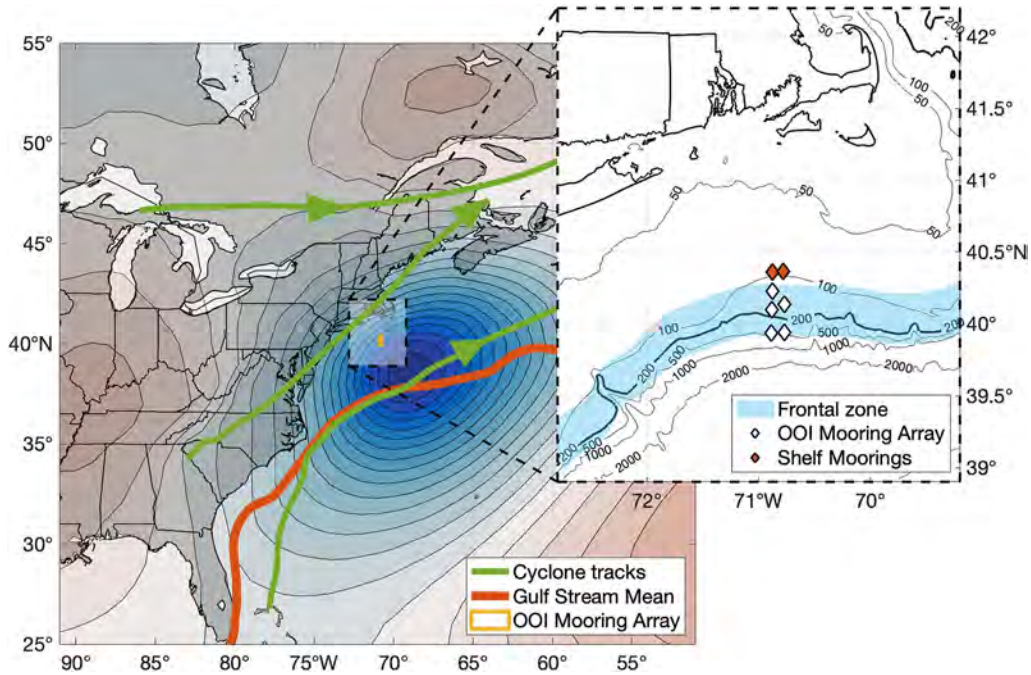

Figure 1. Map of Eastern North America and the Northwest Atlantic with a low-pressure system south of the Southern New England shelf (SNES) (contours are sea level pressure). Shown are the two dominant cyclone tracks that pass north of the shelf and one cyclone track passing south, circulation features (shelfbreak frontal zone and mean Gulf Stream position), the SNES bathymetry, and the location of the Ocean Observatories Initiative Coastal Pioneer Array moorings. Mean storm tracks are derived from manually tracked cyclones during the fall seasons 2015–2021. The mean Gulf Stream position is approximated by the 0.25 cm isoline of the absolute dynamic topography climatological mean (generated using AVISO+ products (AVISO+, 2022)).

sensors in the central water column and fixed instrument packages within the surface and bottom boundary layers. This combination of assets makes the mooring array well-suited for quantifying high-wind surface forcing impacts on subsurface temperature, salinity, and density structure.

Table 1 lists the data sources used in this study following the terminology of Gawarkiewicz and Plueddemann (2020). Technical details about instrumentation and array composition are provided in their paper. All data are mapped onto an hourly grid, either via averaging (rows 1 + 3–5) or linear interpolation (row 2). Potential ocean water density (referenced to $p = 0$) is calculated using TEOS-10 (McDougall & Barker, 2011). Hydrography measurements on the shelf are taken at different depths along the 95 m isobath: Surface, 7 m, continuously between ~30–70 m, and 2 m above the bottom. Local wind and atmospheric data are collected by the CP Array's three surface buoys, 3 m above sea level. Surface windstress was computed from bulk variables using the COARE3.5 algorithm (Edson et al., 2013) while neglecting effects from the surface wave field. Occasional data gaps in the Inshore Surface Mooring data were replaced with data from the Central and Offshore Moorings, respectively.

Table 1
Data Sources of the OOI Coastal Pioneer Array[a] Time Series Analyzed in This Study

#	Variables	Mooring	Platform	Platform depth (m)	Ocean depth (m)
1	T, S	Inshore Surface M. (ISSM)	Surface buoy	2	95
2	T, S, P, ρ	Upstr. Inshore Prof. M. (PMUI)	Profiler	~30–70	95
3	U, V (wind)	Inshore Surface M. (ISSM)			95
4	SLP	Central Surface M. (CNSM)	Surface buoy	−3	135
5	T_{air}, RH	Offshore Surface M. (OSSM)			450

Note. OOI, Ocean Observatories Initiative.
[a]From Gawarkiewicz and Plueddemann (2020).

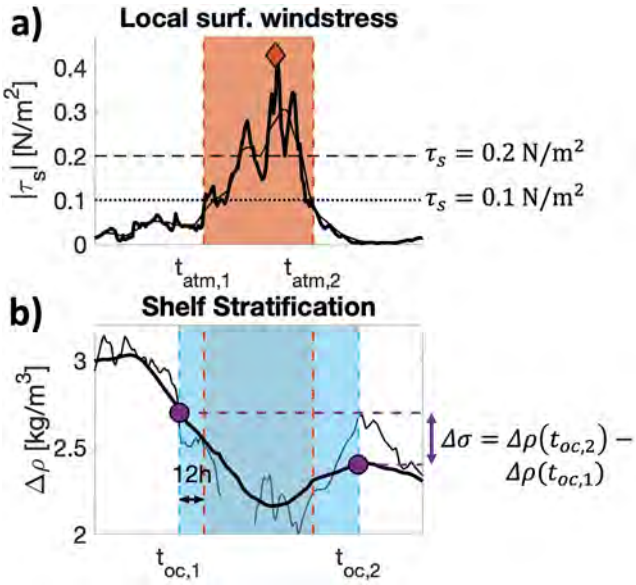

Figure 2. Illustration of how to define a high-wind forcing event, its properties, and subsurface ocean response using local CP Array time series based on an event observed around 10 September 2018. (a) surface windstress (bold line: 1 hr resolution data; thin line: 12 hr-moving mean window). (b) stratification estimate (bold line: 36 hr lowpass-filtered; thin line: 1 hr resolution data). Diamonds and circles are points of interest identified by the algorithm. The algorithm is explained in the text.

This replacement is justified since the maximum horizontal distance between the surface buoys (less than 50 km) is much smaller than the atmospheric synoptic length scale, correlations between surface mooring data are large (>95%), lag-correlations peak at zero-lag, and the residual distribution peak is smaller than the noise.

Since the instrument configuration does not cover the typical depth range of the seasonal pycnocline (i.e., between 7 and 30 m), mixed-layer depths cannot be estimated. Instead, a bulk estimate of shelf stratification strength σ is defined as the density difference $\Delta\rho$ between the shelf interior and the sea surface using data from the inshore moorings:

$$\sigma|_{\text{shelf}} \equiv \Delta\rho|_{\text{shelf}} = \rho(z = 67\,\text{m})|_{\text{PMUI}} - \rho(z = 0\,\text{m})|_{\text{ISSM}}. \quad (1)$$

Similar shelf stratification estimates have been used by Forsyth et al. (2018) and Lentz et al. (2003). The deepest depth of the Upstream Inshore Profiler Mooring range with consistent data turnout is at $z = 67$ m. According to Linder and Gawarkiewicz (1998)'s climatology of the shelfbreak front, this depth should be mostly undisturbed from both variability of the mixed-layer depth and the frontal foot position, making it an appropriate location for extracting lower layer density estimates so close to the shelfbreak front. The (bulk) stratification estimate exploits data from both inshore moorings that are spatially separated by 9.2 km along the same isobath. Since the shelfbreak bathymetry shows little along-shelf variation across the CP Mooring Array area and the horizontal length scale of atmospheric weather patterns is much larger than this distance, the horizontal misalignment is not expected to affect the results.

2.2. Atmospheric Reanalysis Data

Spatial sea level pressure (SLP) and surface wind data over Northeast America and the adjacent Atlantic is taken from the ERA5 atmospheric reanalysis data set (Hersbach et al., 2018). This study utilizes ERA5 data on a 1° × 1°-spatial and 6 hr-temporal grid. When comparing ERA5 data with observations from the CP Array's inshore surface mooring, zonal surface windstress shows a cross-correlation of $r = 0.95$, zero lag-correlation, and a narrow $\left(\mathcal{O}(\sigma) = 10^{-2}\,\text{N m}^{-2}\right)$ residual distribution with its peak around zero $\left(\mathcal{O}(\mu) = 10^{-3}\,\text{N m}^{-2}\right)$. Thus, ERA5 data seem trustworthy for the purpose of this study.

2.3. Connecting Surface Forcing With Subsurface Impact

This study aims to identify high-wind events and link them with shelf stratification changes as a metric for the events' ocean mixing impact. The following algorithm takes time series of local wind forcing and the previously defined shelf stratification index as input and outputs a list of individual events and their associated ocean impact. Event forcing and impact are characterized by a set of simple scalar metrics to allow easy comparison between events. Figure 2 applies the algorithm to an exemplary event around 10 September 2018, while a detailed description is given in the text.

Atmospheric high-wind events are defined as peaks above a 0.2 N m^{-2} surface windstress threshold. By defining high-wind events as the absence of calm conditions, the beginning and end of an event are determined in a two-step process. First, the smoothed surface windstress (thin black line in Figure 2a) is examined, and minima are identified on either side of the initial peak below a threshold of 0.1 N m^{-2}. Secondly, the beginning and end of an event are found by moving inward from the identified minima until the unsmoothed surface windstress hits the 0.1 N m^{-2} threshold. The two-step process, including smoothing, ensures that cyclones whose relatively calm center passes across the CP Array do not get split into two events. If more than one event peak is associated with the same event time period, the event gets linked with the more prominent peak.

Defining the beginning and end of a high-wind event allows for integration of atmospheric forcing variables across the event duration, leading to simplified scalar forcing estimates. This study focuses on the integrated

along-shelf windstress $\int_{t_{a,1}}^{t_{a,2}} \tau_x \, dt$ and the cumulative cubed wind speed $\int_{t_{a,1}}^{t_{a,2}} |U|^3 \, dt$ to distinguish between dominant wind-forcing regimes and their impact on ocean mixing responses. Since the x-direction aligns well with the shelf edge at the location of the CP Array, no coordinate system rotation is required. The choice of these forcing metrics will be justified in Sections 5 and 6.4. The threshold of 0.2 N m^{-2} represents the lower range of force 6 on the Beaufort scale (approx. 22 knots winds), described as a "strong breeze." The comparatively low threshold ensures that the full bandwidth of impact variability associated with wind events is captured. While the chosen threshold affects the number and duration of identified events, the overall results of this study are robust under reasonable threshold parameter variations.

While an event's windstress peak identifies high-wind event forcing, its leading-order ocean response is the net change between the pre- and post-event ocean state, that is, a derivative variable. The impact of a high-wind event on ocean mixing is quantified by the change in shelf stratification as measured throughout the event and immediately following the event. In particular, the potential for restratification due to isopycnal slumping immediately following the high-wind event should be included when estimating the event-induced stratification change. Such restratification is an integral part of the response of an ocean frontal region to wind forcing on the meso- (Tandon & Garrett, 1994) and submesoscales (Boccaletti et al., 2007).

The ocean response signal is defined as the stratification estimate difference between two neighboring points of zero slope $\Delta\sigma = \sigma(t_{o,2}) - \sigma(t_{o,1}) = \Delta\rho(t_{o,2}) - \Delta\rho(t_{o,1})$. This simplified approach assumes that the continental shelf is in steady-state ($\partial_t \Delta\rho = 0$) before and after the event and that the high-wind forcing event dominates other potential forcing mechanisms that might be present and change the shelf stratification. We acknowledge the limitations of this assumption, in particular in the presence of other processes, for example, other high-wind events in the direct vicinity or shelfbreak frontal instability. However, the large number of observed events allows us to identify potential outliers where forcing processes could have interacted with one another.

Before identifying zero-slope points, the stratification signal needs to be lowpass-filtered to identify irreversible stratification changes on the time scale of synoptic atmospheric forcing events, rather than oscillations occurring on shorter scales. A cutoff-frequency of 2 inertial periods ($4\pi/f_0 \approx 36$ hr) was chosen to suppress variability from inertial oscillations $\mathcal{O}$(18h), M2 and K1 tidal frequencies, daily cycle harmonics, internal waves, and other super-inertial oscillations. To the extent that these processes could lead to a net stratification change that persists beyond the oscillation period, the lowpass-filtered signal and ocean response algorithm will include their contributions.

However, since the ocean response may not exactly align with the timing of the locally observed atmospheric forcing, the ocean response time window is allowed to deviate from the timing of the high-wind event within strictly defined bounds. The start (end) of the ocean response period $t_{oc,1}$ ($t_{oc,2}$) are defined by either…

(a) … the local stratification extremum within the 12 hr preceding (following) the pickup $t_{atm,1}$ (decline $t_{atm,2}$) of the winds if $\partial_t \Delta\rho|_{t_{atm}}$ has the same sign than $\Delta\sigma$.
(b) … the start (end) of the wind speed pickup $t_{atm,1}$ (decline $t_{atm,2}$) if the local stratification gradient $\partial_t \Delta\rho|_{t_{atm}}$ has the opposite sign than the net stratification change $\Delta\sigma$ associated with the event.

While case (b) accommodates small deviations from the initial assumption that the continental shelf is in steady-state ($\partial_t \Delta\rho = 0$) before (after) the high-wind forcing event, case (a) accounts for smoothing effects from the $4\pi/f_0$ lowpass-filter if the contamination from immediately neighboring forcing events seems small. The 12 hr-threshold was chosen since the lowpass-filtered signal starts to exhibit variability on this timescale.

If the event is associated with net destratification and condition (a) has been applicable, potential post-event restratification due to isopycnal slumping in the vicinity of the shelfbreak front is incorporated as follows: The end of the ocean response time period gets extended to the next local maximum of the lowpass-filtered stratification signal. The maximum has to lie within the two inertial periods (i.e., $4\pi/f_0 \approx 36$ hr) following the decline $t_{atm,2}$ of the high-wind forcing event, and no overlap with the beginning of the following event's ocean response period can be created. The post-forcing $4\pi/f_0$-threshold is a compromise between accommodating (a) the time scales of mesoscale geostrophic adjustment (Tandon & Garrett, 1994) and submesoscale mixed-layer instabilities and eddies (Boccaletti et al., 2007; Mahadevan et al., 2010) and (b) restricting the post-event frontal slope relaxation period to sub-synoptic time scales to avoid contamination from other processes, for example, the next synoptic event or shelfbreak frontal meander. In the mid-latitudes, synoptic weather systems pass an area every 2–3 days.

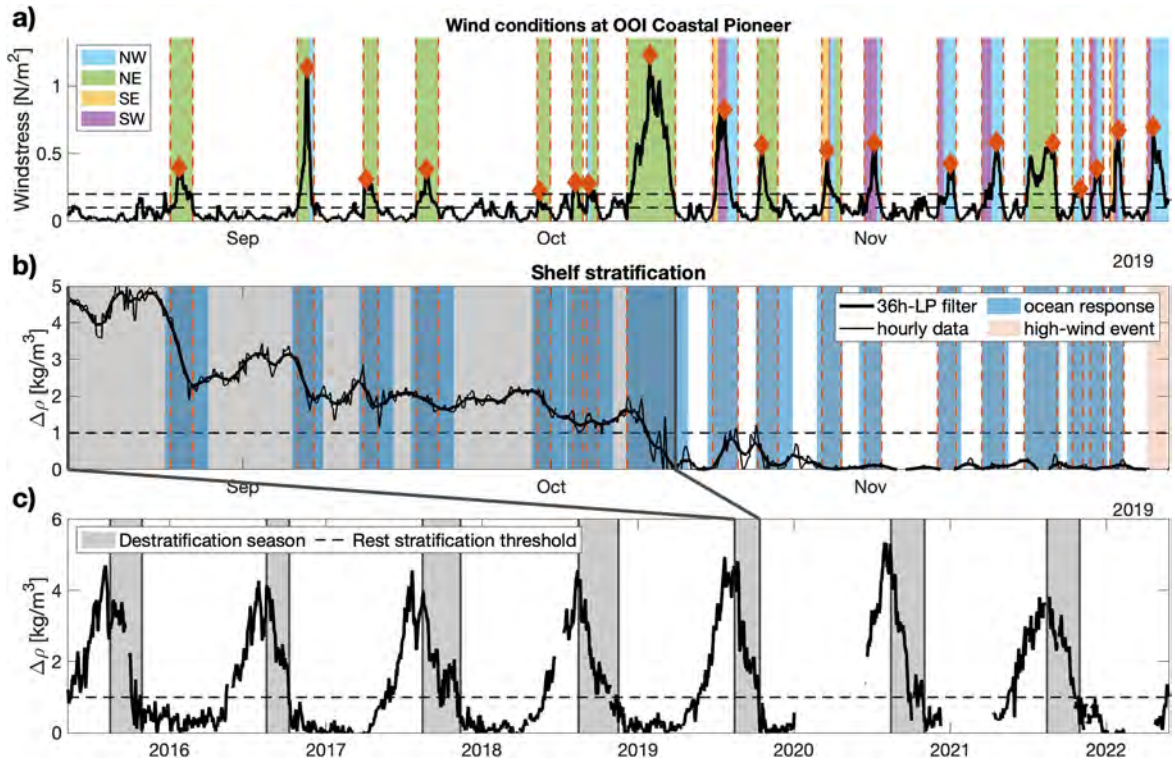

Figure 3. Locally identified high-wind events during fall 2019 and their associated ocean mixing impact by applying the algorithm outlined in Section 2.3. (a) Surface windstress; main wind directions throughout a high-wind event are color-coded. (b) Shelf stratification estimate. Ocean response periods associated with a high-wind event are colored in blue. (c) 36 hr lowpass-filtered stratification estimate $\Delta\rho$ of full time series (May 2015–2022); destratification seasons are colored in gray.

The algorithm provides a robust approach to identifying locally observed high-wind forcing events, defining their start and end, and linking the forcing with its subsurface ocean mixing impact on the outer continental shelf. Extending the time window for detecting the ocean mixing response to high-wind forcing beyond the time period of the high-wind event itself allows to capture the effects from post-event restratification. Since the stratification estimate time series has been lowpass-filtered, small variations in the start and end point of the ocean response period typically have little effect on the net stratification change associated with the high-wind event.

3. Seasonal Breakdown of Shelf Stratification

The algorithm described above has been applied to the time series recorded by the CP Array between May 2015 and 2022 (see fall destratification season 2019 in Figures 3a and 3b). The fall destratification season is defined as the time period of consistent water column homogenization (Figure 3c): The start date is set as August 15. The season's end date is the time point at which the lowpass-filtered stratification signal decreases below the rest stratification threshold $\Delta\rho < 1.0$ kg m^{-3} and remains there for the rest of the year. The event that pushes the stratification below the threshold is included in the destratification season. The 1.0 kg m^{-3}-threshold ensures that late season density fluctuations are not included in the analysis. Since smaller thresholds only increase the number of events with little ocean mixing impact, the overall results of this study are robust to a range of thresholds. The initial late summer stratification $\Delta\rho_0$ is defined as the maximum stratification within the fall destratification season.

The annual cycle of seasonal stratification and shelf homogenization follows the climatology outlined in Linder and Gawarkiewicz (1998) despite noticeable interannual variability (Figure 3c). Interannual variability is observed in the timing of re- and destratification, the occurrence of destratifying high-wind events within a season, and the individual destratification per event (Table 2). Stratification reaches maximum values around mid-August before it rapidly decays to leave the shelf on average homogenized on October 29 ± 15 days. $\langle N \rangle = 6 \pm 2$ destratifying high-wind events are responsible for an average cumulative destratification of $\langle \sum_i^N \Delta\sigma_i \rangle = -3.5 \pm 1.4$ kg m^{-3}

Table 2
Statistics of the Fall Destratification Breakdown on the Southern New England Shelf and Contributions From Destratifying Events

	Destratification season			Destratifying events		
Year	End	Length (days)	$\Delta\rho_0$	N	$\sum_i^N \Delta\sigma_i$	$\overline{\Delta\sigma}$
2015	October 28	74	3.7	4	−2.4	−0.6
2016	October 07	53	4.1	3	−1.6	−0.5
2017	November 11	89	4.0	7	−4.3	−0.6
2018	November 16	93	4.3	9	−2.9	−0.3
2019	October 13	59	4.8	7	−5.9	−0.8
2020	November 01	78	5.0	6	−3.9	−0.6
2021	October 30	76	3.8	8	−3.8	−0.5
Mean	October 29	75 ± 15	4.3 ± 0.5	6 ± 2	−3.5 ± 1.4	−0.6 ± 0.2

Note. The columns display the year, last day of the destratification season, season length, maximum stratification $\Delta\rho_0$ after August 15, number of destratifying high-wind events during the season N, cumulative impact from events $\sum_i^N \Delta\sigma_i$, and average impact per event $\overline{\Delta\sigma}$, respectively. The last row presents the mean and standard deviation across all years. Only events associated with destratification are considered in the right section of the table. Stratification has units kg m^{-3}.

per season. As a consequence, an individual destratifying event causes an average stratification change of $\langle\overline{\Delta\sigma}\rangle = -0.6 \pm 0.2\,\mathrm{kg\,m^{-3}}$. The signal-to-variability ratios of cumulative destratification and individual events are on the same order of magnitude. This suggests that the variability in the timing of the seasonal stratification breakdown is both set by the timing and number of high-wind events throughout the season as well as the characteristics of individual events.

The cumulative destratification from high-wind events alone $\sum_i^N \Delta\sigma_i$ removes on average 83 ± 29% of the initial shelf stratification of late summer ($\langle\Delta\rho_0\rangle = 4.3 \pm 0.5\,\mathrm{kg\,m^{-3}}$). This result aligns well with Lentz et al. (2003) who inferred from just four storm events during fall 1996 that the fall destratification on the continental shelf is primarily caused by high-wind forcing and not the cumulative effects from sustained surface cooling throughout the season. Intermittent restratification, typically between high-wind events, prolongs the destratification breakdown, for example, through surface-heating. The cumulative change in shelf stratification during calm conditions has a magnitude of -0.5 ± 1.2 kg m^{-3}, that is, both weak additional destratification and net restratification during calm conditions have been observed. Restratification associated with high-wind events occurs occasionally; though, high-wind forcing dominantly causes destratification.

The number of high-wind events per destratification season varies widely (Table 2), representing the large variability in the atmospheric forcing on synoptic time scales. As shown in Figure 3a, high-wind events during early winter shortly follow upon each other while they are more sparse during the summer and early fall with large periods of calm conditions. Hurricanes or their extratropical successors can be particularly impactful if they pass close to the shelf. Since the North-Atlantic hurricane season peaks in early September, these events typically influence the shelf when stratification is still high. While each anomaly in the 7-year long data record contains a story worth telling, this study aims to identify the atmospheric patterns that consistently impact the continental shelf every fall.

4. Connecting Local Forcing With Regional Patterns

This work aims to identify the high-wind event patterns with the largest ocean mixing impact and contribution to the fall stratification breakdown on the continental shelf. Each local forcing event is part of a large-scale atmospheric pattern with distinct forcing characteristics on the continental shelf. Thus, zooming out and categorizing spatio-temporal atmospheric patterns allows the partition of the highly variable local forcing when examining the wind-driven ocean mixing impact. The goal is to determine which patterns lead to the greatest destratification on the shelf. While Section 2.3 provides a framework to link locally observed wind forcing with its ocean mixing impact, its purely local approach does not have the ability to differentiate between different atmospheric patterns.

4.1. Categorization Scheme for High-Wind Events

To link local forcing conditions with atmospheric patterns, a categorization scheme is established that clusters spatial SLP patterns whenever a high-wind event gets detected locally by the CP Array. The scheme is motivated by Foukal et al. (2019)'s approach of investigating the origin of storms that are associated with a downwelling ocean response on the Alaskan Beaufort Sea continental shelf. Even though the scheme categorizes atmospheric forcing events, it is designed with the oceanographic application of linking the forcing with ocean mixing impacts in mind. Thus, the location of an atmospheric pattern with respect to the SNES is an integral part of the categorization since distance and wind direction largely contribute to the local forcing characteristics.

The high-wind event categorization scheme aims to identify the SLP pattern which is mainly responsible for the locally measured forcing. Pattern clustering, rather than a storm tracking algorithm was used to categorize events since high-wind forcing events on the SNES are caused by a wide variety of types and scales of synoptic weather systems. Conventional storm tracking algorithms are typically trained toward identifying closed-contour cyclone systems (Neu et al., 2013). The pattern clustering relies on human-based decision-making when categorizing high-wind events based on their spatio-temporal characteristics. To minimize human bias, a clear three-step protocol for assigning events to a particular pattern category has been established:

1. Identification: Weather systems with closed-contour SLP patterns whose isobars reach the CP Array location concurrent with a locally detected wind event (windstress at least 0.2 N m^{-2} at the CP Array) are identified as potential candidates.
2. Selection: The candidate weather systems are ranked based on the alignment between their geostrophically induced winds and the locally observed winds during the $\pm$24 hr period surrounding the local windstress maximum of the event. The weather system with the best alignment gets selected as the one primarily responsible for the locally observed forcing. If there is doubt about the best alignment, the system with the stronger SLP anomaly is selected.
3. Assignment: The selected pattern gets assigned to one of the pre-determined categories based on its spatio-temporal characteristics and location with respect to the CP Array. In the rare case that a clear distinction among the categories is not possible, the event remains uncategorized.

Events have been categorized by the same person in a random order to avoid establishing artificial temporal trends.

As typical for unsupervised learning frameworks, the number of categories is not inherent to the data set and needs to be determined externally. Six categories are sufficient to distinguish between the different locally observed wind forcing patterns while remaining able to unambiguously assign a particular category to an event. While increasing the number of categories would statistically reduce the variability per category, the assignment becomes more ambiguous in reality due to less distinct characteristics of individual categories. While four categories are required to differentiate between the four main wind directions associated with slowly-propagating large-scale patterns, only two categories are required to differentiate between propagating cyclones since storm tracks over New England converge and are mostly oriented in the Northeast direction toward the Icelandic Low (Zielinski & Keim, 2003). Note that there is no separation between tropical and extratropical cyclones. The chosen partitioning of large-scale SLP patterns into the presented four categories is recognizable in the spatial modes and principle component values of an Empirical Orthogonal Function (EOF) analysis (not shown).

4.2. Partitioning Weather Systems Into Six Spatio-Temporal Categories

Applying the human-centered categorization scheme described above, 98% of all locally observed high-wind events have been assigned to one of six categories. Each category is defined by its distinct SLP pattern and named after the location of their associated SLP core (Figure 4). In accordance with geostrophic theory, all high-wind event categories are associated with strong SLP gradients at the location of the CP Array at the time of maximum local windstress. The strength of these gradients is either caused by eastward propagating cyclones/storms with diameters of $\mathcal{O}$(100 km) (Figures 4a and 4b) or typically more steady large-scale patterns of $\mathcal{O}$(1000 km) in spatial extent (Figures 4c–4f). While the SLP patterns provide insight into the origin of the locally observed wind forcing on the continental shelf, the composite time series reveal differences between the patterns' temporal forcing development on the SNES. Abrupt changes in air temperature at an event's beginning or end suggest that the high-wind forcing pattern is associated with a frontal passage.

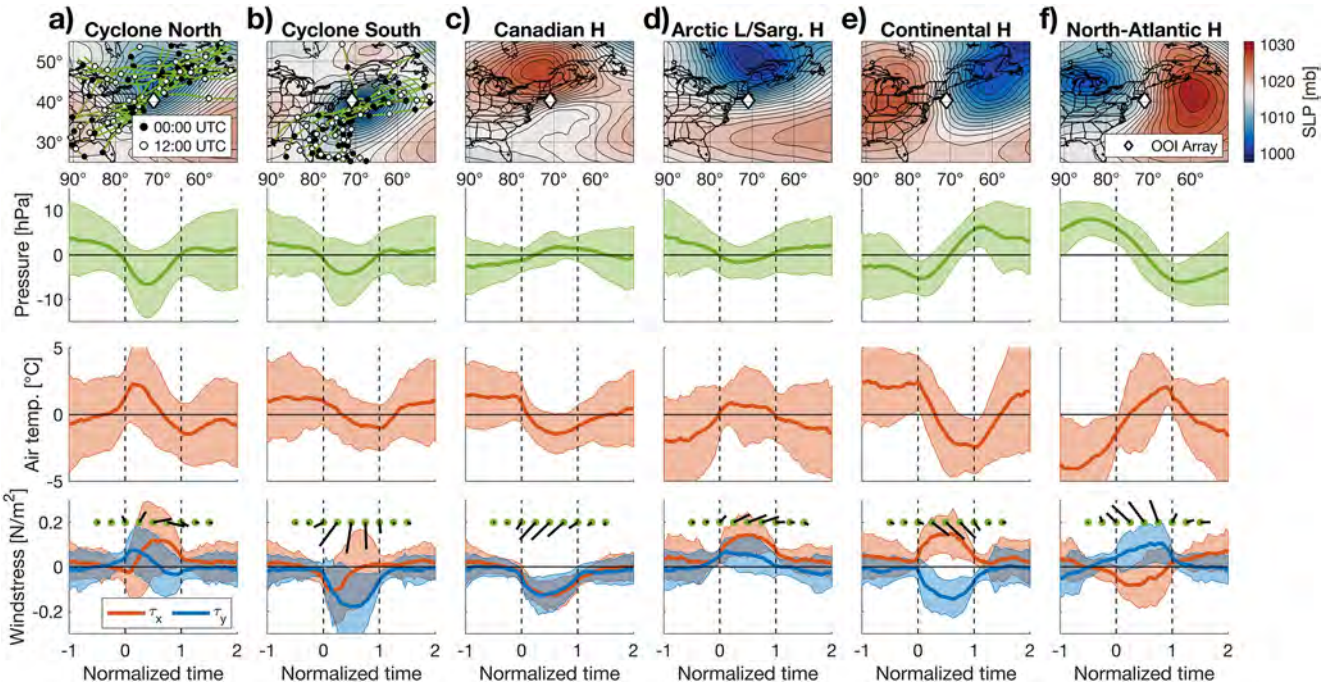

Figure 4. Composites for each high-wind event category (a–f), using categorized high-wind events between May 2015–2022. Row 1: Mean sea level pressure fields at event peaks. Storm tracks (determined manually) are included for all cyclones that occurred during the fall destratification seasons. Row 2–5: Time series composites of sea surface pressure (row 2), surface air temperature (row 3), surface windstress (row 4), as observed by the CP Array. Time axis is normalized with the event's start at $t = 0$ and end at $t = 1$. For better visualization of the wind field, surface windstress vectors (row 4) are shown in black. Time series envelopes represent one-standard deviation.

Cyclones are separated into two categories based on their storm track with respect to the CP Array and the SNES since the local forcing has opposite wind directions: *Cyclones North* and *Cyclones South*. Large-scale dipole structures of opposite SLP anomaly can lead to sufficiently strong SLP gradients between them for generating high-wind events on the shelf. Large-scale high- and low-pressure systems north and south of the SNES, called *Arctic Low/Sargasso High* and *Canadian High* (Figures 4c and 4d), respectively, lead to strong SLP gradients south of New England due to the simultaneous presence of a high-pressure ridge or low-pressure trough of opposite SLP anomaly. The low-pressure anomalies south of Canadian Highs are typically caused by weak cyclones that precede the high-wind event and are associated with a cold frontal passage initiating the high-wind event. *Continental Highs* and *North-Atlantic Highs* (Figures 4e and 4f) are characterized by East-West dipole structures with both pressure cores of similar strength. Continental Highs are associated with distinct cooling during the event, and the extent of the low-pressure system into the Arctic is similar to that of Arctic cold air outbreaks. There are differences in the seasonal occurrence frequencies between the categories as discussed in Section 6.1.

The spatio-temporal characteristics of each category lead to distinguishable surface windstress patterns on the SNES. Large-scale pressure systems cause relatively steady winds throughout the locally detected high-wind event while the cyclones' eastward propagation leads to rotating winds on the continental shelf. The spatial relationship between the cyclone and the CP Array determines the wind direction and how fast the winds rotate locally. Frictional drag in the surface boundary layer likely causes the deviation between the SLP isobar orientation at the CP Array location and the windstress vectors toward the low-pressure systems. While Canadian Highs are associated with steady down-front winds, Arctic Lows/Sargasso Highs cause steady up-front winds.

5. High-Wind Event Pattern Characteristics

Since the high-wind event categories are associated with different forcing characteristics on the SNES, their average ocean mixing impacts should differ as well. The wind forcing direction is expected to be crucial for predicting ocean mixing impacts on the continental shelf due to the existence of a bathymetric boundary (Gill, 1982). Simple scalar metrics to characterize an event's wind forcing directionality are the mean wind direction $\overline{\phi}$ and its

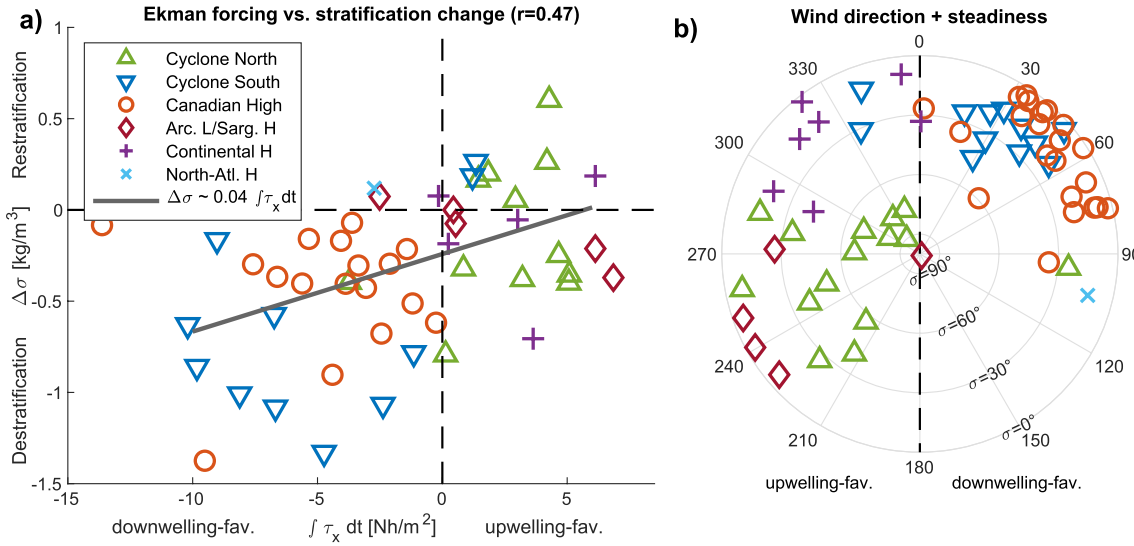

Figure 5. Clustering of high-wind event categories when comparing the local forcing indices with ocean mixing impact for individual events during the fall destratification seasons 2015–2021. (a) Cumulative cross-shelf Ekman forcing $\int_{t_{atm,1}}^{t_{atm,2}} \tau_x \, dt$ and stratification change $\Delta\sigma$. The linear trend is a least-squares fit applied to all data shown, while some extreme events are outside the presented axis intervals. (b) Leading-order forcing characteristics, including the mean wind direction $\overline{\phi}$ (polar angle of wind origin) and its circular standard deviation σ_ϕ (radial axis); the steadier an event's wind direction, the further it is away from the origin.

standard deviation σ_ϕ (see Equation 1 in Yamartino (1984)). A small standard deviation represents steady winds throughout the event. Following a two-dimensional Ekman theory argument for the coastal ocean, down-front winds (with the coast to the right on the Northern hemisphere) will likely cause a downwelling-favorable ocean response. The water transport across the surface Ekman layer will be onshore, causing an opposite flow in the interior to conserve mass which results in downwelling at the coastal boundary. Up-front winds will cause the opposite response. Downwelling-favorable (i.e., westward down-front winds) tend to destratify the shelf by advecting denser slope water onshore at the surface and/or steepening the shelfbreak front, potentially leading to frontal instability and additional shelfbreak exchange (Lentz et al., 2003). The onshore Ekman transport

$$V_{Ek} = -\frac{1}{\rho_0 f_0}\tau_x \tag{2}$$

solely depends on the along-shelf surface windstress component τ_x. Since the SNES shelfbreak is nearly aligned with the zonal East-West axis, no coordinate system rotation is required. From Equation 2, the cumulative (or integrated) zonal surface windstress across an event $\int_{t_{atm,1}}^{t_{atm,2}} \tau_x \, dt$ can act as a first-order estimate for the cross-shelf Ekman forcing strength.

Following the first-order Ekman theory argument outlined above, the cumulative zonal windstress throughout an event is correlated positively with the associated change in stratification (Figure 5a). The observations replicate the trend observed by Forsyth et al. (2018) in their realistic model study further inshore on the New Jersey shelf (at the 55 m isobath). Downwelling-favorable high-wind events ($\int \tau_x \, dt < 0$) are associated with destratification ($\Delta\sigma < 0$) and vice versa with a Pearson correlation coefficient of $r = 0.47$. The linear trend is statistically different from zero on a 99% confidence interval. For the statistical analysis, events have been treated as independent, which is reasonable since temporal relationships between events are not preserved. Nonetheless, the spread between Ekman forcing and ocean response remains large, particularly for positive cumulative Ekman forcing and when treating all high-wind events alike.

The results from the categorization scheme provide additional information about the individual events, and the categories tend to cluster across the forcing and ocean mixing impact indices. Thus, the categorization allows to further distinguish between distinct forcing patterns and their influence on stratification (Figure 5). Both, Canadian Highs and Cyclones South cause downwelling-favorable winds on the SNES and are consistently associated with destratification. Cyclones South are associated with the strongest destratification per event across all categories. However, their respective clusters differ considerably in their spread. Canadian Highs cluster closely and show

comparatively little variability in their forcing magnitude, wind direction, and steadiness. Similar forcing conditions coincide with relatively little spread in their associated ocean mixing impact. Arctic Lows/Sargasso Highs describe opposite local wind conditions since they are associated with fairly steady upwelling-favorable winds. However, these events are not consistently associated with restratification, potentially since local shear-driven destratification can overcome Ekman-driven restratification.

Cyclone clusters show large variability across all characteristics. Since the forcing metrics are purely based on local observations at a defined location, the distance and spatial relationship between a cyclone core and the CP Array contribute to the magnitudes of the established forcing indices. Cyclones take much less time than large-scale weather systems to pass across distances of the order of their horizontal length scale. In addition, their distance to the CP Array is more variable than for large-scale weather patterns. Combining these spatial properties likely adds to the enhanced variability in the local forcing characteristics and reduces the wind direction steadiness throughout the event. Locally rotating winds throughout the event duration strongly indicate the passage of Cyclones, and the rotation direction depicts whether the Cyclone passes north or south of the CP Array.

Since East-West dipole patterns have stronger wind components in the cross-shelf direction, only considering the along-shelf windstress component likely misses important aspects of the wind forcing. Thus, it is not surprising that East-West dipoles show the strongest deviation from the linear trend between cumulative along-shelf forcing and ocean mixing impact (Figure 5a). In accordance with first-order Ekman theory and previous studies (Forsyth et al., 2018; Lentz et al., 2003), the categories with a small along-shelf wind component are not associated with large shelf de- and restratification signals, reiterating that the along-shelf windstress is of first-order importance for predicting the wind-driven effects on coastal stratification.

6. Discussion

6.1. Intra-Seasonal Variability in Event Timing

The high-wind event categorization scheme is solely based on the event characteristics throughout the event, that is, each event is treated as an independent unit while its placement within the annual cycle and potential interaction with other events are not considered. Since the end of the destratification season fluctuates considerably between years (see Table 2), the timing of high-wind events likely affects whether they contribute to the fall stratification breakdown or not. In general, a shift from more downwelling-favorable high-wind events early in the fall to more upwelling-favorable high-wind events later in the fall can be observed in most years (see Figure 3a for 2019). Grouping the high-wind events by category reveals that this observation is indeed caused by differences in the categories' intra-seasonal timing within the fall season (Figure 6).

Most high-wind event categories cluster on sub-seasonal timescales of roughly 1–2 month length and with sharp edges toward both ends of the distribution. Due to the intermittent nature of high-wind events, 7 years of observations are not sufficient to meaningfully determine statistical occurrence distributions. Cyclones South and Canadian Highs tend to occur early in the season, adding to their likelihood to appear in the destratification season. In contrast, East-West dipole patterns and cyclones that propagate further north across New England pick up in late fall/early winter after the stratification breakdown might have already occurred.

The temporal separation between Cyclones South and North can supposedly be traced back to differences in their track and origin. The manually determined fall season cyclone tracks (Figure 4) reveal that Cyclones South tend to be of Atlantic origin while Cyclones North are separable into two distinct storm tracks: A continental track crossing the Great Lakes and an East Appalachian track originating in the Gulf of Mexico or the Southern US. The ability to distinguish between cyclone tracks based on their passage with respect to the CP Array speaks to the continued relevance of the “40/70 benchmark” for weather forecasting, introduced in Section 2. The clear divide between a more downwelling-favorable early fall and a more upwelling-favorable late fall season likely assists the rapidness of the stratification breakdown on the SNES by mid-fall. The mean position of the three cyclone tracks for the fall seasons 2015–2021 (shown in Figure 1) are aligned with the clusters of common storm tracks over New England (Zielinski & Keim, 2003).

Shelf stratification decreases consistently throughout the destratification season, leaving weaker rest stratification for events to affect if they occur late in the season. Thus, the intraseasonal differences in timing between

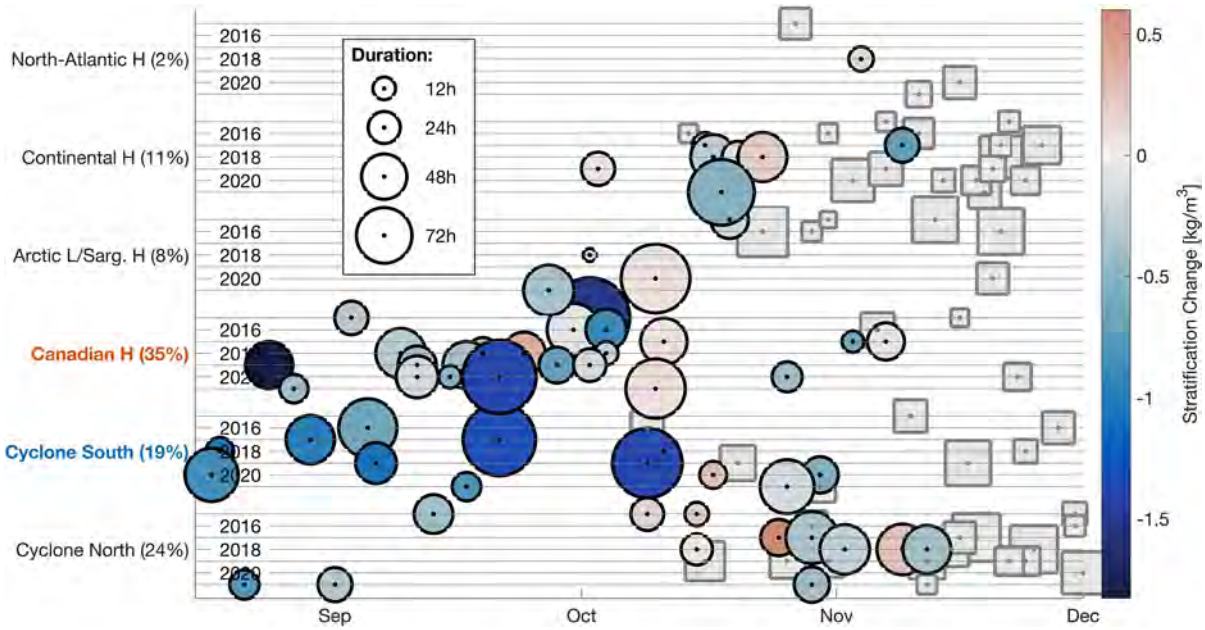

Figure 6. Timing of individual high-wind events within the fall destratification seasons 2015–2021. Events are grouped by category including their frequency of occurrence during the fall destratification season (in %). Both, the event duration (marker size) and the associated change in stratification (marker color) are shown. Events that occurred after the stratification breakdown for a given year (see Table 2) are shown as gray squares.

categories might lead to underestimating the ability of individual events late in the destratification season to impact the shelf stratification. However, this work aims to identify the most impactful high-wind weather patterns for the breakdown of seasonal stratification across the whole destratification season. Both, a high-wind event's timing and forcing are inherent characteristics of each high-wind event category, and both variables contribute to the overall seasonal impact of each category. Thus, disregarding the timing as a characteristic of interest would be unprofitable for the purpose of this work.

6.2. Seasonal Impact

So far, the characteristics of individual high-wind events and their category assignment have been the focus of analysis. A category's contribution to the fall stratification breakdown is given by combining ocean impact of individual events and the pattern's occurrence frequency and timing, that is, $\sum_{i=1}^{N_j} \Delta\sigma_{ij} = N_j \cdot \overline{\Delta\sigma_j}$ (Figure 7). Here, N_j is the number of events per season in the j-th category and $\overline{\Delta\sigma_j}$ the average stratification change per event in the particular season and category.

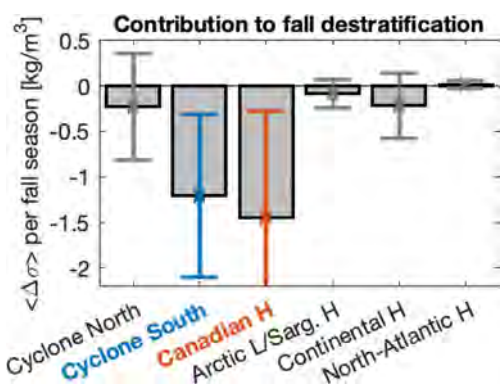

Figure 7. Cumulative contributions of individual high-wind event categories to the fall stratification breakdown. The error bars mark the 1σ-surrounding of interannual variability throughout 2015–2021.

Cyclones South and Canadian Highs are the most important for the fall stratification breakdown on the SNES. Events associated with these categories regularly occur early in the fall season (Figure 6) and individual events are consistently associated with destratification (Figure 5a). Even though Cyclones South, and in particular hurricanes, are associated with larger individual destratification signals, the continuous presence of multiple Canadian Highs every year makes this event category the number one contributor to the fall shelf destratification (Figure 7). Events from other high-wind event categories are occasionally associated with equally strong destratification signals; however, their intermittency and the variability in their impact results in less dominant contributions to the average seasonal destratification.

The interannual variability of a category's cumulative contribution to destratification is large due to the strong differences in a category's occurrence between years and the forcing and impact variability of individual events. On

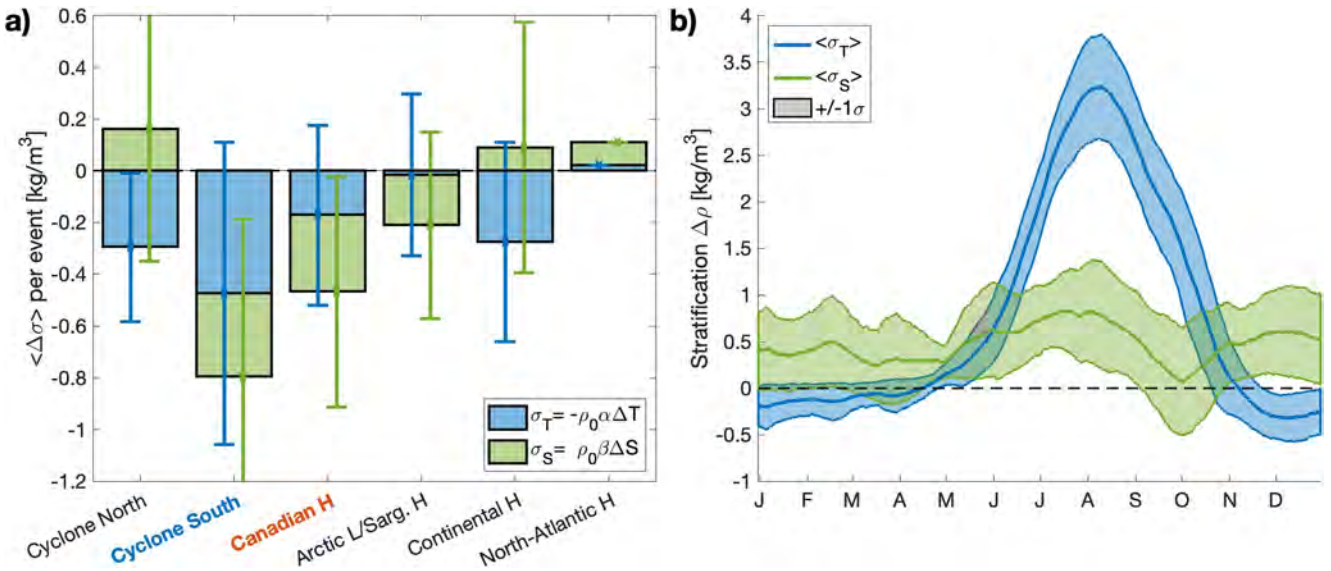

Figure 8. Temperature-(T) and salinity-(S) contributions to stratification on the Southern New England shelf by linearizing the equation of state. (a) T/S-contributions to the fall stratification breakdown from individual events, split by category. (b) T/S-contributions to the annual cycle of shelf stratification. The error bars and envelope mark the 1σ-surrounding of variability.

a year-to-year basis signals can be hidden. Thus, long multi-year time series as provided by the CP Array are vital for investigating the ocean impact from highly variable atmospheric forcing.

6.3. Temperature- and Salinity-Contributions to Stratification Change

High-wind forcing can lead to mixing and destratification on the continental shelf through a variety of processes, and the forcing characteristics determine the relative importance between such mixing processes. The events associated within each high-wind event category, identified based on their spatial SLP patterns, have similar forcing characteristics on the continental shelf (see Figures 4 and 5). Thus, similar mixing processes should be present within a category.

Watermasses can be characterized through temperature (T) and salinity (S), which in turn control density and ultimately stratification via the equation of state (EOS). Thus, distinguishing between T- and S-contributions to the observed stratification changes may allow further insight as to the destratification processes at play. Shelf temperature and salinity can be altered by surface heat- and freshwater-fluxes, respectively, advection, entrainment across the pyncocline, and mixing. By linearizing the EOS and proceeding analogous to Equation 1, the T- and S-contributions to stratification can be estimated as

$$\sigma_T \equiv \Delta\rho_T = -\rho_0\alpha_T\Delta T = -\rho_0\alpha_T[T(z=67\,\mathrm{m}) - T(z=0\,\mathrm{m})]$$

$$\sigma_S \equiv \Delta\rho_S = \rho_0\beta_S\Delta S = \rho_0\beta_S[S(z=67\,\mathrm{m}) - S(z=0\,\mathrm{m})]$$

with the thermal expansion coefficient $\alpha_T(T, S, p) \approx 1.6 \times 10^{-4}$ K^{-1}, the haline contraction coefficient $\beta_S(T, S, p) \approx 7.6 \times 10^{-4}$ PSU^{-1}, and an average reference density $\rho_0 = 1025.8$ kg m^{-3}. If the shelf heats up, cools, gains salt, and/or freshens non-uniformly across the water column, stratification will change. The net change in T- and S-stratification associated with an individual high-wind event $\Delta\sigma_T$ and $\Delta\sigma_S$ is defined as the difference in stratification throughout the event (analog to Section 2.3).

The different high-wind event categories are associated with different relative T- and S-contributions (Figure 8a); although the variability across events regularly exceeds the mean signal when distinguishing between temperature and salinity contributions to the observed stratification change. Though, most categories are associated with net destratification on average, seasonal restratification in T and/or S occurs in individual years. Cyclones South and Canadian Highs are the only high-wind event categories that are consistently associated with destratification within the one-sigma surrounding. Note the different y-axes between Figures 7 and 8a. While the former shows

the categories' cumulative impact on stratification per season, Figure 8a focuses on the mean and variability of individual events.

The composition of shelf stratification changes rapidly throughout the destratification season (Figure 8b). Thus, the initial stratification conditions on the shelf, preceding a high-wind event, likely affect *T*- and *S*-contributions to stratification changes. Caused by surface heating during spring and summer, the seasonal stratification is mostly driven by temperature and the seasonal pycnocline typically coincides with the seasonal thermocline (Li et al., 2015). At the end of October, the water column becomes fully temperature-homogenized, and the temperature gradient even reverses with cooler surface temperatures due to surface cooling. Thus, *T*-destratification becomes less likely for event categories that tend to occur late in the destratification season. In contrast, the *S*-stratification stays comparatively constant throughout the year since deeper shelf water stays slightly saltier than the surface layer water. However, interannual variability is higher than for temperature, potentially since salinity anomalies are more persistent than temperature anomalies.

Cyclones North, Arctic Lows/Sargasso Highs, and the East-West Dipole patterns cluster later in the destratification season, and *S*-driven stratification changes are present irrespective of their associated wind directions. In contrast, cyclones that pass south of the continental shelf and Canadian Highs occur early in the season. Nonetheless, they are associated with opposite *T*/*S*-signatures of stratification change. The dominance of *S*-destratification for Canadian Highs exceeds that of any other category. Since timing differences between the two categories are small, differences in the underlying mixing dynamics are likely responsible for the difference.

6.4. Attribution to Dynamical Processes

Opposite temperature-(*T*) and salinity-(*S*) contributions to stratification changes may act as fingerprints of different destratification processes. Since the dynamics of the ocean response depends on the high-wind forcing, the observed *T*/*S*-fingerprints in the ocean impact should coincide with differences in the forcing characteristics across categories. Even though both Cyclones South and Canadian Highs cause downwelling-favorable winds, Canadian Highs are associated with more steady winds throughout the event. In the following, we utilize two simplified scalar forcing metrics $\int_{t_{atm,1}}^{t_{atm,2}} |U|^3 \, dt$ and $\int_{t_{atm,1}}^{t_{atm,2}} \tau_x \, dt$ to distinguish between mixing contributions from local one-dimensional (1D) turbulent kinetic energy (TKE) input into the ocean and two-dimensional (2D) Ekman-driven cross-shelf advection, respectively. Here, U is the near-surface wind speed and τ_x is the along-shelf surface windstress.

The integrated $|U|^3$ throughout a high-wind event represents a simplified estimate for the one-dimensional (1D) mixing potential. In a horizontally isotropic ocean, the impact of surface forcing on stratification has been modeled by 1D mixed-layer theory. Surface windstress causes shear in the surface boundary layer, leading to instability, mixing, and entrainment of interior water into the mixed-layer (Price et al., 1986). As a result, the seasonal pycnocline deepens and weakens. As long as ocean currents are negligibly small compared to the high-wind forcing, impacts are identical irrespective of a category's wind direction. The production of TKE from windstress shear $P = -\overline{u'w'}\frac{\partial U}{\partial z} \approx \rho_0^{-1}\tau_x \cdot \frac{\partial U}{\partial z}$ with the horizontal $u = U + u'$ and vertical $w = W + w'$ wind velocity (mean and fluctuation, respectively) is to first-order proportional to $P \sim |U|^3$ (Niiler & Kraus, 1977). Assuming an Osborn-relationship between the eddy diffusivity K_v and the dissipation ϵ (Osborn, 1980) and neglecting buoyancy and transport terms in the TKE-budget, that is, $P = \epsilon$, the vertical eddy diffusion term from shear-induced mixing scales as well with $|U|^3$:

$$\mathcal{O}\left(K_v \frac{\partial^2 \rho}{\partial z^2}\right) = \mathcal{O}\left(\Gamma \frac{\epsilon}{N^2} \cdot \frac{\partial^2 \rho}{\partial z^2}\right) \overset{P \approx \epsilon}{\downarrow} \approx \Gamma \cdot \frac{\overbrace{\rho_0^{-1}\tau_x \cdot \frac{|U|}{H}}^{\mathcal{O}(P)}}{\underbrace{\frac{g}{\rho_0}\frac{\Delta\rho}{H}}_{\mathcal{O}(N^2)}} \cdot \frac{\Delta\rho}{H^2} = \frac{\Gamma C_D \rho_a}{gH^2} \cdot |U|^3 \tag{3}$$

with the mixing efficiency Γ, the drag coefficient of wind C_D, air density ρ_a, and vertical length scale H of the pycnocline width and mixed-layer depth (~20 m). In the last step, a bulk formula for the surface windstress $\tau_x = \rho_a C_D U^2$ with $C_D \approx const$ was applied.

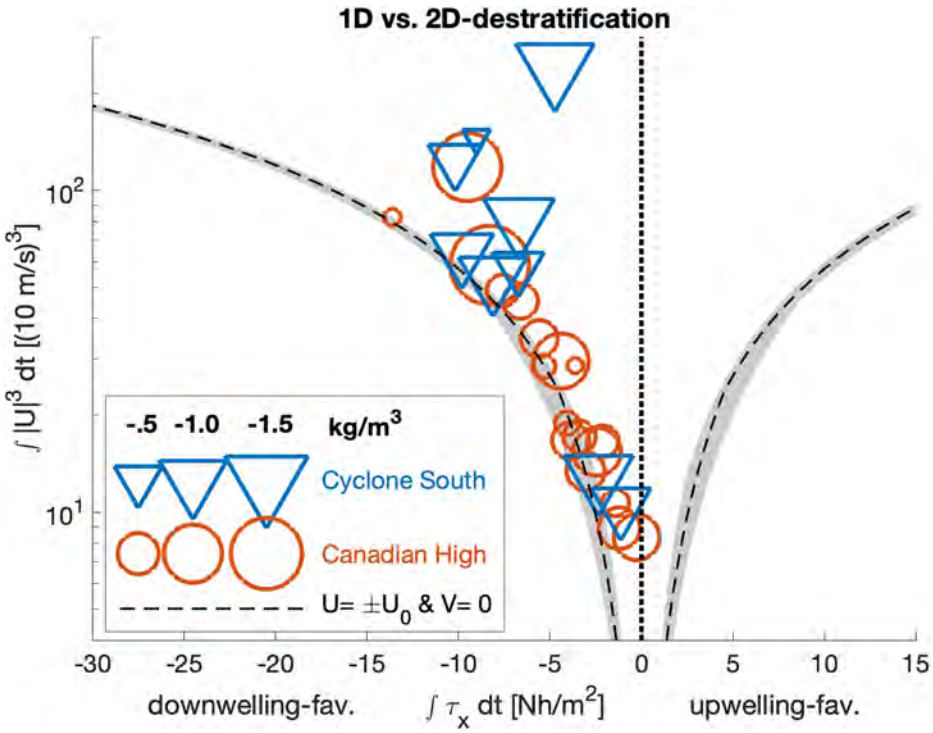

Figure 9. Clustering of Cyclones South and Canadian Highs based on their wind forcing. *Y*-axis: 1D mixing potential $\int_{atm,1}^{atm,2} |U|^3 dt$. *X*-axis: Cross-frontal Ekman forcing, that is, cumulative zonal surface windstress $\int_{atm,1}^{atm,2} \tau_x dt$. A fully zonal and steady wind event of average duration would lead to values on the two dashed branches while the gray shading covers the one-sigma envelope of the distribution of high-wind event duration. Marker size depicts the associated destratification strength.

The SNES coastline and shelfbreak challenge the 1D mixed-layer theory's isotropy assumption. Two-dimensional (2D) Ekman theory applied to the coastal ocean is consistent with observations of de- and restratification based on the wind directionality as shown in Section 5. The cross-shelf Ekman transport is proportional to the along-shelf surface windstress τ_x and given in Equation 2. Thus, $|U|^3$ and τ_x are two wind forcing variables that are representative of two different ocean response mechanisms: 1D mixing from shear and 2D advection across the shelfbreak, respectively. While τ_x is strictly restricted to the along-shelf wind component and aligned with the assumption of a 2D shelfbreak framework, $|U|^3$ does not discriminate between any wind direction and includes the full wind.

While Cyclones South and Canadian Highs are both associated with downwelling-favorable mean winds, differences in their wind direction steadiness and typical wind speeds lead to deviations between the wind forcing estimates associated with 1D- and 2D-driven destratification (Figure 9). The strongest winds on the SNES are caused by a subset of Cyclones South, leading to the largest 1D mixing potential estimates $\int_{t_{atm,1}}^{t_{atm,2}} |U|^3 dt$ from local shear production and the largest destratification signals per individual event (Figure 8a). However, since the cyclones cause comparatively unsteady rotating winds on the SNES, their cross-shelf Ekman forcing estimate $\int_{t_{atm,1}}^{t_{atm,2}} \tau_x dt$ does not exceed that of the Canadian Highs despite their elevated local wind forcing. In contrast, the Canadian Highs show little variability in their wind direction (Figure 5b); thus they tend to line up with the branch representing steady downwelling-favorable zonal wind forcing. This bathymetry-wind interaction and anticipated setup of a cross-shelf Ekman cell results in comparable destratification magnitudes between Cyclones South and strong Canadian Highs (Figure 5a) despite the Canadian Highs' smaller overall wind speeds and energy input into the ocean.

Relating the wind forcing estimates associated with 1D- and 2D-driven destratification to the shelf/slope hydrography, the two estimates should be associated with opposite *T*/*S*-fingerprints in the stratification changes from high-wind events. While isotropic mixed-layer theory describes how the 1D mixing potential from shear production is associated with enhanced surface cooling and entrainment of interior winter-cooled cold pool water into the summer-heated mixed-layer, the 2D Ekman forcing causes advection across the shelfbreak. Thus,

downwelling-favorable wind forcing causes a surface-intensified onshore advection of salty slope water onto the shelf while cross-shelf temperature gradients throughout the summer mixed-layer are relatively weak.

Applying the *T*/*S*-fingerprint concept to the observational record, the spatial clustering of Cyclones South and Canadian Highs in wind forcing space (Figure 9) aligns well with the differences in *T*/*S*-contributions to stratification changes (Figure 8a): The 1D mixing potential magnitudes are the strongest for Cyclones South that are associated with *T*-driven destratification while 2D Ekman advection is expected to lead to *S*-driven destratification. Canadian Highs show such a forcing and ocean response behavior. Further analysis of the velocity fields and cross-shelf gradients would be required to allow a direct comparison between contributions from the two forcing processes in a 2D cross-shelf framework. Unresolved 3D processes from along-shelf gradients and frontal oscillations/instabilities continue to add to the variability.

6.5. Frontal Pre-Conditioning

Fingerprints of different forcing processes in the shelf stratification signal have been motivated theoretically and rely on spatial gradients. For example, the simple 2D Ekman-argument to explain the shelf stratification's sensitivity to steady downwelling-favorable winds, and the influx of high-salinity offshore water relies on cross-frontal density gradients across the shelfbreak. The shelfbreak front south of New England consistently separates cooler and fresher continental shelf water from warmer and saltier Slope Sea water, leading to the strongest horizontal density gradients in the region. However, these gradients have not yet been considered despite the CP Array's proximity to the front. In the climatological mean, the frontal jet core is at the 200 m-isobath (Linder & Gawarkiewicz, 1998), while the CP Array's inshore moorings measure around the 95 m-isobath. The shelfbreak front is inherently unstable (e.g., Flagg and Beardsley, 1978; Gawarkiewicz & Chapman, 1991; Lozier et al., 2002), leading to ubiquitous meandering and frontal eddies on top of an annual cycle of varying frontal strength.

Frontal pre-conditioning describes the hypothesis that the physical state of the shelfbreak front preceding a high-wind forcing event affects the wind-driven shelf mixing and needs to be included to quantitatively assess the contribution of different forcing processes to destratification. Variability in the frontal state likely adds to the spread observed when comparing the wind forcing with an event's impact on stratification (Figure 5a). The data record reveals that large stratification changes are regularly associated with rapid changes in temperature and salinity across the water column (not shown). Since the magnitudes of typical surface buoyancy forces are insufficient to explain such observations, onshore advection of the shelfbreak front across the mooring position likely causes these anomalies. Various wind-driven cross-frontal exchange processes have been identified (Gawarkiewicz et al., 1996; Houghton et al., 1988; Mahadevan et al., 2010), and the CP Array is well designed to assess frontal pre-conditioning and shelfbreak exchange events in the future.

7. Conclusion

Atmospheric high-wind forcing events and their impact on ocean stratification on the Southern New England Shelf (SNES) have been investigated to identify which high-wind event patterns contribute most to the rapid breakdown of stratification during the fall. The multi-year data record from the OOI Coastal Pioneer Array allowed to assess the interannual variability of the fall stratification breakdown for the first time using observations. The variability in the timing of the stratification breakdown is large (±15 days) and depends on both the number and distribution of high-wind events across the season and the individual forcing characteristics.

A high-wind categorization scheme has been developed to group weather events into six categories based on their spatio-temporal sea-level pressure signal and locally observed wind field on the SNES. Mean composites capture the distinct forcing characteristics inherent in each category. Two event categories are particularly impactful for the seasonal stratification breakdown: Cyclones that pass south of the SNES (*Cyclones South*) and high-pressure systems over East Canada (*Canadian Highs*) tend to occur during early fall and are associated with downwelling-favorable winds on the SNES. This result is in good accordance with Ekman theory for the coastal ocean (Gill, 1982) and provides an observation-based measure of interannual variability for the first time.

Cyclones are the most ubiquitous high-wind event pattern in the extratropics. However, cyclones noticeably deviate from the idealized Ekman theory case since local wind vectors tend to continuously rotate throughout a cyclone's

passage. As a result, their Ekman cross-shelf circulation cell should be less pronounced than for the steady Canadian Highs. The Canadian Highs establish a real-life representation of the idealized downwelling-favorable Ekman-forcing case on the SNES since the wind forcing is relatively steady throughout the event. Thus, while the strong wind speeds associated with Cyclones South have notable impact on local vertical mixing, Canadian Highs produce a similarly strong ocean response with weaker, steadier winds. In addition, their ocean response more likely extends the high-wind forcing duration due to enhanced horizontal advection, post-event restratification, and frontal relaxation.

Differences in mixing processes associated with Cyclones and Canadian Highs are suggested by the opposite temperature-(T) and salinity-(S) contributions to the wind-driven shelf destratification. Cyclones South are associated with larger T-destratification, likely due to their intense wind speeds leading to enhanced local mixing, cold pool water entrainment, and turbulent surface cooling. In contrast, Canadian Highs are weaker; however, their secondary Ekman circulation in the cross-shelf direction causes enhanced S-destratification. Frontal pre-conditioning by the nearby shelfbreak front likely adds to the observed variability in wind-driven ocean impact and should be included to quantify the contribution of cross-shelf exchange processes to destratification on the shelf.

The high-wind event categorization scheme has shifted the focus from solely interpreting local wind forcing on the continental shelf to studying the ocean impacts of realistic spatio-temporal atmospheric weather patterns. Since local conditions are the product of large-scale weather systems potentially affected by climate change, the categorization results are a first step toward exploring how climate change trends may affect the atmospheric ocean-forcing and contribute to the immense environmental pressure on the New England ecosystem (Pinsky et al., 2013). For example, it is well established that enhanced polar jet stream variability leads to more persistent weather patterns in the mid-latitudes (Francis & Vavrus, 2012), and Chen et al. (2014) have established the impacts of jetstream anomalies on the SNES and beyond.

Data Availability Statement

The data set of identified high-wind events, their impact on shelf stratification, and their corresponding high-wind event category, as well as the associated code to reproduce the figures is available at https://doi.org/10.5281/zenodo.8079891. This work heavily relies on gridded bulk meteorology and hydrography data observed by the OOI Coastal Pioneer Array which is available at https://doi.org/10.26025/1912/66379 (Taenzer et al., 2023). Unprocessed OOI data is publicly available through multiple pathways, for example, through the OOI Data Explorer ERDDAP server erddap.dataexplorer.oceanobservatories.org (NSF Ocean Observatories Initiative, 2022). ERA5 hourly data on single levels was downloaded from the Copernicus Climate Change Service (C3S) Climate Data Store (https://doi.org/10.24381/cds.adbb2d47) and been used to gain spatio-temporal information on high-wind event patterns (Hersbach et al., 2018). Registration is required for download. The mean Gulf Stream position was estimated from Monthly Climatology maps of Mean Absolute Dynamic Topography (MADT-H) for 1993-2020, a global gridded (1/4° x 1/4°) Ssalto/Duacs data product distributed in delayed time by AVISO+. Data is available through multiple gateways upon registration, for example, through the Thredds data server (AVISO+, 2022). Thermodynamic properties of seawater have been determined by using the Gibbs-SeaWater (GSW) Oceanographic Toolbox (McDougall & Barker, 2011), Version 3.06.12, available at teos-10.org/software.htm.

Acknowledgments
We are grateful for financial support from the German Federal Ministry for Economic Affairs and Climate Action's ERP scholarship fund (LL), Grants N00014-21-1-2559 and N00014-19-1-2646 from the Office of Naval Research (GG), and the Scripps Chair for Excellence in Oceanography (AP). We thank Paula Fratantoni for enriching discussions during the early phase of the project. Paula Fratantoni and Svenja Ryan provided valuable comments on the manuscript. Two anonymous reviewers have helped improving the manuscript. Observations are provided by the OOI, which is a major facility fully funded by the National Science Foundation under Cooperative Agreement No. 1743430. The results contain modified Copernicus Climate Change Service information, 2022. The Ssalto/Duacs altimeter products were produced and distributed by the Copernicus Marine and Environment Monitoring Service (CMEMS) (http://www.marine.copernicus.eu).

References

AVISO+. (2022). Ssalto/Duacs gridded Mean Absolute Dynamic Topography (MADT-H) Monthly Climatology product (1993–2020) [Dataset]. Thredds Data Server. Retrieved from tds.aviso.altimetry.fr/thredds/catalog/dataset-duacs-climatology-global/delayed-time/monthly_clim/madt_h/catalog.html

Beardsley, R., Boicourt, W., & Hansen, D. (1976). Middle Atlantic continental shelf and New York Bight. In M. Cross (Ed.), *Special symposia* (Vol. 2, pp. 20–34). American Society of Limnology and Oceanography.

Boccaletti, G., Ferrari, R., & Fox-Kemper, B. (2007). Mixed layer instabilities and restratification. *Journal of Physical Oceanography*, *37*(9), 2228–2250. https://doi.org/10.1175/JPO3101.1

Chen, K., Gawarkiewicz, G., Lentz, S. J., & Bane, J. M. (2014). Diagnosing the warming of the Northeastern U.S. Coastal Ocean in 2012: A linkage between the atmospheric jet stream variability and ocean response. *Journal of Geophysical Research: Oceans*, *119*(1), 218–227. https://doi.org/10.1002/2013JC009393

Edson, J. B., Jampana, V., Weller, R. A., Bigorre, S. P., Plueddemann, A. J., Fairall, C. W., et al. (2013). On the exchange of momentum over the open ocean. *Journal of Physical Oceanography*, *43*(8), 1589–1610. https://doi.org/10.1175/JPO-D-12-0173.1

Flagg, C. N., & Beardsley, R. C. (1978). On the stability of the shelf water/slope water front south of New England. *Journal of Geophysical Research*, *83*(C9), 4623–4631. https://doi.org/10.1029/JC083iC09p04623

Forsyth, J., Gawarkiewicz, G., Andres, M., & Chen, K. (2018). The interannual variability of the breakdown of fall stratification on the New Jersey shelf. *Journal of Geophysical Research: Oceans*, *123*(9), 6503–6520. https://doi.org/10.1029/2018JC014049

Foukal, N. P., Pickart, R. S., Moore, G. W. K., & Lin, P. (2019). Shelfbreak downwelling in the Alaskan Beaufort Sea. *Journal of Geophysical Research: Oceans*, *124*(10), 7201–7225. https://doi.org/10.1029/2019JC015520

Francis, J. A., & Vavrus, S. J. (2012). Evidence linking Arctic amplification to extreme weather in mid-latitudes. *Geophysical Research Letters*, *39*(6), L06801. https://doi.org/10.1029/2012GL051000

Gawarkiewicz, G., & Chapman, D. C. (1991). Formation and maintenance of shelfbreak fronts in an unstratified flow. *Journal of Physical Oceanography*, *21*(8), 1225–1239. https://doi.org/10.1175/1520-0485(1991)021〈1225:FAMOSF〉2.0.CO;2

Gawarkiewicz, G., Linder, C. A., Lynch, J. F., Newhall, A. E., & Bisagni, J. J. (1996). A surface-trapped intrusion of slope water onto the continental shelf in the Mid-Atlantic Bight. *Geophysical Research Letters*, *23*(25), 3763–3766. https://doi.org/10.1029/96GL03427

Gawarkiewicz, G., & Plueddemann, A. (2020). Scientific rationale and conceptual design of a process-oriented shelfbreak observatory: The OOI Pioneer Array. *Journal of Operational Oceanography*, *13*(1), 19–36. https://doi.org/10.1080/1755876X.2019.1679609

Gill, A. (1982). Atmosphere-ocean dynamics. In *International geophysics series* (Vol. 30). Academic Press.

Hersbach, H., Bell, B., Berrisford, P., Biavati, G., Horányi, A., Muñoz Sabater, J., et al. (2018). ERA5 hourly data on single levels from 1959 to present. *Copernicus Climate Change Service (C3S) Climate Data Store (CDS)*. https://doi.org/10.24381/cds.adbb2d47

Houghton, R., Aikman, F., & Ou, H. (1988). Shelf-slope frontal structure and cross-shelf exchange at the New England shelf-break. *Continental Shelf Research*, *8*(5), 687–710. https://doi.org/10.1016/0278-4343(88)90072-6

Lentz, S., Shearman, K., Anderson, S., Plueddemann, A., & Edson, J. (2003). Evolution of stratification over the New England shelf during the Coastal Mixing and Optics study, August 1996–June 1997. *Journal of Geophysical Research*, *108*(C1), 3008. https://doi.org/10.1029/2001JC001121

Li, Y., Fratantoni, P. S., Chen, C., Hare, J. A., Sun, Y., Beardsley, R. C., & Ji, R. (2015). Spatio-temporal patterns of stratification on the Northwest Atlantic shelf. *Progress in Oceanography*, *134*, 123–137. https://doi.org/10.1016/j.pocean.2015.01.003

Linder, C. A., & Gawarkiewicz, G. (1998). A climatology of the shelfbreak front in the Middle Atlantic Bight. *Journal of Geophysical Research*, *103*(C9), 18405–18423. https://doi.org/10.1029/98JC01438

Lozier, M. S., Reed, M. S. C., & Gawarkiewicz, G. (2002). Instability of a shelfbreak front. *Journal of Physical Oceanography*, *32*(3), 924–944. https://doi.org/10.1175/1520-0485(2002)032〈0924:IOASF〉2.0.CO;2

Mahadevan, A., Tandon, A., & Ferrari, R. (2010). Rapid changes in mixed layer stratification driven by submesoscale instabilities and winds. *Journal of Geophysical Research*, *115*(C3), C03017. https://doi.org/10.1029/2008JC005203

McDougall, T. J., & Barker, P. M. (2011). *Getting started with TEOS-10 and the Gibbs Seawater (GSW) Oceanographic Toolbox* (p. 28). SCOR/IAPSO WG127. ISBN 978-0-646-55621-5.

Neu, U., Akperov, M. G., Bellenbaum, N., Benestad, R., Blender, R., Caballero, R., et al. (2013). IMILAST: A community effort to intercompare extratropical cyclone detection and tracking algorithms. *Bulletin of the American Meteorological Society*, *94*(4), 529–547. https://doi.org/10.1175/BAMS-D-11-00154.1

Niiler, P., & Kraus, E. (1977). One-dimensional models of the upper ocean. In E. B. Kraus (Ed.), *Modelling and prediction of the upper layers of the ocean* (pp. 143–172). Pergamon.

NSF Ocean Observatories Initiative. (2022). Bulk Meteorology Instrument Package (METBK) and CTD (cp03issm-sbd11-06-metbka000, cp01cnsm-sbd11-06-metbka000, cp01cnsm-sbd12-06-metbka000, cp04ossm-sbd11-06-metbka000, cp03issm-rid27-03-ctdbpc000, cp02pmui-wfp01-03-ctdpfk000) data from Pioneer NES Array from 2015-05-09 to 2022-06-01. [Dataset]. Data Explorer. Retrieved from ERDDAP. dataexplorer.oceanobservatories.org

O'Reilly, J., & Zetlin, C. (1998). *Seasonal, horizontal, and vertical distribution of phytoplankton chlorophyll a in the northeast U.S. continental shelf ecosystem*. (Tech. Rep.), NOAA Tech. Rep. NMFS 139. U.S. Department of Commerce.

Osborn, T. R. (1980). Estimates of the local rate of vertical diffusion from dissipation measurements. *Journal of Physical Oceanography*, *10*(1), 83–89. https://doi.org/10.1175/1520-0485(1980)010〈0083:EOTLRO〉2.0.CO;2

Pinsky, M. L., Worm, B., Fogarty, M. J., Sarmiento, J. L., & Levin, S. A. (2013). Marine taxa track local climate velocities. *Science*, *341*(6151), 1239–1242. https://doi.org/10.1126/science.1239352

Price, J. F., Weller, R. A., & Pinkel, R. (1986). Diurnal cycling: Observations and models of the upper ocean response to diurnal heating, cooling, and wind mixing. *Journal of Geophysical Research*, *91*(C7), 8411–8427. https://doi.org/10.1029/JC091iC07p08411

Roller, C. D., Qian, J.-H., Agel, L., Barlow, M., & Moron, V. (2016). Winter weather regimes in the Northeast United States. *Journal of Climate*, *29*(8), 2963–2980. https://doi.org/10.1175/JCLI-D-15-0274.1

Schofield, O., Chant, R., Cahill, B., Castelao, R., Gong, D., Kahl, A., et al. (2008). The decadal view of the mid-Atlantic bight from the COOLroom: Is our coastal system changing? *Oceanography*, *21*(4), 108–117. https://doi.org/10.5670/oceanog.2008.08

Taenzer, L. L., Gawarkiewicz, G., & Plueddemann, A. (2023). Gridded hydrography and bulk air-sea interactions observed by the Ocean Observatory Initiative (OOI) Coastal Pioneer New England Shelf Mooring Array (2015-2022) [Dataset]. WHOAS Woods Hole Open Access Server. https://doi.org/10.26025/1912/66379

Tandon, A., & Garrett, C. (1994). Mixed layer restratification due to a horizontal density gradient. *Journal of Physical Oceanography*, *24*(6), 1419–1424. https://doi.org/10.1175/1520-0485(1994)024〈1419:MLRDTA〉2.0.CO;2

Xu, Y., Cahill, B., Wilkin, J., & Schofield, O. (2013). Role of wind in regulating phytoplankton blooms on the mid-Atlantic bight. *Continental Shelf Research*, *63*, S26–S35. (Coastal Ocean Observing System: Retrospective Reanalysis and Real-Time Forecasting). https://doi.org/10.1016/j.csr.2012.09.011

Yamartino, R. J. (1984). A comparison of several "Single-Pass" estimators of the standard deviation of wind direction. *Journal of Applied Meteorology and Climatology*, *23*(9), 1362–1366. https://doi.org/10.1175/1520-0450(1984)023〈1362:ACOSPE〉2.0.CO;2

Zielinski, G. A., & Keim, B. D. (2003). *New England weather, New England climate*. University Press of New England.

JGR Oceans

RESEARCH ARTICLE
10.1029/2024JC021270

Seasonal Salinification of the US Northeast Continental Shelf Cold Pool Driven by Imbalance Between Cross-Shelf Fluxes and Vertical Mixing

Lukas L. Taenzer[1,2], Ke Chen[2], Albert J. Plueddemann[2], and Glen G. Gawarkiewicz[2]

[1]Massachusetts Institute of Technology, Cambridge, MA, USA, [2]Woods Hole Oceanographic Institution, Woods Hole, MA, USA

Key Points:

- The US Northeast continental shelf cold pool erodes and salinifies with a mean rate of 0.18 PSU/month throughout the stratified season
- A salinity budget shows that the seasonal erosion is caused by cross-shelf transport from offshore, unopposed by vertical mixing
- Seasonal variability in the cross-shelf position of the US Northeast shelfbreak front is too small to explain the observed salinification

Supporting Information:

Supporting Information may be found in the online version of this article.

Correspondence to:

L. L. Taenzer,
lukas.taenzer@whoi.edu

Citation:

Taenzer, L. L., Chen, K., Plueddemann, A. J., & Gawarkiewicz, G. G. (2025). Seasonal salinification of the US Northeast continental shelf cold pool driven by imbalance between cross-shelf fluxes and vertical mixing. *Journal of Geophysical Research: Oceans*, *130*, e2024JC021270. https://doi.org/10.1029/2024JC021270

Received 27 APR 2024
Accepted 10 APR 2025

Author Contributions:

Conceptualization: Lukas L. Taenzer, Albert J. Plueddemann, Glen G. Gawarkiewicz
Data curation: Lukas L. Taenzer
Formal analysis: Lukas L. Taenzer
Funding acquisition: Glen G. Gawarkiewicz
Investigation: Lukas L. Taenzer
Methodology: Lukas L. Taenzer, Ke Chen
Project administration: Albert J. Plueddemann, Glen G. Gawarkiewicz
Resources: Ke Chen
Software: Lukas L. Taenzer
Supervision: Ke Chen, Albert J. Plueddemann, Glen G. Gawarkiewicz
Validation: Lukas L. Taenzer

Abstract The US Northeast continental shelf "cold pool" comprises winter-cooled Shelf Water that is trapped below the warm surface layer during the stratified season. The regional ecosystem relies on the preservation of winter temperatures within the cold pool throughout the year. Here, we present first evidence of a significant increase in the cold pool's salt content on the US Northeast continental shelf throughout the stratified season, suggesting that shelfbreak exchange contributes strongly to the seasonal erosion of the cold pool. Cold pool salinification rates of 0.18 PSU/month remain steady throughout the stratified season, leading to salinity differences of over 1 PSU between April and October. A cold-pool salinity budget reveals that the observed salinification is caused by an imbalance between cross-shelf salt fluxes, which deposit salt into the cold pool at all times of year, and the strong seasonal cycle of vertical mixing. During the stratified season, vertical mixing is inhibited and no longer counteracts the cross-shelf flux, leading to net salinification of the cold pool over the summer. Along-shelf freshwater advection from upstream is only present in the fall and contributes some additional freshening to shut down the salinification trend. Seasonal variability in the position of the US Northeast shelfbreak front is too small and out of phase to contribute to the salinity increase. The strong relationship between the seasonal cycle of cold pool modification and seasonal stratification points toward the importance of the timing of spring re- and fall de-stratification on near-bottom continental shelf temperature and salinity.

Plain Language Summary Near-bottom water on the US Northeast continental shelf—called the "cold pool"—preserves the cold temperatures from the previous winter and provides a sustained cold-water habitat during the warm summer season. However, ocean mooring observations from the OOI Coastal Pioneer Array show that the cold pool gets saltier by 0.18 PSU/month between April and October every year when the cold pool is trapped below a warm surface layer. We use salt as a tracer to investigate how much the influx of salty offshore water onto the continental shelf contributes to the observed erosion of the seasonal cold pool. Salt is brought from offshore and across the US Northeast shelfbreak front at all times of year, both by mean and fluctuating currents. During the summer, vertical mixing is inhibited by the warm surface layer, and the seasonal salinity increase is unopposed. In contrast, vertical mixing in the winter introduces fresher surface water to the cold pool and stops the salinity increase. Thus, the start/end of the seasonal changes in cold pool salinity coincide with the formation/breakdown of a warm summer surface layer above the cold pool, and surface conditions affect bottom conditions.

1. Introduction

The Middle Atlantic Bight (MAB) "cold pool" was first described by Bigelow (1933) as a bottom-trapped, and relatively homogeneous reservoir of winter-cooled continental shelf water that stretches across the mid-continental shelf from west of Nantucket Shoals to just north of Cape Hatteras. The cold pool forms in the spring with the development of a seasonal thermocline (Bigelow, 1933; Houghton et al., 1982), which inhibits interactions between the cold pool and the atmosphere. The breakdown of stratification in the fall fully erodes the cold pool and ventilates the bottom shelf waters (Lentz et al., 2003). At all times of year, the cold pool is bounded by the MAB shelfbreak front on its offshore side, which separates cool/fresh Shelf Water from warm/salty Slope Sea Water (Linder & Gawarkiewicz, 1998). Traditionally, all shelf waters within the 10°C-isothermal are categorized as Cold Pool Water, which is distinctly cooler than all surrounding water during the summer (Figures 1b and 1c). By preserving winter temperatures throughout the summer, the cold pool supports the

Visualization: Lukas L. Taenzer
Writing – original draft: Lukas L. Taenzer
Writing – review & editing: Lukas L. Taenzer, Ke Chen, Albert J. Plueddemann, Glen G. Gawarkiewicz

recruitment and settlement of species (Miller et al., 2016; Sullivan et al., 2005) and acts as a nutrient reservoir for the continental shelf (Marra et al., 1990).

The cold pool warms gradually throughout the stratified season, which sparked a number of investigations of whether such warming can be more attributed to along-shelf advection from upstream (Houghton et al., 1982), local vertical mixing (Lentz, 2017), local cross-shelfbreak mixing (Ketchum & Corwin, 1964), or a combination of these processes depending on the location along the MAB (Ou & Houghton, 1982). Z. Chen et al. (2018) affirm that advection strongly contributes to seasonal cold pool warming rates in a regional model study; however, the source and direction of such advective fluxes have not been specified. Ketchum and Corwin (1964) point out that salinity can be used as a tracer to evaluate how much of the seasonal cold pool warming resulted from mixing of warm high-salinity Slope Sea Water, the only source of high-salinity water in the region, across the shelfbreak front and onto the continental shelf. Figure 2 displays the temperature-salinity characteristics across the US Northeast shelfbreak front, as observed by moorings of the Ocean Observatories Initiative (OOI) Coastal Pioneer Array during peak summer stratification. Subsurface water across the shelfbreak shows strong correlation between temperature and salinity, which suggest that cold pool variability (called "erosion" if waters below 10°C vanish) affects both quantities similarly. In addition, salinity is the more conservative tracer compared to temperature since spatial salinity gradients across the MAB shelfbreak persist throughout the year. In contrast, the strong seasonal cycle of atmospheric surface heating/cooling can easily overwhelm other contributions to the shelf heat budget. Here, we apply salinity as a tracer of cold pool properties to differentiate between the relative flux contributions to the seasonal cold pool erosion. We focus on the northeastern edge of the cold pool on the US Northeast shelf just east of Nantucket Shoals, motivated by multi-year observations of the US Northeast shelfbreak by the OOI Coastal Pioneer Array between 2015 and 2022.

To identify the largest contributors to the seasonal cold pool erosion, a finite-volume water mass budget can differentiate between different flux contributions, particularly between along-shelf advection, cross-shelfbreak fluxes, and vertical mixing. Lentz (2010) provides a climatological depth-, space-, and time-averaged MAB continental shelf budget by aggregating observations across several decades. By treating the budget's control volume like a Lagrangian parcel advected westward along the MAB, the magnitude of an "eddy" salt flux across the roughly geostrophic shelfbreak front is inferred indirectly as the budget's residual. Houghton et al. (1988) assessed cross-shelfbreak eddy temperature fluxes $\langle v'T' \rangle$ directly, but without statistically significant results for most of the year. Nonetheless, it is well established that internal frontal instability of the US Northeast shelfbreak front (Flagg & Beardsley, 1978; Garvine et al., 1988) can lead to intermittent exchange across the front when meanders grow and become non-linear (Gawarkiewicz et al., 2004). For example, Lentz (2003) estimates that salinity-maximum intrusions, which bring Slope Water onto the shelf, on average lead to a 0.3 PSU salinity increase of the MAB Shelf Water throughout the summer. Interactions between the shelfbreak front and external forcing—Warm Core Rings spun off from the Gulf Stream (e.g., Joyce et al., 1992; Silver et al., 2023; Zhang & Gawarkiewicz, 2015a) and/or strong storm systems passing over the site (Todd, 2020)—can lead to particularly large cross-shelfbreak exchange fluxes. Each of these processes occurs on timescales between days and weeks while the cold pool erodes over the timescale of months, similar to the climatological shelfbreak mean circulation. Thus, instead of focusing on the individual impact by each of the described cross-shelfbreak exchange processes, this work uses an integrative approach to estimate the net effect of cross-shelfbreak transport by all of these transient processes on the cold pool evolution in a multi-year mean sense.

This paper provides first evidence for a seasonal salinification of the cold pool on the US Northeast continental shelf, as consistently observed in the multi-year mooring record of the OOI Coastal Pioneer Array (Section 3). By applying output from the representative realistic NESS model in the same region, a cold pool salinity budget quantifies the different salinity flux contributions that annually erode the cold pool during the stratified season: Along- and cross-shelf mean-advection, eddy-advection, and vertical mixing (Section 4). In addition, we rule out seasonal onshore movements of the shelfbreak front as the main contributor to the observed salinification (Section 5). In Section 6, we discuss the importance of the seasonal cycle of stratification for seasonal cold pool trends and the relation between eddy-covariance fluxes and shelfbreak exchange.

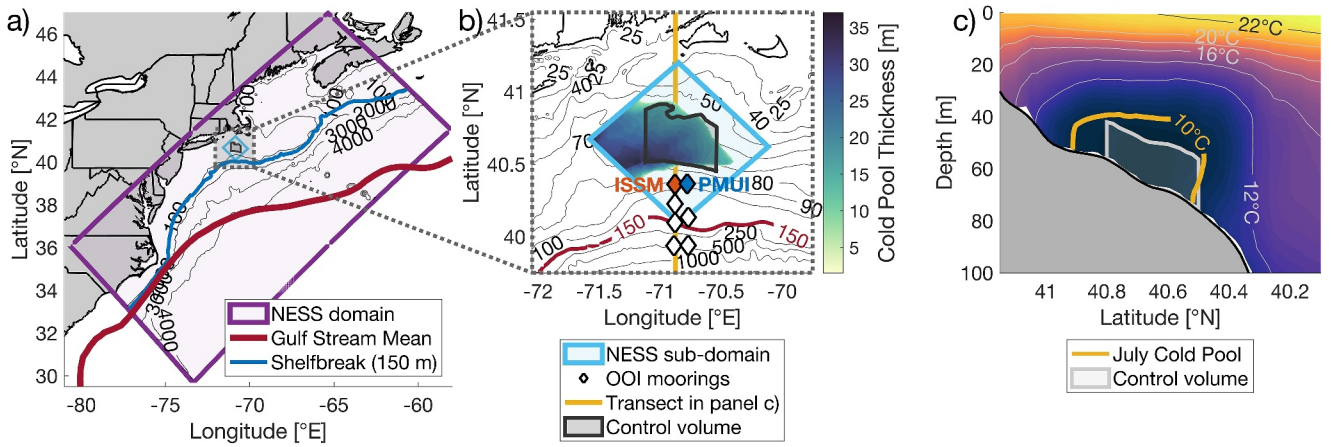

Figure 1. Map of the Middle Atlantic Bight (MAB) and Slope Sea, highlighting the data sources of this study: In situ observations come from the Ocean Observatories Initiative (OOI) Coastal Pioneer Array, supplemented with output from the realistic NorthEast Shelf and Slope (NESS) model. (a) Full NESS model domain (purple), mean Gulf Stream position (red), approximated by the 0.25 cm isoline of the absolute dynamic topography climatological mean from the "Archiving, Validation and Interpretation of Satellite Oceanographic" (AVISO, 2022) data archive, and location of the climatological MAB shelfbreak jet, which roughly follows the 150 m isobath (blue). (b) US Northeast continental shelf. The colorbar depicts the mean cold pool thickness during July within an NESS sub-domain (light-blue). Highlighted moorings are the Inshore Surface Mooring (ISSM) and Upstream Inshore Profiler Mooring (PMUI), which conjointly capture the hydrography on the outer continental shelf. The gray polygon displays the horizontal area of the cold pool control volume for the cold pool salinity budget, described in Section 2.3. (c) Meridional cross-section of the NESS cold pool edge (yellow) and control volume (gray) along 70.875°W during July.

2. Data and Methods

2.1. OOI Coastal Pioneer Data

The OOI Coastal Pioneer Array (henceforth "Pioneer Array") spans across the shelfbreak south of the US Northeast shelf, and the two most inshore moorings, the Inshore Surface Mooring (ISSM) and the Upstream Inshore Profiler Mooring (PMUI), represent the hydrography on the outer continental shelf (Gawarkiewicz & Plueddemann, 2020). While the ISSM provides hydrographic data at 2 m, 7 m, and two meters above the ocean floor, the PMUI captures the mid-depth water column with consistent data output between 28 − 67 m depth. Both moorings are located at the 95 m-isobath, and by combining data from both moorings, a full water column profile on the outer continental shelf can be estimated. For reference, the climatological shelfbreak jet follows the 150 m-isobath, and the foot of the shelfbreak front is roughly at the 100 m-isobath (Linder & Gawarkiewicz, 1998). Data are provided on an hourly grid between May 2015 and June 2022 with few gaps in between. The processing of Pioneer Array mooring data is described in more detail in Taenzer et al. (2023a). For the purpose of this study, time series data of ocean hydrography at 67 m is used to describe conditions of the US Northeast continental shelf cold pool. Data were 36 h-lowpass filtered to remove variability from dominant tidal frequencies and inertial oscillations (36 h $\approx 2 \cdot T_i = 2 \cdot 2\pi/f$ at 40° latitude). The Pioneer Array measures Practical Salinity, and units PSU will be used. While the Pioneer Array provides an unprecedented multi-year observational data set of the US Northeast shelfbreak, the observational data have several shortcomings with respect to the goal of this study: (a) Data coverage does not extend through the full water column, and (b) assets are restricted to the shelbreak, which prevents closure of a subsurface continental shelf budget. Thus, while the Pioneer Array observations motivate this study, model fields will be used to investigate the underlying dynamics of the observed cold pool salinification.

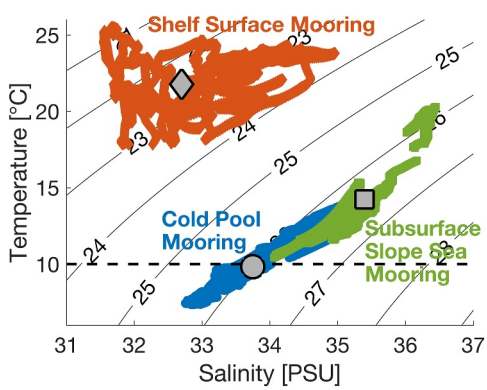

Figure 2. Water mass characteristics of the US Northeast cold pool and its surrounding water during July, observed by OOI Coastal Pioneer Moorings (2015–2022). Blue: Upstream Inshore Profiler Mooring at 67 m depth. Red: Inshore Surface Mooring. Green: Upstream Offshore Profiler at 67 m depth. Gray symbols depict the mean values in temperature and salinity for each mooring. Data were lowpass-filtered with a 1/36h lowpass frequency to avoid variability from the M2 barotropic tide. Water below 10°C is classified as Cold Pool Water.

2.2. New England Shelf and Slope (NESS) Model

Output from the high-resolution NorthEast Shelf and Slope (NESS) model is used to complement observations from the Pioneer Array and set up a cold

pool salinity budget on the US Northeast shelf south of New England. In contrast to data-assimilation efforts, the NESS model is a purely forward model and therefore reaches budget closure. The NESS model is based on the hydrostatic Regional Ocean Modeling System (ROMS) (Shchepetkin & McWilliams, 2005) and covers the MAB and Gulf of Maine on a 1 km grid (Figure 1a) in a bathymetry-following depth-coordinate system with 40 vertical layers. This study uses output from 2010 to 2017 during which the model was forced at the surface with the ECMWF ERA5 atmospheric reanalysis product (Hersbach et al., 2020) with a 3-hr temporal resolution. To capture fine-scale sea-surface temperature (SST) variations, a thermal correction was applied to adjust surface heat fluxes based on Multi-scale Ultra-high Resolution (MUR) SST data (Chin et al., 2017). Initial conditions and open ocean boundary forcing combine the mesoscale variability from an assimilative global ocean circulation model, Hybrid Coordinate Ocean Model (Chassignet et al., 2007) and Navy Coupled Ocean Data Assimilation (HYCOM/NCODA, GOFS3.0), and the monthly mean temperature/salinity Northwest Atlantic regional climatology from the National Center for Environmental Information (NCEI) on a $1/10°$ grid, using World Ocean Database (WOD) data (Seidov et al., 2016). This combination of data sources avoids coastal biases of the HYCOM-derived reanalysis product, while continuing to include realistic variability. Geostrophic velocities are inferred from the density-fields. In addition, the model includes freshwater runoff from nine major rivers and tidal forcing to capture coastal processes realistically. The model uses a 4th-order Akima scheme for advection and parameterizes vertical diffusion effects from sub-grid scale mixing via a GLS vertical mixing scheme (k-kl) (Warner et al., 2005). The NESS-model is the latest iteration of a realistic high-resolution regional forward model in use since 2010 (K. Chen & He, 2010). It was used to investigate interannual variability of MAB shelf conditions (K. Chen et al., 2016) and cross-shelfbreak exchange (K. Chen et al., 2022), which makes the model suitable for this study. The model's fidelity has been continuously assessed through comparison against observations, and the Supporting Information S1 provides a comparison between model output and Pioneer Array data. To minimize the potential for impact from the misalignment in data availability between the observations (2015–2022) and model (2010–2017), this study focuses on investigating the multi-year mean salinification of the US Northeast cold pool instead of its interannual variability. Since the NESS model advects Absolute Salinity, units g/kg will be used whenever describing modeled salinity output (in contrast to units PSU for in situ mooring data). More detailed information about the model setup can be found in K. Chen et al. (2022).

2.3. Cold Pool Salinity Budget

To determine the primary agent that causes the subsurface shelf salinification throughout the summer and explain the observations of seasonal cold pool erosion, we set up a cold pool salinity budget for the US Northeast shelf. Concretely, we investigate the net flux contributions to a control volume V north of the Pioneer Array on the US Northeast shelf. The cold pool control volume has been deliberately chosen to be within the conventionally defined Cold Pool Water ($T < 10°C$) at the time of peak stratification (Figures 1b and 1c). This choice ensures that this study focuses on hydrography changes within the cold pool core and avoids contaminating the budget by including processes that are restricted to the cold pool's boundaries.

Specifically, the control volume is confined to the lowest 8 model layers (roughly $15 - 20$ m above the ocean floor) and restricted by the 55 m and 75 m isobath in the North and South, respectively. Zonally, the control volume extends 20 km to the West and East of the Pioneer Array moorings ISSM and PMUI, respectively, resulting in a 50 km-wide sleeve. Despite the cold pool's continuity to the West, the control volume is limited zonally to ensure that the NESS model budget and observations from the Pioneer Array remain comparable. The chosen volume is 27 km^3, includes roughly 70,000 grid cells, and strives for a balance between increasing the signal-to-noise ratio by averaging across more grid cells and the necessity to restrict the budget to a region of persistent dynamics to allow meaningful interpretation of the results. Mean salinification rates remain robust when varying the control volume's extent zonally ($30 - 70$ km wide sleeve) or vertically (6–10 lowest model layers). When moving the control volume closer to the shelfbreak, mean salinity and temperature values increase but salinification rates remain unchanged.

Since the bathymetry-following shelfbreak jet is approximately in geostrophic balance, cross-shelf velocities tend to be significantly smaller than along-shelf velocities on the outer continental shelf. Thus, small variations in the angle between the local coordinate system and the mean flow orientation can significantly affect the magnitude and sign of the cross-jet velocity component (Brink, 2016). For this study, the cold pool budget's coordinate

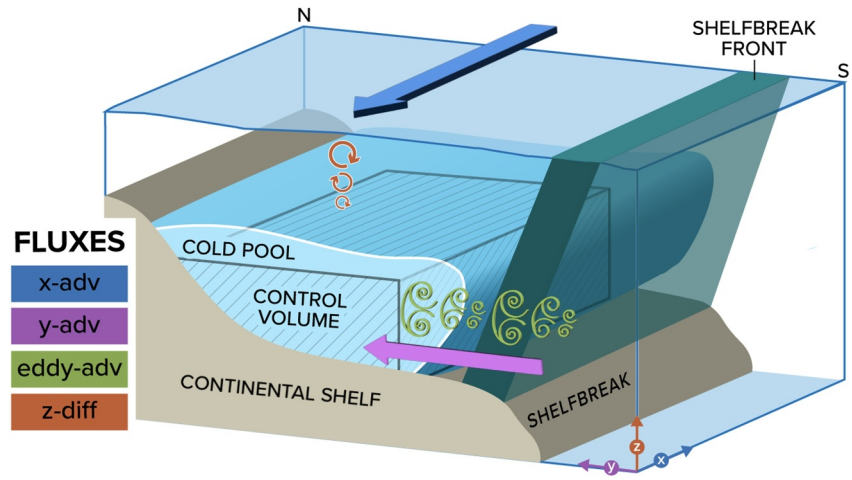

Figure 3. Sketch of the cold pool salinity budget on the US Northeast shelf with salinity fluxes in/out of the finite-volume cold pool control volume (gray streaked box). The budget distinguishes between the tendency/net term $\partial S/\partial t$ and multi-year mean fluxes of along-shelf (x) mean-advection $-\bar{u}\cdot\partial\bar{S}/\partial x$ (blue), cross-shelf (y) mean-advection $-\bar{v}\cdot\partial\bar{S}/\partial y$ (purple), eddy-advection $-\left(\nabla_h\cdot\langle\mathbf{u}_h'S'\rangle + w\cdot\partial S/\partial z\right)$ (green), and vertical (eddy) diffusion $\kappa_v\,\partial^2 S/\partial z^2$ (red). Horizontal diffusion is negligible (see Section 4). Illustration: Natalie Renier (WHOI).

system was rotated anti-clockwise by $\Delta\varphi = \arctan(\bar{v}/\bar{u}) = +10°$ with respect to the east/north-directions to successfully distinguish between geostrophic along-shelf and ageostrophic cross-shelf advection. Here,

$$(\bar{u},\bar{v}) = \int_{2010}^{2017}\left[\int_A\left(\int_{h(x,y)}^{0}(u,v)\,\mathrm{d}z\right)\mathrm{d}x\,\mathrm{d}y\right]\mathrm{d}t \tag{1}$$

are the time- and depth-averaged zonal $(\bar{u})$ and meridional $(\bar{v})$ velocity across the cold pool control volume area A, and h is the local ocean depth. Accordingly, cross-shelf fluxes into/out of the control volume are now perpendicular to the time- and depth-averaged mean flow. The correction angle $\Delta\varphi$ remains constant throughout the analysis.

Mean salinity changes across the cold pool control volume are driven by advective and diffusive fluxes. In the following cold pool salinity budget, we partition the different salinity flux contributions as follows (Figure 3):

$$\frac{1}{V}\int_V \underbrace{\frac{\partial S}{\partial t}}_{\text{rate}}\mathrm{d}V = \frac{1}{V}\int_V\Bigg[\overbrace{-\bar{u}\cdot\frac{\partial\bar{S}}{\partial x}-\bar{v}\cdot\frac{\partial\bar{S}}{\partial y}}^{\text{along-shelf }(x)/\text{cross-shelf }(y)\text{ mean-flux}} \underbrace{-\left(\nabla_h\cdot\langle\mathbf{u}_h'S'\rangle + w\cdot\frac{\partial S}{\partial z}\right)}_{\text{eddy-advection flux}} + \overbrace{\kappa_h\nabla_h^2 S}^{\text{horiz. diffusion}} + \underbrace{\kappa_v\frac{\partial^2 S}{\partial z^2}}_{\text{vert. diffusion}}\Bigg]\mathrm{d}V \tag{2}$$

The chosen budget partition distinguishes between three temporal/spatial scales to link budget terms to processes that act on these respective scales and identify the main contributors to the seasonal salinification signal: (a) Mean-advection fluxes driven by the climatological shelf- and shelfbreak velocity fields and salinity gradients (along-shelf (x)/cross-shelf (y) mean-flux). (b) Grid-resolved submesoscale advection and stirring driven by non-linear synoptic variability such as frontal meanders, continental shelf eddies, or external forcing, for example, Warm Core Rings and storm systems interacting with the shelfbreak front (eddy-advection flux). (c) Diffusion effects from sub-grid scale mixing scaled by a parameterized eddy-diffusivity, including mixing from shear-driven or convective instability on small timescales (horiz./vert. diffusion). While the NESS model inherently distinguishes between grid-resolved advective processes (a and b) and sub-grid scale parameterized diffusive processes (c), an additional mean-eddy timescale was introduced to separate mean flow advection (a) from advection driven by synoptic variability (b). A mean-eddy separation timescale of 30 d was chosen since the climatological hydrography becomes visible when averaging fields across this timescale while synoptic

variability is inherently three-dimensional and can obscure the two-dimensional cross-shelfbreak hydrography on timescales below, for example, through double-fronts, meanders, streamers, subsurface salinity-maximum intrusions, the presence of Warm-Core Rings, or wind forcing. Thus, the chosen 30 d timescale separation can be understood as the attempt to distinguish the mean-advection flux, a well-known flux from climatology (e.g., Linder & Gawarkiewicz, 1998), from a less well-known intermittent submesoscale eddy-advection flux. The former is driven by the mean gradient and velocity fields, whereas the latter is driven by fluctuating currents and gradients during synoptic events (e.g., WCRs, large frontal meanders, wind forcing) and is still captured by the submesoscale-permitting 1 km NESS model grid (in contrast to parameterized sub-grid scale processes).

Based on the above considerations, mean- and eddy-advection fluxes were separated by computing the mean-advection fluxes $-\overline{u}_i \cdot \partial\overline{S}/\partial x_i$ and eddy-covariance fluxes $-\partial/\partial x_i\langle u_i' S'\rangle$ $(i \in \{1,2\})$ offline. First, mean-advection fluxes were calculated with the same advection scheme as used for forwarding the full NESS model (4th-order Akima); but mean-advection was driven by tracer and velocity fields which were first averaged across the chosen mean-eddy separation timescale of 30 d. In addition, the averaged advection velocity was treated as constant across the grid cell and opposing grid cell interfaces. Then, the eddy-covariance flux was defined as the residual between the complete and the offline computed mean-advection flux

$$-\frac{\partial}{\partial x_i}\langle u_i' S'\rangle \equiv \left(-u_i\frac{\partial S}{\partial x_i}\right) - \left(-\overline{u}_i\frac{\partial \overline{S}}{\partial x_i}\right) \tag{3}$$

$(i \in \{1,2\})$, preserving budget closure. While the offline computation of mean-advection fluxes was made on the native (ξ,η)-model grid, horizontal mean-advection flux components were rotated afterward such that the coordinate axes align with the along- and cross-shelfbreak jet direction from Equation 1, respectively.

The eddy-advection flux $-\left(\nabla_h \cdot \langle \mathbf{u}_h' S'\rangle + w\cdot\frac{\partial S}{\partial z}\right)$ does not distinguish between the flux directions and combines both the along-shelf and cross-shelf eddy-covariance flux and the full vertical advection component (mean + eddy). Including the full vertical advection component $-w\cdot\frac{\partial S}{\partial z}$ is justified because of the misalignment between isopycnal frontal slopes and the vertical axis as well as the inherent ageostrophic nature of all vertical motion on the continental shelf. Thus, vertical motion on all timescales contributes to eddy-driven advection. In addition, by partitioning the advection flux into directional mean components and a cumulative eddy component, we avoid reproducing the finding by Z. Chen et al. (2018) that the individual directional advection fluxes (mean + eddy component) tend to be large and of opposite sign with a small advection residual. Instead, the proposed partition absorbs the large directional flux variability into the eddy-advection flux, which allows for more meaningful comparison of the mean along- and cross-shelf advection fluxes with the tendency/net term. Considering that the chosen cold pool control volume size is on the same order of magnitude as frontal meanders, it is not surprising that eddy-covariance advection on synoptic scales has components in all three directions that tend to partly compensate each other with a small net eddy-covariance flux. The eddy-advection flux defined above combines these highly correlated large-amplitude advection terms to a net residual at the expense of losing the ability of identifying where the synoptic variability advection signal comes from.

2.4. Seasonal Cycle and Interannual Variability

To focus on the mean seasonal cycle of salinity and cold pool fluxes, and not their synoptic variability in individual years, the same smoothing was applied to the results presented in Sections 3 and 4 (Figures 4–7 and 8a): Before computing the multi-year averaged seasonal cycle, a 30-day moving mean filter was applied to the full time series to avoid focusing on extreme events within individual years. Then, the same filter was applied again to the multi-year seasonal cycle. However, when analyzing the time series of individual years instead of the multi-year seasonal cycle in Sections 4.2 and 6.1, smoothing beyond a 30-day filter was required due to the enhanced influence of synoptic variability. A lowpass-filter with a frequency of $1/90$ days (instead of a 30-day moving mean filter as described above) was applied to the full time series to robustly identify the start and end date of the annual salinification period without ambivalence and assess interannual variability in Figures 8 and 11. In

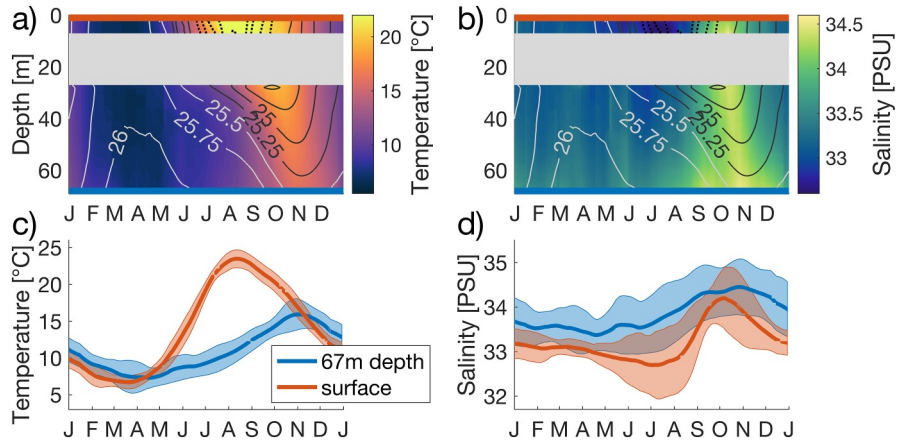

Figure 4. Annual Salinification of the outer US Northeast continental shelf and cold pool as observed by the Pioneer Array Inshore Moorings. (a and b) Observed temperature and salinity by combining data from the Inshore Surface Mooring (ISSM) (surface and 7 m depth) and the Upstream Inshore Profiler Mooring (PMUI) (28 − 67 m depth). Contours are isopycnals; solid and dotted lines have 0.25 kg/m^3 and 0.5 kg/m^3 spacing, respectively. (c and d) Seasonal cycle of temperature and salinity at two selected depths representing the surface mixed layer (orange; ISSM surface) and the continental shelf cold pool (blue; PMUI 67 m). $\pm 1\sigma$ envelopes represent interannual variability.

addition, an exception to continuous smoothing was made in Section 5 (Figure 9) for working within a non-stationary coordinate system: To compute the seasonally varying strength of the US Northeast shelfbreak jet from NESS model output, the jet core position was determined based on monthly averaged velocity fields instead of applying a 30-day moving mean filter. The monthly varying stream-following coordinate system captures meridional variability of the jet core position throughout the year.

3. Annual Salinity Increase of the Continental Shelf Cold Pool

Multi-year observations on the outer US Northeast continental shelf show that the subsurface shelf gets both warmer and saltier throughout the stratified season (Figure 4). For significant portions of the year, the Pioneer Array Inshore Moorings were within waters of below 10°C and 34.5 PSU, respectively, which are the conventional temperature and salinity signatures to separate winter-cooled Shelf Water from subtropical Slope Sea Water (Linder & Gawarkiewicz, 1998). Generally, bottom salinities are larger than surface layer salinities due to the offshore sloping of the buoyancy-controlled shelfbreak front. The mean subsurface Shelf Water, observed by the Pioneer Array PMUI at 67 m depth, gets warmer and saltier at a roughly constant rate throughout the stratified season between April and October (blue curves in Figures 4c and 4d). The lower depth range of the PMUI profiler is well suited for representing cold pool conditions on the US Northeast continental shelf since it is both well below the seasonal pycnocline and sufficiently above the ocean floor to not experience strong contamination from cross-shelf movements of the foot of the shelfbreak front (Taenzer et al., 2023a). The coherence in the timing and characteristics of the subsurface temperature and salinity trends suggest a similar origin, while trends within the surface layer (orange curves) are distinctly different, attending to the seasonal cycle of surface heating and freshwater advection from upstream. For the purpose of this study, we focus on the observed subsurface salinity trend.

We would like to assess whether the observed seasonal subsurface salinity increase on the outer continental shelf is indicative of a trend within the cold pool inshore of the Pioneer Array. Thus, we compare the Pioneer Array PMUI observations with the mean salinity trend within a conventionally defined cold pool at the same longitude, using NESS model output (Figure 5). The respective cold pool estimates contain a similar seasonal salinity trend in the multi-year mean of 0.18 ± 0.13 PSU/month and 0.19 ± 0.04 g/kg/month (1 month = 365/12 days) during the stratified season between April and October. Along the chosen transect at 70.875°W, the modeled cold pool is fully eroded by September (i.e., there are no waters below 10°C left), and Cold Pool Water properties reappear in December. The uncertainty of the linear trend depicts interannual variability only, that is, shown is the

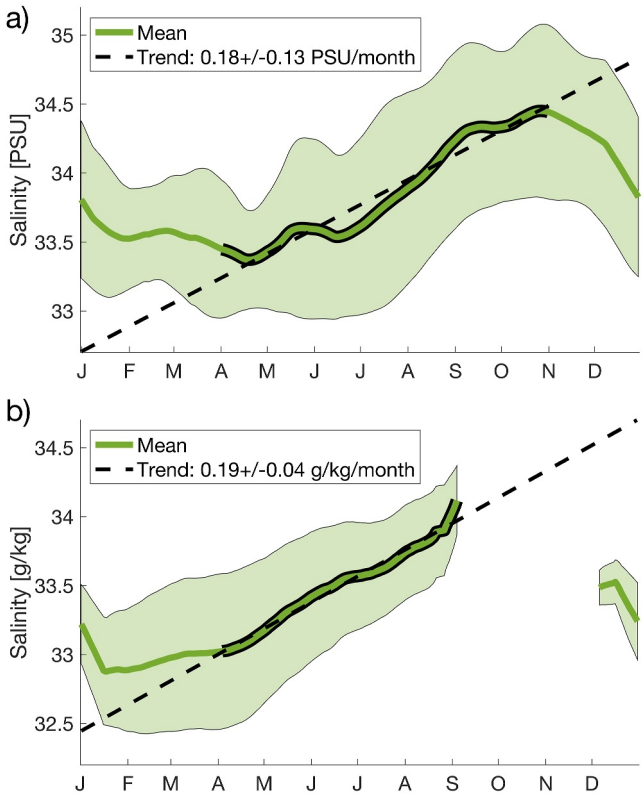

Figure 5. Annual cycle of continental shelf cold pool salinity. A linear trend has been fitted to the black-highlighted data during the stratified season (April–October) with its error depicting the trend's interannual variability from fitting constant slopes to individual years. (a) Pioneer Array PMUI salinity at 67 m depth. The $\pm 1\sigma$ envelope depicts one standard deviation of interannual variability. (b) NESS model salinity for all waters below the 10°C cold pool temperature threshold along 70.875°W, as long as the cold pool area is not below 1% of its mean maximum extent (March 15). The cold pool along 70.875°W is fully eroded by September and no mean cold pool salinity can be computed for the rest of the fall. The $\pm 1\sigma$ envelope depicts the combined variability across the cold pool volume on a given day and across all eight model years. The Pioneer Array (a) measures Practical salinity (PSU) while the NESS model (b) advects absolute salinity (g/kg).

standard deviation of the collection of linear trends fitted to individual years. The large uncertainty of the linear trend in the observations is rather driven by the strong interannual variability in the timing of the start/end of the salinification period and less by differences in the magnitude of seasonal salinification.

The Pioneer Array observations and NESS model show strong similarity in their seasonal cold pool salinification trend despite the misalignment in data availability pointed out in Section 2.2 and the two different approaches of capturing the cold pool's hydrography. While Figure 5 presents the multi-year average, seasonal salinification is unambiguously present in both the NESS model output (2010–2017) and the Pioneer Array PMUI record (2015–2022) for each individual year, with one exception. Thus, we conclude: (a) The salinification trend is a robust feature of the seasonal hydrography on the US Northeast shelf, and (b) the Pioneer Array PMUI profiler bottom range at 67 m depth is capable of capturing the mean trend of watermass transformation within the cold pool despite only measuring its outer edge. Even though the salinification trends are very similar between observations and the model, the PMUI registers overall larger salinity magnitudes and variability due to its location close to the shelfbreak front, which separates fresh Shelf Water from salty Slope Sea Water. In addition to a variety of studies that have demonstrated the NESS's and its predecessors' ability to capture the hydrography of the US Northeast continental shelf (e.g., K. Chen & He, 2010; K. Chen et al., 2016, 2022), a direct comparison between model output and Pioneer Array data shows strong correspondence in the annual cycle of temperature, salinity, and the velocity of the US Northeast shelfbreak jet (see Supporting Information S1).

4. Cold Pool Salinity Budget

4.1. Seasonal Cycle of Salinity Fluxes

Subsurface salinity on the US Northeast continental shelf increases with an approximately steady rate between spring and fall, which promotes the hypothesis that the cold pool salinity budget is seasonally unbalanced and differs considerably between the stratified and the unstratified season. The cold pool salinity budget for a cold pool control volume has a positive salinity flux residual into the control volume between April and October (Figure 6). While Figure 6a provides an overview of all fluxes constituting the salinity budget outlined in Equation 2, panels b–d focus on individual flux contributions and their interannual variability. The average salinity trend of 0.19 g/kg/month (April–October) across the cold pool control volume (Figure 6b) coincides well with the seasonal salinification trend across the traditionally defined cold pool (Figure 5b). This agreement provides additional confidence that the chosen cold pool control volume captures the hydrography of the cold pool on the US Northeast continental shelf well.

The biggest contributors that carry salt into the cold pool control volume are the submesoscale eddy-advection flux (green) and the cross-shelfbreak mean-advection flux (purple). These two fluxes make the cold pool saltier at all times of year. In contrast, vertical diffusion/mixing (red) has a freshening effect since the continental shelf is weakly salinity-stratified at all times of year (Li et al., 2015; Taenzer et al., 2023a). The vertical diffusion/mixing flux has the strongest seasonal cycle across all flux contributions. While vertical mixing balances the cross-shelf salt flux during winter, weak vertical mixing during the summer leaves the steady salt flux seasonally unopposed. Thus, the observed seasonal cold pool salinification signal originates from combining the following two ingredients: (a) A consistent deposit of salt into the cold pool by mean- and eddy-advection fluxes at all times of year and (b) a seasonal weakening of the vertical diffusion/mixing flux that no longer opposes the net salinity flux and no longer mixes fresher surface layer water into the subsurface cold pool during the stratified season. Note that the eddy-advection flux encapsulates the flux associated with grid-resolved synoptic variability, while the vertical

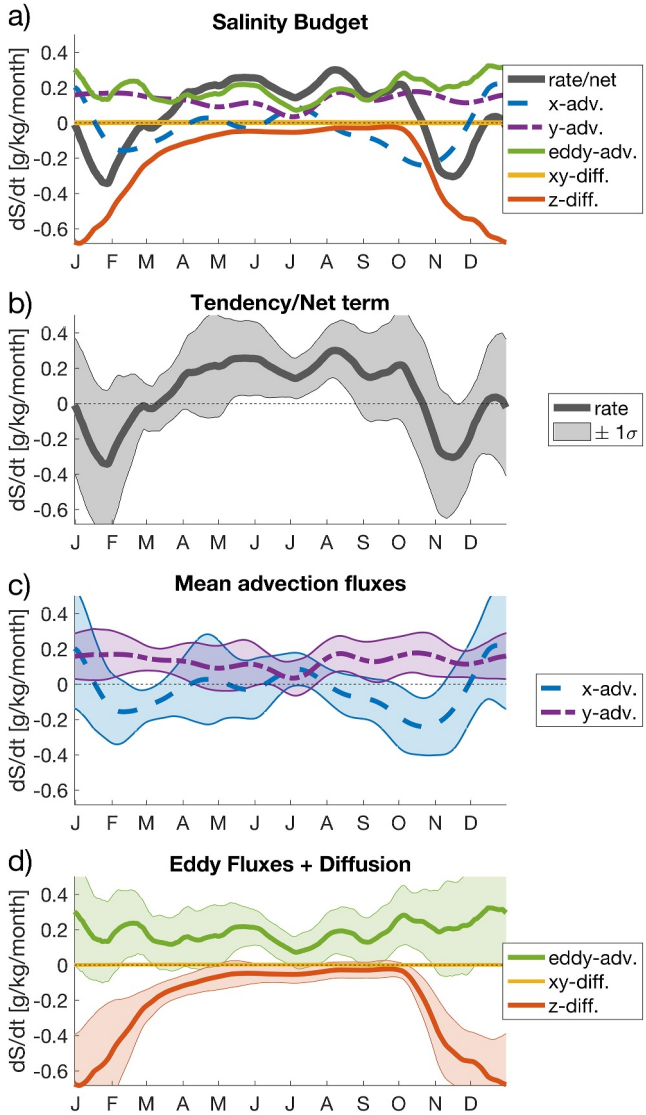

Figure 6. Seasonal cold pool salinity budget for a control volume on the US Northeast continental shelf. (a) Budget includes the tendency/net term $\partial S/\partial t$ (gray) and multi-year mean fluxes of along-shelf mean-advection $-\overline{u} \cdot \partial \overline{S}/\partial x$ (blue), cross-shelf mean-advection $-\overline{v} \cdot \partial \overline{S}/\partial y$ (purple), eddy-advection $-\left(\nabla_h \cdot \langle \mathbf{u}_h' S' \rangle + w \cdot \partial S/\partial z\right)$ (green), vertical (eddy) diffusion $\kappa_v \, \partial^2 S/\partial z^2$ (red), and horizontal diffusion $\kappa_h \nabla_h^2 S$ (yellow). (b)–(d) Individual budget net/flux terms and their interannual variability shown by their $\pm 1\sigma$ envelope. All budget terms are based on NESS model output. The color scheme is the same as introduced in Figure 3.

(red) and horizontal (yellow) diffusion fluxes parameterize the diffusive effects from sub-grid scale eddy-driven mixing.

The mean-advection salt flux components can be compared to climatology, that is, the climatological mean velocity field and salinity gradients averaged across the continental shelf cold pool region. As expected for an approximately geostrophically balanced shelfbreak frontal system, along-shelf velocities exceed cross-shelf velocities (Figure 7a), while cross-shelf mean salinity gradients exceed along-shelf mean gradients (Figure 7b) (Brink, 2016). The along-shelf velocities within the cold pool control volume have the same order of magnitude as the observed 3 cm/s along-shelf flow in the bottom boundary layer during the Coastal Mixing and Optics experiment in the same location (Shearman & Lentz, 2003). Scaling shows that the differences between along-/cross-shelf salinity gradients and velocity tend to compensate when computing the order of magnitude of the mean-advection flux components along and across the shelfbreak

$$\mathcal{O}(u \cdot \partial S/\partial x) = U \cdot \Delta S/L_x \approx 10^{-6} \text{ g/kg/s} \approx V \cdot \Delta S/L_y = \mathcal{O}(v \cdot \partial S/\partial y), \quad (4)$$

although, their respective seasonal cycles differ strongly (Figure 6c). Here, $U = 0.1$ m/s, $V = 0.01$ m/s, $\Delta S = 0.2$ g/kg, $L_x = 100$ km, and $L_y = 10$ km for the along- and cross-shelf component within the cold pool control volume, respectively. In contrast to the mean salinity gradients on the continental shelf, estimated by the mean gradients across the control volume (Figure 7b), the salinity gradient across the shelfbreak front is typically on the order of 1 g/kg/10 km (Linder & Gawarkiewicz, 1998) and thus significantly larger.

The seasonal cycle of the mean-advection fluxes into the control volume $-\overline{u}_i \cdot \partial \overline{S}/\partial x_i$ ($i \in \{1,2\}$) (Figure 6c) qualitatively resembles the climatology of the product of their components (Figure 7). Considering that the cross-shelfbreak mean salinity gradient $\partial \overline{S}/\partial y < 0$ persists throughout the year and the cold pool cross-shelfbreak flow $\overline{v}$ is northward at all times of year, it is no surprise that the net contribution from the cross-shelfbreak mean-advection flux to the cold pool salinity budget $-\overline{v} \cdot \partial \overline{S}/\partial y$ is positive at all times of year. Neither $\overline{v}$ nor $\partial \overline{S}/\partial y$, nor their product follow a strong seasonal cycle. In contrast, the along-shelf mean-advection flux closely follows the seasonal cycle of the mean along-shelf velocity across the cold pool (Figure 7a). Along-shelf salinity gradients $\partial \overline{S}/\partial x$ are comparatively weak throughout the stratified season and become more negative in the fall when upstream conditions get fresher. Thus, the along-shelf mean salinity flux contributes little to the seasonal cold pool salinification until the fall when advection of freshwater from upstream increases.

4.2. Cumulative Flux Contributions to the Seasonal Cold Pool Salinification

To quantify the net contribution of each flux component to the seasonal salinification signal, we integrate each flux component in time across the salinification period (Figure 8). The start/end of each year's salinification period is determined by the zero-crossing of the tendency/net term $\partial S/\partial t$ within that year, resulting in a mean salinification season that is 218 days long and lasts from March 11 $\pm$ 14 d to October 15 $\pm$ 28 d. Over the course of the mean salinification season, the mean control volume salinity increases by 1.3 g/kg. The timing of the mean salinification season coincides well with the seasonal cold pool warming, investigated in previous studies (e.g., Houghton et al., 1982; Lentz, 2017). Panels (a) and (b) of Figure 8 have the same y-axis, and panel (b) shows the

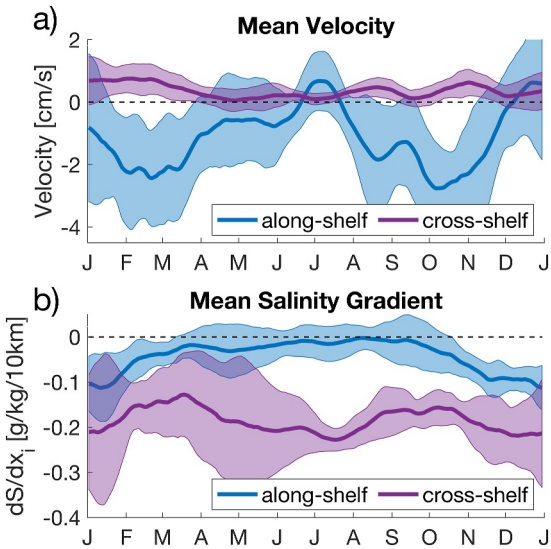

Figure 7. Seasonal cycle of horizontal mean velocity (a) and salinity gradients (b), averaged across the cold pool control volume on the US Northeast shelf. The coordinate system is aligned with the mean flow on the continental shelf. All panels show NESS model output, and the $\pm 1\sigma$ envelopes depict interannual variability.

interannual spread of the cumulative flux at the end of the salinification season between different years. Fluxes are integrated for each year individually to accommodate interannual differences in the timing of the salinification season. The required smoothing is described in Section 2.4. All cumulative flux contributions except the along-shelf advection flux have the same sign across all model years, which makes most cumulative flux signals robust across different years. In contrast, the uncertainty envelopes of the various fluxes at an individual point in time are only partly different from zero (Figure 6). Thus, seasonal salinification is a robust signal of the annual cycle while synoptic variability can obscure the seasonal trend on smaller timescales. The provided estimates of cumulative interannual variability are applied in Section 6.2 when comparing the results of this study with the peer-reviewed literature.

The eddy-advection flux (green) and the mean cross-shelfbreak flux (purple) together contribute more than 150% of the cumulative salinification signal (Figure 8a). The eddy-advection flux has the strongest signal and shows less interannual variability than the mean cross-shelfbreak flux. In contrast, vertical mixing (red) freshens the control volume by 0.5 g/kg across the stratified season, despite being weakest during the summer (Figure 6d). The along-shelf mean-advection flux (blue) advects freshwater from upstream; though, this contribution is restricted to the fall only. During the fall, the along-shelf mean-advection flux assists the vertical diffusion flux in terminating the seasonal cold pool salinification period. However, it shall be noted that the along-shelf advection flux is not strictly negative across all years (Figure 8b), which could contribute to interannual variability in the timing of the end of the salinification season (see Section 6.1).

5. Seasonal Cross-Shelf Movements of the Shelfbreak Front

While the cold pool salinity budget points toward the importance of salinity fluxes across the US Northeast shelfbreak front (Section 4), seasonal onshore movements of the shelfbreak front itself could also contribute to the observation of a seasonal salinity increase on the outer continental shelf (Figure 5a). Cross-shelfbreak salinity fluxes act as irreversible cross-shelfbreak exchange, salinifying the cold pool; in contrast, linear cross-shelfbreak movements of the shelfbreak front temporarily shift the cold pool boundary further inshore, leading to reversible and temporary salinification of the outer shelf without lasting net exchange. In the Pioneer Array PMUI hydrography, both processes would look similar. The shelfbreak front is a partly temperature-salinity

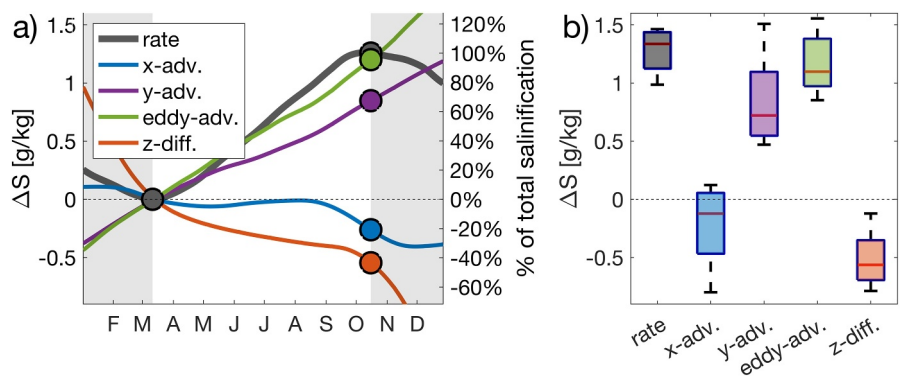

Figure 8. Cumulative contributions of individual fluxes to the seasonal salinification of the cold pool on the US Northeast shelf: Tendency/Net term $\partial S/\partial t$ (gray), along-shelf mean-advection $-\overline{u} \cdot \partial \overline{S}/\partial x$ (blue), cross-shelf mean-advection $-\overline{v} \cdot \partial \overline{S}/\partial y$ (purple), eddy-advection $-\left(\nabla_h \cdot \langle \mathbf{u}_h' S' \rangle + w \cdot \partial S/\partial z\right)$ (green), and vertical (eddy) diffusion $\kappa_v \, \partial^2 S/\partial z^2$ (red). (a) Time series of cumulative fluxes since the start of the mean seasonal salinification season on 11 March. The mean salinification season ends on 15 October. (b) Interannual variability of the cumulative contributions to the seasonal cold pool salinification at the end of each year's salinification season.

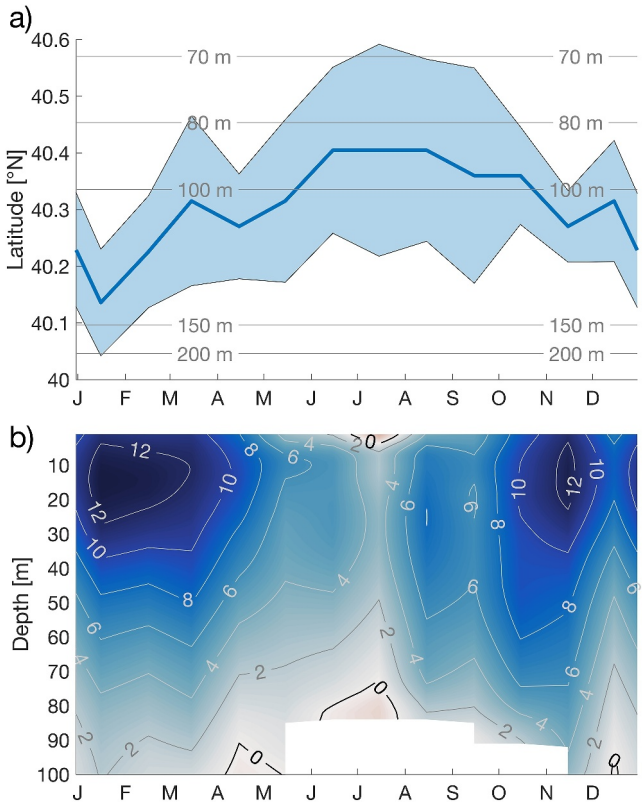

Figure 9. Seasonal cycle of the US Northeast shelfbreak jet at 70.875°W, based on multi-year monthly averages using NESS model output. (a) Latitude position of the shelfbreak jet core based on the along-shelf velocity maximum, averaged across the upper 50 m depth. The $\pm 1\sigma$ envelope depicts interannual variability, and local bathymetry is shown as overlaid contours. (b) Depth structure of the along-shelf shelfbreak jet in a jet-following coordinate system. Zonal velocities are shown in units of cm/s, and positive velocities are westward.

compensated buoyancy-driven frontal system that can be understood as the edge of a coastal freshwater plume (Chapman & Lentz, 1994), accumulating both river discharge and modified subpolar water. Traditionally, Shelf and Slope Sea Water are distinguished by the 34.5 PSU isohaline at all times of year (Linder & Gawarkiewicz, 1998) with salinity gradients of the order 1 PSU/10 km across the shelfbreak front. However, in individual synoptic transects, it can be difficult to identify the location of the shelfbreak front, that is, the location of the maximum buoyancy gradient $\partial b/\partial y$ across the front due to synoptic variability. Instead, we can take advantage of the fact that the climatological shelfbreak jet is mostly baroclinic and approximately in thermal-wind balance (Linder & Gawarkiewicz, 1998), that is, the cross-shelfbreak position of the climatological shelfbreak jet core coincides with the location of the strongest vertically integrated buoyancy gradient across the climatological shelfbreak front. Locating the cross-shelfbreak position of the shelfbreak jet core is restricted to NESS model output since the Pioneer Array Moorings are spaced too far apart to detect small differences in position.

The seasonal cycle of the shelfbreak jet position was determined based on multi-year monthly averages (Figure 9a). For each month, the jet core position across the shelfbreak was identified as the most offshore maximum of the depth-integrated (upper 50 m) westward flow across the Pioneer Array main transect at 70.875°W, north of 40°N. The approach is motivated by Fratantoni et al. (2001); and even though the NESS model captures both the shelfbreak jet and the barotropic slope jet, confusion between both currents is not expected since the slope jet is located further offshore at all times of year. When comparing the NESS jet core position and the cross-shelfbreak salinity field along 70.875°W, their seasonal cycles are distinctly different (Figure 10). A cross-shelfbreak slice through the cold pool at 67 m depth (Figures 10a and 10b) and vertical profile in a jet core-following coordinate system (Figure 10c) both confirm that the cold pool salinity is smallest during late winter and largest in the fall, aligned with the observations made by the Pioneer Array Inshore Moorings (Figure 4). In contrast, the seasonal cycle of the shelfbreak jet position is smaller and has a different timing, reaching its northernmost position in the summer (and not the fall) when jet speeds are the weakest (Figure 9b). Even though the Pioneer Array cannot be used to detect small meridional shifts in the shelfbreak jet location, the seasonal cycle and depth structure of the modeled jet shows strong similarity compared to a multi-year ADCP average from the Pioneer Array Central Moorings, located around the climatological shelfbreak jet position (see Supporting Information S1). In contrast to the speeds within the shelfbreak jet frontal zone (Figure 9b), along-shelf velocities on the continental shelf (Figure 7a) are smaller by about a factor 2–3, setting up a horizontal velocity shear on the outer continental shelf.

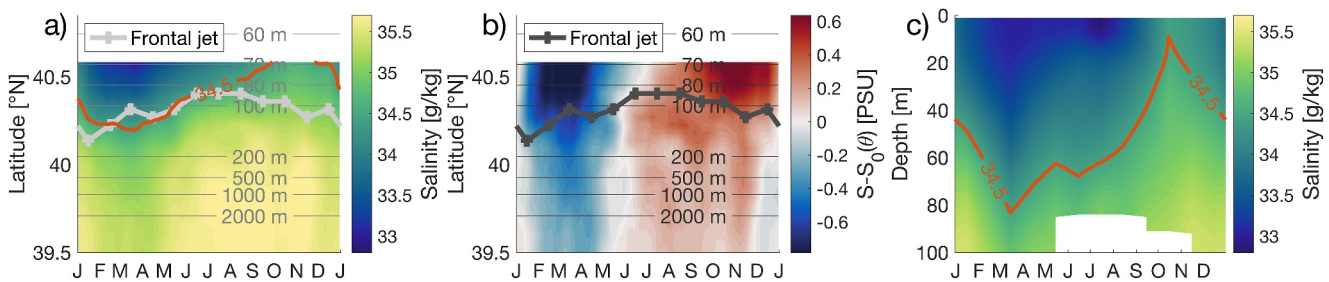

Figure 10. Comparison of interior continental shelf salinification and meridional shelfbreak frontal movements in the NESS model along 70.875°W. (a) Seasonal salinity at 67 m depth and frontal jet position. (b) Seasonal salinity anomaly per latitude at 67 m depth and frontal jet position. (c) Vertical salinity profile at the monthly jet position in a jet-following coordinate system (Figure 9). All panels show NESS model output. The annual cycle of the shelfbreak jet position is overlaid in gray, and the 34.5 g/kg isohaline is highlighted.

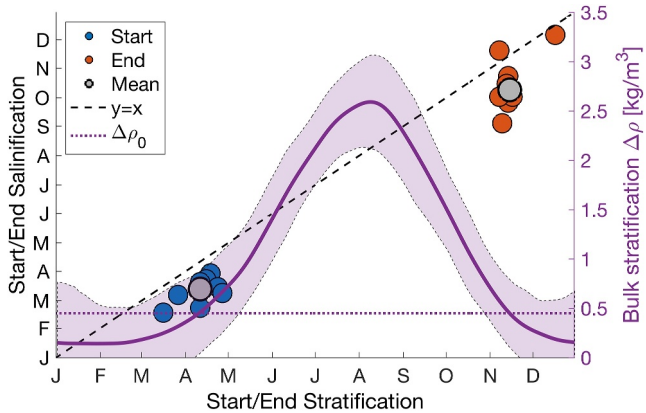

Figure 11. Interannual variability between the start/end of the seasonal cold pool salinification season (zero-crossings of the tendency term $\partial S/\partial t$) and the seasonal stratification season (bulk stratification $\Delta\rho$ above/below the stratification threshold $\Delta\rho_0 = 0.45$ kg/m^3, i.e., $\Delta\rho \gtrless \Delta\rho_0$). Each dot represents the start (blue) and end (red) of the salinification/stratification season of an individual year, and the center of each cluster is shown in gray. The bulk stratification $\Delta\rho$ is defined as the potential density difference between the averaged cold pool control volume and the surface layer above it, estimated by the mean across the upper 8 NESS-layers. The $\pm 1\sigma$ envelope depicts interannual variability.

Theoretically, cross-shelfbreak movements of a geostrophic buoyancy-driven shelfbreak front would shift the watermass transition zone between cool/fresh Shelf and warm/salty Slope Sea Water, leading to a linear, that is, reversible, salinification of the outer shelf during the summer. However, seasonal salinity anomalies are not restricted to the outer shelf (Figure 10b), but extend at least beyond the 67 m isobath with weaker anomaly signals south of the shelfbreak front and in the Slope Sea. Thus, the cold pool salinification signal originates from a process that alters the hydrography across the entire continental shelf, which is not achievable by linear cross-frontal movements restricted to the cold pool's southern edge. Rather, the salinity signal's distinct minimum and maximum in spring and fall, respectively, at least qualitatively align with the onset and breakdown of the seasonal stratification signal on the US Northeast shelf with a steady mean salinification rate in between. Thus, even though the shelfbreak jet moves onshore during the stratified season, these cross-shelfbreak movements are too weak in magnitude to cause the seasonal cold pool salinification across the US Northeast shelf. Instead, the seasonal salinification is caused by a steady irreversible transport of salt across the shelfbreak as the cold pool salinity budget reveals (Section 4).

6. Discussion

6.1. Seasonal Stratification Promotes Cold Pool Salinification

The cold pool salinity budget (Section 4) and the evaluation of cross-shelfbreak frontal movements (Section 5) have demonstrated that the seasonal salinification of the near-bottom US Northeast continental shelf cold pool is driven by a seasonal flux imbalance between cross-shelfbreak exchange and vertical mixing, and not by cross-shelfbreak movements of the shelfbreak front. The start/end of the seasonal cold pool salinification period is largely set by the strong annual cycle in the vertical diffusion/mixing signal. Vertical mixing and seasonal stratification are inherently connected since vertical mixing destroys stratification while stratification has a stabilizing effect on the water column and weakens shear-driven vertical mixing. Lentz (2017) notes that interannual variability of the annual cold pool persistence is driven by the timing of the fall breakdown of stratification, caused by storms. Similarly, the timing of the seasonal cold pool salinification period aligns well with the seasonal cycle of stratification, not just in the multi-year mean, but as well in individual years (Figure 11). The start of the cold pool salinification period aligns particularly well with the start of the salinification period (blue dots) throughout the model time period, and the cluster has the same slope as the slope-1-line. The roughly 1-month offset in time is likely an artifact of the chosen $\Delta\rho_0$-threshold. In contrast, there is more interannual scattering with respect to the end of the salinification season when compared to the timing of the stratification breakdown (red dots). The scatter along the y-axis could be caused by interannual variability in the along-shelf mean-advection of freshwater from upstream that only contributes to the cold pool budget during the fall and shows comparatively large interannual variability compared to the other cumulative fluxes (Figure 8b).

The relationship between the seasonal cold pool salinification and the seasonal cycle of stratification allows separating the year into two regimes. Panels (a) and (b) of Figure 12 summarize cold pool salinity flux conditions for the unstratified and stratified season, respectively. While the steady cross-shelfbreak salt flux and the freshwater flux from vertical mixing tend to cancel each other out during the unstratified season, the shutdown of vertical mixing during the stratified season creates an imbalance and leaves the steady cross-shelfbreak salt flux (from both cross-shelfbreak mean (purple) and eddy- (green) advection) unopposed. Thus, upper ocean conditions have a direct impact on near-bottom continental shelf hydrography. The timing of separation into the two regimes is roughly aligned with the gray/white shading presented in Figure 8a. The dominant role of the seasonal cycle of stratification in facilitating the seasonal cold pool modification also explains the robustness of summer cold pool warming and salinification every single year. While the seasonal cycle of temperature-dominated stratification is the strongest mode of annual variability across the MAB, along-shelf advection of salinity is subject to strong interannual variability (Mountain, 1991) from a combination of local freshwater input and offshore forcing (Ryan et al., 2024).

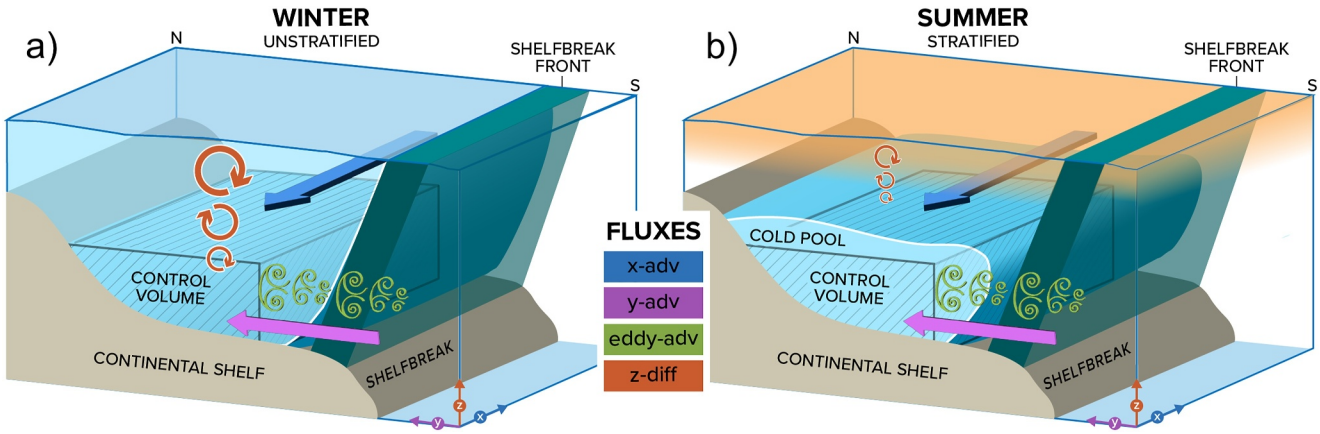

Figure 12. (a) Winter and (b) summer flux regimes explaining the seasonal cold pool salinification on the US Northeast shelf as the result of an imbalance between steady cross-shelfbreak salt advection and diminished vertical mixing during the stratified season in panel (b). The arrows qualitatively outline the magnitude of the salinity budget fluxes, introduced in Section 2.3, for the unstratified (a) and stratified (b) season: Along-shelf (x) mean-advection $-\overline{u} \cdot \partial\overline{S}/\partial x$ (blue), cross-shelf (y) mean-advection $-\overline{v} \cdot \partial\overline{S}/\partial y$ (purple), eddy-advection $-\left(\nabla_h \cdot \langle \mathbf{u}_h' S' \rangle + w \cdot \partial S/\partial z\right)$ (green), and vertical (eddy) diffusion $\kappa_v \, \partial^2 S/\partial z^2$ (red). The cold pool is depicted in light blue and a schematic control volume is shown as a streaked gray box. Illustration: Natalie Renier (WHOI).

In contrast to this study, Lentz (2017) argues that cross-shelfbreak advection can be neglected when applying temperature instead of salinity as a tracer, and seasonal cold pool modification appears mostly driven by vertical mixing. However, the choice of tracer might influence the assessment of what type of fluxes impact the cold pool the most. The heat and salt flux due to vertical mixing have opposite signs in the cold pool heat and salt budget, adding heat and freshwater to the summer cold pool, respectively. Since Cold Pool Water has the lowest temperature of all surrounding watermasses (Figure 2) aside from the weak along-shelf temperature gradient, most budget flux terms contribute to cold pool warming; and because vertical temperature gradients in the summer are large, even diminished vertical mixing during the stratified season (Figure 6d) contributes strongly to cold pool warming. In contrast, the cold pool is surrounded by both slightly fresher water from above and saltier water from offshore. Thus, using salinity as a tracer allows for better distinction between flux contributions that can either add or remove salt from the cold pool. In addition, the strong seasonal cycle of surface heating and cooling alters the conditions of the surface tracer reservoir on the same timescale as the observed cold pool changes. In contrast, both vertical (Li et al., 2015; Taenzer et al., 2023a) and cross-shelfbreak (Linder & Gawarkiewicz, 1998) salinity gradients remain approximately constant throughout the year, that is, seasonal variability in salinity flux magnitudes is likely less driven by the seasonality of the salinity gradients and more by the seasonality of the underlying dynamical processes.

6.2. Understanding of the Eddy-Advection Flux Term

The eddy-advection flux $\left(-\left(\nabla_h \cdot \langle \mathbf{u}_h' S' \rangle + w \cdot \partial S/\partial z\right)\right)$ is associated with intermittent synoptic events of ageostrophic shelfbreak exchange; in contrast to the cross-shelf mean-advection flux $\left(-\overline{v} \cdot \partial\overline{S}/\partial y\right)$, which is advected by the mean flow. By design, the eddy-advection flux does not include a directionality since the different eddy-advection components tend to partly compensate each other with a small net residual (see Section 2.3). However, the eddy-advection flux term adds salt to the cold pool control volume at all times of year and the only ubiquitous source of high salinity water is the contiguous Slope Sea across the continental shelfbreak (Ketchum & Corwin, 1964). Thus, we expect the eddy-advection flux term to predominantly capture synoptic processes associated with cross-shelfbreak salinity fluxes. Since the US Northeast shelfbreak front is inherently unstable (Flagg & Beardsley, 1978; Garvine et al., 1988), intermittent cross-shelfbreak exchange occurs regularly, either due to internal instability (Gawarkiewicz et al., 2004) or external forcing (Silver et al., 2023; Todd, 2020; Zhang & Gawarkiewicz, 2015a). If the eddy-advection flux is exclusively driven by cross-shelfbreak eddies, one can estimate the order of magnitude of a horizontal cross-shelfbreak bulk eddy-diffusivity K_h within the frontal region by applying a simple Fickian diffusion model:

$$-\left(\nabla_h \cdot \langle \mathbf{u}_h' S' \rangle + w \cdot \partial S/\partial z\right) \approx -\frac{\partial}{\partial y}\langle v' S' \rangle = K_h \frac{\partial \bar{S}}{\partial y^2} \sim K_h \frac{\Delta S}{(L_y)^2}. \quad (5)$$

Then, $K_h \sim 10^1$ m^2/s in the presence of a cross-shelfbreak salinity gradient $\Delta S/L_y = 1$ PSU/10 km (Linder & Gawarkiewicz, 1998). In comparison, Sundermeyer and Ledwell (2001) observed a lateral diffusivity between 0.3−4.9 m^2/s from a dye-release experiment on the US Northeast continental shelf, which is slightly lower than this very simple estimate. However, in contrast to the continental shelf, the presence of the shelfbreak jet with its secondary circulation likely makes lateral eddy-driven diffusion highly anisotropic within the frontal zone.

In the absence of external forcing, Spall and Chapman (1998) developed the simple analytical expression $\langle v' \rho' \rangle = c_e U \Delta\rho$, which links the magnitude of an eddy-buoyancy flux across an idealized narrow front with more easily observable mesoscale frontal properties, assuming that the eddy-transport is facilitated by baroclinic eddy pairs under the presence of stratification. Here, U is a scale for the frontal jet speed difference between two layers and $\Delta\rho$ is the mesoscale density difference across the front. In an eddy-resolving idealized model, they determined the eddy-flux efficiency c_e to be between 0.02 and 0.04 across a wide range of frontal parameters. Assuming that the multi-year mean eddy-advection flux of 0.17 ± 0.03 g/kg/month (i.e., 1.3 ± 0.2 g/kg over 218 days (Figure 8)) originates solely from a Spall and Chapman (1998)-like eddy flux $\langle v' S' \rangle / \Delta W$ across the modeled shelfbreak front of width $\Delta W = 20$ km, we estimate an eddy-flux efficiency of $c_e = 0.02 \pm 0.01$ (with $U = 5 \pm 2$ cm/s during peak stratification (Figure 9b) and $\Delta S = 1.5 \pm 0.5$ PSU as the mean salinity difference between the subsurface outer shelf and the northern Slope Sea (Figure 2)). The uncertainty estimate was propagated assuming that all variables are normally distributed and uncorrelated. The eddy-flux efficiency estimate from the cold pool salinity budget overlaps largely with the range presented in Spall and Chapman (1998), which is particularly remarkable considering the strong differences in the assumptions of each estimate. While the efficiency estimate from the cold pool eddy-advection flux includes all grid-resolved synoptic variability, it relies on the non-trivial assumption that eddy-advection fluxes are solely directed across the shelfbreak front. In contrast, Spall and Chapman (1998)'s eddy-flux efficiency only captures eddy-fluxes generated by baroclinic eddy-pairs. Furthermore, the eddy-advection flux originates from both internal instability and external forcing, while the idealized and analytical model by Spall and Chapman (1998) only captures the subsection of the net cross-shelfbreak eddy-driven advection that is caused by heton eddy pairs.

The cumulative cross-shelfbreak flux across all processes and timescales has previously been inferred indirectly as the residual to close the shelf salinity budget. Houghton et al. (1988) consider the gradient of oxygen isotope ratios along the MAB, reported by Fairbanks (1982), to indirectly infer a cross-shelfbreak salinity flux of $2.2 \cdot 10^{-3}$ kg/m^2/s per unit width and depth. By aggregating salinity observations across multiple decades, Lentz (2010) estimates a depth-averaged multi-year mean cross-shelfbreak "eddy" salt flux of $7 \cdot 10^{-3}$ kg/m^2/s per unit width and depth across the 100 m isobath. Here, we complement previous efforts to constrain a shelf salinity budget by investigating the seasonality of eddy-advection and focusing on the near-bottom continental cold pool, which shows less variability than the surface layer. To compare the eddy-advection flux into the cold pool control volume with the residual estimates from Houghton et al. (1988) and Lentz (2010), we approximate the sum of the cross-shelfbreak flux components into the 30 km^3 large control volume as a salt flux across the southern border only (area $A = W \cdot H = 50$ km $\cdot$ 20 m $= 1$km^2), assuming advection flux contributions across other control volume boundaries to be negligible. The sum of the cross-shelfbreak mean-advection flux and the eddy-advection flux amounts to a multi-year mean of 2.0 ± 0.3 g/kg across the almost 7-month long stratification season (Figure 8), which corresponds to a salt flux of $(3.3 \pm 0.5) \cdot 10^{-3}$ kg/m^2/s per unit width and depth across the offshore control volume boundary. This estimate is on the same order of magnitude than previous residual estimates. While Lentz (2010) describes the depth-averaged flux across the 100 m isobath, the cold pool control volume only extends southward to the 75 m isobath, which could explain the difference in the cross-shelfbreak flux magnitude due to the control volume's larger distance from the shelfbreak front. In contrast to the mean residual salinity flux estimated above, Gawarkiewicz et al. (2004) observed flux rates of nearly $20 \cdot 10^{-3}$ kg/m^2/s for an individual synoptic non-linear large-amplitude frontal meander. However, the flux magnitude varied strongly on synoptic timescales, and even a negative flux was observed just 2 days after the strong positive cross-shelfbreak flux event. Considering that the mean eddy-advection flux magnitude of this study is in good agreement with flux estimates of various observed and modeled cross-shelfbreak eddy processes

reported on in the literature (see above), we can assume that the eddy-advection flux, that is, the largest contributor to cold pool salinification, predominantly captures eddy-driven cross-shelfbreak exchange.

While the annual cycle of seasonal stratification is essential for establishing the seasonal imbalance between the eddy-advection and vertical diffusion flux, the eddy-advection flux itself remains fairly constant throughout the year and across all years. This result is not necessarily expected considering the strong seasonal cycle of both the shelfbreak jet's velocity (Figure 9b) and stratification (Figure 11). According to a linear stability analysis by Zhang and Gawarkiewicz (2015b), the growth rate of frontal meanders along an idealized front, which resembles properties of the US Northeast shelfbreak front, depends on stratification. Houghton et al. (1988) observed a weak indication for a seasonal cycle in the cross-shelf eddy heat flux $\langle v'T' \rangle$, which was only significant during the fall. Irrespective of the eddy-advection flux's seasonal cycle, the smoothed multi-year mean curves in Figures 6 and 8 hide the strong intermittency of the eddy-advection flux on synoptic timescales. In fact, the eddy-advection flux is only positive 60% of the time (when averaged across two M2 tidal cycles), but its net positive mean is caused by intermittent strong bursts of salt fluxes into the cold pool control volume, while negative salt flux peaks tend to be smaller. Thus, the smoothed seasonal cycle primarily provides an estimate of what flux magnitude to expect in a multi-year mean, offering little information about its variability on any given day.

6.3. Moving Beyond the US Northeast Shelf

The results of this study apply to the US Northeast continental shelf where the Pioneer Array first observed the seasonal cold pool salinification trend and a direct comparison between NESS model results and multi-year observations is possible. The applicability of these results to the entire MAB is unknown; however, we can learn from observations of seasonal cold pool modification in temperature across the entire MAB (Castelao et al., 2008; Houghton et al., 1982; Ou & Houghton, 1982). The seasonal cycle of stratification is the dominant mode of seasonal variability of the MAB hydrography, which suggests that the seasonal shutdown of vertical mixing is the dominant cause for cold pool erosion everywhere across the MAB. Strong temporal coherence in the formation and breakdown of seasonal stratification across the MAB (Li et al., 2015) even suggests that the timing of the start/end of cold pool modification across the MAB could be similar. Frontal meanders (Garvine et al., 1988) and cross-shelfbreak exchange are ubiquitous across the MAB as Lozier and Gawarkiewicz (2001) observed from drifter releases. And mean cross-shelf advection points onshore in the interior water column when aggregating observations across the MAB (Lentz, 2008).

In contrast, the impact of along-shelf advection likely differs across the MAB. Houghton et al. (1982) have shown that the seasonal cold pool warming is not steady everywhere and estimated the along-shelf advection velocity of the cold pool minimum along the MAB. Hudson Bight is likely the MAB-region where along-shelf temperature advection matters the most (Brown et al., 2023; Lentz, 2017), and Hudson Bight's comparatively large continental shelf width gives it a large local “heat/salt capacity” (Ou & Houghton, 1982). The cold pool evolution in the southern MAB is likely complex due to a combination of strong local heating and varying advection from upstream (Castelao et al., 2008). Thus, it can be assumed that the along-shelf differences in the strength and timing of the along-shelf mean-advection flux modify the cold pool temperature and salinity to second order throughout the summer, resulting in a more complex cold pool development along the MAB and further downstream of the US Northeast continental shelf. Further upstream, forcing conditions are sufficiently different from the rest of the MAB (Lentz, 2017), such that the results of this study are likely not applicable. In particular, strong tidal mixing on Georges Bank (Brown, 1984) differentiates the upstream region from the rest of the MAB.

While shelfbreak exchange plays an important role for the cold pool erosion on the mid-continental shelf, the role of vertical mixing increases toward the coast (Lentz, 2017). While Lentz (2017)'s simplified cold pool heat budget without cross-shelfbreak exchange works well for shallow water depths near the coast, vertical mixing alone underestimates the cold pool warming rates on the US Northeast shelf in deeper waters closer to the shelfbreak. The strong correlation between temperature and salinity across Cold Pool Water and subsurface Slope Sea Water (Figure 2) likely resembles the mixing line between both water masses and points toward the influence of shelfbreak exchange on the mid-shelf hydrography. In contrast to Lentz (2017), this study applies a more strict definition to identify the cold pool and thus excludes the shallow inner shelf, which warms much faster and experiences different dynamics than the mid- and outer continental shelf, for example, enhanced tidal mixing and interaction between the bottom and surface boundary layer. The cold pool control volume in this study is restricted to the area between the 55- and 75 m isobaths to ensure that the control volume only captures the

homogeneous core of the cold pool on the mid-shelf (Figures 1b and 1c), which preserves winter conditions for longer than the inner and outer shelf.

7. Conclusion

The US Northeast continental shelf cold pool preserves winter conditions within the near-bottom shelf waters and serves as a habitat for the regional marine ecosystem when regional waters become too warm and/or salty elsewhere during the summer. While a seasonal warming of the cold pool has first been observed by Bigelow (1933), we provide evidence that the cold pool also gets saltier throughout the stratified season. By using salinity instead of temperature as a tracer, a cold pool salinity budget for the US Northeast continental shelf reveals that cross-frontal fluxes deposit salt into the cold pool at all times of year, and along-shelf advection contributes little to the salinification signal. The cold pool exhibits two seasonal regimes, shaped by the seasonal cycle of stratification. During the unstratified season, vertical mixing is large, and the cold pool gets replenished with fresh water from the surface layer, which inhibits salinification. During the stratified season, vertical mixing is significantly reduced, resulting in an imbalance as steady cross-shelfbreak salt fluxes salinify the cold pool without any opposing flux present. The cold pool salinifies with a mean rate of 0.18 PSU/month during the stratified season. Seasonal cross-shelfbreak movements of the shelfbreak front are shown to be too small to noticeably contribute to the seasonal cold pool salinification. In addition, cross-shelfbreak movements of the frontal jet and cold pool salinification do not align temporally, and cold pool salinification stretches across the entire shelf rather than being confined to the shelfbreak.

This study quantifies the multi-year mean contribution of the eddy-advection flux, which captures cross-shelfbreak fluxes due to synoptic variability, to the observed change of the subsurface US Northeast hydrography on seasonal timescales. The smoothed, multi-year mean eddy-advection flux is roughly constant throughout the year, despite the strong seasonal cycle of stratification and shelfbreak jet speed, and consists of intermittent eddy-flux events occurring on synoptic timescales. These events are likely associated with submesoscale shelfbreak frontal processes that cause the ageostrophic cross-shelfbreak transport. However, it remains an open question how individual eddy-flux events can be attributed to the variety of known frontal exchange processes.

Data Availability Statement

Code and model output to reproduce the figures can be found at https://doi.org/10.5281/zenodo.14605057. In situ observations of the US Northeast shelfbreak hydrography and velocity originate from the OOI Coastal Pioneer Array Moorings (NSF Ocean Observatory Initiative, 2022), and data are publicly available through multiple gateways, for example, through the Data Explorer ERDDAP server erddap.dataexplorer.oceanobservatories.org. A gridded version of the hydrography data set (Taenzer et al., 2023b, 10.1029/2022JC019625), described in Taenzer et al. (2023a), was used to identify seasonal watermass variability in the US Northeast cold pool. The NESS regional ocean model is described in K. Chen et al. (2022). Thermodynamic properties of seawater have been determined by using the Gibbs-SeaWater (GSW) Oceanographic Toolbox (McDougall & Barker, 2011), Version 3.06.12, available via teos-10.org/software.htm.

Acknowledgments
We are grateful for financial support from NASA under Grant 80NSSC22K0995 (LT, GG), National Science Foundation (NSF) Ocean Science Division under Grant OCE-2241407 and the George E. Thibault Early Career Scientist Fund (KC), and the Scripps Chair for Excellence in Oceanography (AP). Comments from two anonymous reviewers have greatly improved the structure and clarity of the manuscript. Observations are provided by the Ocean Observatories Initiative (OOI), a major facility fully funded by NSF under Cooperative Agreements No. 1026342 and 1743430. The Ssalto/Duacs altimeter products were produced and distributed by the Copernicus Marine and Environment Monitoring Service (CMEMS) (http://www.marine.copernicus.eu). Open Access funding enabled and organized by MIT Hybrid 2025.

References

AVISO. (2022). Ssalto/Duacs gridded Mean Absolute Dynamic Topography (MADT-H) monthly climatology product (1993-2020) [Dataset]. Thredds Data Server. https://tds.aviso.altimetry.fr/thredds/catalog/dataset-duacs-climatology-global/delayed-time/monthly_clim/madt_h/catalog.html

Bigelow, H. B. (1933). Studies of the waters on the continental shelf, Cape Cod to Chesapeake Bay. I. The cycle of temperature. *Papers in Physical Oceanography and Meteorology*, *2*(4). https://doi.org/10.1575/1912/1144

Brink, K. (2016). Cross-shelf exchange. *Annual Review of Marine Science*, *8*(1), 59–78. https://doi.org/10.1146/annurev-marine-010814-015717

Brown, W. S. (1984). A comparison of Georges Bank, Gulf of Maine and New England shelf tidal dynamics. *Journal of Physical Oceanography*, *14*(1), 145–167. https://doi.org/10.1175/1520-0485(1984)014<0145:ACOGBG>2.0.CO;2

Brown, W. S., Schofield, O., Glenn, S., Kohut, J., & Boicourt, W. (2023). Mid-Atlantic Bight cold pool based on ocean glider observations. *Continental Shelf Research*, *264*, 105040. https://doi.org/10.1016/j.csr.2023.105040

Castelao, R., Glenn, S., Schofield, O., Chant, R., Wilkin, J., & Kohut, J. (2008). Seasonal evolution of hydrographic fields in the central Middle Atlantic Bight from glider observations. *Geophysical Research Letters*, *35*(3), L03617. https://doi.org/10.1029/2007GL032335

Chapman, D. C., & Lentz, S. J. (1994). Trapping of a coastal density front by the bottom boundary layer. *Journal of Physical Oceanography*, *24*(7), 1464–1479. https://doi.org/10.1175/1520-0485(1994)024<1464:TOACDF>2.0.CO;2

Chassignet, E. P., Hurlburt, H. E., Smedstad, O. M., Halliwell, G. R., Hogan, P. J., Wallcraft, A. J., et al. (2007). The HYCOM (HYbrid Coordinate Ocean Model) data assimilative system. *Journal of Marine Systems*, *65* (1), 60–83. https://doi.org/10.1016/j.jmarsys.2005.09.016

Chen, K., Gawarkiewicz, G., & Yang, J. (2022). Mesoscale and submesoscale shelf-ocean exchanges initialize an advective marine heatwave. *Journal of Geophysical Research: Oceans*, *127*(1). https://doi.org/10.1029/2021JC017927

Chen, K., & He, R. (2010). Numerical investigation of the Middle Atlantic Bight shelfbreak frontal circulation using a high-resolution ocean hindcast model. *Journal of Physical Oceanography*, *40*(5), 949–964. https://doi.org/10.1175/2009JPO4262.1

Chen, K., Kwon, Y.-O., & Gawarkiewicz, G. (2016). Interannual variability of winter-spring temperature in the Middle Atlantic Bight: Relative contributions of atmospheric and oceanic processes. *Journal of Geophysical Research: Oceans*, *121*(6), 4209–4227. https://doi.org/10.1002/2016JC011646

Chen, Z., Curchitser, E., Chant, R., & Kang, D. (2018). Seasonal variability of the cold pool over the Mid-Atlantic Bight continental shelf. *Journal of Geophysical Research: Oceans*, *123*(11), 8203–8226. https://doi.org/10.1029/2018JC014148

Chin, T. M., Vazquez-Cuervo, J., & Armstrong, E. M. (2017). A multi-scale high-resolution analysis of global sea surface temperature. *Remote Sensing of Environment*, *200*, 154–169. https://doi.org/10.1016/j.rse.2017.07.029

Fairbanks, R. G. (1982). The origin of continental shelf and slope water in the New York Bight and Gulf of Maine: Evidence from $H_2{}^{18}O/H_2{}^{16}O$ ratio measurements. *Journal of Geophysical Research*, *87*. https://doi.org/10.1029/JC087iC08p05796

Flagg, C. N., & Beardsley, R. C. (1978). On the stability of the shelf water/slope water front south of New England. *Journal of Geophysical Research*, *83*(C9), 4623–4631. https://doi.org/10.1029/JC083iC09p04623

Fratantoni, P. S., Pickart, R. S., Torres, D. J., & Scotti, A. (2001). Mean structure and dynamics of the shelfbreak jet in the Middle Atlantic Bight during fall and winter. *Journal of Physical Oceanography*, *31*(8), 2135–2156. https://doi.org/10.1175/1520-0485(2001)031<2135:MSADOT>2.0.CO;2

Garvine, R. W., Wong, K.-C., Gawarkiewicz, G. G., McCarthy, R. K., Houghton, R. W., & Aikman, F. III. (1988). The morphology of shelfbreak eddies. *Journal of Geophysical Research*, *93*(C12), 15593–15607. https://doi.org/10.1029/JC093iC12p15593

Gawarkiewicz, G., Brink, K. H., Bahr, F., Beardsley, R. C., Caruso, M., Lynch, J. F., & Chiu, C.-S. (2004). A large-amplitude meander of the shelfbreak front during summer south of New England: Observations from the Shelfbreak PRIMER experiment. *Journal of Geophysical Research*, *109*, C03006. https://doi.org/10.1029/2002JC001468

Gawarkiewicz, G., & Plueddemann, A. (2020). Scientific rationale and conceptual design of a process-oriented shelfbreak observatory: The OOI Pioneer Array. *Journal of Operational Oceanography*, *13*(1), 19–36. https://doi.org/10.1080/1755876X.2019.1679609

Hersbach, H., Bell, B., Berrisford, P., Hirahara, S., Horányi, A., Muñoz-Sabater, J., et al. (2020). The ERA5 global reanalysis. *Quarterly Journal of the Royal Meteorological Society*, *146*(730), 1999–2049. https://doi.org/10.1002/qj.3803

Houghton, R., Aikman, F., & Ou, H. (1988). Shelf-slope frontal structure and cross-shelf exchange at the New England shelf-break. *Continental Shelf Research*, *8*(5), 687–710. https://doi.org/10.1016/0278-4343(88)90072-6

Houghton, R., Schlitz, R., Beardsley, R., Butman, B., & Chamberlin, J. L. (1982). The Middle Atlantic Bight cold pool: Evolution of the temperature structure during summer 1979. *Journal of Physical Oceanography*, *12*(10), 1019–1029. https://doi.org/10.1175/1520-0485(1982)012<1019:TMABCP>2.0.CO;2

Joyce, T. M., Bishop, J. K., & Brown, O. B. (1992). Observations of offshore shelf-water transport induced by a warm-core ring. *Deep-Sea Research, Part A: Oceanographic Research Papers*, *39*, S97–S113. https://doi.org/10.1016/S0198-0149(11)80007-5

Ketchum, B., & Corwin, N. (1964). The persistence of "winter" water on the continental shelf south of Long Island, New York. *Limnology & Oceanography*, *9*(4), 467–475. https://doi.org/10.4319/lo.1964.9.4.0467

Lentz, S. J. (2003). A climatology of salty intrusions over the continental shelf from Georges Bank to Cape Hatteras. *Journal of Geophysical Research*, *108*(C10), 3326. https://doi.org/10.1029/2003JC001859

Lentz, S. J. (2008). Observations and a model of the mean circulation over the Middle Atlantic Bight continental shelf. *Journal of Physical Oceanography*, *38*(6), 1203–1221. https://doi.org/10.1175/2007JPO3768.1

Lentz, S. J. (2010). The mean along-isobath heat and salt balances over the Middle Atlantic Bight continental shelf. *Journal of Physical Oceanography*, *40*(5), 934–948. https://doi.org/10.1175/2009JPO4214.1

Lentz, S. J. (2017). Seasonal warming of the Middle Atlantic Bight cold pool. *Journal of Geophysical Research: Oceans*, *122*(2), 941–954. https://doi.org/10.1002/2016JC012201

Lentz, S. J., Shearman, K., Anderson, S., Plueddemann, A., & Edson, J. (2003). Evolution of stratification over the New England shelf during the Coastal Mixing and Optics study, August 1996–June 1997. *Journal of Geophysical Research*, *108*(C1), 3008. https://doi.org/10.1029/2001JC001121

Li, Y., Fratantoni, P. S., Chen, C., Hare, J. A., Sun, Y., Beardsley, R. C., & Ji, R. (2015). Spatio-temporal patterns of stratification on the Northwest Atlantic shelf. *Progress in Oceanography*, *134*, 123–137. https://doi.org/10.1016/j.pocean.2015.01.003

Linder, C. A., & Gawarkiewicz, G. (1998). A climatology of the shelfbreak front in the Middle Atlantic Bight. *Journal of Geophysical Research*, *103*(C9), 18405–18423. https://doi.org/10.1029/98JC01438

Lozier, M. S., & Gawarkiewicz, G. (2001). Cross-frontal exchange in the Middle Atlantic Bight as evidenced by surface drifters. *Journal of Physical Oceanography*, *31*(8), 2498–2510. https://doi.org/10.1175/1520-0485(2001)031<2498:CFEITM>2.0.CO;2

Marra, J., Houghton, R. W., & Garside, C. (1990). Phytoplankton growth at the shelf-break front in the Middle Atlantic Bight. *Journal of Marine Research*, *48*(4), 851–868. https://doi.org/10.1357/002224090784988665

McDougall, T. J., & Barker, P. M. (2011). *Getting started with TEOS-10 and the Gibbs Seawater (GSW) Oceanographic Toolbox* (p. 28). SCOR/IAPSO WG127.

Miller, T. J., Hare, J. A., & Alade, L. A. (2016). A state-space approach to incorporating environmental effects on recruitment in an age-structured assessment model with an application to southern New England yellowtail flounder. *Canadian Journal of Fisheries and Aquatic Sciences*, *73*(8), 1261–1270. https://doi.org/10.1139/cjfas-2015-0339

Mountain, D. G. (1991). The volume of shelf water in the Middle Atlantic Bight: Seasonal and interannual variability, 1977–1987. *Continental Shelf Research*, *11*(3), 251–267. https://doi.org/10.1016/0278-4343(91)90068-H

NSF Ocean Observatory Initiative. (2022). CTD data from Pioneer NES Array (cp03issm-sbd11-06-metbka000, cp01cnsm-sbd11-06-metbka000, cp01cnsm-sbd12-06-metbka000, cp04ossm-sbd11-06-metbka000, cp03issm-rid27-03-ctdbpc000, cp02pmui-wfp01-03-ctdpfk000) from 2015-05-09 to 2022-06-01 [Dataset]. https://erddap.dataexplorer.oceanobservatories.org/erddap/index.html

Ou, H. W., & Houghton, R. (1982). A model of the summer progression of the cold-pool temperature in the Middle Atlantic Bight. *Journal of Physical Oceanography*, *12*(10), 1030–1036. https://doi.org/10.1175/1520-0485(1982)012<1030:AMOTSP>2.0.CO;2

Ryan, S., Ummenhofer, C. C., & Gawarkiewicz, G. G. (2024). Seasonal and interannual salinity variability on the Northeast U.S. continental shelf: Insights from satellite sea surface salinity and implications for stratification. *Journal of Geophysical Research: Oceans*, *129*(11), e2024JC021534. https://doi.org/10.1029/2024JC021534

Seidov, D., Baranova, O. K., Boyer, T., Cross, S. L., Mishonov, A. V., & Parsons, A. R. (2016). Northwest Atlantic regional ocean climatology. *NOAA Atlas NESDIS*, *80*. https://doi.org/10.7289/V5/ATLAS-NESDIS-80

Shchepetkin, A. F., & McWilliams, J. C. (2005). The regional oceanic modeling system (ROMS): A split-explicit, free-surface, topography-following-coordinate oceanic model. *Ocean Modelling*, *9*(4), 347–404. https://doi.org/10.1016/j.ocemod.2004.08.002

Shearman, R. K., & Lentz, S. J. (2003). Dynamics of mean and subtidal flow on the New England shelf. *Journal of Geophysical Research*, *108*(C8), 3281. https://doi.org/10.1029/2002JC001417

Silver, A., Gangopadhyay, A., Gawarkiewicz, G., Fratantoni, P., & Clark, J. (2023). Increased Gulf Stream warm core ring formations contributes to an observed increase in salinity maximum intrusions on the Northeast Shelf. *Scientific Reports*, *13*(1), 7538. https://doi.org/10.1038/s41598-023-34494-0

Spall, M. A., & Chapman, D. C. (1998). On the efficiency of baroclinic eddy heat transport across narrow fronts. *Journal of Physical Oceanography*, *28*(11), 2275–2287. https://doi.org/10.1175/1520-0485(1998)028<2275:OTEOBE>2.0.CO;2

Sullivan, M. C., Cowen, R. K., & Steves, B. P. (2005). Evidence for atmosphere–ocean forcing of yellowtail flounder (Limanda ferruginea) recruitment in the Middle Atlantic Bight. *Fisheries Oceanography*, *14*(5), 386–399. https://doi.org/10.1111/j.1365-2419.2005.00343.x

Sundermeyer, M. A., & Ledwell, J. R. (2001). Lateral dispersion over the continental shelf: Analysis of dye release experiments. *Journal of Geophysical Research*, *106*(C5), 9603–9621. https://doi.org/10.1029/2000JC900138

Taenzer, L. L., Gawarkiewicz, G., & Plueddemann, A. (2023a). Categorization of high-wind events and their contribution to the seasonal breakdown of stratification on the southern New England shelf. *Journal of Geophysical Research: Oceans*, *128*(7), e2022JC019625. https://doi.org/10.1029/2022JC019625

Taenzer, L. L., Gawarkiewicz, G. G., & Plueddemann, A. J. (2023b). Gridded hydrography and bulk air-sea interactions observed by the ocean observatory initiative (OOI) Coastal Pioneer New England shelf mooring Array (2015-2022) [Dataset]. *Woods Hole Open Access Server*, *128*(7). https://doi.org/10.1029/2022JC019625

Todd, R. E. (2020). Export of Middle Atlantic Bight shelf waters near Cape Hatteras from two years of underwater glider observations. *Journal of Geophysical Research: Oceans*, *125*(4), e2019JC016006. https://doi.org/10.1029/2019JC016006

Warner, J. C., Sherwood, C. R., Arango, H. G., & Signell, R. P. (2005). Performance of four turbulence closure models implemented using a generic length scale method. *Ocean Modelling*, *8*(1), 81–113. https://doi.org/10.1016/j.ocemod.2003.12.003

Zhang, W. G., & Gawarkiewicz, G. G. (2015a). Dynamics of the direct intrusion of Gulf Stream ring water onto the Mid-Atlantic Bight shelf. *Geophysical Research Letters*, *42*(18), 7687–7695. https://doi.org/10.1002/2015GL065530

Zhang, W. G., & Gawarkiewicz, G. G. (2015b). Length scale of the finite-amplitude meanders of shelfbreak fronts. *Journal of Physical Oceanography*, *45*(10), 2598–2620. https://doi.org/10.1175/JPO-D-14-0249.1

James Boyle

From: Brian Collins <brian.c1@me.com>
Sent: Tuesday, July 22, 2025 12:12 PM
To: James Boyle
Subject: Re: [External] Menhaden Technical Committee Cancellation

Thanks yes please add me to the followers list

I am concerned that there are zero schools of Menhaden making it into the Bay past industrial fishing nets in the Bay into Maryland

I hear too much extrapolation of Ocean Menhaden science as applicable to the Bay - 2 distinct and separate ecosystems.

I appreciate the response and support!

Thanks, Brian

> On Jul 22, 2025, at 12:02 PM, James Boyle <JBoyle@asmfc.org> wrote:
>
> Hi Brian,
>
> Once we have the date, we will post it to the Commission's calendar (https://asmfc.org/events/). If you like, I can also add you to our Followers list to be notified when menhaden meetings are scheduled.
>
> The Management Board will be meeting from 8:30-9:30am on August 7th to continue discussing next steps in response to the Work Group Report on Precautionary Management in Chesapeake Bay. More information on submitting a public comment and attending the meeting, including a webinar registration link, can be found here: https://asmfc.org/events/2025-summer-meeting/.
>
> Best,
> James
>
> James Boyle (he/him) | FMP Coordinator Atlantic States Marine
> Fisheries Commission
> 1050 N. Highland Street, Suite 200 A-N Arlington, VA 22201
> Phone: 703.842.0715 | Fax: 703.842.0741 jboyle@asmfc.org |
> www.asmfc.org
>
>
>
> -----Original Message-----
> From: Brian Collins <brian.c1@me.com>
> Sent: Friday, July 18, 2025 4:43 PM
> To: James Boyle <JBoyle@ASMFC.org>
> Subject: [External] Menhaden Technical Committee Cancellation
>
> Hello James happy Friday. I just saw the meeting on Monday is canceled for Menhaden technical committee.
>
> What is the best way to find a reschedule date?

>
> What is the best way to find out what ASMFC plans to do to address the Menhaden and Osprey crisis in the Chesapeake Bay?
>
> Thanks, Brian
>
>
>
>
> CAUTION: This email originated from outside of the organization. Do not click links or open attachments unless you recognize the sender and know the content is safe.
CAUTION: This email originated from outside of the organization. Do not click links or open attachments unless you recognize the sender and know the content is safe.

From:	Tom Lilly
To:	John Clark; James Boyle; Bob Beal; Marty Gary; Allison Colden; Lynn Fegley; Russell Dize; Comments; Tina Berger
Cc:	Sen. Craig A. Miner; Robert Lafrance; William Hyatt; Justin Davis; Roy Miller; Rep. William J Carson; Jessica Mccawley; Erica.Burgess@myfwc.com; gjennings@asafishing.com; Spud Woodward; Doug Haymans; Carolyn N Belcher; Rep. Trey Rhodes; Stephen R. Train; David Sikorski; nichola.meserve@state.ma.us; Raymond Kane; Dennis Abbott
Subject:	[External] Ethical treatment of Maryland aka the "Golden Rule"
Date:	Friday, July 25, 2025 1:10:27 PM

Tina Please copy this to the menhaden board and policy board for the August meetings.

To John Clark chair of the menhaden board, James Boyle coordinator and all the board members

If I have this right, each of your states affected by menhaden from North Carolina up, except Virginia, have required that the factory fishing be in the US Atlantic zone to protect the ecology of your bays, rivers and coastal zone. You have seen spectacular results from the abundant menhaden now that the factory ships are gone. I think New York and New Jersey are the latest examples. But Maryland is the only state that cannot prevent the menhaden trying to migrate to it from being caught in Virginia. Only you can protect Maryland by requiring the factory fishing not be in the bay and Virginia coast but just in the US Atlantic zone.but you have not included that in your protective options for some reason.

Perhaps the oldest rule of ethics is the "Golden Rule". When I checked, I found that the origin of this is the sermon on the mount delivered by Jesus Christ more than 2500 years ago. Where he said " whatever you desire for men to do to you you shall also do to them…" Mathew 7….7-12.

So, am I out of line when I say to you that if you were to observe this "golden rule" of ethics, the first protective option that you should be considering is the same rule that you have taken advantage of to protect your fisherman and your ecology and that is moving the factory fishing out into the US Atlantic zone, which is providing you with so many benefits. Please think about this as you prepare for the meeting on August 7 and I would hope that one of you or all of you would join in a motion to protect Maryland using the same rule that you have used to protect yourselves. Sincerely Tom Lilly